



<https://theses.gla.ac.uk/>

Theses Digitisation:

<https://www.gla.ac.uk/myglasgow/research/enlighten/theses/digitisation/>

This is a digitised version of the original print thesis.

Copyright and moral rights for this work are retained by the author

A copy can be downloaded for personal non-commercial research or study,  
without prior permission or charge

This work cannot be reproduced or quoted extensively from without first  
obtaining permission in writing from the author

The content must not be changed in any way or sold commercially in any  
format or medium without the formal permission of the author

When referring to this work, full bibliographic details including the author,  
title, awarding institution and date of the thesis must be given

Enlighten: Theses

<https://theses.gla.ac.uk/>  
[research-enlighten@glasgow.ac.uk](mailto:research-enlighten@glasgow.ac.uk)

**NONLINEAR OPTICAL WAVEGUIDE DEVICES IN GaAs/AlGaAs**

A Thesis submitted to the  
Faculty of Engineering at the  
University of Glasgow  
for the degree of

**Doctor of Philosophy**

by

**Binderpal Singh Bhumbra**

**May, 1990.**

**© B. S. Bhumbra, 1990.**

ProQuest Number: 11007354

All rights reserved

INFORMATION TO ALL USERS

The quality of this reproduction is dependent upon the quality of the copy submitted.

In the unlikely event that the author did not send a complete manuscript and there are missing pages, these will be noted. Also, if material had to be removed, a note will indicate the deletion.



ProQuest 11007354

Published by ProQuest LLC (2018). Copyright of the Dissertation is held by the Author.

All rights reserved.

This work is protected against unauthorized copying under Title 17, United States Code  
Microform Edition © ProQuest LLC.

ProQuest LLC.  
789 East Eisenhower Parkway  
P.O. Box 1346  
Ann Arbor, MI 48106 – 1346

*In dedication to my parents*

## ACKNOWLEDGEMENTS

This thesis would never have been completed without the support and encouragement of my family. To them I am completely indebted.

I thank Dr. Charles Ironside for his continual supervision and invaluable guidance throughout the course of this project. His support is much appreciated. I also wish to thank Prof. Richard De La Rue for his advice and numerous words of wisdom and Dr. John Marsh for many helpful discussions. I owe much to Dr. Toshiaki Suhara of Osaka University, Japan, with whom I had the opportunity of working during his sabbatical at Glasgow. I learned much by experiencing the high standards of the Japanese way.

I appreciate the use of the facilities at the Department of Electrical Engineering and wish to thank Prof. John Lamb.

I am grateful to Dr. David Wight, Dr. John Heaton and Dr. Jerry Birbeck at the Royal Signals and Radar Establishment, Malvern, for providing me with facilities, help and material. I also thank Prof. Wilson Sibbett, Dr. Nigel Langford and Mr. Robert Grant at the Dept. of Physics, University of St. Andrews for their help and use of their laser facilities.

Many a crisis was prevented or mitigated by the help of Ray Hutchins. I therefore acknowledge his significant practical contribution to this project and his notable approach to race relations.

The help of the technical staff in the department was needed and gratefully received. Harry Anderson, George Boyle and Lois Hobbs deserve a special thanks.

Much support was given by my colleagues in the Ultra-Short Pulse Group. I thank Mary O'Neill, Norman Bett, Tom Cullen and John Bell. The camaraderie and friendship of many other fellow researchers in the department proved invaluable both practically and spiritually and did not go amiss.

This project was funded by an SERC CASE studentship with the Royal Signals and Radar Establishment.

# CONTENTS

<b><u>Acknowledgements</u></b>	(ii)
<b><u>Contents</u></b>	(iii)
<b><u>Summary of Thesis</u></b>	1
<b><u>Chapter One - Nonlinear Optical Waveguide Devices.</u></b>	2
1.1 Introduction	2
1.2 The Formalism of Classical Nonlinear Optics	2
1.3 Resonant and Non-resonant Nonlinearities	4
1.4 Relaxation Time Considerations	4
1.5 Nonlinear Optical Waveguide Devices	5
1.6 Contents of Thesis	8
1.7 References to Chapter One	9
<b><u>Chapter Two - Nonlinear Optical Effects in Semiconductors.</u></b>	12
2.1 Introduction	12
2.2 The Kramers-Kronig relations	12
2.3 Dynamic Nonlinear Effects	14
2.3.1 Plasma Theoretical models	14
2.3.2 Two-level saturation model	15
2.3.3 Band-filling and the Dynamic Burstein-Moss shift	16
2.3.4 Other theoretical models	18
2.4 Many-body effects	18
2.5 Multiple Quantum Well systems	19
2.5.1 Quantum confinement and excitonic absorption	19
2.5.2 Nonlinear Properties of MQWs	23
2.6 Thermal Effects	24
2.7 Conclusions	24
2.8 References to Chapter Two	24

<b><u>Chapter Three - Design of Multiple Quantum Well Waveguides.</u></b>	<b>27</b>
3.1 Introduction	27
3.2 Dielectric Waveguide Theory and Design	27
3.2.1 Three- and Four-layer slab waveguides	27
3.2.2 Computer modelling of the Four-layer slab	29
3.2.3 Two-dimensional waveguides	31
3.2.4 Summary of the design procedure for AlGaAs waveguides	33
3.3 The refractive index of MQW structures	35
3.3.1 Determination of the excitonic absorption energies	36
3.3.2 Application of the Kramers-Kronig relations to MQW structures	40
3.3.3 The Root-Mean-Square model	43
3.4 Waveguide structures designed in this thesis	43
3.5 Conclusions	45
3.6 References to Chapter Three	46
<b><u>Chapter Four - Wafer Processing and Waveguide Fabrication.</u></b>	<b>50</b>
4.1 Introduction	50
4.2 Material growth	50
4.2.1 Liquid Phase Epitaxy	50
4.2.2 Metal Organic Chemical Vapour Deposition	51
4.2.3 Molecular Beam Epitaxy	52
4.2.4 Conclusions and Growth Details of wafers used in this project	53
4.3 Material Analysis	53
4.3.1 Methods of Assessment	53
4.3.2 Photoluminescence studies	54
4.3.3 Photoluminescence data	57
4.4 Wafer Processing and Patterning	60
4.4.1 Wafer cleaning	61
4.4.2 Patterning of the photoresist	62
4.4.3 Metallisation	63
4.4.4 Cleaving of the sample	63
4.4.5 Back polishing of samples	64
4.5 Wet and Dry etching of Waveguides	65

4.5.1	Wet etching of AlGaAs	66
4.5.2	Reactive Ion Etching of AlGaAs	67
4.6	Summary and conclusions	68
4.7	References to Chapter Four	68

**Chapter Five - Waveguide Measurements.** 71

5.1	Introduction	71
5.2	The Ultra-short pulse laser system	71
5.2.1	The pump laser system	71
5.2.2	The dye laser system	73
5.2.3	The autocorrelator	74
5.2.4	Characterisation of the dye laser	76
5.2.5	Use of mNA for Second Harmonic Generation	78
5.3	Waveguide Characterisation	79
5.3.1	Endfire coupling	79
5.3.2	Observation of Guided modes	81
5.3.3	Loss measurements in AlGaAs waveguides	82
5.3.4	Loss measurements in MQW waveguides	86
5.3.5	Discussion of loss results in MQW structures	87
5.3.6	Conclusions on loss measurements	90
5.4	Nonlinear Characterisation of Waveguides	91
5.4.1	Self Phase Modulation	91
5.4.2	Interferometric Measurements of Nonlinear Refractive Index	95
5.4.3	Nonlinear Absorption in waveguides	97
5.4.4	Thermal and Carrier Diffusion effects	99
5.4.5	Pump-probe experiments	102
5.4.6	Summary of nonlinear measurements	104
5.5	Conclusions	104
5.6	References to Chapter Five	105

**Chapter Six - The Asymmetric Mach-Zehnder Interferometer.** 109

6.1	Introduction	109
6.2	The Asymmetric Mach-Zehnder Interferometer: a simple model	109

6.2.1	The Y-junction	110
6.2.2	The Scattering Matrix model	112
6.3	The BPM model	114
6.3.1	Application of the BPM	115
6.3.2	BPM analysis of the Asymmetric Mach-Zehnder Interferometer	118
6.4	Experimental Characterisation of the Asymmetric Mach-Zehnder Interferometer	120
6.4.1	Fabrication details	120
6.4.2	Splitting ratio measurements in Asymmetric Y-junctions	121
6.4.3	Experimental investigations of the AMZI	123
6.5	The Thermal Asymmetric Mach-Zehnder Interferometer	125
6.5.1	Fabrication details	125
6.5.2	Testing of thermal properties in straight waveguides	126
6.5.3	Theoretical considerations	127
6.5.4	Thermally induced switching in the AMZI	131
6.6	Conclusions	132
6.7	References to Chapter Six	133

**Chapter Seven - Conclusions.** 135

7.1	Summary of thesis	135
7.2	Conclusions and suggestions for future work	135

**Appendices**

I	Derivation of the eigenvalue equation for a single finite well with change of mass included in boundary conditions.	A1
II	Program Listings	A4
III	Wafer Specifications	A18
IV	Relevant Publications	A22

## SUMMARY OF THESIS.

This thesis is concerned with the design, characterisation and implementation of an all-optical logic waveguide device. Operation of such a device depends crucially on the fact that it includes a nonlinear material whose refractive index changes if it is subjected to sufficiently intense optical excitation. (This intensity dependence of the refractive index is often expressed by the relation  $n = n_0 + n_2 I$ , where  $n_0$  is the low intensity refractive index,  $n_2$  is the nonlinear coefficient, and  $I$  is the intensity of the incident optical radiation.) The optically induced variation in the refractive index is transformed into a nonlinearity in the device transmission by use of certain waveguide properties thus enabling the device to perform all-optical logic operations. The particular work in this thesis concentrates on the Asymmetric Mach-Zehnder Interferometer (AMZI) which is described in Chapter One. The nonlinear material used in this thesis is  $\text{Al}_x\text{Ga}_{1-x}\text{As}$  because (i), waveguide fabrication technology in this material is well established and reliable, and (ii), the material has a significant optical nonlinearity easily accessible with laser radiation.

The thesis begins by introducing nonlinear optical waveguide devices. Chapter Two then reviews the various optical nonlinearities in semiconductors and presents the current theoretical models available for the description of these effects. Chapter Three describes the nonlinear waveguide design process. Included in this chapter are considerations which have to be made for the attainment of optimum optical nonlinear effects. Chapter Four contains the device fabrication details and describes the considerations made during device production. The results of linear and nonlinear characterisation of waveguides are presented in Chapter Five where descriptions of the various experimental details are also given. The Asymmetric Mach Zehnder Interferometer is then examined in Chapter Six where results of both the theoretical and experimental studies are presented. Finally, in Chapter Seven, the conclusions are presented and suggestions for future work are given.

# CHAPTER ONE

## NONLINEAR OPTICAL WAVEGUIDE DEVICES

### 1.1 Introduction.

It is almost three decades since the invention of the laser sparked off a renewed interest in optical physics. Since then, much theoretical and experimental work has been done in many fields. In particular, the advantages of optical communication have become apparent and a tremendous effort has been injected into the implementation of such systems. One of the most important components of an optical communications system is the optical waveguide. Optical energy is confined in a waveguide and can be efficiently transmitted over distances without being limited by diffraction. There are generally two categories of waveguide in use today. These are: (i) optical fibres which are used to transmit signals over distances ranging from perhaps a metre to hundreds of kilometres, or (ii) integrated optical waveguides which are produced in optical chips and may vary in length from a few tens of microns to a few centimetres.

In parallel with the development in optical communications technology, laser light sources have made available large optical field strengths which are comparable with interatomic fields ( $\approx 3 \times 10^8 \text{ V cm}^{-1}$  [1]). Intense fields cause changes in the dielectric properties of materials and this has brought to attention many interesting and useful nonlinear phenomena. The study of these properties is known as *Nonlinear Optics*. In optical waveguides, it is possible to maintain high optical power densities over long distances and this enhances the nonlinear interaction of the optical field with the guiding material. This makes the optical waveguide particularly useful for the implementation of nonlinear optical devices.

### 1.2 The Formalism of Classical Nonlinear Optics.

It is necessary to first establish some definitions pertaining to the nonlinear properties of optical materials. Consider what happens in an insulating dielectric medium when it is subjected to optical excitation. On applying an electric field, the positive and negative charge distributions in the material are displaced in opposite directions and a dipole moment is induced. The dipole moment per unit volume, or polarisation,  $\mathbf{P}$ , is proportional to *small* applied fields and can be expressed as

$$\mathbf{P} = \epsilon_0 \chi \mathbf{E} \quad (1.2.1)$$

where  $\epsilon_0$  is the dielectric constant,  $\chi$  is the electric susceptibility and  $\mathbf{E}$  is the incident electric field. The optical field driving the dipole is sinusoidal and therefore, for small incident fields, the induced polarisation is varying similarly. However, by using an intense optical field and "overdriving" the dipoles, it is possible to obtain a nonsinusoidally varying polarisation. When this is the case higher optical harmonics are introduced in the polarisation field produced by the oscillating dipoles. The energy of the incident electric field has therefore been coupled to fields of different frequency by the nonlinear response of the dipoles. Under these conditions, equation (1.2.1) is no longer valid and has to be modified to include the higher frequency terms. The equation can then be rewritten as

$$\frac{1}{\epsilon_0} P_i = \sum_j \chi_{ij}^{(1)} E_j(\omega_j) + \sum_{j,k} \chi_{ijk}^{(2)} E_j(\omega_j) E_k(\omega_k) + \sum_{j,k,l} \chi_{ijkl}^{(3)} E_j(\omega_j) E_k(\omega_k) E_l(\omega_l) + \dots \quad (1.2.2)$$

where  $P_i$  is the component of  $\mathbf{P}$  in direction  $i$ ,  $\chi^{(n)}$  is the  $n$ th term in the susceptibility tensor and couples together  $n$  electric fields  $E_j, \dots, E_z$  of angular frequencies  $\omega_j, \dots, \omega_z$  where  $z$  is the  $n$ th label. This equation is the formal starting point of nonlinear optics. Note that the term 'nonlinear' pertains to the susceptibility which is no longer a constant of proportionality as in equation (1.2.1). The different orders of  $\chi^{(n)}$  couple together electric fields of different frequencies and are associated with different nonlinear phenomena including second and third harmonic generation, three- and four-wave mixing, Pockels (linear electro-optic) effect and the intensity dependant refractive index. These various effects and their associated frequencies are listed in figure 1.1 from Miller et al[2]. The actual values of  $\chi^{(n)}$  are dependant on the material. This thesis is mainly concerned with the intensity dependant refractive index which arises from the  $\chi^{(3)}$  term in equation (1.2.2). It is often more convenient to express the intensity dependant refractive index in the form

$$n = n_0 + n_2 I \quad (1.2.3)$$

where  $n_0$  is the low intensity value,  $n_2$  is the nonlinear coefficient and  $I$  is the intensity. The value of  $n_2$  is often quoted instead of  $\chi^{(3)}$  when quantifying third order nonlinearities in materials. It should be noted that  $n_2$  is not necessarily a constant and may indeed saturate at sufficiently large intensities. It can be shown

Frequencies of incident fields	Frequencies of fields generated by the nonlinear polarisation	Relation between fields	Susceptibility	Nonlinear process
$\omega_1$	$\omega_1$		$\chi^{(1)}$	linear dispersion
$\omega_1, \omega_2$	$\omega_3$	$(\omega_3 = \omega_1 + \omega_2)$	$\chi^{(2)}$	Sum mixing
$\omega_1$	$\omega_3$	$(\omega_3 = 2 \omega_1)$	$\chi^{(2)}$	Second Harmonic Generation
$\omega_1, 0$	$\omega_1$		$\chi^{(2)}$	Electro-optic linear Kerr effect
$\omega_1$	$\omega_2, \omega_3$	$(\omega_1 = \omega_2 + \omega_3)$	$\chi^{(2)}$	Difference-frequency mixing
$\omega_1$	$\omega_2$	$(\omega_1 = 2 \omega_2)$	$\chi^{(2)}$	Degenerate difference frequency
$\omega_1$	$\omega_4$	$(\omega_1 = 3 \omega_4)$	$\chi^{(3)}$	Third Harmonic Generation
$\omega_1, \omega_2, \omega_3$	$\omega_4$	$(\omega_4 = \omega_1 + \omega_2 + \omega_3)$	$\chi^{(3)}$	Four-wave difference-frequency mixing processes
$\omega_1, \omega_2$	$\omega_3, \omega_4$	$(\omega_1 + \omega_2 = \omega_3 + \omega_4)$	$\chi^{(3)}$	
$\omega_1$	$\omega_2, \omega_3, \omega_4$	$(\omega_1 = \omega_2 + \omega_3 + \omega_4)$	$\chi^{(3)}$	
$\omega_1$	$\omega_1$		$\chi^{(3)}$	Intensity-dependant refractive index
$\omega_1, 0$	$\omega_1$		$\chi^{(3)}$	Quadratic Kerr Effect

Summary of 1st, 2nd and 3rd order passive nonlinear optical processes.  
 (After Miller et al [2])

Figure 1.1

that  $n_2$  and  $\chi^{(3)}$  are related by the following expressions for S.I. and e.s.u. units.[1]:

$$n_2 \text{ (cm}^2/\text{W)} = \frac{1}{3} \left[ \frac{4\pi}{n_o} \right]^2 \chi^{(3)} \quad (\text{e.s.u.}) \quad (1.2.4a)$$

or

$$n_2 \text{ (S.I.)} = \frac{\chi^{(3)}}{n_o^2 2 c \epsilon_o} \quad (\text{S.I.}) \quad (1.2.4b)$$

### 1.3 Resonant and Non-resonant Nonlinearities

In the above description of nonlinear optical effects, only classical nonlinear effects have been considered, i.e. those effects where the nonlinear dipole moment couples optical fields of different frequencies. In semiconductors however, there are also additional effects occurring. When photons of energy close to, or larger than, the bandgap are incident on a semiconductor, a photoexcited carrier population is induced. The presence of these carriers modifies the dielectric constant and consequently alters the material's refractive index. These carrier dependant effects are to be reviewed more fully in Chapter Two.

Carrier effects tend to be resonant because of their dependance on the photon energy of the incident radiation. For this reason, the carrier effects are also described as *Resonant* effects as opposed to the classical *Nonresonant* effects arising from the nonlinear dipole moment. Resonant effects can of course also be expressed in terms of the classical formalism and a value of  $\chi^{(3)}$  associated with carrier dependant nonlinearities can be obtained. Because resonant effects depend on carrier population density, the relaxation time of the nonlinearity is determined by the relaxation time of the excited carriers. This is of the order of 10ns compared with the relaxation time of a few femtoseconds for the nonresonant effect. As well as being slower, resonant effects also generally tend to be larger than nonresonant effects. Figure 1.2 compares values of  $n_2$  and the relaxation time,  $\tau$ , for some materials.

### 1.4 Relaxation Time consideration.

It should be mentioned that the nature of the laser excitation and the relaxation time of the nonlinearity play an important role in determining the character of the nonlinear effect. Assuming that the nonlinear material is subjected to a pulsed laser source, if the relaxation time of the nonlinearity is larger than

Material	Effect	$n_2$ ( $m^2/W$ )	$\tau$ (s)	Ref
Silica	Nonres	$3 \times 10^{-21}$	$10^{-14} - 10^{-15}$	[3]
GaAs	Nonres	$4 \times 10^{-18}$	$10^{-14} - 10^{-15}$	[3]
InSb	Nonres	$2.3 \times 10^{-16}$	$10^{-14} - 10^{-15}$	[3]
Semiconductor -Doped Glass	Res	$-10^{-15} - 10^{-13}$	$10^{-11}$	[4]
GaAs	Res	$-2 \times 10^{-10}$	$\approx 10^{-8}$	[5]
(GaAs/AlGaAs) MQW	Res	$-10^{-9}$	$\approx 10^{-8}$	[10]

Figure 1.2

A comparison of  $n_2$ 's and  $\tau$ 's for some nonlinear materials

the pulse width, then the effect is integrated over the duration of the pulse so that the size of the net effect depends on the energy of the pulse. If, however, the relaxation time of the nonlinearity is much less than the pulse width, then the effect is proportional to the instantaneous intensity of the pulse. It is thus possible to make a distinction between energy dependant and intensity dependant effects.

### 1.5 Nonlinear Optical Waveguide Devices.

The nonlinear properties of optical materials make it possible to produce all-optical switching devices. These can be classed into one of two categories depending on whether or not their operation depends on feedback. Nonlinear devices whose operation depends on an inherent feedback generally exhibit nonlinear transmission and transmission hysteresis effects. These types of devices are said to possess *Optical Bistability*. In such devices it is the physical state of the entire device which determines the logical state of the output. This means that such devices can only process one bit of information at a time. Furthermore, if multiple beam passes are necessary for a logical output (e.g. as in a Fabry-Perot cavity) then the switching speed is limited by the minimum length of pulse required to provide the multiple passes. However, both of these limitation can be overcome by using devices which do not require feedback. Under these conditions the response time of the device is limited solely by the relaxation time of the material nonlinearity. Such an all-optical switch can be implemented by suitably configured nonlinear waveguides. In a nonlinear waveguide, an increase in the intensity of

guided light results in a change in the refractive index of the waveguide. This correspondingly modifies the propagation constant of the guided mode. In fact, if the refractive index change is large enough then this may result in a significant modification in the optical field distribution of the guided mode. However, for this to occur, the nonlinear refractive index change has to be comparable to the index step defining the waveguide. (This is of the order of  $10^{-4}$  in the GaAs/AlGaAs based devices examined in this project.) The operation of most nonlinear devices does not depend on such large changes in the refractive index but more so on smaller changes which modify the waveguide propagation constant.

The most thoroughly investigated (non-Bistable) nonlinear waveguide device to date is undoubtedly the *Nonlinear Directional Coupler (NLDC)* as proposed by Jensen<sup>[7]</sup> in 1982. A linear directional coupler consists of two closely spaced parallel waveguides. Power propagating in one waveguide is eventually coupled into the second after a characteristic interaction length  $L_c$ . However, for a complete power exchange to occur, it is essential that the two waveguides are phase-matched and this requires that both waveguides possess identical propagation constants. In the nonlinear version of this device, it is possible to alter the propagation constant of the first waveguide if the guided light is sufficiently intense. The phase matching and hence the energy transfer between the two guides is consequently reduced. The NLDC thus exhibits an intensity dependant transmission and can be configured as an all-optical switch.

Successful operation of this device was first reported in 1985 by Li-Kam-Wa et al<sup>[6]</sup> in a directional coupler based on strain induced waveguides in an AlGaAs multiple quantum well structure. Since then there have been several reports of observed switching in NLDCs. S. R. Friberg et al<sup>[8]</sup> observed 100fsec switching in a dual core silica fibre. (This, of course, makes use of the nonresonant Kerr-type nonlinear effect.) There have also been other results pertaining to NLDCs fabricated in AlGaAs multiple quantum well waveguides. M. Cada et al<sup>[9]</sup> report switching in two coupled slab waveguides. Berger et al<sup>[10]</sup> employed a similar structure but a rib was etched through the two guiding layers to form a vertical directional coupler. R. Jin et al<sup>[11]</sup> go further and report results of time resolved measurements on a picosecond timescale and showed switching times to be less than 10ps. The latter device was based on a stripe-loaded waveguide geometry. Finlayson et al<sup>[12]</sup> have observed switching in an NLDC based on semiconductor-doped-glass waveguides<sup>[4]</sup>. However, switching in this was attributed to a saturation of absorption and not due to nonlinear coupling. The key experimental features of these different NLDCs are summarised below in figure 1.3.

It should be realised that in the case of the AlGaAs based devices, the device geometry and the nature of the laser source play an important part in determining

the device speed and the effective size of the nonlinearity. These factors arise from carrier lifetime and diffusion effects as well as on the thermal properties of the structure. (These effects are discussed in Chapters Five and Six.)

The device of particular interest in this thesis is the *Asymmetric Mach-Zehnder interferometer*. This consists of a waveguide which is split in an asymmetric manner by an asymmetric Y-junction (see Figure 1.4(a)) so that a differential nonlinear phase-shift occurs between the two arms of the device. The power coupled into the output waveguide depends on the relative phases of the two beams incoming from each of the branches and the device therefore serves as an intensity dependant optical switch. This particular configuration of the Mach-Zehnder interferometer is one which, to the author's knowledge, has not been investigated before. However, other versions of nonlinear Mach-Zehnder devices have been examined. Indeed, switching was reported in this device before the first observation of switching in a NLDC. This was in a device fabricated in  $\text{LiNbO}_3$  in 1983 by Lattes et al<sup>[13]</sup> and is shown in figure 1.4(b). The device was

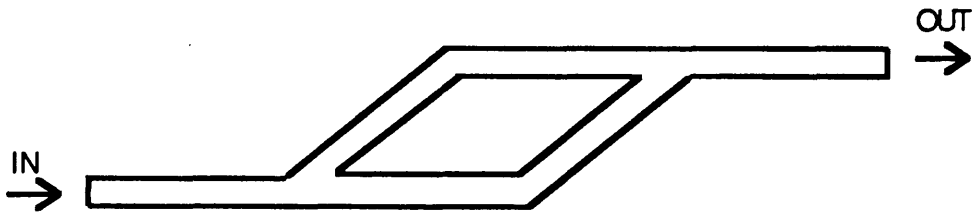
Device	Res/ NonRes	Speed	$n_2$	Switching Power/ Energy	Ref
MQW strain waveguides	Res	-	$10^{-7}$ $\text{cm}^2/\text{W}$	1mW	[6]
Dual Core Fibre	Nonres	<100fs		900W	[8]
MQW slab waveguides	Res	-	-	$16\mu\text{W}$	[9]
MQW vertically aligned waveguides	Res	-	$1.67 \times 10^{-5}$ $\text{cm}^2/\text{W}$	$6.8\mu\text{W}$	[10]
MQW strip- loaded waveguides	Res	<10ps	-	400pJ/ 40W	[11]
SDG waveguides	Res	<30ps		1nJ/500W	[12]

Figure 1.3

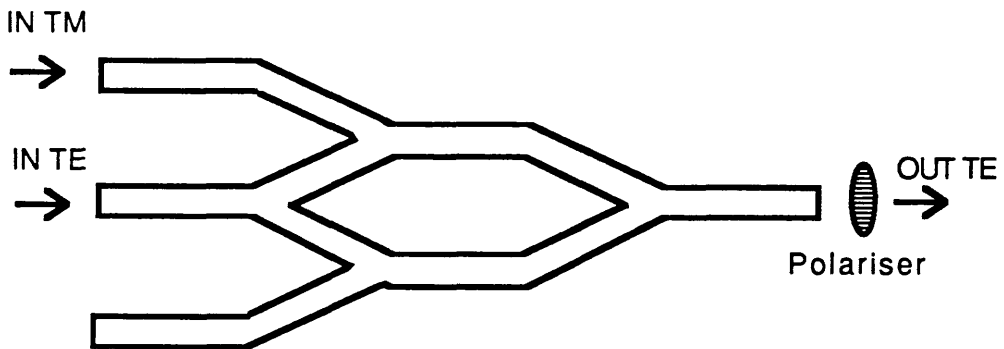
Summary of NLDC's investigated to date.

symmetric but included one other input waveguide coupled into each of the arms.

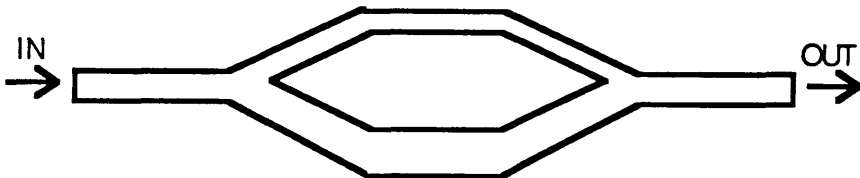
## Integrated Nonlinear Mach-Zehnder Interferometers



(a) the device investigated in this thesis



(b) the device investigated by Lattes et al [13].



(c) the device investigated theoretically  
by Thylen et al [13]

The figure shows three types of nonlinear Mach-Zehnder interferometers. The operation of each device depends on the presence of an intensity imbalance between the two arms. In device (a) this is provided by the asymmetrically angled Y-junction. In (b), extra power can be coupled into any one of the arms via the additional input waveguides, and in (c), different widths of the arms results in an intensity imbalance.

Figure 1.4

A differential phase shift could thus be induced by coupling another beam into one of the arms. There has also been theoretical work done on other configurations of the asymmetric Mach–Zehnder. H. Kawaguchi<sup>[14]</sup> has proposed a fibre based device where the arms of the device consists of two fibres of different lengths. The difference in fibre lengths results in the necessary differential nonlinear interaction which causes the nonlinear switching. An integrated optical device was analysed by L. Thylen et al<sup>[15]</sup> where the two arms of the device comprised of waveguides of different widths (see figure 1.4(c)). Switching arises from the differing power densities and hence the differing index changes in the two arms. An interesting point made by these latter authors was that the Mach–Zehnder type device is more power efficient than the NLDC. The reason for this is that, although both devices depend on a differential phase shift between two waveguides, in the NLDC there is some "useless" length where the powers are comparable in both guides. In this region the induced nonlinearity does not contribute to the switching action of the device. A more recent theoretical investigation of a nonlinear Mach–Zehnder device in GaAs has been carried out by W. M. Gibbons and D. Sarid<sup>[16]</sup> where the structures shown in figures 1.4(b) and 1.4(c) were analysed.

As far as other nonlinear (and non–bistable) devices are concerned there has been very little experimental work done<sup>[17,18]</sup> and most effort has been directed at the Nonlinear Directional Coupler and the Nonlinear Mach–Zehnder devices.

## 1.6 Contents of this thesis.

The material chosen for the nonlinear waveguide work in this thesis was AlGaAs. This is well suited for the implementation of nonlinear waveguide devices. Waveguide fabrication in AlGaAs is a fairly routine procedure and depends on well established technologies. Furthermore, the material has been noted for its nonlinear properties<sup>[2]</sup> which can be enhanced if quantum confinement effects are introduced by use of multiple quantum well (MQW) structures<sup>[19]</sup>.

This thesis is a study of nonlinear optical effects in AlGaAs and the particular application of these effects to the Asymmetric Mach–Zehnder Interferometer (AMZI). Investigations of nonlinear effects in bulk AlGaAs as well as Multiple Quantum Well structures have been carried out. Chapter Two begins by reviewing the various resonant carrier induced optical nonlinearities in semiconductors and presents the current theoretical models available for the description of these effects. Chapter Three describes the nonlinear waveguide design process. Included in this chapter are considerations which have to be made for the attainment of optimum

optical nonlinear effects. Chapter Four contains the device fabrication details and describes the considerations made during device production. The results of linear and nonlinear characterisation of waveguides are presented in Chapter Five where descriptions of the various experimental details are also given. The Asymmetric Mach Zehnder Interferometer is then examined in Chapter Six where results of both the theoretical and experimental studies are presented. Finally, in Chapter Seven, the conclusions are presented and suggestions for future work are given.

### 1.7 References to chapter one.

- [1] Y. R. Shen, "Principles of Nonlinear Optics", J. Wiley, New York, 1984.
- [2] A. Miller, D. A. B. Miller, S. D. Smith, "Dynamic non-linear processes in semiconductors", Adv. Phys., vol 30, no 6, 1981.
- [3] Y. T. Chang, "Fast self-induced refractive index changes in optical media: a survey", Opt. Eng., vol 20, no 2, pp220-232, 1981.
- [4] C. N. Ironside, T. J. Cullen, B. S. Bhumbra, J. Bell, W. C. Banyai, N. Finlayson, C. T. Seaton, G. I. Stegeman, "Nonlinear optical Effects in ion-exchanged semiconductor-doped glass waveguides", J. Opt. Soc. Am. B, vol 5, no 2, pp492-495, 1988.
- [5] S. W. Koch, N. Peyghambarian, H. M. Gibbs, "Band-edge nonlinearities in direct-gap semiconductors and their application to optical bistability and optical computing", J. Appl. Phys., vol 63, no 2, 1988.
- [6] P. Li-Kam-Wa, J. H. Marsh, P. N. Robson, J. S. Roberts, N. J. Mason, "Nonlinear propagation in GaAs/GaAlAs MQW waveguides", SPIE proc., vol 578, pp110-115, 1985.
- [7] S. M. Jensen, "The Nonlinear Coherent Coupler", IEEE J. Quant. Elec., vol QE-18, no 10, 1982.
- [8] S. R. Friberg, A. M. Weiner, Y. Silberberg, B. G. Sfez, P. W. Smith, "Femtosecond switching in a dual-core-fibre nonlinear coupler", Opt. Lett., vol 13, no 10, pp904-908, 1988.

- [9] M. Cada, B. P. Keyworth, J. M. Glinski, A. J. Springthorpe, P. Mandeville, "Experiment with multiple quantum well waveguide switching element", *J. Opt. Soc. Am. B.*, vol 5, no 2, pp462–465, 1988.
- [10] P. R. Berger, Y. Chen, P. Bhattacharya, J. Pamulapati, G. C. Vezzoli, "Demonstration of all-optical modulation in a vertical guided-wave nonlinear coupler", *Appl. Phys. Lett.*, vol 52, no 14, 1988.
- [11] R. Jin, C. L. Chuang, H. M. Gibbs, S. W. Koch, J. N. Polky, G. A. Pubanz, "Picosecond all-optical switching in single mode GaAs/AlGaAs strip-loaded nonlinear directional couplers", *Appl. Phys. Letts.*, vol 53, no 19, pp1791–1793, 1988.
- [12] N. Finlayson, W. C. Banyai, E. M. Wright, C. T. Seaton, G. I. Stegeman, T. J. Cullen, C. N. Ironside, "Picosecond switching induced by saturable absorption in a nonlinear directional coupler", *Appl. Phys. Lett.*, vol 53, no 13, pp1144–1146, 1988.
- [13] A. Lattes, H. A. Haus, F. J. Leonberger, E. Ippen, "An Ultrafast All-optical Gate", *IEEE J. Quant. Elec.*, vol QE-19, no 11, pp1718–1723, 1983.
- [14] H. Kawaguchi, "Proposal for a new all-optical waveguide functional device", *Opt. Lett.*, vol 10, no 8, pp411–413, 1985.
- [15] L. Thylen, N. Finlayson, C. T. Seaton, G. I. Stegeman, "All-optical guided-wave Mach-Zehnder switching device", *Appl. Phys. Lett.*, vol 51, no 17, pp1304–1306", 1987.
- [16] W. M. Gibbons, D. Sarid, "Model of a Nonlinear Mach-Zehnder interferometer in Gallium Arsenide", *Optical Bistability IV*, Aussois, France, March 1988.
- [17] G. I. Stegeman, E. M. Wright, N. Finlayson, R. Zanoni, C. T. Seaton, "Third Order Nonlinear Integrated Optics", *J. Lightwave Tech.*, vol 6, no 6, pp953–970, 1984.
- [18] P. Sabini, N. Finlayson, G. I. Stegeman, "All-optical switching in

nonlinear X junctions", Appl. Phys. Lett., vol 55, no 12, pp1176-1178, 1988.

[19] D. S. Chemla, D. A. B. Miller, P. W. Smith, A. C. Gossard, W. Weigmann, "Room Temperature Excitonic Nonlinear Absorption and Refraction in GaAs/AlGaAs Multiple Quantum Well Structures", IEEE J. Quant. Elec., vol QE-20, no 3, 1984.

## CHAPTER TWO

### NONLINEAR OPTICAL EFFECTS IN SEMICONDUCTORS

#### 2.1 Introduction.

It was explained in the previous chapter that the nonlinear optical properties of semiconductors are enhanced by the interaction of the electric field with carriers. The nature of this interaction depends both on the material and the photon energy of the incident field. In particular, the nonlinear properties of semiconductors may be significantly enhanced by the presence of carrier quantum confinement as is the case in Multiple Quantum Well (MQW) structures. This chapter presents a review of the different mechanisms which account for nonlinear carrier dependant effects in III–V semiconductors. These carrier effects are discussed in this chapter and descriptions are given of the theoretical models adopted for the calculation of these nonlinearities. Note that the effects discussed in this chapter are resonant effects.

#### 2.2 The Kramers–Kronig relations.

The Kramers–Kronig integrals relate the real and imaginary parts of a response function. These can be applied to dielectrics to give a relation between the real and imaginary parts of the refractive index. Consider a response function  $\epsilon(\omega)$  for a system where an output  $Y(t)$  corresponds to an input  $X(t)$  such that  $Y(t) = \epsilon X(t)$ . Now if this function is linear, i.e.  $c_1 Y_1 + c_2 Y_2 = \epsilon(c_1 X_1 + c_2 X_2)$ , and obeys the principle of causality, (i.e. if  $X(t)=0$  for  $t < t_0$ , then  $Y(t)=0$  for  $t < t_0$ ), then it is possible to relate the real and imaginary parts of this function by the Kramers–Kronig relations<sup>[1]</sup>. The case of interest is when  $\epsilon(\omega) = \epsilon_1(\omega) + i\epsilon_2(\omega)$  is the dielectric constant<sup>[2]</sup>, and  $X(t)$  and  $Y(t)$  are the electric field  $\mathbf{E}$  and the polarisability  $\mathbf{P}$  respectively. In this case the Kramers–Kronig relations are

$$\epsilon_1(\omega) - 1 = \frac{2}{\pi} P \int_0^{\infty} \frac{\omega' \epsilon_2(\omega')}{(\omega')^2 - \omega^2} d\omega' \quad (2.2.1)$$

$$\epsilon_2(\omega) = -\frac{2}{\pi} P \int_0^{\infty} \frac{\epsilon_1(\omega')}{(\omega')^2 - \omega^2} d\omega' \quad (2.2.2)$$

where  $P$  denotes the Cauchy principal value. These relations can be applied to

conductors if an additional term  $\sigma/\omega$  is included in  $\epsilon_2$ . Equation (2.2.2) then becomes[2]

$$\epsilon_2(\omega) - \frac{\sigma}{\omega} = -\frac{2}{\pi} P \int_0^{\infty} \frac{\epsilon_1(\omega')}{(\omega')^2 - \omega^2} d\omega' \quad (2.2.3)$$

The analogue to equation (2.2.1) for the complex refractive index  $n(\omega) + ik(\omega)$  is

$$n(\omega) - 1 = \frac{2}{\pi} P \int_0^{\infty} \frac{\omega' k(\omega')}{\omega'^2 - \omega^2} d\omega' \quad (2.2.4)$$

( $k$  is related to the absorption coefficient:  $\alpha = 2\omega k/c$ .) This equation is of considerable significance since it implies that if there is a change in the absorption, then there is a corresponding change in refractive index. In semiconductor nonlinear optics, the most important third-order ( $\chi^{(3)}$ ) nonlinear effects can be understood in terms of changes in absorption.

It is important to realise that the Kramers-Kronig equations only relate the real and imaginary parts of a linear response function. In a passive nonlinear optical system (i.e. one in which no real carrier population change is induced) these equations are invalid because the susceptibility,  $\chi$ , does not relate  $\mathbf{E}$  and  $\mathbf{P}$  linearly. However the situation is somewhat different when considering carrier induced refractive index changes in semiconductors. Photons of energy close to that of the bandgap will excite electrons (or holes) into the conduction (or valence) band. As will be seen later in the chapter, these excited carriers cause a change in the absorption and, consequently, a change in the refractive index. The excited carrier distribution within the bands stabilises to a thermal distribution within about 50–100 femtoseconds[3] after the excitation and remains like this until the excited carriers recombine. The carrier recombination time is of the order of 10ns for GaAs[4] and therefore the carrier distribution (and hence the absorption) remains unchanged for about a million or more optical cycles. The carriers are said to be in a state of *quasi-equilibrium* and during this time, because the absorption is unchanged, it is correct to say that the original dielectric response function  $\epsilon$  is modified to a new **linear** form. This satisfies the validity condition of the Kramers-Kronig relations. Kramers-Kronig relations are therefore valid before and after excitation as long as the carriers within the bands have attained a state of quasi-equilibrium.

The absorption spectra of the material for these two states can be denoted as  $\alpha_1(E)$  and  $\alpha_2(E)$  respectively and the corresponding refractive indices, as obtained by equation (2.2.4), are  $n_1(E)$  and  $n_2(E)$  respectively. It is therefore possible to

relate  $\alpha_1 - \alpha_2$  to  $n_1 - n_2$ , which are denoted  $\Delta\alpha$  and  $\Delta n$  respectively, by subtraction of equation (2.2.4) for each of the two cases.

$$\Delta n(E) = \frac{ch}{2\pi^2} P \int_0^\infty \frac{\Delta\alpha(E')}{(E')^2 - E^2} dE' \quad (2.2.5)$$

This latter equation means that it is only necessary to measure a *change* in absorption to calculate the *change* in refractive index. Usually, in nonlinear experiments, the absorption change is localised to a small part of the spectrum and so the complete absorption spectrum does not need to be measured. The index change can be calculated by performing the integral (2.2.5) over this restricted integration range.

It should be mentioned that if the change in induced carrier population is large then there is a corresponding index change due to the change in the electron-hole plasma density. This will be discussed later in the chapter. This relates to the conductivity term in equation (2.2.3). Also, the increase in the number of free carriers leads to a change in the free carrier absorption and an additional nonresonant index change<sup>[5]</sup>. These effects are smaller than the effects due to changes in absorption when close to the bandgap.

## 2.3 Dynamic Nonlinear effects.

Refractive index changes caused by a change in real carrier populations are often termed *dynamic* nonlinear effects since their characteristics are determined by the dynamics of carriers. These differ from *passive* effects where the effect is due to the nonlinear polarisability of dipoles. In this section, some of the physics of observed nonlinear effects in bulk semiconductors is discussed. In particular, expressions for the nonlinear coefficient  $n_2$ , are obtained for different conditions of excitation.

### 2.3.1 Plasma Theoretical models.

The free carriers in a semiconductor can be likened to an ionised gas or plasma where the absorption of photons results in a change in the plasma density. The complex dielectric constant of a plasma is dependant on the density of charged particles. Therefore by modelling the excited carriers in semiconductors by

a plasma, the nonlinear coefficient can be calculated. The refractive index of a free carrier plasma at photon energy  $\hbar\omega$  is given by [6]

$$n^2 = 1 - \frac{Ne^2}{\epsilon_0 m^* \omega^2} \quad (2.3.1.1)$$

where  $N$  is the free carrier density,  $m^*$  is the effective mass of the carriers,  $e$  is the electronic charge and  $\epsilon_0$  is the free space permittivity. Since the energy absorbed per unit volume is  $\alpha I$ , the density of photo-excited carriers is given by

$$N = \frac{\alpha I \tau_r}{\hbar\omega} \quad (2.3.1.2)$$

where  $\tau_r$  is the carrier recombination time. The change in the refractive index of a free carrier plasma can therefore be expressed by combining (2.3.1.1) and (2.3.1.2) as

$$\Delta n = - \frac{\alpha I \tau_r e^2}{2 \hbar \omega^3 \epsilon_0 n_0 m^*} \quad (2.3.1.3)$$

And since  $\Delta n = n_2 I$ ,  $n_2$  can be written as

$$n_2(\text{plasma}) = - \frac{\alpha \tau_r e^2}{2 \hbar \omega^3 \epsilon_0 n_0 m^*} \quad (2.3.1.4)$$

This expression gives the nonlinear coefficient due to the creation of free carriers and hence applies to interband excitations and not free carrier absorption. Note that  $n_2(\text{plasma})$  is proportional to the absorption coefficient  $\alpha$ .

The plasma model explains changes in refractive index due to a change in the density of carriers. In most cases however there is also a change in the absorption and this gives a change in the refractive index as described by the Kramers-Kronig relations. Different types of absorption changes are now discussed.

### 2.3.2 Two-level saturation model.

The absorption coefficient at any given photon energy is proportional to the density of filled initial states and empty final states. Any change therefore in the densities of these states results in a change in the absorption. In a two-level system, *state filling* can occur when all states in the upper level are occupied.

Due to the Pauli exclusion principle, further transitions from the lower level to the upper level are prohibited. If there is a large number of two-level systems with a smooth distribution of parameters (i.e. separation energy) it is possible to integrate the effect of the individual systems to obtain the overall response. Under certain conditions this two-level interpretation can be applied to absorption saturation in semiconductors. The conduction band and valence bands can be considered as an effective continuum of many two-level systems but only if coupling between systems can be neglected.

An example of this condition is when carrier excitation is caused by a femtosecond laser pulse. In this case, immediately after excitation, there is a non-thermal carrier distribution which remains until electron-phonon interactions scatter excited carriers into other states in  $k$ -space, or if the excited carriers recombine. In AlGaAs the phonon scattering time is typically less than 100 fs<sup>[3]</sup> and the recombination time is about two orders of magnitude higher than this. For time scales less than 100 fs the two-level approach is valid. The nonlinear coefficient due to state filling under these conditions can be calculated using a density matrix formalism as described by Miller et al<sup>[7]</sup> to give

$$n_2(\text{SF}) = - \frac{1}{\hbar^3} \left[ \frac{eP}{\hbar\omega} \right]^4 \frac{T_1}{T_2} \frac{2\pi}{15n_0^2c} \left[ \frac{2m_r}{\hbar\omega_G - \hbar\omega} \right]^{3/2} \quad (2.3.2.1)$$

In this expression  $P$  is the transition matrix element which indicates the transition probability between the two states,  $\hbar\omega_G$  is the band gap energy and  $m_r$  is the electron-hole reduced effective mass. The constants  $T_1$  and  $T_2$  denote time constants which characterise a two-level system:  $T_1$  is the relaxation time within which the excited population decays, and  $T_2$  is inversely proportional to the uncertainty<sup>[8]</sup>.  $T_2$  is known as the *dephasing time* and is the time taken for the material excitation to lose phase with the light field. The subscript "SF" denotes state-filling.

### 2.3.3 Band-filling and the Dynamic Burstein-Moss shift.

If carrier scattering causes coupling between different  $k$  states then the above model is incorrect. Instead of state filling in a very localised part of  $k$ -space, there is now a saturation of a band of states. When this kind of *band filling* occurs in the vicinity of the bandgap there is effectively an increase in the bandgap. This is known as the *Dynamic Burstein-Moss Effect*. (In linear optics the Burstein-Moss effect describes a shift in the bandgap energy caused by appropriate

donor or acceptor concentrations.)

For low temperatures, where it can be assumed that the states beneath a Fermi wave vector  $k_f$  in the conduction band are filled and those above are empty, the nonlinear coefficient resulting from band filling is given by<sup>[9]</sup>

$$n_2(\text{BM}) = \frac{-1}{6 \epsilon_0 n_0} \left[ \frac{eP}{\hbar\omega} \right]^2 \frac{\alpha \tau_r}{\hbar\omega(\hbar\omega_G - \hbar\omega)}. \quad (2.3.3.1)$$

The absorption,  $\alpha$ , and the carrier relaxation time,  $\tau_r$ , have been introduced. For direct-gap semiconductors, the effective mass can be related approximately<sup>[9]</sup> to the transition matrix element P by

$$\frac{1}{m^*} \approx \frac{4P^2}{3\hbar^3\omega_g}. \quad (2.3.3.2)$$

Using this relation, the three expressions for the different  $n_2$ s given by equations (2.3.1.4), (2.3.2.1) and (2.3.3.1) can be related:

$$n_2(\text{BM}) = \frac{5}{3} n_2(\text{SF}) = \frac{\omega_g}{4(\omega_g - \omega)} n_2(\text{plasma}) \quad (2.3.3.3)$$

There are limitations to (2.3.2.1) in that  $T_2$  is not easily derivable and is effectively an adjustable parameter. Also, the value of  $n_2$  given by (2.3.3.1) is for low temperatures and the temperature dependant distribution of the carriers has not been taken into account.

None of the above treatments makes apparent the detailed resonance of  $n_2$ . The approach of Miller et al<sup>[10]</sup>, who have calculated the nonlinear coefficient for III-V's taking into account the thermal carrier distribution, shows a clear peak in the value of  $n_2$  near the bandgap. The authors have applied a density-matrix approach combined with a thermal carrier distribution approximated by a Boltzmann factor (valid for room temperature conditions) to obtain the following expression:

$$n_2 = \frac{-8J\pi}{3} \frac{e^2\hbar^2}{m} \frac{\mu}{m_c} \frac{mP^2}{\hbar^2} \frac{1}{n_0} \frac{1}{kT} \frac{\alpha(\hbar\omega)\tau_r}{(\hbar\omega)^3} J \left[ \frac{\mu(\hbar\omega - E_g)}{m_c kT} \right] \quad (2.3.3.4)$$

where

$$J(a) = \int_0^\infty \frac{x^{1/2} e^{-x}}{x - a} dx \quad (2.3.3.5)$$

Here  $m_c$  is the conduction band effective mass,  $\mu$  is the electron-hole reduced

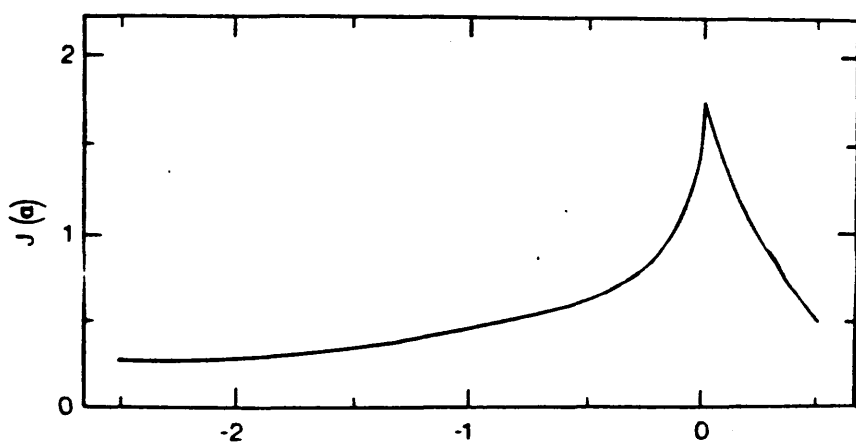
effective mass and  $k$  is the Boltzmann constant. All other symbols are as defined earlier. Figure 2.3.1 shows the function  $J(a)$  from which the resonance in  $n_2$  is apparent.

#### 2.3.4 Other theoretical models.

There are two other models which, on account of their complexity, can only be briefly mentioned in this thesis. These theoretical models use linear response theory<sup>[11]</sup> where the optical response of semiconductors is computed in terms of expectation values of products of the polarisation operator. The material parameters depend on the density of photoexcited carriers which are assumed to be in a quasi-equilibrium state. The approach described by Haug and Schmitt-Rink<sup>[12]</sup> makes use of a Green's function method for calculating the nonlinear absorption in a self-consistent manner. However a drawback with this theory is that it requires a significant computing capability for the iterative solution of integral equations. The second model, proposed by Banyai and Koch<sup>[11]</sup>, uses a partly phenomenological theoretical description of the optical nonlinearities in an electron-hole plasma. This approach makes it possible to derive closed, easily evaluable expressions for the density dependant absorption spectrum. Excellent agreement with experimental measurements in GaAs has been achieved with both of these methods<sup>[13]</sup>.

#### 2.4 Many-body effects.

So far the effect of the presence of many excited carriers on the crystal states has been assumed negligible. If the electron-hole density is sufficiently high then the scattering between the various "particles" (electrons, holes and excitons) gives rise to modifications of particle energies. These are generally known as *many-body effects*. In a dense electron-hole plasma the Coulombic potential of each particle is reduced by the screening effects of the other charged particles<sup>[7]</sup>. This effect is present for each of the charged particles and therefore each particle sees a potential which has been reduced partly by its own presence. This reduction in the potential can be interpreted as an increase in the particle's *self-energy*. In effect the energy required to create an electron-hole pair in the plasma has been reduced and this is equivalent to a reduction in the band-gap. This effect is known as *band-gap renormalisation*. The calculation of the actual size of the band-gap shift is not a trivial problem and has to be solved using a



The dimensionless resonance function  $J(a)$  plotted against dimensionless energy parameter  $a = \mu(\hbar \omega - E_g) / m_c kT$   
(After Miller et al [10])

**Figure 2.3.1**

self-consistent Green's function method<sup>[12]</sup> similar to that described in the previous section. Screening effects of this type where the single particle Coulombic potential is modified by the presence of other charged particles are of importance when considering the nonlinear properties of MQW structures.

## 2.5 Multiple Quantum Well Systems.

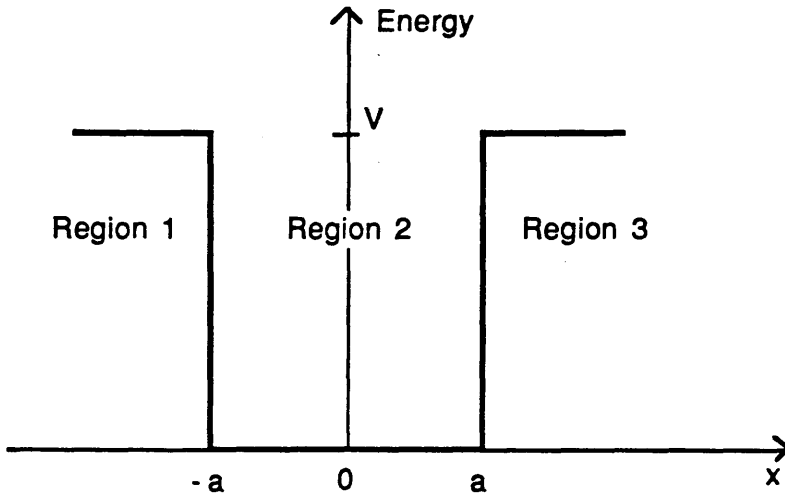
In recent years there has been significant advancement in the understanding of multiple quantum well (MQW) systems. These systems exploit the quantum confinement effects of potential wells formed in the conduction and valence bands of ultrathin semiconductor layers. The progress in the understanding of these structures has occurred in parallel with the development of material growth techniques such as MBE and MOCVD (see Chapter Four) which allow growth of multilayer III-V semiconductor systems with layer thickness control of almost monolayer precision. Figure 2.5.1 shows a schematic of such a quantum well. Electrons and holes are confined in the potential wells formed in the conduction and valence bands respectively. These give rise to discrete energy levels which modify the density of states functions for electrons and holes. It should be noted that in multiple quantum well systems the separation between adjacent wells is large enough to ensure that there is no coupling of wavefunctions of different wells. This isolation between the wells is the distinguishing feature which separates MQWs from *superlattices*.

Not every aspect of MQWs can be discussed in this thesis and some topics such as the interesting electroabsorption properties of these structures<sup>[14]</sup> have been purposefully omitted.

### 2.5.1 Quantum confinement and excitonic absorption.

The band discontinuities which occur at an AlGaAs-GaAs heterojunction make it possible to engineer potential wells in the conduction and valence bands. These wells give rise to electron and hole bound states as described by simple application of the Schrodinger wave equation. The derivation of the solutions for the wavefunction in a single finite potential well is a classic quantum mechanics textbook problem. However, most treatments assume that the mass of the confined particle is equal in both the barrier and the well regions but this assumption is not true in semiconductor quantum wells. The electron and hole effective masses depend on the composition of the material and these differ between the well and

## Finite Potential well



A schematic representation of a finite potential well as used in the calculation of bound state particle wavefunctions.

**Figure 2.5.1**

barrier layers. The solution to the Schrodinger wave equation applied to a finite potential well is therefore derived in Appendix I where the change in mass has been included in the boundary conditions. From Appendix I, the solution is given by:

$$2a\beta - \tan^{-1} \left[ \frac{m_w^* \alpha}{m_b^* \beta} \right] - n\pi = 0 \quad (2.5.1.1)$$

where

$$\alpha^2 = \frac{2m(V-E)}{\hbar^2} \quad \beta^2 = \frac{2mE}{\hbar^2}$$

and the symbols are as defined in Figure 2.5.1. The quantum number  $n$  ( $=0,1,2..$ ) labels the energy eigenvalue  $E$ . This equation will be used in Chapter Three where the MQW waveguide design procedure will be described.

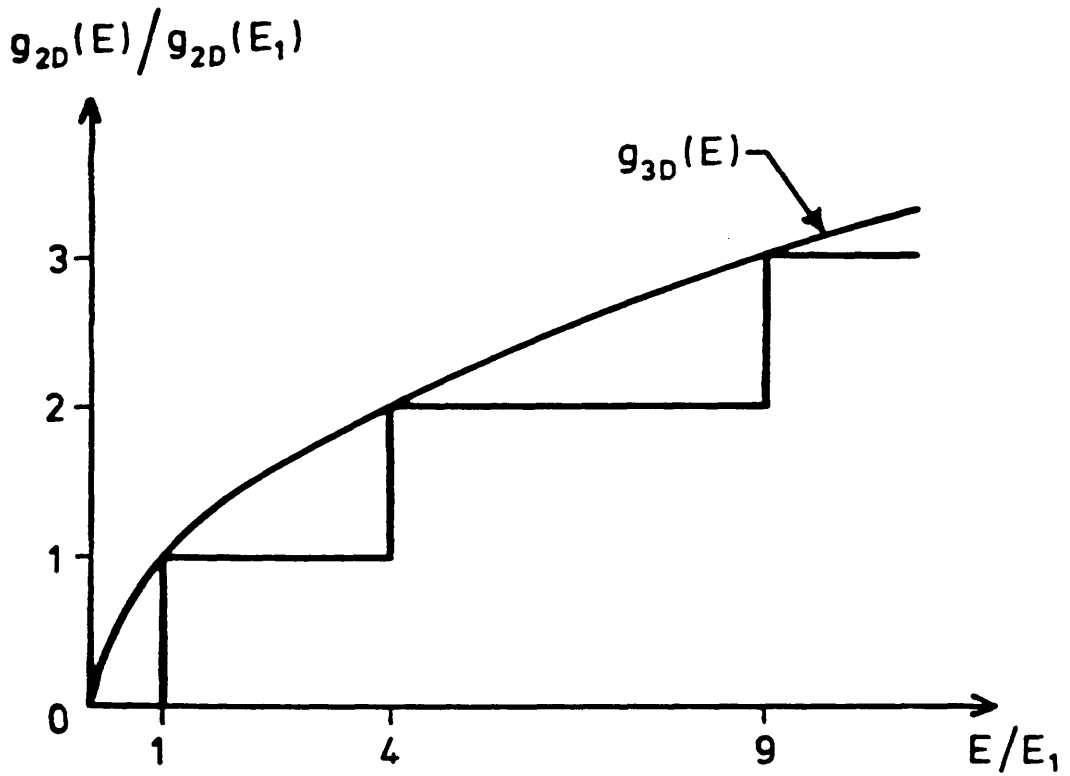
In a multilayer semiconductor quantum well system quantisation of states occurs only in one dimension and the particles have a continuously varying energy-momentum in the other two dimensions. If the direction of confinement is  $z$ , then the energy of such a particle in the well layer is given by

$$E = E_n + \frac{\hbar^2 k_x^2}{2m^*} + \frac{\hbar^2 k_y^2}{2m^*} \quad (2.5.1.2)$$

$E_n$  is the energy eigenvalue for level  $n$  and  $k_x$  and  $k_y$  are the De Broglie wave numbers in the  $x$  and  $y$  directions. One dimensional confinement gives rise to a step-like density of states for the electron and hole states which results in a step-like absorption as shown in Figure 2.5.2. This feature is one important characteristic of the absorption spectrum of quantum well structures.

Since the energy eigenvalue depends partly upon the particle mass (equation 2.5.1.1), different eigenvalues result for the confined light and heavy holes in the valence band wells. The absorption spectrum therefore actually consists of two superimposed step-like density of states: one associated with the creation of an electron and heavy-hole pair and the other with an electron and light-hole pair. The quantum confinement due to the potential well has therefore removed the heavy and light hole valence band degeneracy, i.e. the energies associated with the two types of holes have been differentiated.

Another feature of importance in MQWs is the enhancement of absorption due to the creation of *excitons*. An exciton is a composite particle consisting of a bound electron-hole pair and is analogous to a hydrogen atom. The energy



The 2-D step-like density of states function  $g_{2D}(E)$  for a quantum well structure. The 3-D density of states, where  $g_{3D} \propto E^{1/2}$ , is also included.  
(after M. D. A. Macbean [15].)

**Figure 2.5.2**

required to separate an electron–hole pair is called the *binding energy* and, using the hydrogen atom model, is given by

$$B_{3D} = \frac{-e^4\mu}{8\epsilon^2h^2} \quad (2.5.1.3)$$

for a ground state exciton. Here  $\mu$  is the reduced mass of the electron–hole pair. The negative value of  $B_{3D}$  is the Rydberg constant,  $R_y$  (i.e.  $B_{3D} = -R_y$ ). For higher quantum levels, the binding energy decreases as

$$B_{3D} = \frac{-R_y}{n^2} \quad (2.5.1.4)$$

The separation between the electron–hole pair is the Bohr radius and is given by

$$a_{3D} = \frac{4\pi\epsilon\hbar^2}{\mu e^2} \quad (2.5.1.5)$$

The Bohr radius of a ground state exciton in bulk GaAs is of the order of 140 Å. The introduction of carrier confinement by potential wells of width less than twice the Bohr radius tends to "flatten" the normally "spherical" exciton. However, and more importantly, the exciton binding energy is modified severely due to the reduced dimensionality of the confined charge distribution. Solving Schrodinger's wave equation in two–dimensional space, gives a result quite different from (2.5.1.4)[17]:

$$B_{2D} = \frac{-R_y}{(n - \frac{1}{2})^2} \quad (2.5.1.6)$$

The  $1/n^2$  variation of binding energy with the quantum number in (2.5.1.4) has been replaced by a  $1/(n - \frac{1}{2})^2$  dependence and the ground state energy of the two–dimensional exciton has increased by a factor of 4. A reduction of the dimensions of the electron and hole distributions has led to an increase in the binding energy of the exciton.

In practise, a purely two–dimensional charge distribution cannot be obtained. As the well width is reduced, the two–dimensional electron gas reaches a minimum thickness but then begins to increase again due to the evanescent penetration of the wavefunction into the finite potential barriers. In fact, the maximum binding energy for the exciton occurs for a well thickness  $L_z$  somewhere within the range given by

$$0.5 < (L_z/a_{3D}) < 1$$

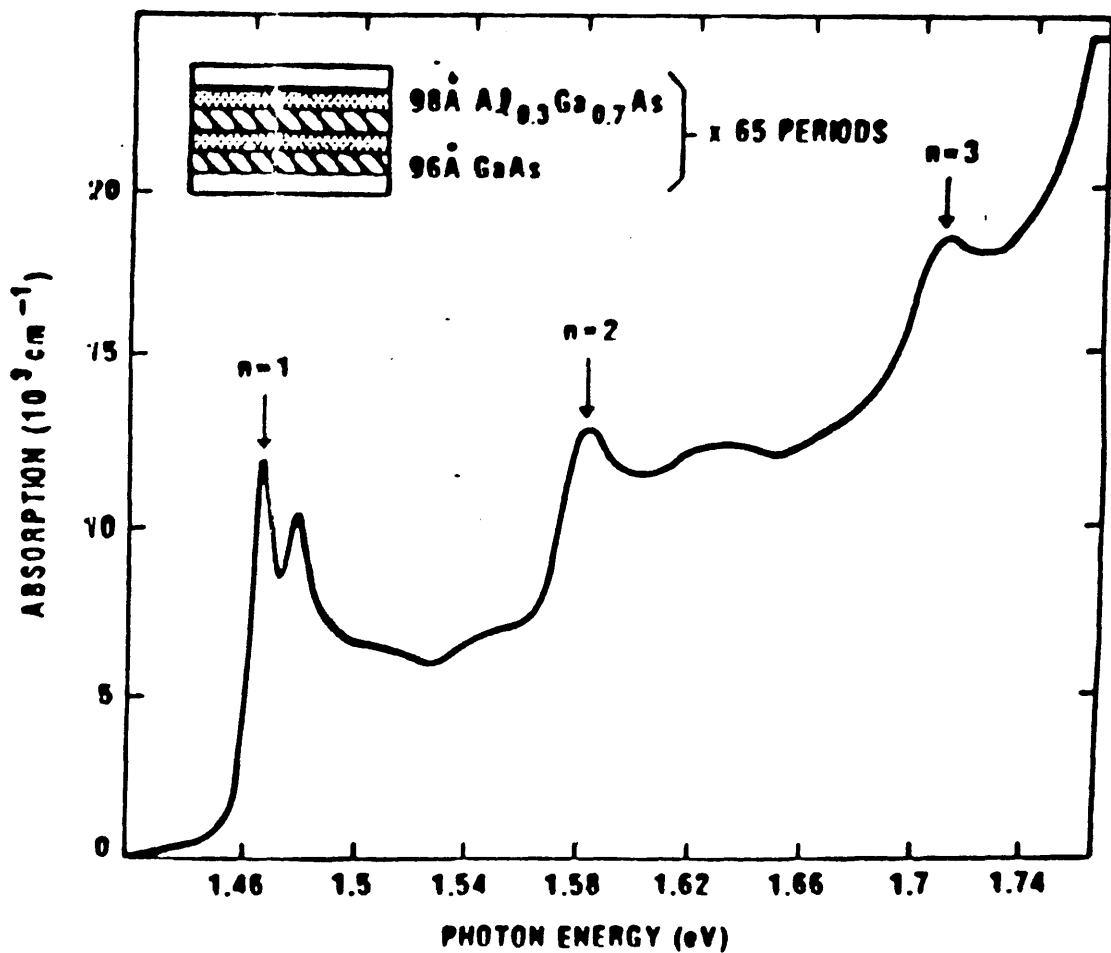
where, for GaAs/AlGaAs systems, it reaches a maximum lying somewhere between  $2B_{3D}$  and  $3B_{3D}$ .

The existence of these bound excitonic states modifies the density of states and gives rise to distinct absorption resonances corresponding to the creation of excitons. There are two series of resonances associated with the light-hole and heavy-hole excitons. The resonances are positioned just below each of the steps in the absorption spectrum by amounts equal to the binding energies. In actual structures, the absorption peaks are not infinitely narrow but are broadened due to the interaction of the exciton with quantised lattice vibrations or *phonons*. This results in the ionisation of the exciton and the electron-hole pairs are scattered into states within the conduction and valence bands respectively to become free carriers. In bulk GaAs, the binding energy of the exciton is smaller than the excitonic linewidth and therefore the resonant absorption peaks cannot be resolved from the band edge unless the material is at low temperature. In quantum wells however the exciton binding energy is larger and distinct absorption peaks can be seen at room temperature.

In summary, the absorption spectra in MQWs is described as a combination of two superimposed step-like functions and excitonic resonances. The absorption of a typical MQW structure is shown in Figure 2.5.3 after reference [16].

One characteristic unique to quantum well structures is their polarisation sensitive absorption or dichroism. This property arises from the nature of the light and heavy hole valence bands. The light hole band has associated with it a wavefunction which has spherical symmetry. The heavy hole wavefunction however has a p-like symmetry and is "dumbbell" shaped<sup>[18]</sup>. This introduces an orientation dependant interaction with linearly polarised optical fields. In bulk GaAs, this polarisation dependence is not apparent because of the symmetry possessed by the crystal. However, in MQW structures, this symmetry is removed by the presence of the one dimensional confinement and consequently there is no interaction between heavy hole excitons and optical fields polarised in the direction of the layer planes. The relative sizes of the hh and lh excitonic absorption peaks are 3/4 and 1/4 respectively for light polarised perpendicularly to the layers, and 0 and 1 for light polarised parallel to the layers<sup>[19]</sup>. It should be noted that this dichroism can only be observed if light is propagating in the plane of the MQW layers. Light propagating perpendicularly to the layers interacts with both heavy-hole and light-hole excitons because in this case the optical field is always parallel to the layers.

The main linear absorption features of MQW structures have been summarised



Absorption spectrum of an MQW structure.  
 (After Chemla et al [16].)

Figure 2.5.3

in this section. The problem of the calculation of excitonic energy levels in AlGaAs MQW structures has been left to be discussed in Chapter Three where the design process of a MQW waveguide is described. A review of the data available for the determination of band parameters and carrier effective masses is also to be included in Chapter Three.

### 2.5.2 Nonlinear properties of MQWs.

The presence of the excitonic absorption peak in MQW structures results in a considerably enhanced dynamic nonlinearity. The effect is resonant and is largest when the incident photon energy is equal to or greater than that of the excitonic absorption peak. When photons of energy equal to that of the excitonic peak are absorbed, excitons are created. These ionise within about 300 fs<sup>[20]</sup> resulting in the formation of an electron-hole plasma. If the incident photons have energy greater than that of the excitons, such a free carrier plasma may be created directly. The presence of these carriers reduces the band-gap via bandgap renormalisation. The energies of the exciton however do not change significantly and therefore the binding energy is effectively reduced and the excitonic absorption diminishes. The point at which the bandgap renormalisation exceeds the exciton binding energy is the Mott transition<sup>[16]</sup>. As long as the electron-hole plasma is present, the absorption peak is effectively removed and, a corresponding refractive index change results.

Although the ionisation or scattering time of the exciton is fast, the relaxation time of the carrier plasma is of the order of tens of nanoseconds. It is this latter time which dominates the speed of the MQW nonlinearity. The above description applies to the case where the incident beam is cw or pulsed with a pulse width of the order of a picosecond or greater. If the incident light consists of pulses of width comparable to the exciton scattering time then other considerations have to be made. If the photon energy is greater than that of the exciton, the effects are carrier density dependant and are attributable to plasma screening effects. However for resonant pumping, where the photon energy equals the exciton energy, and for pulses of width less than scattering time, excitonic state saturation is apparent. This type of nonlinearity gives absorption changes of up to 2 times larger than the screening effects<sup>[20]</sup>. These types of absorption change last only as long as the excitons remain unscattered and are observable only with pulse widths of less than 300 fs. For times greater than this, the carriers thermalise and screening effects again dominate. Because this kind of state saturation is apparent only for unthermalised carrier populations, this is also said to be a "cold" excitonic

nonlinear effect.

## 2.6 Thermal effects

One other very important effect associated with absorption induced nonlinearities is that of heating. As photoexcited electrons and holes relax within the conduction and valence bands respectively, they impart energy to the crystal as phonons are created and this results in an increase in the crystal temperature. The resulting thermal expansion changes the lattice constant and the periodic potential seen by the electrons and this causes a decrease in the bandgap. This is also accompanied by an increase in the refractive index. Note that the changes in the bandgap and in the refractive index due to sample heating are opposite in sign to the changes caused by band-filling and excitonic saturation. It will be seen in this thesis that thermal effects play an important role in the performance of optical nonlinear devices in AlGaAs.

## 2.7 Conclusions

In this chapter, the nonlinear properties of GaAs/AlGaAs have been reviewed. The discussion has focussed only on resonant effects which arise from photon absorption. The various models for dynamic nonlinear effects have been presented without going into the details of mathematical derivations. These effects are larger than the passive nonresonant effects which were described in Chapter One. The subject of nonlinear effects in semiconductors is a particularly large one and the review presented here relates mainly to the work described in this thesis.

## 2.8 References to Chapter Two.

- [1] A. Abragam, "Principles of Nuclear Magnetism", p93, Clarendon Press, 1961.
- [2] F. Stern, "Elementary Theory of the Optical Properties of Solids", Solid State Physics, vol 15, p299, 1963.
- [3] A. J. Taylor, D. J. Erskine, C. L. Tang, "Ultrafast relaxation dynamics of photoexcited carriers in GaAs and related compounds", J. Opt. Soc. Am. B., vol 2, no 4, pp663- 673, 1985.

- [4] H. A. Haus, N. A. Whittaker Jr, M. C. Gabriel, "All-optical Logic Devices using Group III-V Semiconductor Waveguides", SPIE proc., vol 578, 1985.
- [5] B. S. Wherret, A. C. Walker, F. A. P. Tooley in 'Optical Nonlinearities and Instabilities in Semiconductors', Ed H. Haug, Academic Press, 1988.
- [6] C. Kittel, "Introduction to Solid State Physics", 5th Edition, John Wiley & Sons, 1976.
- [7] A. Miller, D. A. B. Miller, S. D. Smith, "Dynamic non-linear processes in semiconductors", Adv. Phys., vol 30, no 6, 1981.
- [8] D. S. Chemla, D. A. B. Miller, S. Schmitt-Rink, "Nonlinear Optical Properties of Semiconductor Quantum Wells" in 'Optical Nonlinearities and Instabilities in Semiconductors' Ed. H. Haug, Academic Press, 1988.
- [9] E. Abraham, S. D. Smith, "Optical Bistability and related devices", Rep. Prog. Phys., vol 45, 1982.
- [10] D. A. B. Miller, C. T. Seaton, M. E. Prise, S. D. Smith, "Band-Gap-Resonant Nonlinear Refraction in III-V Semiconductors", Phys. Rev. Lett., vol 47, no 3, pp197-200, 1981.
- [11] L. Banyai, S. W. Koch, "A simple Theory for the Effects of Plasma Screening on the Optical Spectra of Highly Excited Semiconductors", Z. Phys. B. - Condensed Matter, vol 63, pp283-291, 1986.
- [12] H. Haug, S. Schmitt-Rink, "Basic mechanisms of the optical nonlinearities of semiconductors near the band edge", J. Opt. Soc. Am. B., vol 2, no 7, pp1135-1142, 1985.
- [13] S. W. Koch, N. Peyghambarian, H. M. Gibbs, "Band-edge nonlinearities in direct-gap semiconductors and their application to optical bistability and optical computing", J. Appl. Phys., vol 63, no 2, 1988.
- [14] D. A. B. Miller, J. S. Weiner, D. S. Chemla, "Electric-Field Dependence of Linear Optical Properties in Quantum Well structures: Waveguide Electroabsorption and sum rules", IEEE J. Quant. Elec., vol QE-22, no 9,

pp1816-1830, 1986.

- [15] M. D. A. Macbean, Ph.D. Thesis, University of Glasgow, 1986.
- [16] D. S. Chemla, D. A. B. Miller, "Room-temperature excitonic nonlinear-optical effects in semiconductor quantum-well structures", *J. Opt. Soc. Am. B.*, vol 2, no 7, pp1155-1173, 1985.
- [17] D. S. Chemla, D. A. B. Miller, P. W. Smith, A. C. Gossard, W. Weigmann, "Room Temperature Excitonic Nonlinear Absorption and Refraction in GaAs/AlGaAs Multiple Quantum Well Structures", *IEEE J. Quant. Elec.*, vol QE-20, no 3, 1984.
- [18] M. Asada, Y. Suematsu, "Density-Matrix Theory of Semiconductor Lasers with Relaxation Broadening Model- Gain and Gain-suppression in Semiconductor Lasers", *IEEE J. Quant. Elec.*, vol QE-21, no 5, pp434-442, 1985.
- [19] J. S. Weiner, D. S. Chemla, D. A. B. Miller, H. A. Haus, A. C. Gossard, W. Weigmann, C. A. Burrus, "Highly Anisotropic optical properties of single quantum well waveguides", *Appl. Phys. Lett.* vol 47, no 7, 1985.
- [20] S. Schmitt-Rink, D. S. Chemla, D. A. B. Miller, "Theory of transient excitonic optical nonlinearities in semiconductor quantum-well structures", *Phys. Rev. B.*, vol 32, no 10, pp 6601-6609, 1985.

## CHAPTER THREE

### DESIGN OF MULTIPLE QUANTUM WELL WAVEGUIDES.

#### 3.1 Introduction.

The design procedure for a MQW waveguide will be discussed in this chapter. There are several aspects to the design of a nonlinear MQW waveguide and consideration has to be given to each of these. The primary consideration however is that the position of the excitonic absorption peak suits the wavelength of operation of the laser source. Both the refractive index and the excitonic energy levels of the MQW layer therefore have to be considered in the waveguide design and in fact both these parameters are partly interdependent because of the relation between the refractive index and the excitonic absorption. (See section 2.2 on the Kramers–Kronig integral).

The chapter begins by reviewing basic waveguide theory and design in section 3.2. The procedure for determining the refractive index of MQW structures is then presented in section 3.3 where a detailed literature review of the MQW parameters has also been included. Finally, in section 3.4, a summary of the complete waveguide design procedure is given.

#### 3.2 Dielectric Waveguide Theory and Design.

Confinement of light within either a dielectric slab or a channel can be obtained if either is surrounded by a material with a lower refractive index. The mechanism of waveguiding is well understood and much work has been done on the theory of waveguiding<sup>[1,2]</sup>. Only some of the basic properties of waveguides will therefore be discussed here.

##### **3.2.1 Three– and Four– layer slab waveguides.**

The three–layer dielectric slab waveguide is the simplest of waveguide structures. This is shown in figure 3.2.1. Only confinement in one dimension is present in such a structure. The guiding layer here has refractive index  $n_2$ , and the lower and upper cladding regions have refractive indices  $n_1$  and  $n_3$  respectively. One can obtain the dispersion relation in this structure by considering the transverse resonance condition<sup>[1]</sup> which is an expression of the condition for

The three layer slab guide geometry.

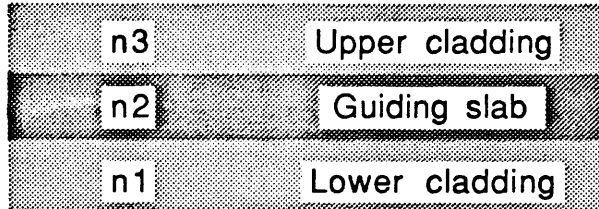


Figure 3.2.1

The fourlayer slab guide geometry.

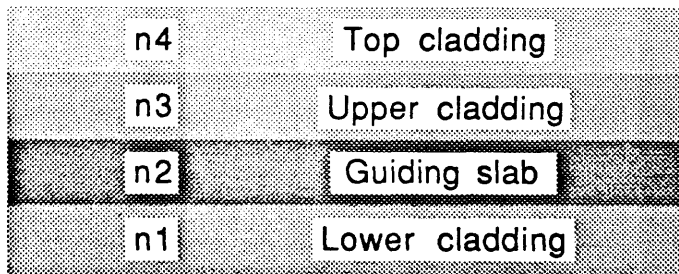


Figure 3.2.2

constructive interference within the waveguide. One thus obtains:

$$k_2 d_2 = \tan^{-1} \left[ \frac{\eta_1 k_1}{\eta_2 k_2} \right] + \tan^{-1} \left[ \frac{\eta_3 k_3}{\eta_2 k_2} \right] + M\pi \quad (3.2.1.1)$$

where

$$\begin{aligned} k_1^2 &= \beta^2 - n_1^2 k_0^2 \\ k_2^2 &= n_2^2 k_0^2 - \beta^2 \\ k_3^2 &= \beta^2 - n_3^2 k_0^2 \end{aligned} \quad (3.2.1.2)$$

with refractive index  $n_i$  for layer  $i$ , free space propagation constant  $k_0$ , and the modal propagation constant  $\beta$ . The effective index of the mode  $n_{\text{eff}}$  is given by

$$\beta = k_0 n_{\text{eff}}$$

where the integer  $M$  ( $=0,1,2,\dots$ ) is the mode number. The terms  $\eta_i$  have been included to take into account the two sets of boundary conditions for TE and TM propagating waves and are defined:

$$\begin{aligned} \eta_i &= 1 && \text{for TE fields} \\ \eta_i &= \frac{1}{n_i^2} && \text{for TM fields} \end{aligned}$$

A convenient parameter for representing the degree of confinement in a waveguide is the normalised thickness  $V$  as defined by Kogelnik and Ramaswamy<sup>[3]</sup> where

$$V = k_0 d_2 \sqrt{n_2^2 - n_1^2} \quad (3.2.1.3)$$

The condition for single mode guiding in a symmetric structure (i.e. where  $n_1 = n_3$ ) is then given by  $V < \pi$ . It can be seen that  $V$  can be adjusted by either changing the guiding layer thickness or by changing the refractive index difference between the guiding layer and the lower cladding. In other words it is possible to have the same confinement in a thin guiding layer with a large index difference as a thick guiding layer with a small index difference. It should be noted that, as  $V$  is varied, there is an optimum condition for confinement where the mode size is at its smallest. This occurs at  $V = 1.73$  for symmetric structures and  $V = 2.55$  for

antisymmetric structures (i.e. where  $n_3=1$ ). If  $V$  is reduced below this value then the mode size begins to increase. A fuller discussion of this behaviour is given by Kogelnik and Ramaswamy in [3]. It is generally true to say that increasing the waveguide confinement results in an increase in the number of guided modes supported by the structure. An important property of symmetric structures is that there is always at least one TE mode supported regardless of the size of  $V$ .

A more useful waveguide configuration is that of a four-layer slab waveguide, as shown in figure 3.2.2. For this case, the following dispersion equation is obtained<sup>[4]</sup>:

$$k_2 d_2 = \tan^{-1} \left[ \frac{\eta_1 k_1}{\eta_2 k_2} \right] + \tan^{-1} \left[ \frac{\eta_3 k_3}{\eta_2 k_2} \cdot \frac{e^{(k_3 d_3)} (\eta_3 k_3 + \eta_4 k_4) - e^{(-k_3 d_3)} (\eta_3 k_3 - \eta_4 k_4)}{e^{(k_3 d_3)} (\eta_3 k_3 + \eta_4 k_4) + e^{(-k_3 d_3)} (\eta_3 k_3 - \eta_4 k_4)} \right] + M\pi \quad (3.2.1.4)$$

where now the extra term  $k_4$  has been introduced:

$$k_4^2 = \beta^2 - n_4^2 k_0^2 \quad (3.2.1.5)$$

The four layer structure is the basis of the waveguides used in this thesis. By application of equation (3.2.1.4) it is possible to design an optimum waveguide geometry. To assist with this process, a Turbo Pascal computer program was written.

### 3.2.2 Computer modelling of the Four-layer slab.

This dispersion equation can be solved by defining a function  $F(\beta)$  of the modal propagation constant  $\beta$  (as given by equations (3.2.1.2) and (3.2.1.5) ) where

$$F(\beta) = k_2 d_2 - \tan^{-1} \left[ \frac{\eta_1 k_1}{\eta_2 k_2} \right] - \tan^{-1} \left[ \frac{\eta_3 k_3}{\eta_2 k_2} \cdot \frac{e^{(k_3 d_3)} (\eta_3 k_3 + \eta_4 k_4) - e^{(-k_3 d_3)} (\eta_3 k_3 - \eta_4 k_4)}{e^{(k_3 d_3)} (\eta_3 k_3 + \eta_4 k_4) + e^{(-k_3 d_3)} (\eta_3 k_3 - \eta_4 k_4)} \right] - M\pi \quad (3.2.2.1)$$

This is essentially the difference between the right hand side and the left hand side of equation (3.2.1.4). The value of  $\beta$  where  $F(\beta)=0$  corresponds to the propagation constant of a mode. Since the modal effective index  $n_{eff}$  lies between the refractive indices of the guiding layer and of the cladding layer which has the highest index, the value of  $\beta$  lies either within the range  $n_1k_0 < \beta < n_2k_0$  if  $n_1 > n_3$ , or within the range  $n_3k_0 < \beta < n_2k_0$  if  $n_3 > n_1$ .

The propagation constant, and hence the effective index, for any mode M can be found by calculating  $F(\beta)$  through the range of values given above and searching for any roots. It was verified by calculating over this range that  $F(\beta)$  is monotonically increasing for increasing  $\beta$ . This very important fact enables the use of the Bisection Method<sup>[5]</sup> to locate the root with considerable ease. In this method the position of the root in a given interval is found by first evaluating the function at the midpoint and endpoints of the interval. Depending on the sign of the midpoint value, and the signs of the values at the endpoints of the interval, it can be determined which half of the interval contains the root. The procedure can be repeated successively halving the interval each time until the position of the root is determined to within a sufficient accuracy. If there is no root then the mode corresponding to the particular value of M is not supported. This can be quickly determined by looking at the signs of the value of the function at the endpoints i.e. if the sign of  $F(\beta)$  is the same at both endpoints then there is no root.

A Turbo Pascal program called FOURLAY was written to solve the dispersion equation and is listed in Appendix II. Given the layer parameters, the program either calculates the effective index for any mode specified or it identifies the mode as not guided. Three-layer structures can also be analysed by setting  $d_3=0$  which reduces equation the four-layer eigenvalue equation (3.2.1.4) to the three layer equation (3.2.1.1)

The above method can in principle be applied for a slab waveguide comprising of any number of layers but it quickly becomes very complicated since many simultaneous equations given by the boundary conditions first have to be solved. Only then can the resulting eigenvalue equation be solved by a root finding method. This root finding procedure will, in general, not be as straightforward as the Bisection Method. A more efficient means of solving for a higher number of layers would be to use a tunneling resonance technique as described by Vassel<sup>[6]</sup> which can be simply adapted for any arbitrary multilayer structure. It is also possible to include the effects of absorption by considering a complex refractive index<sup>[7]</sup>. The development of multilayer waveguide models can therefore be taken to further stages but for the structures considered here, the fourlayer model is sufficiently adequate.

### 3.2.3 Two dimensional waveguides.

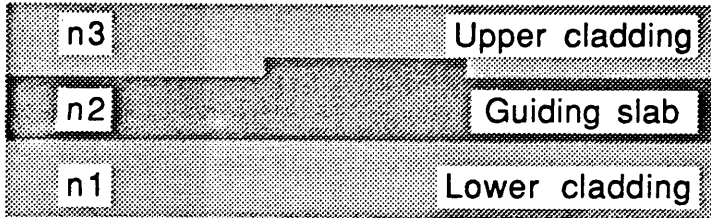
In the above sections only optical confinement in one dimension has been considered. Confinement in the lateral direction can be obtained by defining a rib or ridge. The rib laterally confines light since the guided optical field in the slab (layer 2) has a larger effective index in the region directly below the rib compared with the outer regions. Two dimensional confinement is thus obtained and a channel waveguide results. Figure 3.2.3 shows rib waveguides formed by etching of three-layer and four-layer structures. The lateral confinement differs between the two cases: in the four-layer case it is the evanescent part of the field which interacts with the rib whereas in the three layer case, the mode in the guiding layer is perturbed directly by the rib. Both of these structures are known as 'rib' or sometimes 'ridge' waveguides. The case where the rib interacts with the mode via the evanescent field is sometimes specified by terming the structure a 'stripe-loaded waveguide'.

There are some practical considerations to be made when comparing the two types of structures. The variation of the effective index with the thickness etched is smaller for a four layer structure than for the threelayer case and it is found that to obtain the same degree of lateral confinement, the stripe-loaded geometry requires a deeper etch (i.e. a greater rib height). Also, in stripe-loaded waveguides, the guided light is less susceptible to scattering losses due to rib wall imperfections because most of the optical mode lies below the rib sides and the interaction with the rib walls is minimised.

The calculation of the modal fields and effective indices of rib waveguides is not trivial and there is no simple and quick way to evaluate these accurately. One approximate technique however is to use the *effective index method*<sup>[1]</sup>. Essentially, this technique converts the analysis of a two dimensional waveguide into two one dimensional problems. Figure 3.2.4 illustrates this. The waveguide structure is first divided laterally into three regions. Each of these can be represented by an infinite slab waveguide so that the effective index for each of the regions can be calculated by the method discussed above. The second stage of the method is to use these effective indices to construct an infinite slab waveguide consisting of vertical layers with the respective refractive indices. This can be considered as a three layer waveguide. The effective index for this new "three-layer" structure is assumed to be equal to that of the original rib waveguide.

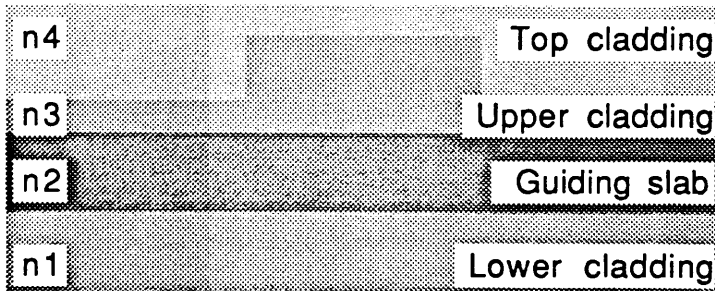
In the application of the effective index method, if one applies TE boundary conditions in the first part of the problem, TM boundary conditions should be applied in the second part (and vice versa). In practical cases however, where the layer index changes are relatively small, the effect of these different boundary

### Rib or ridge waveguide



(a)

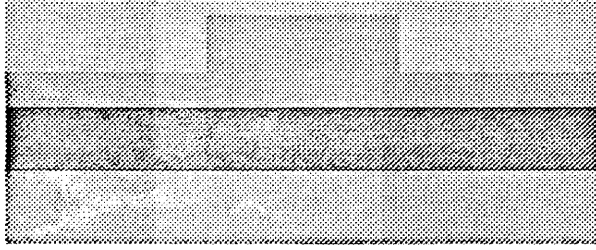
### Stripe loaded waveguide.



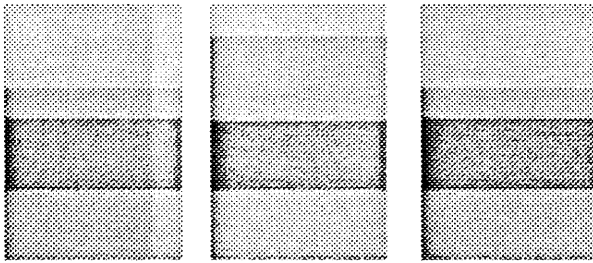
(b)

Figure 3.2.3

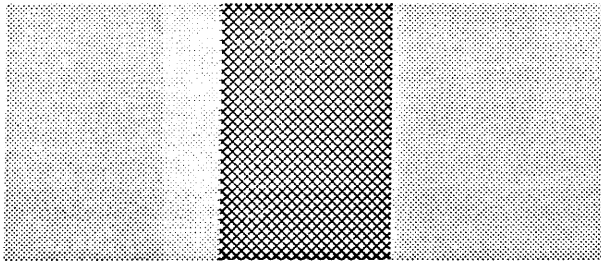
# The Effective Index Method



The rib waveguide structure



Consider each region as a separate 4-layer problem



Consider the effective indices of each region to now represent a vertical 3-layer problem.

The effective index method is illustrated where a two-dimensional problem is transformed into two one-dimensional ones.

Figure 3.2.4

conditions is usually negligible

For accurate calculations of the modal parameters in rib waveguides one has to resort to more powerful numerical means. One such method has been used in the implementation of a program called NWAVE which was originally written by Prof. C. D. W. Wilkinson and Dr. J. A. H. Wilkinson in this department. Further work on this was done by R. G. Walker who has described the workings of NWAVE in considerable detail<sup>[8]</sup>. Briefly, NWAVE calculates the field in structures by using a variational analysis technique to solve the Helmholtz scalar wave equation

$$\nabla^2_{xy}E + k^2E = \beta^2E.$$

A trial solution to E for a specified structure is expressed as a series of parabolic cylinder (Hermite–Gaussian) functions and this is then optimised using the Rayleigh–Ritz procedure. The accuracy of this numerical method has been compared by Austin<sup>[9]</sup> to the effective index method as well as with actual rib waveguides fabricated in GaAs. It was found that the effective index method is a good approximation as long as the relative height of the rib to the unetched layer is small compared to the mode size. If the rib height is too large then corner effects occur which distort the mode. This means that it is not accurate to represent the modal field by separable functions in the two dimensions of confinement and the effective index method gives poor results. The approximation of the two dimensional modal field by separable one dimensional distributions lies at the crux of the effective index approximation. Austin found that the effective index method always gives a propagation constant larger than that calculated by NWAVE and it fails completely if the etched region is below cut–off and supports no slab modes. Empirically it was found that if this was the case, good results could be obtained by the effective index method if the index of the etched region was put equal to unity. The results from NWAVE agreed well with the modal fields observed in the fabricated structures.

In the work described here all the waveguides are of the stripe–loaded geometry. As mentioned earlier, the optical modes in this type of structure lie below the etched rib. Therefore the distortions due to corner effects are minimised and in this case the effective index method is sufficiently accurate. The effective index method was used to design the waveguides in this project.

### 3.2.4 Summary of the design procedure for AlGaAs waveguides.

The procedure used in designing AlGaAs waveguides is now discussed. The process has been divided into several stages and each of these is presented below.

#### Stage (1):

Firstly, the operating wavelength of the waveguide device has to be chosen. This depends on the laser sources available and waveguide material. In this project the material of interest was AlGaAs and was compatible with the available laser source which was a Styryl 9 dye laser (see Chapter Five) with a wavelength tunable from 790nm to 860nm. The maximum output power from the laser occurred at about the centre of this tuning range and so the design wavelength was therefore chosen to be 830nm.

#### Stage (2):

Next the composition of the guiding layer has to be decided. This will depend on the type of nonlinear effect of interest. If one is looking at resonant nonlinear effects then the material composition is determined by positioning the band edge at the optimum laser wavelength. If the effect to be investigated is non-resonant, and a low absorption loss is required, then the band edge has to be located far enough from the operating wavelength to minimise interband absorption and hence maintain the intensity of the propagating light. The composition therefore depends on the type of nonlinearity to be used and the desired bandgap energy. The variation of the bandgap with Al content has been given by Aspnes et al<sup>[10]</sup> to be

$$E_g(x) = 1.424 + 1.594x + x(1-x)(0.127 - 1.310x)$$

and this can be used to determine the Al content in the guiding layer. If multiple quantum wells are required in the waveguide then the well thicknesses and composition depend on the desired position of excitonic absorption resonances. The procedure for this is described in section 3.3.

#### Stage (3):

The next stage of the waveguide design is to determine the refractive index of the guiding region. It is necessary to have available accurate values of the refractive indices for all layers in the waveguide structure. Much theoretical and experimental work has been done in determining the refractive index of  $\text{Al}_x\text{Ga}_{1-x}\text{As}$  as a function of Al content and as a function of wavelength. Early measurements were performed by Marple<sup>[11]</sup> in 1964 by investigating refraction in

GaAs prisms. A decade later more data based on reflectance measurements was published by Casey et al<sup>[12]</sup>. More recently, results have been reported by Aspnes et al<sup>[10]</sup> for varying Al content for photon energies between 1.5 and 6eV. Theoretical calculations based on the band structure of  $Al_xGa_{1-x}As$  have also been presented as a means of calculating the refractive index<sup>[13,14]</sup>.

At the time of the waveguide design work, the results of Aspnes were the most recent and these were therefore used in the design. Figure 3.2.5 shows a graph derived from the results of Aspnes et al<sup>[10]</sup> and gives the variation of the refractive index of  $Al_xGa_{1-x}As$  as a function of x at a photon energy of 1.5ev (827nm) for  $0 < x < 0.8$ . A curve has been fitted to the data using a 3rd order polynomial. Using this fit, the refractive index can be expressed:

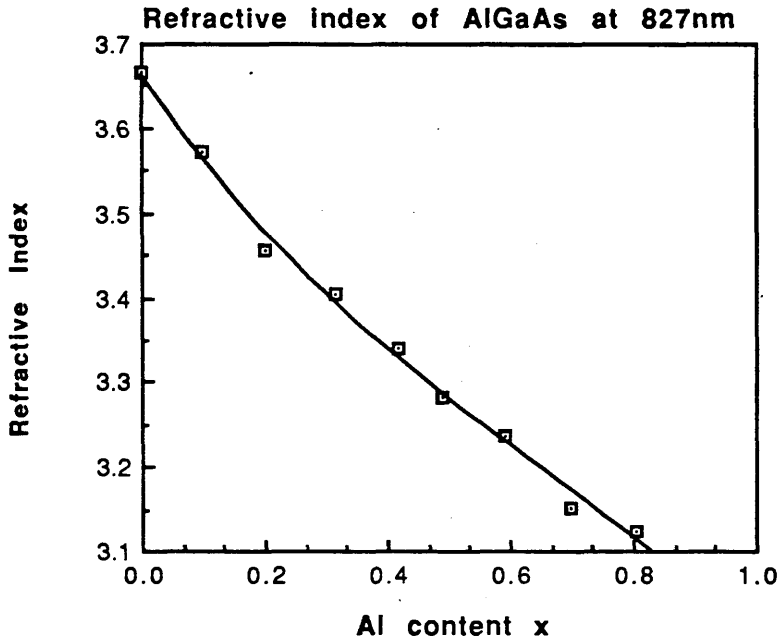
$$n = 3.664 - 1.0774x + 0.8416x^2 - 0.4369x^3$$

Stage (4):

Having determined its refractive index, the next part of the waveguide design was to determine the guiding layer thickness and the cladding layer compositions and thicknesses. All of these are chosen to give suitable optical confinement within the guiding layer.

The waveguides used in this project were all designed for single mode operation. There are many reasons why this is desirable. In a multimode waveguide each mode has associated with it a different propagation constant. Light coupled into the guide excites several modes and modal dispersion causes broadening of the optical light pulses which limits the switching speed of device. Single moded guiding is also important from the point of view of designing Y-junctions for Mach-Zehnder interferometers. If the waveguides were not single moded then it would not be possible to achieve a complete power extinction in the output port of the interferometer. This will be discussed in more detail in Chapter Six.

There is some degree of freedom at this stage of the waveguide design because it is possible to have single mode guiding either by use of a large guiding layer thickness with a small guiding/cladding layer index difference or by having a small guiding layer thickness with a large index difference. However, one has to consider the size and shape of the resulting optical mode. If the mode size is large then there may be some penetration of the evanescent field of the slab mode into the GaAs substrate. Even for small penetrations of the field there may still be a significant propagation loss since the GaAs substrate is highly absorbing at wavelengths shorter than  $\approx 870nm$  where  $\alpha$  is about  $10^4 cm^{-1}$ <sup>[15]</sup>. If a low-loss structure is required then it is desirable therefore to have a small mode. Also, for the exploitation of intensity dependant nonlinear effects it is advantageous to have



Refractive index as a function of Al content in AlGaAs.  
The data points were obtained from Aspnes et al[10]  
and the curve is a 3rd order polynomial fit

**Figure 3.2.5**

small modal areas because then larger guided light intensities are possible.

Having made these considerations it is a straightforward procedure to determine the most suitable values for the above parameters. One merely solves the four layer slab waveguide eigenvalue equation (e.g. by use of program FOURLAY) for a trial structure and modifies the cladding indices and/or guiding layer thickness until a satisfactory layer configuration is obtained. However one must ensure that the lower cladding layer is sufficiently thick to prevent either modal leakage into the substrate or substrate absorption. This can be checked by use of equations (3.2.1.2) from which the decay constants of the evanescent modal fields can be calculated.

Stage (5):

The final stage of the design procedure is to decide on the width and height of the rib. The rib is produced by etching of the surrounding material. The more the layer is etched, the larger the effective index difference between the etched and unetched regions. The required etch depth can be calculated using the effective index method as long the resulting mode is larger than the rib height for reasons discussed in section 3.2.3.

Some actual structures designed in the project will be discussed in section 3.4 but first the method for determining the refractive index of MQW structures has to be established. The next section deals with this problem.

### 3.3 The refractive index of MQW structures

Before the dimensions and layer compositions of an MQW waveguide are determined, one needs to know the refractive index of the MQW layer. This depends on the refractive index and thickness of each of the well and barrier layers as well as on the position and magnitude of the excitonic absorption.

The refractive index can be written as a sum of two terms:

$$n_{\text{MQW}} = n_{\text{rms}} + n_{\text{ex}} \quad (3.3.1)$$

The term  $n_{\text{rms}}$  is a weighted average term and depends on the barrier and well layer indices and thicknesses and on the polarisation of the optical field. The term  $n_{\text{ex}}$  arises from the excitonic absorption which contributes to the refractive index via the Kramers–Kronig relations.

The primary design requirement for the MQW structure, however, is that the

excitonic absorption peak lies at the appropriate photon energy. A procedure for determining the excitonic energy as a function of the MQW parameters (particularly the well width) is therefore necessary and is discussed initially in this section. Having determined the position of the excitonic absorption peak, it is then possible to estimate the term  $n_{ex}$  by application of the Kramers–Kronig integral. The procedure for doing this is also outlined. Finally, the method for calculating  $n_{rms}$  is discussed.

### 3.3.1 Determination of The excitonic absorption energies.

The finite potential well model for calculation of bound state energies in MQW structures was described in Chapter Two. That model will now be used for the calculation of the excitonic energy levels from which the position of the excitonic absorption peaks can be determined. Figure 3.3.1 shows the configuration of the wells in the conduction and valence bands in a GaAs/AlGaAs system. The conduction band well gives rise to bound states for electrons and the valence band well gives rise to heavy hole and light hole bound states.

A Turbo Pascal computer program called XTON was written to calculate the excitonic transition energies for a given set of well and barrier parameters. This program initially calculates the bound state energy eigenvalues for single finite potential wells in the conduction band and in the valence band. This gives the energy levels of the electrons and the holes in the well region. The exciton energy is then calculated by summing the energies of the electron level, the hole level and the temperature dependant bandgap in the well region (see figure 3.3.1). The binding energies of the heavy and light hole excitons is calculated and subtracted from the sum.

The solution for the finite potential well can be written (see Chapter Two):

$$2a\beta - \tan^{-1} \left[ \frac{m_w^* \alpha}{m_b^* \beta} \right] - n\pi = 0 \quad (3.3.1.2)$$

where

$$\alpha^2 = \frac{2m(V-E)}{\hbar^2} \quad \beta^2 = \frac{2mE}{\hbar^2} \quad (3.3.1.3)$$

and the symbols are as defined in Chapter Two. Equation (3.3.1.2) can be solved by the same manner used to solve the waveguide eigenvalue equation in program FOURLAY. The energy eigenvalue can be found by defining a function  $F(E)$ :

## Schematic of energy levels in a single quantum well

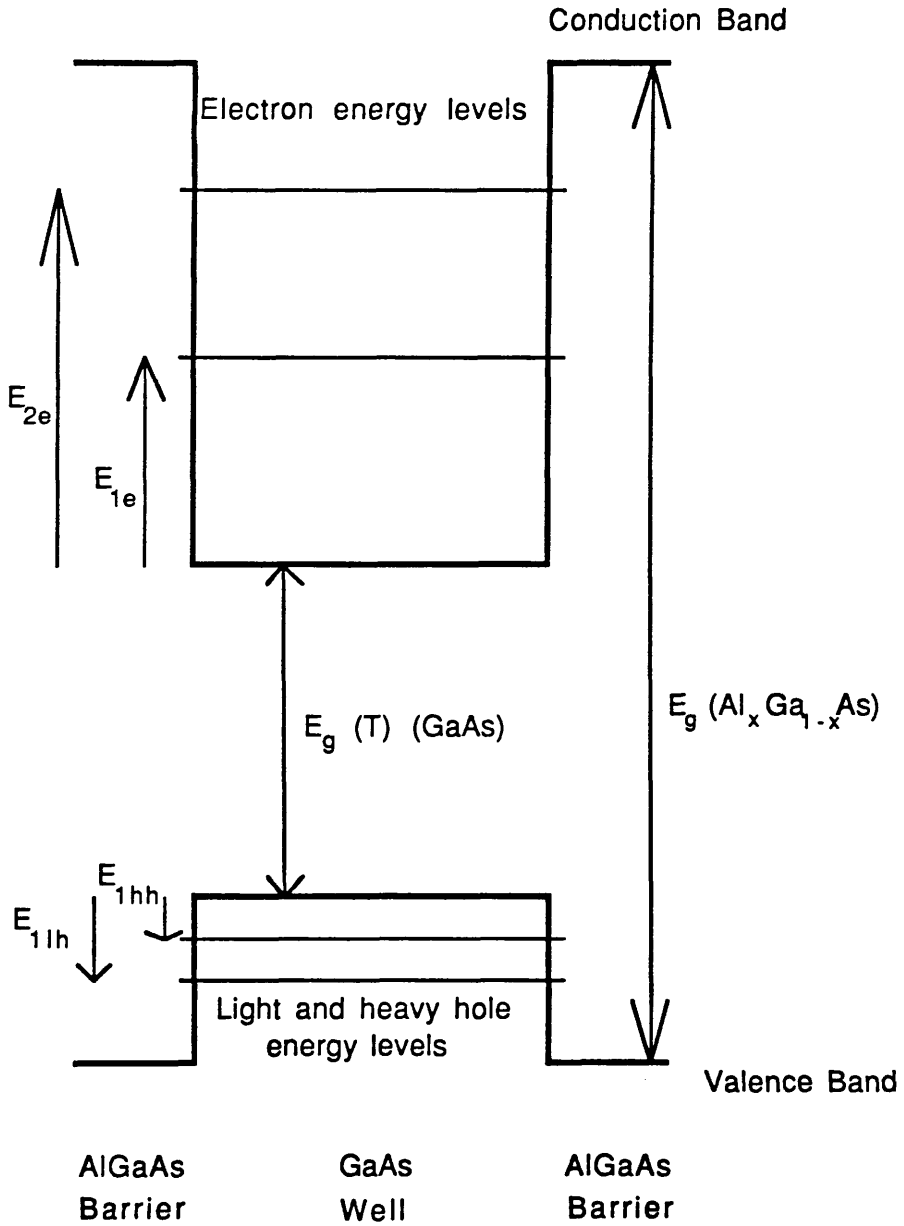


Figure 3.3.1

$$F(E) = 2a\beta - \tan^{-1} \left[ \frac{m_w^* \alpha}{m_b^* \beta} \right] - n\pi \quad (3.3.1.4)$$

The value of  $E$  when  $F(E)=0$  then corresponds to a bound state energy. The function  $F(E)$ , like  $F(\beta)$  in FOURLAY, is monotonic and so the Bisection method can again be used to find the root, with the value of  $E$  this time searched within the range  $0 < E < V$ . Note that, as earlier, there is an integer variable,  $n$ , present in equation (3.3.1.4) to label the bound states.

A similar approach to this was used by Kawai et al<sup>[16]</sup> to calculate excitonic recombination energies as part of their photoluminescence studies of AlGaAs MQW structures. These authors however used equation (3.3.1.4) in a form with  $n=0$  and only investigated the lowest excitonic transitions. (Note that there is a mistake in this paper: the terms  $m_w^*$  and  $m_b^*$  should be interchanged in the eigenvalue equation.) Equation (3.3.1.2) however is more general and can be used to also calculate higher level transitions.

To apply the program to an  $Al_xGa_{1-x}As/Al_yGa_{1-y}As$  system it necessary to first determine the well and barrier parameters. The well dimensions can be calculated from a knowledge of the bandgaps of the well and barrier regions and from the bandgap alignment at the heterojunction. The conduction band and valence band discontinuities (i.e. the well depths) will be denoted  $\Delta E_c$  and  $\Delta E_v$  respectively here. The band alignment is usually expressed as a ratio of the discontinuity in the conduction band to the total bandgap discontinuity,  $\Delta E_g$ , and is given as  $\Delta E_c/\Delta E_g$ . From a knowledge of these parameters, the well dimensions in the conduction band and the valence band can be calculated using  $\Delta E_c + \Delta E_v = \Delta E_g$ . Reported values of the energy band alignment ratio  $\Delta E_c:\Delta E_v$  have varied from 0.85:0.15 to 0.65:0.35<sup>[17,18]</sup> by various groups over the last few years. This spread in the published data has been reviewed by Batey and Wright<sup>[19]</sup> who have concluded that the band alignment is a function of the barrier composition in GaAs/AlGaAs heterostructures. The band alignment as reported by these authors was

$$\Delta E_v = 0.55x\Delta E_g$$

and this dependance of the band alignment on the Al content was used in the program.

The temperature dependance of the bandgap was included in the program to enable identification of low temperature excitonic photoluminescence transitions. The bandgap as a function of temperature is given by<sup>[16]</sup>

$$E_g(T)_{\text{GaAs}} = 1.519 - \frac{5.405 \times 10^{-4} T^2}{204 + T} \quad (\text{eV}) \quad (3.3.1.5)$$

The electron and heavy hole effective masses used in the program were obtained from Duggan et al[20]. The dependance of electron and hole masses on the particle energy (due to band nonparabolicity) was as described by the model proposed by Nelson et al[21] for electron and light hole bands. (The nonparabolicity of the heavy hole band is negligible.) The energy dependant mass is written as

$$m_w^*(E) = m_{0w}^*(1+E/E_w)$$

$$m_b^*(E) = m_{0b}^*(1+(E-V)/E_b)$$

with

$$E_i = \frac{\hbar^2}{2m_{0i}^* \gamma_i}, \quad (i=w, b)$$

where  $m_{0i}^*$  is the zero energy effective mass (in barrier or well as denoted by the subscript  $i$ ) and  $\gamma_i$  are the nonparabolicity parameters as used by Stevens et al [22].

A correction to the sum of the energy levels and the well bandgap due to the finite but relatively small excitonic binding energy was also included. The binding energy has typically been reported as being around 9 to 15meV[23–26]. Koteles et al[27] have reported experimentally determined values for both heavy and light hole exciton binding energies as functions of well width and have determined an empirical relation between well thickness and excitonic binding energy. These results are in good agreement with recently published values by other groups and have been incorporated into the program. The variation of the binding energy with the quantum number has not been taken into account since the higher  $n$  transitions are generally not of importance in the operation of MQW devices. (This variation is  $1/(n-\frac{1}{2})^2$  in the 2-D hydrogen atom model as opposed to the  $1/n^2$  dependance of the more familiar 3-D model[28] as discussed in Chapter Two.) The reviewed results in Koteles however indicate no clear correlation between the binding energy and the barrier composition. This scatter may be due to the varying data parameters used by the different authors in performing their calculations.

All of the parameters used in the program and their respective sources are summarised in figure 3.3.2.

Equations used in program	Reference
$E_g(x) = 1.424 + 1.594x + x(1-x)(0.127 - 1.310x)$	[10]
$E_g(T)_{\text{GaAs}} = 1.519 - \frac{5.405 \times 10^{-4} T^2}{204 + T} \quad (\text{eV})$	[16]
$m_e^*(x) = 0.0665 + 0.0835x$	[20]
$m_{hh}^*(x) = 0.34 + 0.45x$	[20]
$m_{lh}^*(x) = 0.087 + 0.063x$	[29]
$\Delta E_v = 0.55x\Delta E_g$	[19]
$\gamma_{lh} = 7.35 \times 10^{-19} \text{ m}^2$	[22]
$\gamma_e = 4.9 \times 10^{-19} \text{ m}^2$	[22]
hh-exciton BE (meV) = $14.47 - 0.0645L - 0.000141L^2$	[27]
lh-exciton BE (meV) = $15.74 - 0.0611L - 0.000119L^2$	[27]
(L in Angstroms)	

Figure 3.3.2 – Summary of the equations used in the program for the calculation of the required parameters in  $\text{Al}_x\text{Ga}_{1-x}\text{As}$ .

The results of two runs of program XTON are shown in figure 3.3.3. Included here are the input data parameters, the calculated band parameters (energy gaps, well depths in the conduction band and the valence) and the results in terms of the electron and hole energy eigenvalues and the exciton energies. From these results the penetration of the wavefunction into the barrier can be calculated. The decay constant, which is defined here as the distance over which the wavefunction decays by  $1/e$ , is equivalent to  $1/\alpha$  where  $\alpha$  is as defined in equation (3.3.1.3). It can be calculated for the electron wave function that the decay constant is  $11.5\text{\AA}$  for  $100\text{\AA}$  wells and  $12.7\text{\AA}$  for  $50\text{\AA}$  wells. Therefore, over a distance of  $50\text{\AA}$  from the well into the barrier, the electron wavefunction has decayed by a factor  $\approx 1/50$ . It is reasonable to say that the carriers confined in a layer are not affected by the potentials of adjacent wells. The single isolated quantum well model used in the calculations is therefore a valid one. If the wells are closely spaced then another approach has to be used such as the Kronig-Penney<sup>[30]</sup> model or the

Al concentration in well (%) 0  
 Al concentration in barrier (%) 30  
 Well width (Angstroms) 50  
 Temperature (K) 300

Well depth in conduction band = 0.353 eV  
 Well depth in valence band = 0.070 eV  
 Well bandgap = 1.4225 eV  
 Barrier bandgap = 1.8448 eV  
 HH exciton binding energy (n=1) = 11.6meV  
 LH exciton binding energy (n=1) = 13.0meV

n	Electron energy (eV)	Heavy Hole Energy (eV)	Light Hole Energy (eV)	Heavy Exciton Transition (eV)	Heavy Exciton Transition (nm)	Light Exciton Transition (eV)	Light Exciton Transition (nm)
1	0.0943	0.0171	0.0366	1.5223	815.0	1.5403	805.0
2	0.2920	0.0620	- - - - -	1.7736	699.5	- - - - -	- - - - -

No more bound states

Al concentration in well (%) 0  
 Al concentration in barrier (%) 30  
 Well width (Angstroms) 100  
 Temperature (K) 300

Well depth in conduction band = 0.353 eV  
 Well depth in valence band = 0.070 eV  
 Well bandgap = 1.4225 eV  
 Barrier bandgap = 1.8448 eV  
 HH exciton binding energy (n=1) = 9.4meV  
 LH exciton binding energy (n=1) = 10.8meV

n	Electron energy (eV)	Heavy Hole Energy (eV)	Light Hole Energy (eV)	Heavy Exciton Transition (eV)	Heavy Exciton Transition (nm)	Light Exciton Transition (eV)	Light Exciton Transition (nm)
1	0.0360	0.0065	0.0179	1.4556	852.3	1.4656	846.5
2	0.1301	0.0259	0.0599	1.5761	787.1	1.6098	770.7
3	0.2563	0.0561	- - - - -	1.7338	715.5	- - - - -	- - - - -

No more bound states

Results from program XTON for excitonic transition energies for GaAs wells of widths 50 and 100 Angstroms. In each case the barrier layers are 30% AlGaAs and T= 300K.

Figure 3.3.3

tunnelling resonance method as used by Stephens et al[22].

Program XTON was used to calculate the room temperature excitonic transition energies for a "typical" quantum well as a function of well width and this variation is shown in figure 3.3.4. The parameters used in the calculation are shown beside this graph. It can be seen that the excitonic energy varies more rapidly with well width for narrower wells than it does for the wider wells.

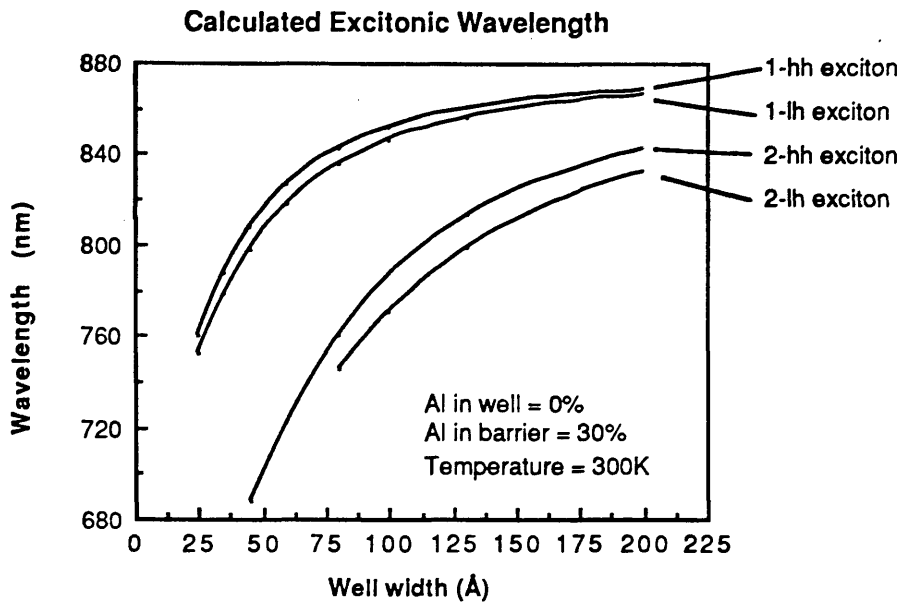
The results of this calculation are obviously sensitive to the data used in determining the band and carrier parameters. In order to see how significant this dependence was, the calculations were performed with different band parameters. It was found that the use of different band alignment parameters ( $\Delta E_c = 0.6\Delta E_g$  and  $\Delta E_c = 0.85\Delta E_g$ ) gave a discrepancy of 8.2meV (5.0nm) for the  $n=1$  hh transition in a 50Å well and a discrepancy of 2.3meV (1.3nm) for a 100Å well. Also it was seen that the effect of ignoring the band nonparabolicities resulted in shifts of the hh-exciton positions by 7meV (3nm) for the 50Å well and 3meV (1.5nm) for the 100Å well. The discrepancies between the results vary with the well widths and are larger for the narrower wells. This is obviously related to the gradient of graph 3.3.4 which is larger for narrower wells.

The excitonic energy can suffer from variation over the sample as a result of well layer thickness fluctuations. Considering variations of the order of a monolayer (i.e. 2.83Å<sup>[31]</sup>), the slope of the graph in figure 3.3.4 indicates that, for a well width of 50Å, the excitonic energy varies by about 4nm in wavelength. A similar thickness fluctuation for a 100Å well gives a wavelength variation of 1.0nm. The layer thickness should only vary by the order of a monolayer in good quality material. Low temperature photoluminescence studies (see later) performed in material grown for this project and published results in the literature indicate that the fluctuations are in fact of the order of 10Å. The program above is therefore capable of calculating the layer thickness to accuracies better than the well thickness uniformities in grown material.

### 3.3.2 Application of the Kramers–Kronig relations to MQW structures.

If the excitonic absorption is known it is possible to calculate its contribution to the refractive index by means of the Kramers–Kronig relations.

The shape of the excitonic absorption peak has been represented by both Lorentzian<sup>[32]</sup> and Gaussian<sup>[17]</sup> lineshapes by different authors. The broadening of the excitonic absorption line is a result of exciton–phonon interactions and of well thickness fluctuations. The excitonic absorption peak (heavy or light hole) can be expressed as:



The calculated wavelengths for the  $n=1$  and  $n=2$  heavy and light hole excitons are shown as a function of well width .

**Figure 3.3.4**

$$\alpha_{\text{ex}} = \alpha_0 \exp \left[ - \frac{E-E_0}{\tau} \right]^2 \quad (3.3.2.1)$$

if the Gaussian form is assumed, where the full-width at half maximum (FWHM) is given

$$\text{FWHM}_{\text{Gauss}} = 2\tau\sqrt{\ln 2} \quad (3.3.2.2)$$

and

$$\alpha_{\text{ex}} = \frac{\alpha_0}{\left[ \frac{E-E_0}{\nu} \right]^2 + 1} \quad (3.3.2.3)$$

if the Lorentzian form is assumed where the FWHM is given

$$\text{FWHM}_{\text{Lorentz}} = 2\nu \quad (3.3.2.4)$$

In both cases  $\alpha_0$  is the magnitude of the peak and  $E_0$  is the position of the peak. Figure 3.3.5 compares these lineshapes curves where the same FWHM and  $E_0$  values have been used. As can be seen, the Gaussian curve decreases much more steeply moving away from the peak, whereas the Lorentzian has a much slower descent. Consider the Kramers-Kronig transform (equation (2.2.4)):

$$n(\omega) - 1 = \frac{2}{\pi} P \int_0^{\infty} \frac{\omega' k(\omega')}{\omega'^2 - \omega^2} d\omega' \quad (2.2.4)$$

This can be transformed using integration by parts to give

$$n(\omega) - 1 = \frac{1}{\pi} \int_0^{\infty} \frac{dk(\omega')}{d\omega'} \ln |\omega'^2 - \omega^2|^{-1} d\omega' \quad (3.3.2.5)$$

Qualitatively, it can be seen from this equation that the integral tends to follow the gradient of  $k$  since the "ln" term is large near  $\omega = \omega'$ . Therefore a Gaussian absorption line, which has a steeper descent from the peak than the Lorentzian, is expected to give a larger index change.

A Turbo Pascal computer program called KRAMERS was written to generate these absorption lineshapes and to calculate the Kramers-Kronig transformed refractive indices. Integration was done using the Trapezoidal rule and the program

### Comparison of Gaussian and Lorentzian Lineshapes.

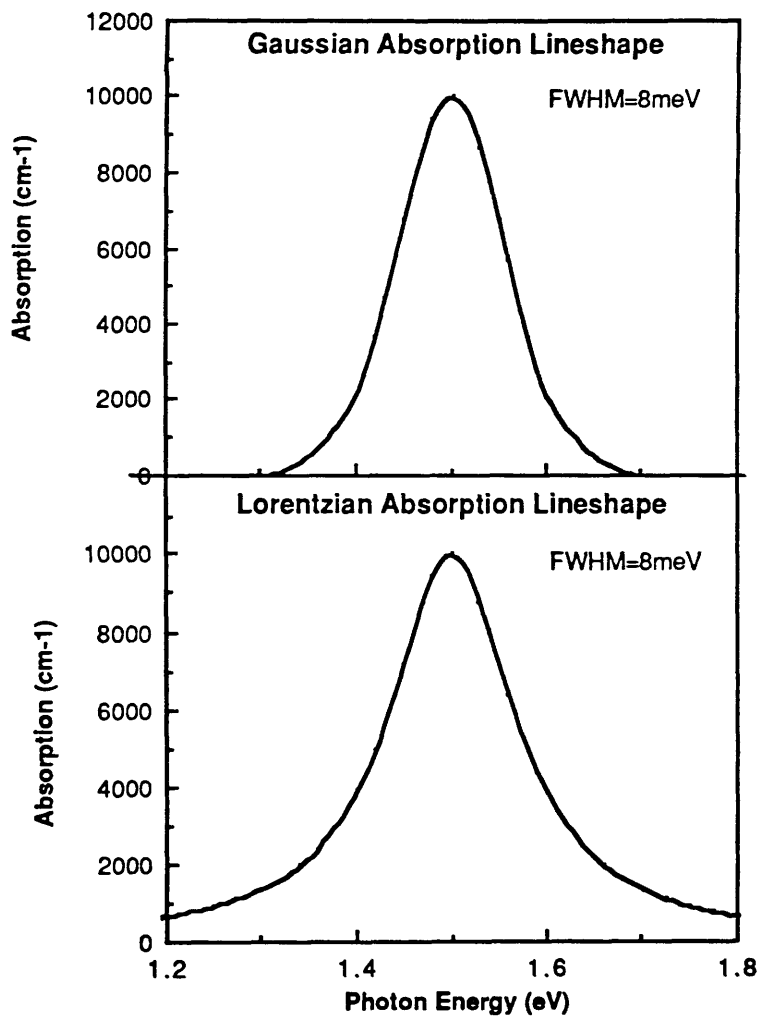


Figure 3.3.5

listing is included in Appendix II. The program was used to calculate the refractive index contribution due to the lineshapes of figure 3.3.5 and the results of this are shown in figure 3.3.6. It can be seen that, as discussed above, the Gaussian form does indeed give the larger refractive index contribution (by a factor of 6). It is therefore important that the correct lineshape is used because the value of the refractive index can vary quite significantly depending on this. The Lorentzian form has been used in the past by Sonek et al[32] but as discussed by Chemla et al[17] the Gaussian curve gives a better fit to experimentally observed excitonic absorption. Following the work of Chemla et al, the FWHM of the exciton absorption can be written

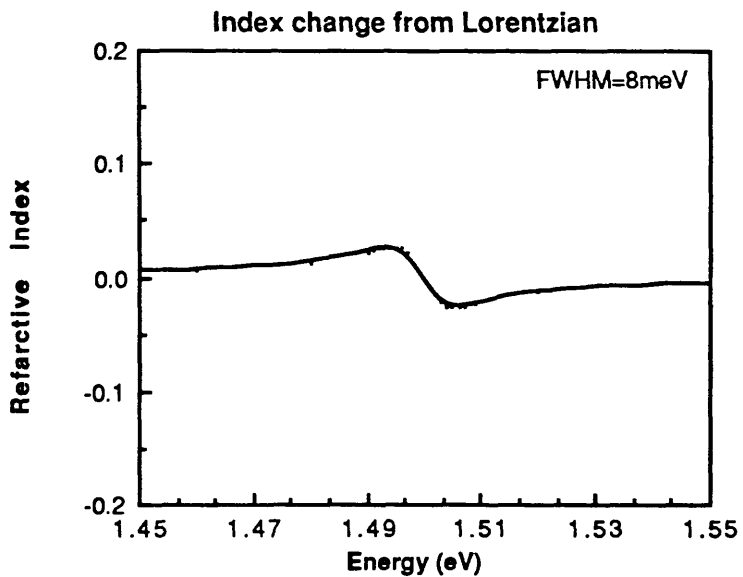
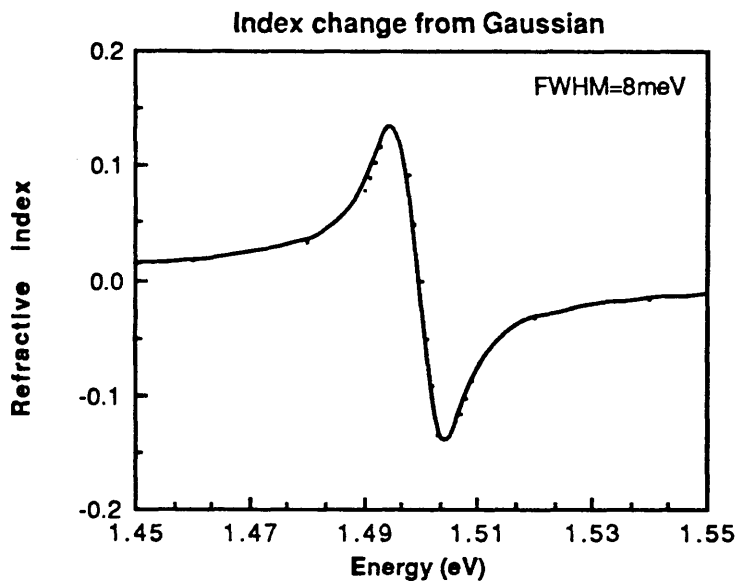
$$\Gamma = \Gamma_0 + \frac{\Gamma_{ph}}{\exp\left[\frac{\hbar\Omega_{LO}}{kT}\right] - 1} \quad (3.3.2.6)$$

The first term,  $\Gamma_0$ , is a constant inhomogeneous term due to energy variations arising from well width fluctuations and the second term is proportional to the density of LO phonons and consists of a Bose-Einstein distribution factor[33] and a constant of proportionality  $\Gamma_{ph}$ . The first term can be obtained from low temperature (16K) photoluminescence analysis because the second term then becomes insignificant. The LO phonon energy,  $\hbar\Omega_{LO}$ , is 37meV. The results of Chemla et al indicate  $\Gamma_0 \approx 4\text{meV}$  and  $\Gamma_{ph} = 11\text{meV}$  where this data was found to give good fits to both light and heavy hole excitonic features. Using this data at room temperature (300K), a FWHM of 7.5meV is calculated.

It is a straightforward procedure to calculate the refractive index of a MQW layer if the peak absorption values of the excitonic resonances, their widths and their respective positions are known. However for a structure which is only in the design stages and has not yet been grown, one has to make an estimate of these values from the literature[34]. The polarisation dependant selection rules which govern the transition strengths[35] have to be borne in mind. As described in Chapter Two, for light polarised parallel to the layers there is a relative transition strength of 3/4 to 1/4 for the heavy hole and light hole transitions. For light polarised perpendicularly the relative strength is 0 to 1. This polarisation dependent absorption introduces a strong birefringence into MQW waveguides.

The exact form of the excitonic absorption lineshape is dependant on the quality of the material and depends on how well the wafer is grown[36]. If the well layers are nonuniform then this results in an unduly broadened peak. The designer does not have much control over this except maybe by specifying the material growth process. The lineshape is therefore likely to differ from that of

## Comparison of Kramers-Kronig Transform of Gaussian and Lorentzian lineshapes.



These graphs show that for Gaussian and Lorentzian lineshapes of the same magnitude ( $10000 \text{ cm}^{-1}$ ) the maximum refractive index contribution is larger for the Gaussian lineshape.

Figure 3.3.6

samples reported in the literature but even so, by making an estimate of this from published data, an approximate value of the excitonic contribution to the refractive index can be obtained. The calculation of the refractive index of an MQW structure designed in this thesis is contained below in section 3.4 where the values of the excitonic contributions to the refractive index have been considered.

### 3.3.3 The Root-Mean-Square model.

Equation (3.3.1) expresses that the refractive index of a MQW structure can be expressed as a sum of two contributions. One of these, the excitonic contribution  $n_{ex}$ , has been examined in the previous section. The second term,  $n_{rms}$ , represents an equivalent "bulk" refractive index for the composite multilayer structure. When considering a multilayer slab comprising of alternating layers of two dielectrics  $\epsilon_w$  and  $\epsilon_b$  with thicknesses  $d_w$  and  $d_b$ , the refractive index of the composite structure can be evaluated by taking a weighted average of the contributions from both types of layers. A formula which takes the thicknesses of the layers into account and averages the squares of the layer indices is given by the following expressions[37]:

$$\epsilon_{TE} = \frac{\epsilon_w d_w + \epsilon_b d_b}{d_w + d_b} \quad (3.3.3.1)$$

$$\epsilon_{TM} = \frac{d_w + d_b}{(d_w/\epsilon_w) + (d_b/\epsilon_b)} \quad (3.3.3.2)$$

for light fields polarised parallel to and perpendicular to the layers respectively. The polarisation dependence of these equations is due to the difference in boundary conditions for the two situations. These expressions give a *root-mean-square* (RMS)[38] of the refractive index equivalent to the term  $n_{rms}$  in equation (3.3.1).

Using this expression in conjunction with the method described in the previous section, one is able to determine the refractive index for any given MQW structure. This information can then be used to design a suitable waveguide geometry.

## 3.4 Waveguide structures designed in this thesis

There were three kinds of AlGaAs waveguides investigated in this project. These were designed for characterisation of (i) resonant near-bandgap

nonlinearities, (ii) Kerr-type nonresonant effects and, (iii) MQW nonlinear effects.

The first of these categories comprised of an AlGaAs guiding layer with an Al composition of the order of 5%. This gave a bandgap of about 1.5eV (830nm). The near-bandgap properties were thus accessible for characterisation with the Styryl 9 dye laser. The second category of devices required a bandgap which was larger than the laser photon energy. For these structures an Al composition of the order of 30% was used which gave a bandgap of approximately 1.8eV (690nm) and was essentially transparent to the laser. Both of these waveguide types were designed by following the procedure of section 3.2.4. The design of the third category, MQW waveguides, required more consideration.

It was required that the absorption losses in the MQW waveguides were low enough to allow measurable amounts of light through samples of lengths of the order of several millimetres. This was necessary for the characterisation of the Asymmetric Mach-Zehnder interferometer which requires long waveguide lengths to attain sufficient separation between Y-junction branches. However the losses of conventional MQW structures, where the well and barrier layers are each 100Å thick, are of the order of  $10^4\text{cm}^{-1}$  at the excitonic resonance. A MQW structure was therefore designed where the transparent barrier layers were much thicker than than the well layers which effectively "dilutes" the absorption of the MQW layer. Barrier layers of thickness 1000Å and well layers of thickness 65Å were used which corresponds to a heavy-hole excitonic transition energies of 1.491eV (832nm) as calculated by program XTON.

The refractive index for TE polarised light in this structure is now calculated. As described in section 3.3, this consists of an average index term,  $n_{\text{rms}}$ , given by the RMS approximation, and an excitonic correction term,  $n_{\text{ex}}$ , calculated using the Kramers-Kronig relations. The lineshape used for the exciton absorption was a Gaussian taken from the literature and this was scaled accordingly for the reduced density of wells in the "dilute" system.

The calculation of the contributions from both light hole and heavy hole excitons were done using program KRAMERS. The heavy and light hole energies were 1.4912eV and 1.5066eV respectively and the refractive index was calculated for photon energies detuned by both 3meV and 30meV below the heavy hole. The parameters and results are summarised in figure 3.4.1. According to the data of Chemla et al<sup>[17]</sup> the FWHM of the two peaks are approximately equal and only the magnitudes differ. Measurements by these authors on a non-waveguide sample with 96Å wells and 98Å barriers indicate that the peak absorption for the heavy hole transition is  $11000\text{cm}^{-1}$  and that of the light hole transition is  $6300\text{cm}^{-1}$ . The refractive index contributions from the lineshape parameters given by these authors can be calculated using program KRAMERS but have to be scaled

**Summary of the different stages of calculation of the refractive index of the dilute MQW structure.**

	Excitonic Absorption Lineshape parameters			Refractive Index contribution	
	Peak (cm <sup>-1</sup> )	FWHM (meV)	Energy (eV)	3 meV below hh energy	30 meV below hh energy
light hole	6300	7.5	1.4912	0.0241	0.0097
heavy hole	11000	7.5	1.5066	0.1395	0.0219
Total excitonic refractive index contribution for 100A wells and barriers.				0.1636	0.0316
Total excitonic refractive index contribution for 65A wells and 1000 A barriers. (dilute structure)				0.0200	0.0038
RMS contribution to refractive index (TE polarisation) for dilute structure. (at 1.5 eV)				3.421	3.421
Calculated total refractive index of dilute structure:				3.441	3.425

**Figure 3.4.1**

accordingly for application to the "dilute" structure because of the reduced well density. The results of these calculations are summarised in figure 3.4.1. The total refractive index contribution at 3meV detuning below the heavy hole energy is 0.0200 and at 30meV detuning it is 0.0038. It can be seen that the excitonic refractive index contribution varies considerably depending on the wavelength.

It is important to realise that this procedure to determine the refractive index correction is only an estimate because one does not exactly know what the excitonic absorption peak will look like until the material has been grown and characterised. Nevertheless it provides a means of estimating the refractive index of MQW structures with an improved degree of confidence compared with estimate based solely on the RMS method. This becomes important especially close to the excitonic resonance. If the material absorption has been characterised and a good Gaussian (or Lorentzian) fit to the excitonic contribution can be determined then the above procedure enables a precise calculation of the refractive index.

A summary of the wafers used in the project is shown in figure 3.4.2. Detailed wafer specifications are show in Appendix III. Results of loss measurements and waveguiding characterisation of the structures designed using the above procedures are presented in Chapter Five.

### 3.5 Conclusions

The MQW waveguide design procedure has been described in this chapter. A model for a Four-layer slab waveguide was used in conjunction with the Effective Index method to design waveguides. As will be seen from the results in Chapter Five, this method is adequate for rib structures so long as the modal field of the waveguide is not significantly perturbed by the presence of the rib. Particular attention was given to the design of the MQW structure and the determination of the refractive index of this layer. It has been seen by another author<sup>[39]</sup> that if solely the RMS approximation is used, waveguides designed for single moded guiding actually support undesirable higher order modes when the wavelength is close to the excitonic absorption peak. This is because the excitonic contribution to the refractive index has not been accounted for and an underestimated value of the guiding layer refractive index is assumed. The method described in this chapter to calculated the refractive index of a MQW structure should improve the accuracy of the MQW waveguide design and eliminate this problem. It will be seen later that the waveguides designed using this procedure (in samples MV273 and MV330) were indeed single moded.

### Summary of wafer details

Wafer number	Guiding layer composition	Growth method	Source of material
MV273	MQW (dilute)	MOCVD	Sheffield
MV330	MQW (dilute)	MOCVD	Sheffield
CPM333	32% Al	MOCVD	Sheffield
CPM376	5% Al	MOCVD	Sheffield
Varian 1	30% Al	MBE	Varian (USA)
Varian 2	30% Al	MBE	Varian (USA)
MA670	6% Al	MOCVD	RSRE

Figure 3.4.2

### 3.6 References to Chapter Three.

- [1] T. Tamir (Ed), "Integrated Optics", Topics in Applied Physics, vol 7, Springer-Verlag, 1975.
- [2] P. K. Tien, "Light Waves in Thin Films and Integrated Optics", Appl. Opt., vol 10, no 11, pp2395-2413, 1971.
- [3] H. Kogelnik, V. Ramaswamy, "Scaling rules for Thin-Film Optical Waveguides", Appl. Opt., vol 13, no 8, pp1857-1862, 1974.
- [4] D. W. Hewak, J. W. Y. Lit, "Generalised dispersion properties of a four-layer thin-film waveguide", Appl. Opt., vol 26, no 5, pp833-841, 1987.
- [5] "Advanced Engineering Mathematics", Erwin Kreyszig, 5th Ed, John Wiley & Sons, 1983.
- [6] R. G. Walker, PhD Thesis, University of Glasgow, 1981.
- [7] J. F. Vinchant, F. Mallecot, D. Decoster, J. P. Vilcot, "Effects of Absorbing layers on the propagation constants: A four layer model on desktop-computer applied to photodetectors monolithically integrated with optical waveguides", Opt. Comm., vol 67, no 4, pp266-270, 1988.
- [8] D. S. Chemla, D. A. B. Miller, S. Schmitt-Rink, "Nonlinear Optical Properties of Semiconductor Quantum Wells" in 'Optical Nonlinearities and Instabilities in Semiconductors" Ed. H. Haug, Academic Press, 1988.
- [9] M. W. Austin. "theoretical and Experimental Investigations of GaAs/AlGaAs and  $n/n^+$  GaAs Rib Waveguides", J. Lightwave Tech., vol LT-2, no 5, pp688-694, 1984.
- [10] D. E. Aspnes, S. M. Kelso, R. A. Logan, R. Bhat, "Optical properties of  $Al_xGa_{1-x}As$ ", J. Appl. Phys., vol 60, no 2, pp754-766, 1986.
- [11] D. T. F. Marple, "Refractive Index of GaAs", J. Appl. Phys., vol 35, no 4, pp1241-1242, 1964.
- [12] H. C. Casey, D. D. Sell, M. B. Panish, "Refractive Index of  $Al_xGa_{1-x}As$

between 1.2 and 1.8 eV", *Appl. Phys. Lett.*, vol 24, no 2, pp63–65, 1974.

[13] B. Jensen, A. Torabi, "Dispersion of the Refractive Index of GaAs and  $\text{Al}_x\text{Ga}_{1-x}\text{As}$ ", *IEEE J. Quant. Elec.*, vol QE–19, no 5, pp877–882, 1983.

[14] S. Adachi, "Optical properties of  $\text{Al}_x\text{Ga}_{1-x}\text{As}$  alloys", *Phys. Rev. B.*, vol 38, no 17, pp12345–12352, 1988.

[15] J. S. Blakemore, "Semiconducting and other major properties of gallium arsenide", *J. Appl. Phys.*, vol 53, no 10, 1982.

[16] H. Kawai, K. Kaneko, N. Watanabe, "Photoluminescence of AlGaAs/GaAs quantum wells grown by metalorganic chemical vapor deposition", *J. Appl. Phys.*, vol 56, no 2, 1984.

[17] D. S. Chemla, D. A. B. Miller, P. W. Smith, A. C. Gossard, W. Weigmann, "Room Temperature Excitonic Nonlinear Absorption and Refraction in GaAs/AlGaAs Multiple Quantum Well Structures", *IEEE J. Quant. Elec.*, vol QE–20, no 3, 1984.

[18] G. Duggan, H. I. Ralph, K. J. Moore, "Reappraisal of the band–edge discontinuity at the  $\text{Al}_x\text{Ga}_{1-x}\text{As}$  heterojunction", *Phys. Rev. B.* vol 32, no 12, pp8395–8397, 1985.

[19] J. Batey, S. L. Wright, "Energy band alignment in GaAs:(Al,Ga)As heterostructures: The dependence on alloy composition", *J. Appl. Phys.*, vol 59, no 1, 1986.

[20] G. Duggan, H. I. Ralph, P. Dawson, K. J. Moore, C. T. B. Foxon, R. J. Nicholas, J. Singleton, D. C. Rogers, "Transitions to confined states of the split–off band in GaAs–(Al,Ga)As multiple–quantum–well heterostructures", *Phys. Rev. B.*, vol 35, no 14, 1987.

[21] D. F. Nelson, R. C. Miller, D. A. Kleinman, "Band nonparabolicity effects in semiconductor quantum wells", *Phys. Rev. B.*, vol 35, no 14, pp7770–7773, 1987.

[22] P. J. Stevens, M. Whitehead, G. Parry, K. Woodbridge, "Computer modelling of the Electric Field Dependent Absorption Spectrum of Multiple Quantum Well Material", *IEEE J. Quant. Elec.*, vol 24, no 10, pp2007–2016, 1988.

- [23] R. L. Greene, K. K. Bajaj, "Binding energies of Wannier excitons in GaAs-Ga<sub>1-x</sub>Al<sub>x</sub>As Quantum Well Structures", Solid State Comm., vol 45, no 9, pp831-835, 1983.
- [24] R. C. Miller, D. A. Kleinman, W. T. Tsang, A. C. Gossard, "Observation of the excited level of excitons in GaAs quantum wells", Phys. Rev. B., vol 24, pp1134- , 1981.
- [25] D. C. Rogers, J. Singleton, R. J. Nicholas, C. T. Foxton, K. Woodbridge, "Magneto-optics in GaAs-Ga<sub>1-x</sub>Al<sub>x</sub>As quantum wells", Phys. Rev. B., vol 34, pp4002- , 1986.
- [26] P. Dawson, K. J. Moore, G. Duggan, H. I. Ralph, C. T. Foxon, "Unambiguous observation of the 2s state of the light- and heavy-hole excitons in GaAs-(AlGa)As multiple quantum well structures", Phys. Rev. B., vol 34, pp 6007- , 1987.
- [27] E. S. Koteles, J. Y. Chi, "Experimental exciton binding energies in GaAs/Al<sub>x</sub>Ga<sub>1-x</sub>As quantum wells as a function of well width.", Phys. Rev. B. vol 37, no 11, pp6332-6335, 1988.
- [28] K. Mohammed, J. L. Merz, D. Kasemset, "Effect of Growth Temperature on the photoluminescence spectra of undoped AlGaAs grown by Metalorganic-chemical vapour deposition", Mat. Lett., vol 2, no 1, pp35-38, 1983.
- [29] S. Adachi, "GaAs, AlAs and Al<sub>x</sub>Ga<sub>1-x</sub>As: Material parameters for use in research and device applications", J. Appl. Phys., vol 58, no 3, 1985.
- [30] C. Kittel, "Introduction to Solid State Physics", 5th Edition, John Wiley & Sons, 1976.
- [31] J. L. Merz, A. C. Gossard, W. Wiegmann, "Alternate-monolayer single-crystal GaAs-AlAs optical waveguides", Appl. Phys. Lett., vol 30, no 12, pp629-631, 1977.
- [32] G. J. Sonek, J. M. Ballantyne, Y. J. Chen, G. M. Carter, S. W. Brown, E. S. Koteles, J. P. Salerno, "Dielectric properties of GaAs/AlGaAs Multiple Quantum Well Waveguides", IEEE J. Quant. Elec., vol QE-22 no 7, pp1015-1018, 1986.

- [33] C. Kittel, H. Kroemer, "Thermal Physics", 2nd Ed, W. H. Freeman and company, 1980.
- [34] Y. J. Chen, G. M. Carter, "Measurement of Third Order Nonlinear Susceptibilities by surface plasmons", Appl. Phys. Letts., vol 41, no4, 1982.
- [35] D. S. Chemla, D. A. B. Miller, "Room-temperature excitonic nonlinear-optical effects in semiconductor quantum-well structures", J. Opt. Soc. Am. B., vol 2, no 7, pp1155-1173, 1985.
- [36] H. Lee, A. Kost, M. Kawase, A. Hariz, P. D. Dapkus, E. M. Garmire, "Nonlinear Absorption Properties of AlGaAs/GaAs Multiple Wells Grown by Metalorganic Chemical Vapour Deposition", IEEE J. Quant. Elec., vol 24, no 8, pp1581-1592, 1988.
- [37] J. P. Van Der Ziel, A. C. Gossard, "Optical birefringence of ultrathin  $\text{Al}_x\text{Ga}_{1-x}\text{As}$ -GaAs multilayer heterostructures", J. Appl. Phys., vol 49, no 5, 1978.
- [38] S. Okhe, T. Umeda, Y. Cho, "Optical waveguides using GaAs- $\text{Al}_x\text{Ga}_{1-x}\text{As}$  Multiple Quantum Well", Opt. Comm., vol 56, no 4, 1985.
- [39] M. D. A. Macbean, Ph.D. Thesis, University of Glasgow, 1986.

## CHAPTER FOUR

### WAFER PROCESSING AND WAVEGUIDE FABRICATION.

#### 4.1 Introduction.

This chapter describes the various stages of the device fabrication process. The initial stage of device production is the material growth. Although the author's role in the material growth process was limited only to specification of the wafer, this chapter begins by summarising different growth techniques since there are some features here of relevance to other sections in this thesis. This is followed by a section discussing wafer assessment and, in particular, photoluminescence analysis. Finally, the various wafer processing stages are summarised and brief descriptions of the cleaning, photolithography and etching processes are included. Most of these are part of well established procedures but it is necessary to describe some details here because of their relevance to certain aspects of the work in this thesis.

#### 4.2 Material Growth.

There are three main techniques in widespread use today for the growing of epitaxial semiconductor layers. Each of these is described here in brief. Growth technology in itself is an active area of research and a detailed look at the various methods lies outwith the scope of this thesis. However awareness of the different techniques employed and their respective limitations is necessary since the requirement of certain structural properties can determine the preferred growth method.

##### 4.2.1 Liquid Phase Epitaxy.

The first and simplest of these methods is *Liquid Phase Epitaxy (LPE)*. Here the layers are grown by placing the substrate surface in contact with a saturated solution containing the growth ingredients<sup>[1]</sup>. In the case of GaAs, this is usually arsenic dissolved in a gallium solvent. The temperature is then lowered to between 600–900°C resulting in supersaturation in the solution. The material leaving solution then grows epitaxially onto the substrate surface.

LPE is the simplest and the cheapest growth technology. Because of the near equilibrium growth conditions, fewer defects occur and the material can be of

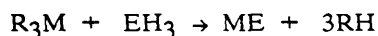
excellent crystalline and optical quality. However there are problems associated with LPE. When growing heterostructures "meltback" may occur at the solid–melt interface while equilibrium is re–established between the differing materials. This results in poor interface quality between different AlGaAs layers and the method is therefore not suited for the growth of ultrathin structures with well defined and abrupt interfaces. It is also difficult to grow layers with uniform composition and thickness. No LPE samples were used in this project.

#### 4.2.2 Metal Organic Chemical Vapour Deposition.

*Metal Organic Chemical Vapour Deposition (MOCVD)*[2] is one of the most important semiconductor growth technologies today. This is also known by other names such as MOVPE (metalorganic vapour phase epitaxy), OMCVD (organometallic chemical vapour deposition), OMVPE and OMP (organometallic pyrolysis). In MOCVD, the material is brought into contact with the substrate in a gaseous form. For GaAs growth the gas containing the gallium is an organic compound and is usually trimethylgallium (TMG) or triethylgallium (TEG). The arsenic source is normally arsine ( $\text{AsH}_3$ ). The growing of AlGaAs is done by mixing trimethylaluminium (TMA) with the TMG where the ratio of the two determines the proportion of aluminium in the AlGaAs. The gases are mixed and are fed into a reaction chamber in which the substrate is placed.

Epitaxial growth occurs when the gas is heated to 600–800°C above the substrate surface. This is normally done by placing the substrate on a graphite susceptor which is heated by a surrounding r.f. induction coil. The susceptor is also tilted at a small angle (3–5°) to improve the flow dynamics and hence give a larger uniform deposition area. A typical arrangement is shown in figure 4.2.1.

The reaction occurring in the growth chamber can be written in the form[2]



where  $\text{M} = \text{Al}$  or  $\text{Ga}$ ,  $\text{R} = \text{CH}_3$  or  $\text{C}_2\text{H}_5$  and  $\text{E} = \text{As}$ . This is a simplified representation of the reaction and ignores any possible intermediate steps.

MOCVD is the most versatile of the growth methods and is not as costly as Molecular Beam Epitaxy (described below) which requires expensive equipment. MOCVD can provide an interface quality far superior than that of LPE and is capable of producing extremely narrow layers. Excitonic transitions in MOCVD material with quantum wells as narrow as 5Å[3] have been observed.

There are however some disadvantages associated with MOCVD. Because of

**Schematic Diagram of a horizontal  
MOCVD Reaction chamber.**

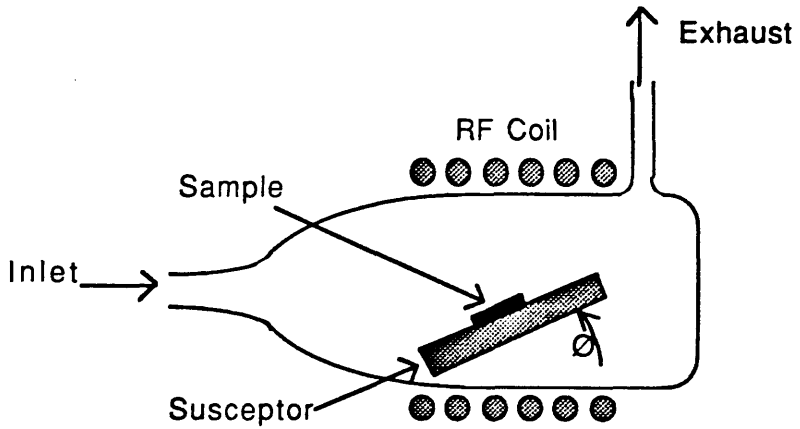


**Figure 4.2.1**

**Schematic Diagram of Molecular Beam  
Epitaxy Growth Apparatus.**

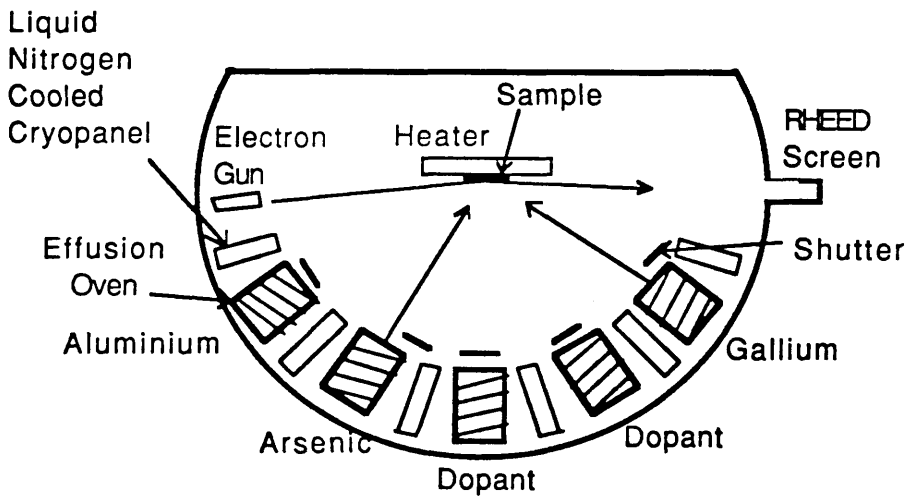


**Figure 4.2.2**

the organic sources used, there are, invariably, carbon impurities incorporated into the layers. (Carbon can dope the material n or p type depending on the growth conditions.) It is difficult to get a doping density significantly lower than  $10^{14}\text{cm}^{-3}$  [4]. One other disadvantage is that the source chemicals are either extremely toxic or spontaneously inflammable in air and rigorous safety precautions are necessary.

#### 4.2.3 Molecular Beam Epitaxy.

The other important material growth technique is *Molecular Beam Epitaxy* (MBE). This is basically an evaporation process applied in an ultrahigh vacuum environment[5]. The compounds or elements are heated in crucibles and are deposited onto the surface of a substrate material. The deposited atoms then migrate across the surface to a point of incorporation which is usually the edge of a layer "terrace" or "island" on the surface. The crystal surface may therefore be strongly smoothed on the atomic level because growth proceeds more rapidly at the lower points on the surface. Alternate monolayers of GaAs and AlAs can be grown easily[6].

In MBE, the growth temperature is important: if the temperature is too low then the deposited atoms will have insufficient motion to find the best site and this results in poor crystal quality. At high temperatures, species can be re-evaporated from the surface and interlayer diffusion may also occur. The growth temperature of GaAs is 550–600°C and for good quality AlGaAs is around 680°C. Figure 4.2.2 shows a schematic of the MBE growth apparatus.

The molecular beams incident on the surface can be stopped by shutters located between the material source and the sample target. The growth rate is slow (often about a monolayer per second) and thickness control of the order of an atomic layer can be obtained. The surface roughness of a sample can be assessed by using a beam of high energy electrons incident on the sample surface and monitoring the intensity of the diffracted electron beam on a fluorescent screen. It is possible to do this as the material is being grown and a characteristic periodically varying signal can be seen with the maxima occurring as each monolayer has been completed and is at its smoothest. These periodical variations in the signal, known as RHEED (Reflected High Energy Electron Diffraction) oscillations, provide a means of monitoring the growth during the epitaxial process.

MBE is well suited for the growth of ultrathin layers with abrupt well-defined interfaces. Because of the ultra-high vacuum and cleanliness requirements the systems are generally built from stainless steel and are expensive.

#### 4.2.4 Conclusions and Growth details of wafers used in the project.

The three main technologies in use today for the growth of epitaxial semiconductor layers have been summarised. It is also worth noting that there are other hybrid growth techniques like metalorganic MBE (MOMBE) which lie between MOCVD and MBE where gaseous compound sources replace the evaporation beam sources.

In this project, material grown by both MOCVD and MBE has been used in device production. The main source of material has been the SERC Facility for III–V Materials at Sheffield University where MOCVD was used. Wafers CPM328, CPM333, MA376, MA273 and MA330 were all obtained from Sheffield and were grown by Dr. J. S. Roberts or by Dr. P. Mistry. Sample MA670 was grown using MOCVD by Dr. J. Birbeck in RSRE, Malvern. The remainder of the samples were grown by MBE. The Varian samples were obtained by Dr. C. R. Stanley for Dr. T. Suhara who was on sabbatical leave from Osaka University, Japan, to visit this department during the period 1986–1987. Sample NTT613 was obtained by Dr. O. Mikami from Nippon Telegraph & Telephone Corporation during his stay in this department in 1986. The details of these wafers have been discussed in Chapter Three and schematic diagrams of all these structures are included in Appendix III.

At the beginning of the project it was assumed that the departmental MBE facility would be the provider of most samples. However, due to the fire in 1986, the MBE facilities in this department were not in operation during the major part of the project and were, unfortunately, not one of the sources of material for this work.

### 4.3 Material Analysis.

It is essential that one is able to assess the quality of semiconductor material before commencing with device fabrication. The material can be characterised by measurement of various properties such as carrier mobility, impurity content and material composition. Each of these involves an accordingly different analytical arrangement with varying degrees of complexity.

#### 4.3.1 Methods of Assessment.

One simple and quick assessment of wafer quality is by observation and measurement of the surface defect density. Some surface defects are shown in

figures 4.3.1. Figures (a) and (b) show oval type defects which tend to be similar in size, shape and orientation. Figures (c) and (d) show some other types.

Impurity concentrations can be assessed in a semiconductor by C-V profiling techniques. Here the capacitance at a metal-semiconductor (or electrolyte-semiconductor) Schottky contact is measured. The capacitance measured is that at the edge of the depletion region. The net impurity content can therefore be determined as a function of depth by varying the bias voltage. This works only up to a certain depth before avalanche breakdown occurs and thus repeated etching and measuring is required for larger depths. If, however, the electrolyte used also acts as an etch, then a continuous impurity concentration profile can be obtained for large depths as the electrolyte-semiconductor interface is etched into the sample. This is the principle of the polaron plotter which was used to determine the doping levels in some of the wafers.

Other assessment techniques include Hall effect measurements, which give the carrier mobility (and hence an indication of the impurity content and material homogeneity) and secondary ion mass spectroscopy (SIMS), where incident particles dislodge ions from the surface of the material (via sputtering) which are analysed in a mass spectrometer.

All these methods are either directly destructive or, as in the case of the Hall effect measurements, render the analysed material useless for device fabrication because of metallised contacts. Photoluminescence analysis provides a non-destructive technique for material quality assessment. This involves the optical excitation of carriers into higher energy states and the study of the various radiative relaxation transition energies. Photoluminescence analysis was used as a major analytical tool for the assessment of wafers in this project. This is now considered in more detail.

#### 4.3.2 Photoluminescence Studies.

There are many possible states a photoexcited carrier may occupy and there are a corresponding number of relaxation transitions which may occur. Each of these has a characteristic energy which can be identified from the material's photoluminescence spectrum. By studying these transitions it is possible to make an assessment of the impurity content and composition of the material. Some of these transitions, which are of relevance in a GaAs/AlGaAs system, are now summarised:

(a) A free electron in the conduction band can be captured at a neutral acceptor site. This is known as a *Free-to-bound* transition and is usually denoted



Scanning Electron Micrographs showing oval defects in samples (a) CPM333 (MOCVD) and Varian 1 (MBE).

Figure 4.3.1



(c)

(d)

Scanning Electron Micrographs showing defects in samples (c) Varian 1 (MBE) and (d) Varian 2 (MBE).

Figure 4.3.1

by the shorthand form  $(e, A^0)$ [7].

(b) A *Donor–Acceptor pair* transition occurs where an electron leaves a neutral donor and joins a neutral acceptor. This is usually denoted by  $(D^0, A^0)$ .

(c) *Free Excitonic* recombination describes an electron hole pair recombination resulting in the annihilation of a free exciton. This transition has been identified in GaAs in reference [8].

(d) A *bound exciton* can be considered as an exciton bound to a neutral impurity or defect. (A defect such as a vacancy (or interstitial) in the lattice is effectively like an acceptor (or donor)). A bound exciton is basically an excitonic molecule analogous to an  $H_2$  molecule comprising of four charged "particles"[9]. One of these particles will be an impurity or a defect which therefore localises the molecule to a particular site. Bound exciton transitions occur when the bound exciton recombines and leaves the impurity or defect in its ground state.

(e) *Phonon assisted* transitions. Any of the above transitions may be assisted by the creation or annihilation of an optical mode phonon[9]. These transitions manifest themselves in photoluminescence spectra through the existence of replica peaks. The separation of these from the direct transition peaks indicates the energy of the optical mode phonon involved. (There are two types of transverse optical phonon and one type of longitudinal optical phonon.)

(f) Transitions involving *deep trapping levels* caused by the presence of certain impurities or dopants (such as oxygen) may occur. These usually result in poor photoluminescence because they are efficient nonradiative transitions. A poor photoluminescence efficiency can thus indicate a large presence of trapping levels. The density of trapping levels due to oxygen impurities can be varied to an extent by adjusting the material growth conditions. The probability of incorporating oxygen impurities in the crystal is reduced if higher growth temperatures are used[10].

(h) In multiple quantum well structures, recombination of bound state electron hole pairs can be observed. Such MQW excitonic transitions can be used to assess the quality of the grown structures. The linewidth of the emission indicates the uniformity of the wells and the emission wavelength can determine the well width.

Some of the above transitions are depicted schematically in figure 4.3.2.

Before examining actual photoluminescence (PL) spectra some considerations regarding transition energies are made.

The binding energy of a free exciton can be estimated using the hydrogen atom model as discussed in section Chapter Two. The binding energy can then be expressed

## Schematic of main Photoluminescence Transitions

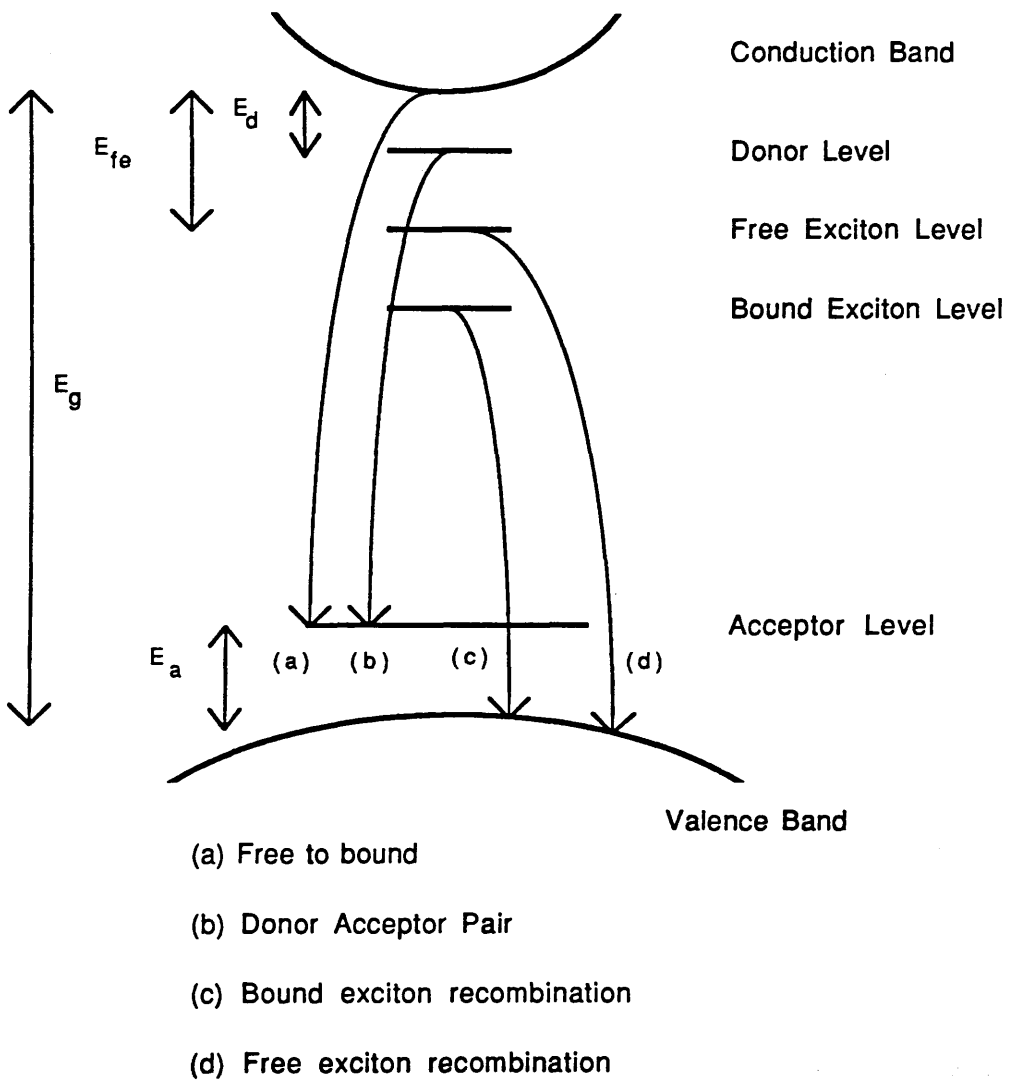


**Figure 4.3.2**

$$E = \frac{\mu E_0}{m_0 \epsilon_r^2 n^2} \quad (4.3.2.1)$$

where  $\mu$  is the reduced mass of the bound electron hole pair (where  $\mu^{-1} = m_e^{-1} + m_h^{-1}$ ),  $m_0$  is the electron mass,  $\epsilon_r$  is the relative permittivity of the semiconductor,  $n$  is the quantum number which will be taken as unity since we will be calculating the ground state binding energy, and  $E_0$  is the hydrogen atom Rydberg constant ( $=13.6\text{eV}$ ). Using values for GaAs, the free exciton ground state binding energy is calculated as  $E_{fe} \approx 4.5\text{meV}$ .

When considering holes (or electrons) captured by acceptors (or donors) it is not possible to use equation (4.3.2.1) to calculate the binding energies because of "core" effects. These arise from lattice distortion at the acceptor (donor) site and result in a local variation of the effective mass of the carrier. However, equation (4.3.2.1) can still be used to qualitatively indicate the variation of binding energy with effective mass remembering that when considering carriers captured by donors or acceptors (which are fixed within the crystal) the reduced mass  $\mu$  is no longer required and can be replaced by the carrier effective mass. It can then be seen that the binding energy depends on the effective mass and is smaller for an electron bound to a donor than that of a hole bound to an "equivalent" acceptor. In fact the binding energies of typical shallow acceptors are greater by approximately 5 times<sup>[7]</sup> to those of typical donors and this makes the identification of donors in GaAs extremely difficult.

Acceptor binding energies can be estimated from measurements of the  $(e, A^0)$  transition energy since  $E_A = E_g - E(e, A^0)$ . (See figure 4.3.2.) In practise it has been found that replacing the value  $E_0 = 13.6\text{eV}$  by a more appropriate constant  $E_H$  gives quite accurate values for carbon and germanium acceptor energies in  $\text{Al}_x\text{Ga}_{1-x}\text{As}$ <sup>[11]</sup>. The values of  $E_H$  are best determined from experiment for the acceptors concerned and a systematic investigation of acceptor binding energies for impurities in GaAs has been carried out by Ashen et al<sup>[7]</sup>.

Transition energies associated with bound excitons are useful in helping to determine the composition of  $\text{Al}_x\text{Ga}_{1-x}\text{As}$ . Several groups have reported the energies of these transitions. Stringfellow et al<sup>[11]</sup> have identified donor bound and acceptor bound excitonic transitions occurring at energies of 1.5144eV and 1.5129eV respectively in GaAs. These compare with Mircea-Roussel et al's<sup>[8]</sup> results of 1.514eV and 1.512eV for these respective transitions. If the former set of results are used, the binding energy of the bound exciton can be calculated to be 4.6meV and 6.1meV for the donor bound and acceptor bound cases respectively. Stringfellow et al have also established a relation between the Al doping concentration  $x$  in  $\text{Al}_x\text{Ga}_{1-x}\text{As}$  and the bound exciton recombination energy  $h\nu_{BE}$ :

$$x = \alpha \left[ h\nu_{BE}(x) - h\nu_{BE}(0) \right] \quad (4.3.2.2)$$

where  $\alpha=0.8032$  and  $h\nu_{BE}(0)=1.512\text{eV}$  in the range  $0 < x < 0.35$ . This very useful relation enables the Al doping concentration in  $\text{Al}_x\text{Ga}_{1-x}\text{As}$  to be determined from photoluminescence spectra. The values of  $\alpha$  and  $h\nu_{BE}$  were determined from measurements taken at  $T=4\text{K}$ . Considering the temperature dependence of the GaAs bandgap (see equation 3.3.1.4), a change in temperature from 2K to 20K only means an approximate change in the bandgap of 1meV. The values of these constants are therefore accurate to within 1meV for temperatures up to at least 20K.

The PL system is a permanent part of the analysis equipment used by the MBE material growth group in this department. The system is illustrated in figure (4.3.3). The samples could be cooled, if necessary, to about 16K by a closed liquid helium cryostat and the photoexcitation of carriers is provided by a HeNe laser operating at 633nm (1.960eV). The luminescence from the sample is focussed into a spectrometer and the spectra were obtained by scanning the spectrometer and measuring the luminescence intensity at the output slit using a Germanium detector with lock-in detection. The signal was plotted directly on a chart recorder. All the photoluminescence spectra plots were obtained by Mr. J. Cochrane. Some of these spectra are now examined.

#### 4.3.3 Photoluminescence data.

Figure 4.3.4 shows the spectrum for wafer CPM333 which was nominally an  $\text{Al}_{0.32}\text{Ga}_{0.68}\text{As}/\text{Al}_{0.34}\text{Ga}_{0.66}\text{As}$  double heterostructure. (See appendix III for the wafer schematic). There are four distinct peaks present. Two of these have been identified as transitions in the GaAs capping layer: the peaks at 1.514eV and 1.494eV are due to donor bound excitonic (BE) recombination and to a free-to-bound ( $e, A^0$ ) transition involving a carbon acceptor<sup>[11,12]</sup> respectively. Carbon impurities are unavoidable in MOCVD due to the organic sources used. The two peaks at 1.934eV and 1.896eV correspond to the AlGaAs cladding and guiding layers. It is reasonable to assume that it is the same transition in each layer which gives these peaks. These are either due to the aforementioned BE or ( $e, A^0$ ) transitions. These peaks are considerably broader in the AlGaAs than in GaAs. One possibility is that this broadening is due to alloy effects, i.e. due to the variations in the local field because of local composition fluctuation, but this is unlikely because the wavefunction extends over quite a large volume and these

# Photoluminescence System Schematic

This shows the components of the system used by the MBE group for measurement of photoluminescence spectra.

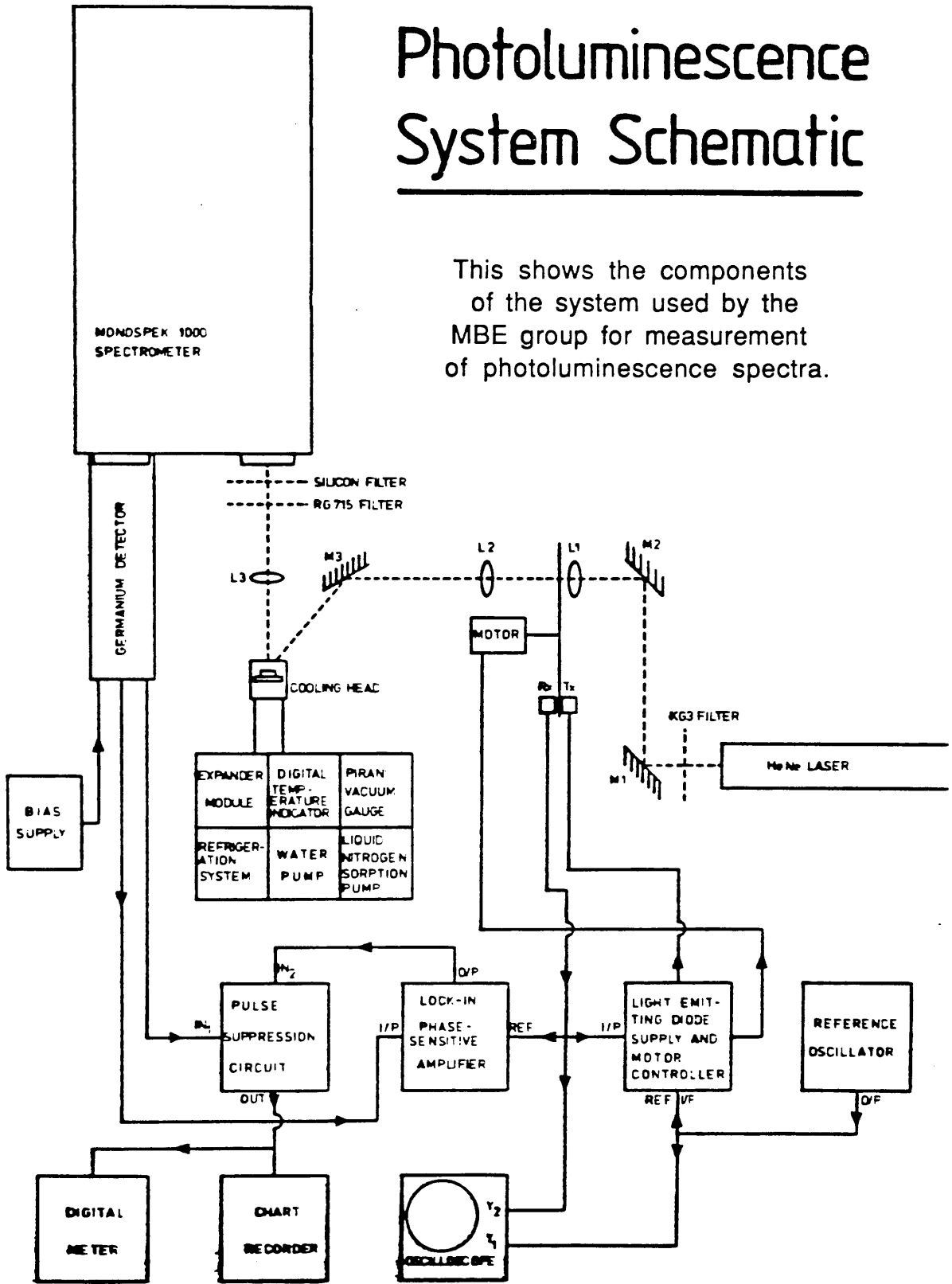
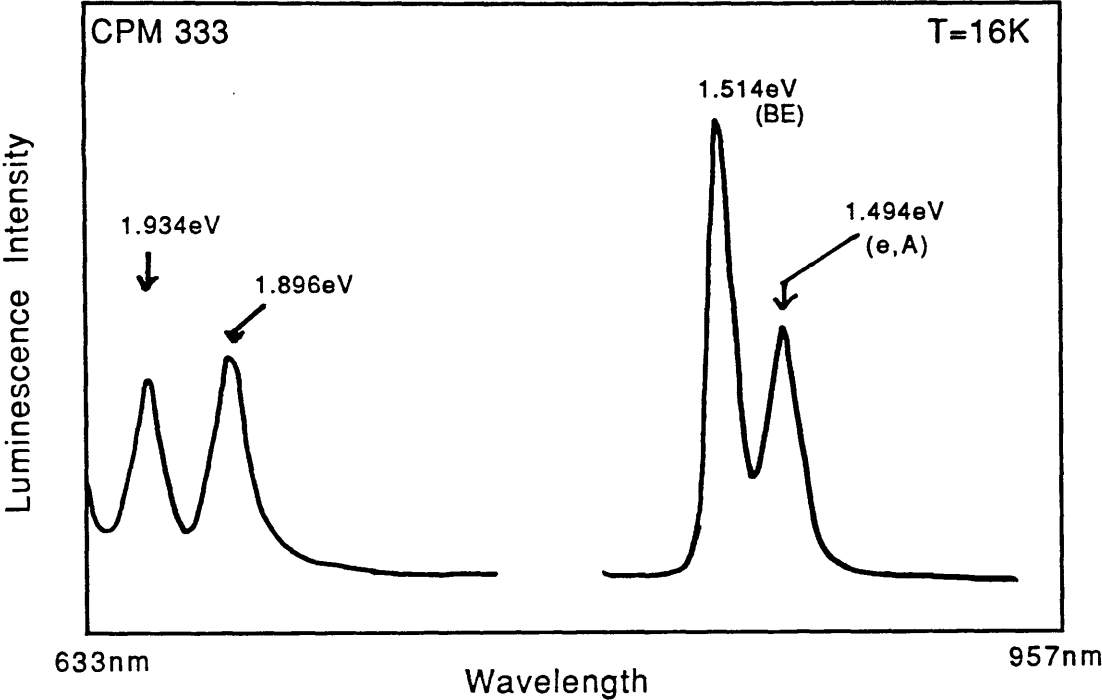


Figure 4.3.3

Photoluminescence Spectrum



Photoluminescence Spectrum for sample CPM333.

Figure 4.3.4

effects average out so the acceptor binding energy actually varies little from impurity to impurity<sup>[13]</sup>. Instead this broadening has been attributed to ionised impurity broadening. It has been established that the total dopant concentration  $N_A + N_D$  tends to increase with increasing  $x$  in  $Al_xGa_{1-x}As$  [11]. If the impurity concentration is sufficiently large then the separation between ionised donors is less than the Bohr radius of the electron bound to the donor and the donor levels broaden eventually forming a continuum with the conduction band. The donor level broadening is more significant than that of the acceptors because the Bohr radius of the electron-donor pair is larger due to the smaller effective mass of electrons. (Bohr radius  $a_r = 4\pi\epsilon\hbar^2/m^*e^2$ .) After the work of Mircea-Roussel et al<sup>[12]</sup>, who have studied these two transitions for varying  $x$  in MOCVD material, the FWHM of the peaks at 1.934eV and 1.896eV seems to indicate that these are probably due to  $(e,A^0)$  transitions associated with carbon impurities as opposed to the BE transitions which have narrower linewidths. The work of Stringfellow<sup>[11]</sup> established that the intensity of the luminescence due to the BE transition decreases relative to the  $(e,A^0)$  transition for AlGaAs with increasing  $x$ . This may be because of screening caused by the fields from ionised impurities thus resulting in reduced exciton formation. Taking all this into account it seems most likely that the two peaks observed in the luminescence are due to  $(e,A^0)$  transitions.

This means that these energies cannot be directly used to determine the Al composition in the guiding and cladding layer since equation (4.3.2.2) relates the BE energy to  $x$ . However it is possible to estimate the BE energy from these peaks by considering the energy difference of the two types of transitions. One can thus write (referring to figure 4.3.2):

$$h\nu_{BE} - h\nu_{(e,A^0)} = (E_g - E_x - E_{bx}) - (E_g - E_A)$$

$$\Rightarrow h\nu_{BE} - h\nu_{(e,A^0)} = E_A - (E_x + E_{bx})$$

where  $E_x$  is the binding energy of the free exciton,  $E_{bx}$  is the additional energy gained by binding to the neutral acceptor, and  $E_A$  is the acceptor ionisation energy. Strictly speaking, both  $E_A$  and  $E_x$  have a dependance on the alloy composition due to the composition dependant permittivity and effective masses but the results of sample CPM376 (see below) indicate that this is not significant and the difference in the position of the peaks remains about 20meV. Adding this correction to the  $(e,A^0)$  gives BE energies of 1.954eV and 1.916eV. Using equation (4.3.2.2) gives  $x$  values of 35.5% and 32.5% for the cladding and guiding layers respectively. These lie to within 2% the specified values of 34% and 32%.

The spectra for samples CPM376 and MA670 are shown in figures 4.3.5 and

Photoluminescence Spectrum

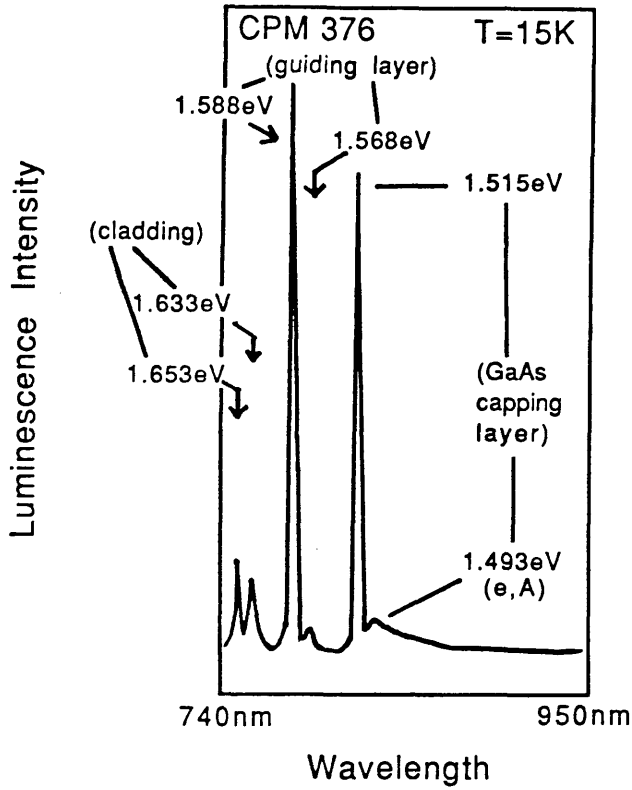
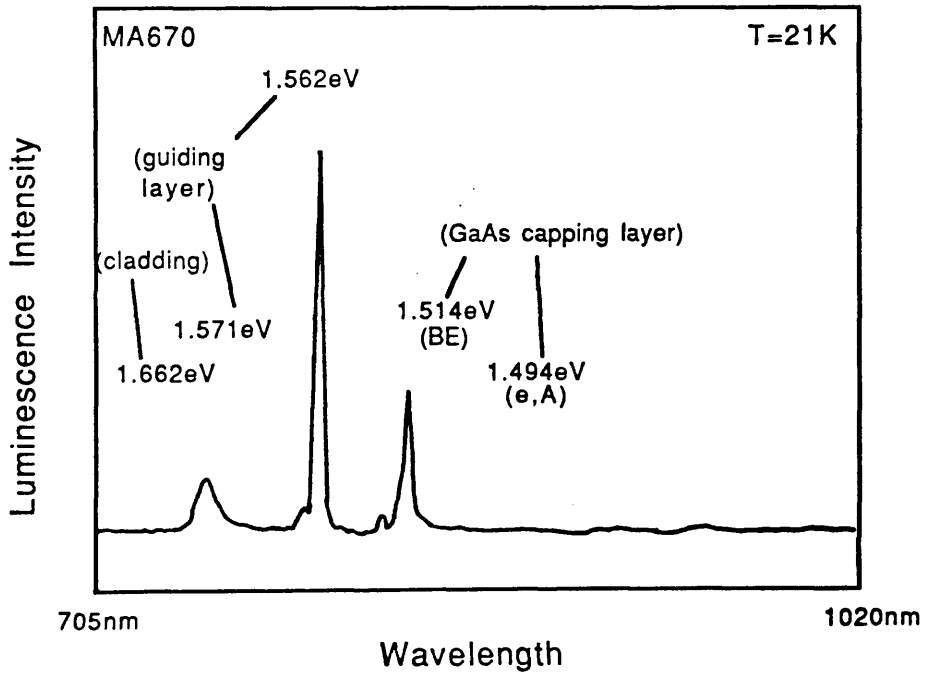


Figure 4.3.5

Photoluminescence Spectrum



Photoluminescence Spectra for samples CPM376 and MA670.

Figure 4.3.6

4.3.6 respectively. The former has a 5% Al guiding layer with 10% Al cladding, and the latter has a 6% Al guiding layer with a 12% Al cladding. (See appendix III for details of the structures.) The two samples are very similar in specification and thus enable a comparison to be made of the material from Sheffield to that from RSRE. The luminescence from CPM376 was about ten times brighter than that of MA670. This might be due to the presence of oxygen trapping levels in the latter material which give rise to efficient nonradiative transitions. Each of the spectra has clearly identifiable BE and  $(e,A^0)$  transitions for the GaAs capping layer and the guiding layers. In MA670, the two transitions for the AlGaAs cladding layer are indistinguishable and only one peak is seen. This indicates that there may be a large amount of background impurities in sample MA670 giving rise to broadening of the  $(e,A^0)$  peak in the cladding layer for reasons discussed above. Again equation 4.3.2.2 can be used to determine the compositions of the AlGaAs layers in these two samples. These results are summarised in figure 4.3.7.

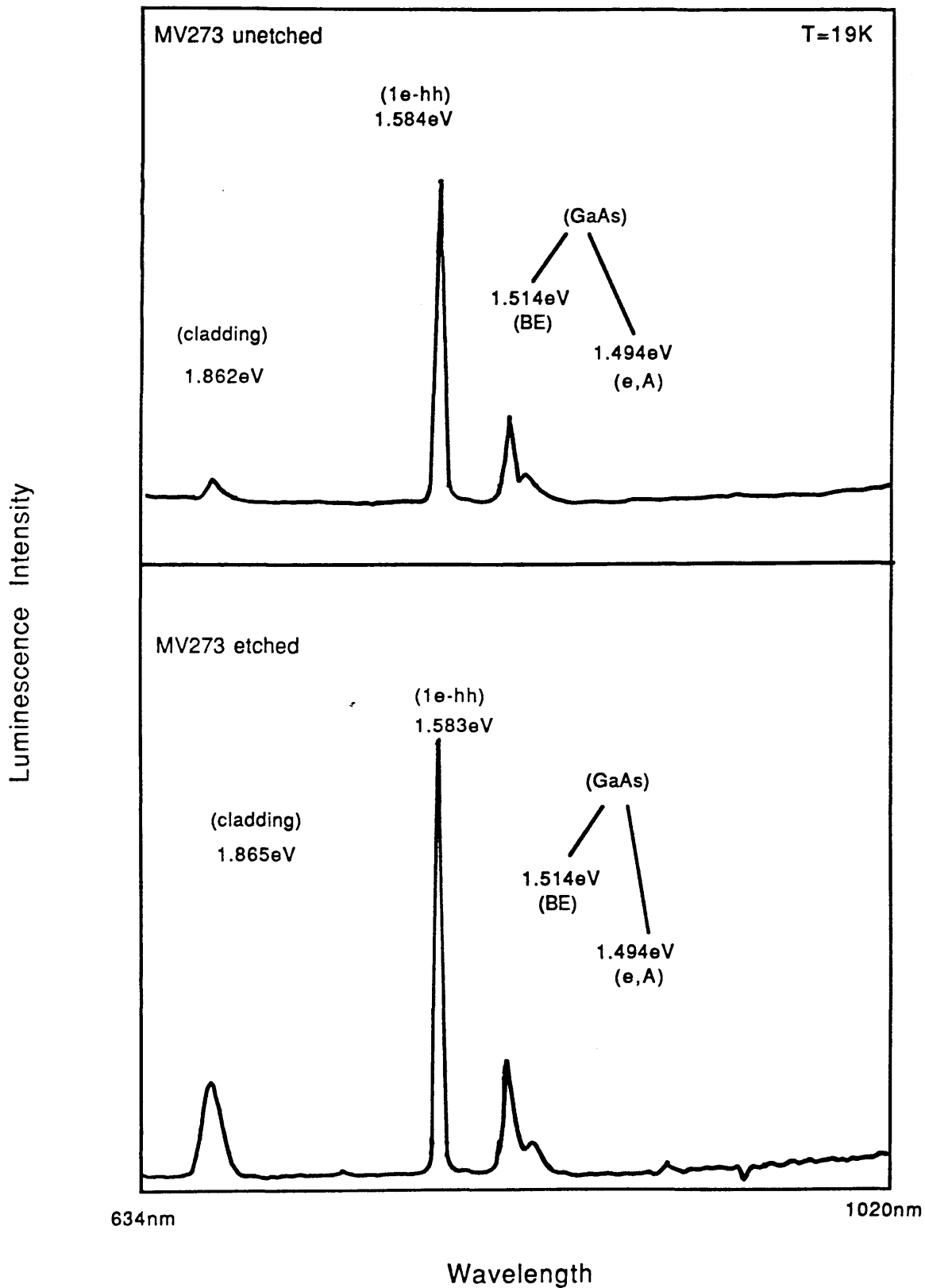
The photoluminescence spectra obtained from MQW structures is now examined. Figure 4.3.8 shows the spectra of sample MV273. One of these is from an unetched sample while the second is that from a sample in which the ribs had been etched. Clear peaks can be identified due to BE and carbon acceptor  $(e,A^0)$  transitions in the GaAs capping layer as well as what are probably  $(e,A^0)$  transitions in the cladding layers. This indicates an Al composition of 30.0% in the cladding. Note that the relative height of this peak is larger in the etched sample because here the absorbing GaAs capping layer has been removed. The GaAs transitions are still present and are probably due to transitions occurring in the buffer layer.

CPM 376		MA 670	
$h\nu_{BE}$	x	$h\nu_{BE}$	x
1.515	0%	1.514	0%
1.588	6.1%	1.571	4.7%
1.653	11.3%	$\approx 1.662$	$\approx 12\%$

Figure 4.3.7 – Results of Al composition determined from PL data for samples CPM 376 and MA 670.

In addition to these peaks, there is a sharp peak due to the recombination of excitons in the quantum well layers. The well width can be estimated from the

# Photoluminescence Spectrum



Photoluminescence Spectra for sample MV273 before and after etching of the upper cladding layer.

Figure 4.3.8

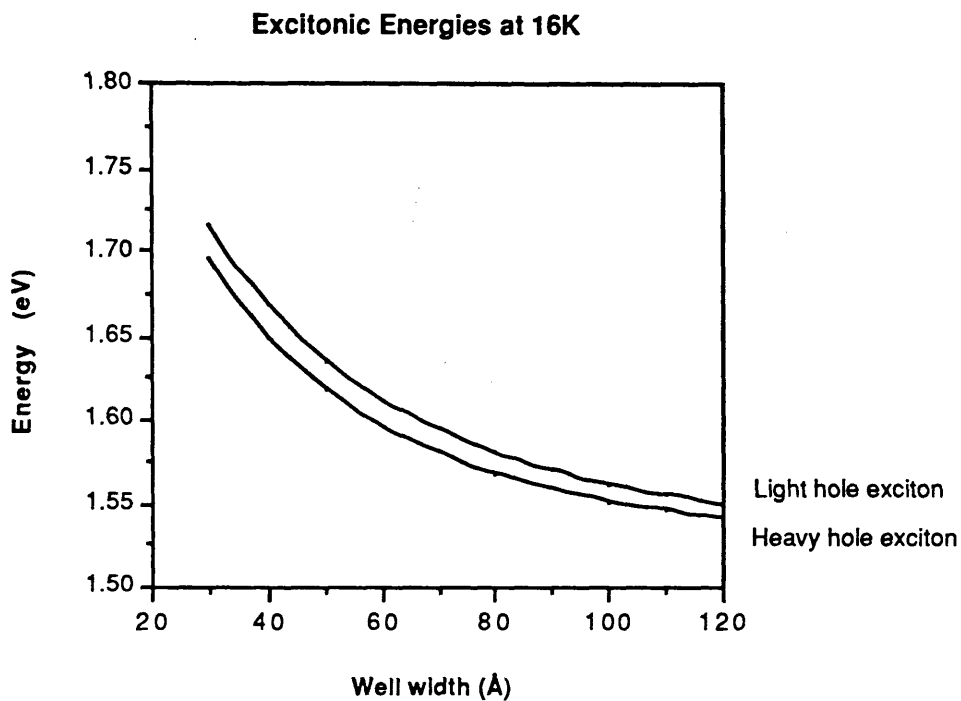
energy of this peak using program XTON. Figure 4.3.9 shows a graph of the variation of exciton energy as a function of well width at  $T = 16\text{K}$ . From this a well width of  $67\text{\AA}$  can be estimated. This is very close to the specified well width of  $65\text{\AA}$ . Sample MA273 has a p-i-n doping variation ( $p \approx n \approx 10^{15}\text{ cm}^{-3}$ ) incorporated in the layers and therefore there is a built-in electric field across the MQW region. This is in the order of  $1.3 \times 10^4\text{ V cm}^{-1}$  and only gives a Stark shift in the excitonic energy of about  $1\text{meV}$  ( $0.5\text{nm}$ )<sup>[14]</sup> and has been ignored in the well width calculation.

Figure 4.3.10 shows the spectrum from MV330 and compares it with that of MV273. These two samples are similar in specification except that MV330 does not include a p-i-n doping variation. Note that now the  $(e, A^0)$  and BE transitions in the cladding layer are resolvable. Noting the widths of these peaks confirms that it is the presence of impurities which tends to broaden the  $(e, A^0)$  peaks. The position of the BE peak indicates a cladding aluminium composition of 31.4%. The position of excitonic peak indicates that the well width is  $71\text{\AA}$ : not as good as before but still within the design specification.

Finally, figure 4.3.11 shows the spectrum obtained from sample NTT 613. This also has included a p-i-n structure but the doping levels are considerably higher. ( $p \approx n \approx 5 \times 10^{17}\text{ cm}^{-3}$ ). The luminescence in this sample is not very bright and the spectrum shows a considerable amount of noise. There are three broad peaks in the regions around  $1.488\text{eV}$ ,  $1.320\text{eV}$  and  $1.159\text{eV}$  and are most likely due to transitions associated with deep impurity levels. The GaAs transitions seen in all of the previous samples (at  $1.424\text{eV}$  and  $1.514\text{eV}$ ) have been masked completely by the peak at  $1.488\text{eV}$ . The peak at  $1.765\text{eV}$  is most likely due to the  $(e, A^0)$  transition in the cladding layer and indicates an Al composition of 22%. The peak at  $1.549\text{eV}$  is interpreted as due to recombination of the 1st heavy-hole exciton in the quantum wells. In this case, because of the high doping levels, there is a larger electric field present in the MQW layer. This was calculated to be in the region of  $3.8 \times 10^4\text{ V cm}^{-1}$  and this gives a Stark shift of around  $0.3\text{meV}$  ( $1.7\text{nm}$ )<sup>[14]</sup>. Taking this into account, a well width of  $99\text{\AA}$  is calculated. (This Stark shift consideration results in a correction of  $-5\text{\AA}$  in the well width.) There is a peak at  $1.532\text{ eV}$  which remains unidentified and has the same energy as the unidentified transition observed by M. D. A. Macbean<sup>[15]</sup>.

#### 4.4 Wafer Processing and Patterning.

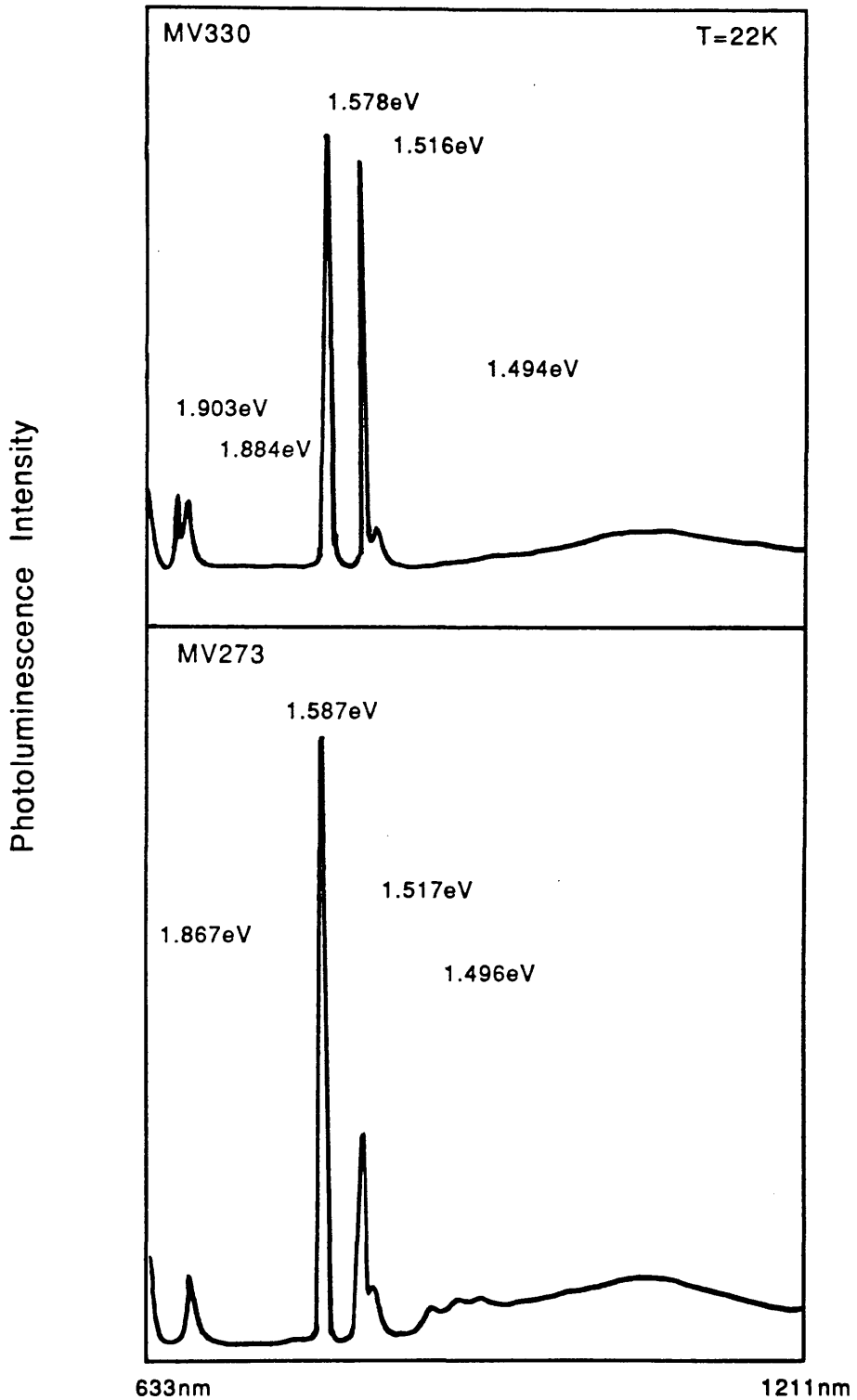
The processes involved in the production of device patterns on the samples are now described. These patterns are either in photoresist or in metal but in both



Excitonic transition energies as calculated  
by XTON for T=16K.

**Figure 4.3.9**

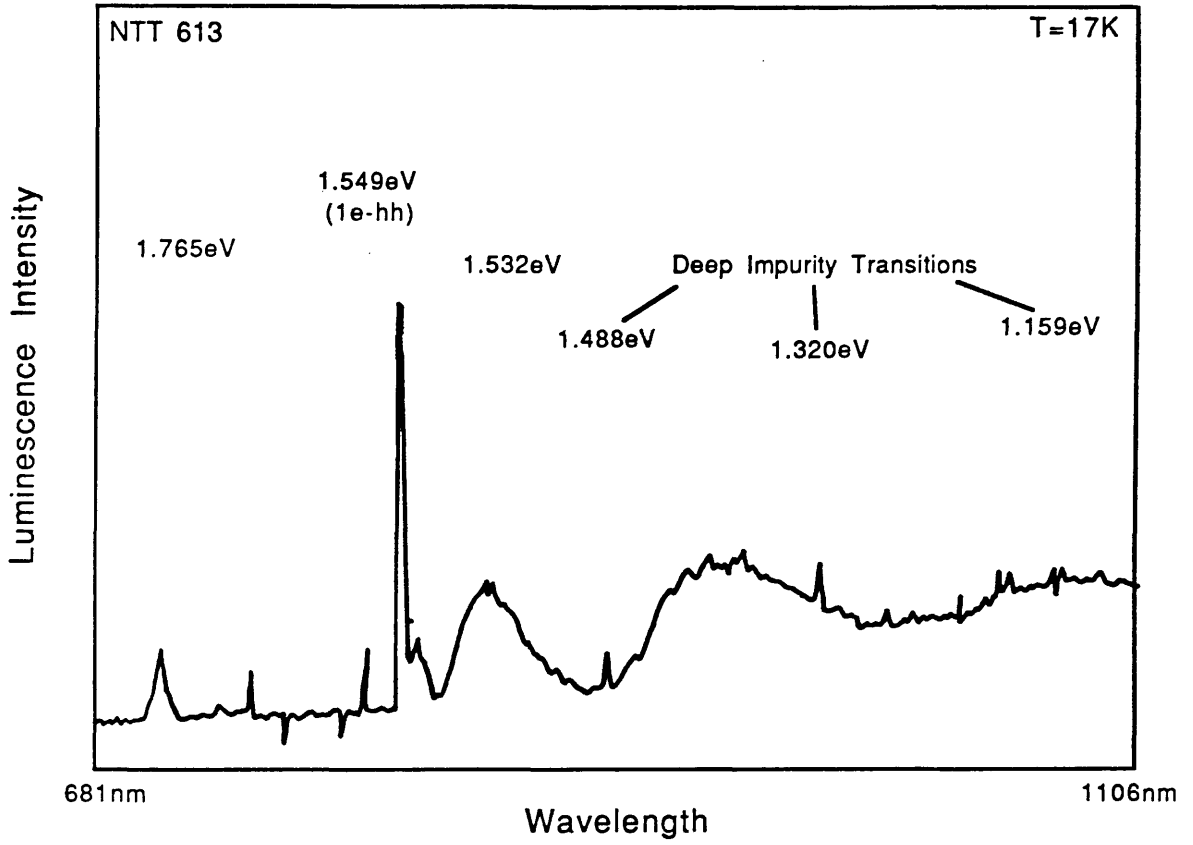
# Photoluminescence Spectra



Comparison of Spectra of samples MV330 and MV273.

**Figure 4.3.10**

# Photoluminescence Spectrum



Photoluminescence Spectrum  
for sample NTT613

Figure 4.3.11

cases act as masks for the etching process. The pattern is initially transferred photolithographically from a glass shadow mask to a photosensitive layer on the sample surface by exposing to ultraviolet light through the mask.

Both metal and photoresist masks were used in this project and there were consequently two slightly differing procedures followed. These are illustrated in figure 4.4.1. For the production of a photoresist etch mask, the pattern in the photoresist was defined using a light field photolithographic mask and after development, the sample was ready for etching. For the other case a dark field mask, which is a negative of the light field, was used. The sample was developed and metallised and the resist and surplus metal were then removed before etching.

The processes of wafer cleaning, spinning and patterning of the photoresist and metallisation are described in this section. Also included is a description of the cleaving process which was used to cut up samples. Shorter samples had to be thinned down to enable reliable cleaving of short samples and so the procedure to back polish these is very briefly described.

#### **4.4.1 Wafer cleaning.**

Wafer cleaning can be done to varying degrees. If the wafer requires degreasing, or has wax on the surface, or the state of cleanliness is unknown, then the first cleaning was done using trichloroethane which dissolves the grease or wax. The wafer was immersed in a beaker of this and subjected to an ultrasonic rinse for 5 minutes. If there is a large amount of wax or grease present then heating of the trichloroethane may be required.

The next step was to clean the sample in acetone to dissolve the trichloroethane. Again it was ultrasonically rinsed. This is followed by a similar rinse in methanol to dissolve the acetone. The final rinse was in ultra-purified water. The sample is then blown dry using a jet of nitrogen and put on a hotplate for 5 minutes.

It is important to ensure that the sample surface remains wet between rinses. This is to prevent the deposition of any residual solutes on the sample surface. If the wafer cleaned is uncleaned and not yet processed then a good precautionary measure is to put on a protective layer of photoresist. This means that the surface will not come into contact with dust particles until the sample is ready for processing. The resist can easily be removed by the above procedure starting with the acetone rinse.



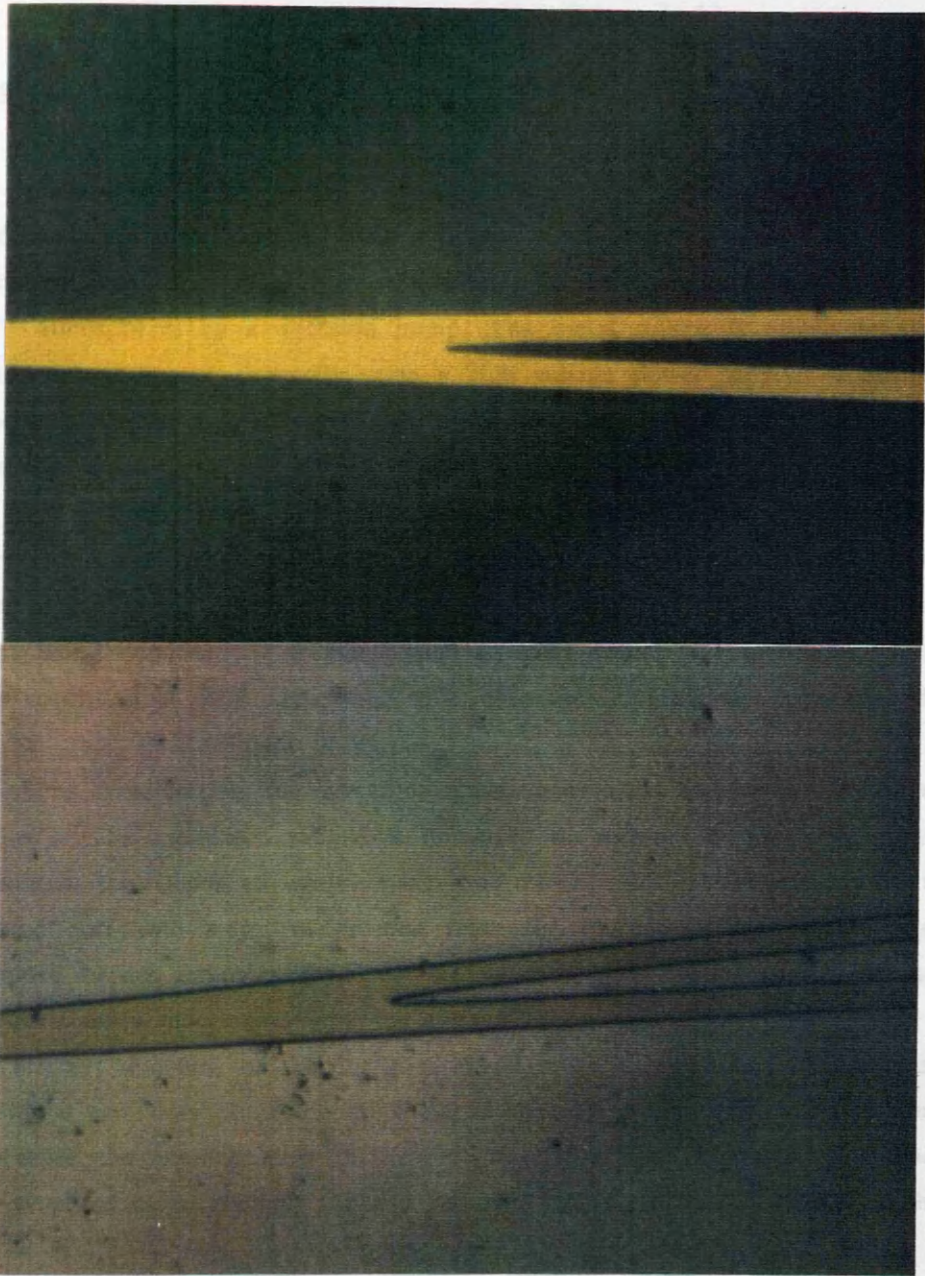
#### 4.4.2 Patterning of the Photoresist.

The sample first has to be coated with a uniform layer of photoresist. This is done by high speed spinning of the sample after a few drops of the liquid resist have been deposited on the cleaned surface. The photoresists used in this project were Shipley AZ1350J, AZ1350 and AZ1350H, the latter of which was used at R.S.R.E. All of these are positive photoresists (i.e. the exposed parts of the resist are removed by the developer action) but they vary in thickness: AZ1350 is thinnest. It was found that the thinner resist gave better lithographically defined Y-junctions when fabricating the Asymmetric Mach-Zehnder devices. Thicker resists contributed to a "blunting" of the Y-junction apex.

Resist was applied onto the sample surface by means of a filtered syringe. The sample was held in position by a vacuum chuck and was then spun at a speed of 4000 r.p.m. for 20 seconds. The resists were then baked dry in an oven. Resist thickness depended on the resist type, spin speed and sample size but was about  $1.5\mu\text{m}$  for AZ1350H and  $0.5\mu\text{m}$  for AZ1350. After the resist had dried the sample was ready for patterning. This was done by exposure to ultraviolet light through a shadow mask. (All the masks were produced by Mr. R. Harkins in this department with the exception of one which was obtained through R.S.R.E.) The masks were made of glass coated on one side with chrome. Parts of the chrome had then been etched away leaving transparent areas according to the lithographic pattern.

Exposure to ultraviolet light was done by contact printing. The coated side of the sample was placed in contact with the metal side of the shadow mask and was then covered by a weight to improve contact. The resist was exposed to an ultraviolet lamp shining from beneath the mask. The resist was then developed by washing in a 1:1 (volume) mixture of Microposit 351 developer to water. The chrome mask required cleaning in acetone after every two exposures due to resist deposits on the mask surface.

Generally, the exposure and development times were varied a little to give the best results in terms of edge definition of the resist and uniform developed resist thickness. Resist uniformity could be easily assessed by looking at the apparent resist colour. For the best results the exposure time was about 5 minutes for AZ1350J and 3 minutes for AZ1350. The developing time was 75 seconds for both cases. After developing it was imperative to look at the quality of the developed features. If the patterning was not good enough, the above procedure could easily be repeated at this stage after removal the resist. Figure 4.4.2 shows a detail of the shadow mask used in fabricating Y-junctions and the resulting resist pattern obtained using Shipley AZ1350 on sample MA670. The narrow waveguides are  $3\mu\text{m}$



Photographs showing detail of Y-junction in (a) the photolithographic mask, and (b) the patterned photoresist (Shipley AZ1350) on sample MA670. The lines are  $3\mu\text{m}$  wide.

**Figure 4.4.2**

wide.

#### 4.4.3 Metallisation.

Metallisation of the sample was done by evaporation in an evacuated chamber. A diagram of the vacuum system is shown in figure 4.4.3. The chamber is evacuated down to  $\approx 3 \times 10^{-2}$  atmospheres by a rotary pump and then to  $\approx 3 \times 10^{-7}$  atmospheres by a diffusion pump. The metal source is placed in a tungsten boat which is heated ohmically using a high voltage power supply. When the metal is seen to melt, a shutter is opened so that the evaporated metal particles are deposited on the sample. The thickness of the deposited metal was monitored by an Intellimetrix sensor positioned adjacent to the sample. This consists of a calibrated crystal which oscillates at a frequency varying according to the thickness of deposited metal. This is calibrated by specifying the material properties of the metal being deposited. The metal used in this project was nichrome which is an alloy consisting of 90% nickel and 10% chromium. This gives good edge definition and has good etch resistant properties.

After metallisation the unwanted metal has to be removed. This is done by *lift-off*. The metallised sample is immersed in acetone to dissolve the resist and to loosen the deposited metal lying on top of this. The metal can then be "blasted" off with a jet of acetone from the dispenser. The sample has to be examined before removing from the acetone otherwise residual pieces of metal can be permanently redeposited onto the surface.

Correct thickness of the deposited metal is of importance. The deposited metal has to be less than the resist thickness or the lift-off process will not work. This is because the acetone must be able to penetrate into the resist lying underneath the unwanted metal through the gap between the metal on the resist and the metal on the sample surface. On the other hand, the layer has to be sufficiently thick so that it is not completely etched away. The etch rate of nichrome in  $\text{SiCl}_4$  (see section 4.5) is 80 times slower than that of GaAs. A rule of thumb to follow is that  $250\text{\AA}$  of nichrome will suffice for a GaAs etch of  $1\mu\text{m}$ [16].

#### 4.4.4 Cleaving of the sample.

Samples were divided into suitably sized pieces by cleaving the wafer along the crystal planes. This process involves first scribing a small shallow groove with a diamond stylus in a direction parallel to either of the [011] or the [0 $\bar{1}$ 1] crystal

**Schematic of vacuum system used for metallisation of samples.**

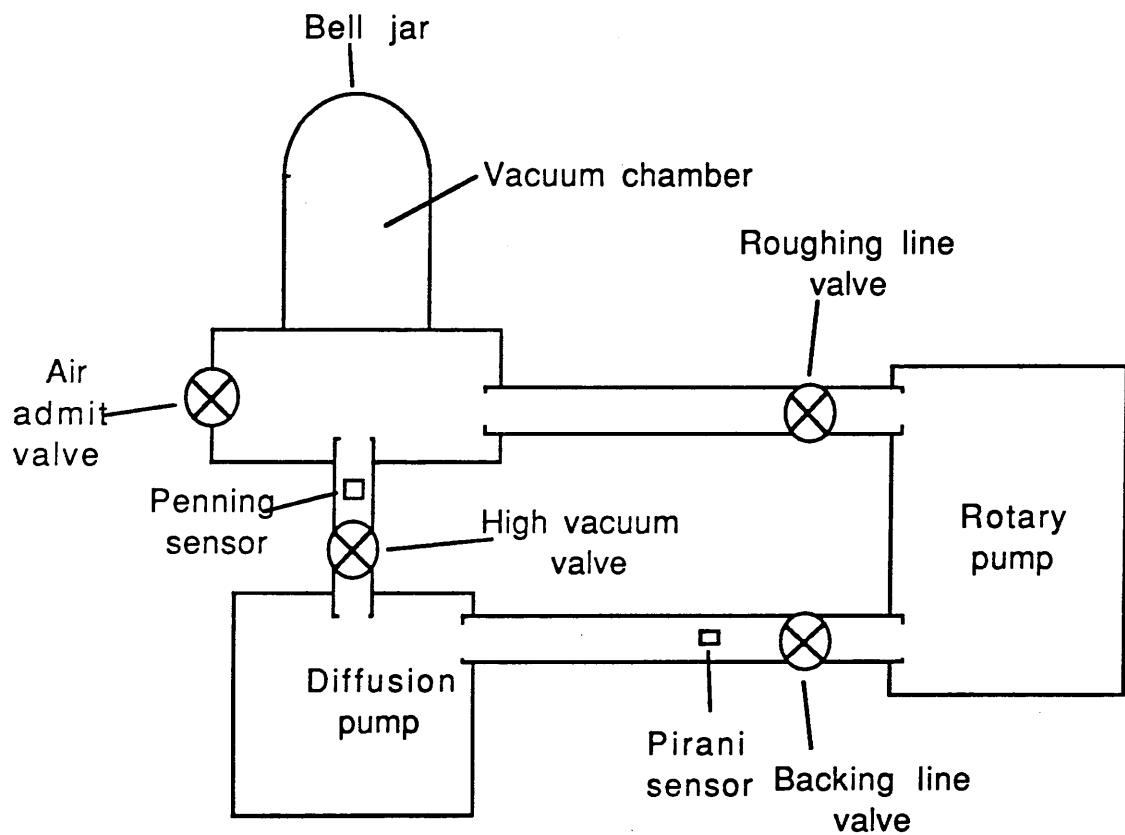


**Figure 4.4.3**

planes. There is usually a previously cleaved edge or wafer flat which can be used as a reference to align the translating stage on the scribing machine. After a groove has been scribed onto the sample surface, pressure is exerted in a manner to induce a fracture, starting from the groove, along the cleavage plane to completely break off the piece of the sample. Cleaving results in extremely smooth edges and in fact are smooth enough to give high quality reflecting facets in waveguide semiconductor lasers.

Generally, the cleaved faces are not as smooth under the scribed line on the edge than that away from it because of the width of the scribe mark. This is illustrate in figure 4.4.4 where two such regions are compared. To get a long good quality facet it is therefore undesirable to scribe an excessively long distance. The minimum necessary scribing distance is determined by the geometry of the sample. Thin slices of material are difficult to cleave off if the scribed groove is too short or if the cleave distance is too long or if the sample is too thick. If a short cleaved sample ( $< 500\mu\text{m}$ ) is required then it is necessary to thin the sample by back polishing.

#### 4.4.5 Back polishing of samples.

Samples were thinned by polishing their back surfaces using an abrasive compound. A quartz polishing tool consisting of a central block and a holder was used and the sample was mounted on this using melted wax with its epilayer side towards the block. It was ensured that the sample surface was not in contact with the block and that there was a layer of wax between the sample and the block to prevent damage to the sample surface. Both block and holder were then placed on a glass surface covered with an abrasive silica carbide powder and water mixture and manually polished. The sample was thinned to about  $100\text{--}200\mu\text{m}$ .

The sample thickness was measured every so often by using a displacement clock gauge accurate to less than  $5\mu\text{m}$ . The gauge measured relative height of the sample's polished surface to the surface of the polishing block. The initial thickness also had to be measured before mounting so that the total thickness could be monitored. Generally speaking the sample's polished surface was not exactly parallel to the top surface but this was not of importance.

After polishing, the sample was removed from the holder using genklene or trichloroethane and cleaned using the procedure described above. Ultrasonic agitation of the sample could not be used excessively because the sample was now extremely fragile and was liable to break. Once the sample was cleaned and dried it could be cleaved extremely easily. In fact no initial scribing was necessary and



(a)

(b)

SEM photographs showing cleaved ends of a sample (a) directly underneath the scribe line and (b) away from the scribe mark. The cleaved surface is considerably better in (b).

Figure 4.4.4

the merest pressure of a scalpel blade was enough to initiate the cleave. To prevent the cleaved piece from being lost the sample was held in place on a microscope slide by covering with cling film prior to cleaving.

#### 4.5 Wet and Dry Etching of Waveguides.

The final step in the waveguide fabrication is the etching process. This can be done using both wet and dry etching techniques. The former is a purely chemical process where a liquid etchant is used to attack and dissolve the unmasked parts of the sample surface. Dry etching can be performed by a pure chemical action as well as by physical processes where accelerated particles "sandblast" and erode unmasked surfaces. Reactive Ion Etching (RIE) is a dry etching technique which is a combination of both chemical and physical etching processes and it was this method which was used for etching of devices.

Most of the etching in this project was done using RIE but some wet etching was also performed at R.S.R.E., Malvern, due to a lack of accessible AlGaAs dry etching facilities there. The results of the two different processes are presented and compared.

##### **4.5.1 Wet Etching of AlGaAs.**

The object of this part of the work was not to investigate the etching process but to instead use an already established recipe and to fabricate waveguides. The following will thus be restricted to a description of etchant used, the etch rate calibration procedure and the results of the wet etching process.

Most wet etching solutions contain chemicals to perform two actions: one to oxidise the constituents and the second to dissolve the resulting oxides. The etch used at R.S.R.E. consisted of equal parts (by volume) of the following constituents:

- (i) 7 ml of 100 vol hydrogen peroxide ( $H_2O_2$ ) in 490 ml of deionised water.
- (ii) 20 ml of 35% ammonium hydroxide ( $NH_3OH$ ) in 490 ml of deionised water.

Here the oxidising agent is hydrogen peroxide and the resulting oxides are dissolved by the ammonium hydroxide. The oxides of Ga are in fact soluble in both acidic and alkaline solutions (i.e. they are amphoteric) and frequently acidic solutions are

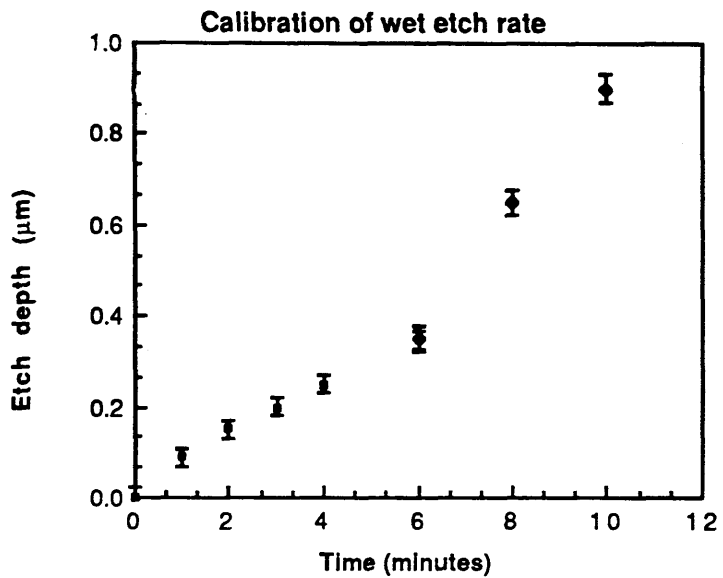
used instead of ammonium hydroxide. The oxides of Al are soluble in water.

The etch rate was determined by repeated etching of patterned test samples and measuring of the etched depth by a Sloan Dektak profile plotter. The etch mask used here was Shipley AZ1350H photoresist which had been postbaked. The thickness of this was measured before etching of the sample took place and since the resist itself was not prone to etching, this thickness was subtracted from the subsequent depth measurements. When etching the sample, the dish containing the etchant was constantly agitated so that the solution in contact with the sample surface constantly being refreshed.

Sample MA661, which was similar to MA670 and comprised of an  $\text{Al}_{0.12}\text{Ga}_{0.88}\text{As}$  cladding and  $\text{Al}_{0.06}\text{Ga}_{0.94}\text{As}$  guiding layer, was etched using the above mixture and the etched depth was measured after one minute intervals. It was realised from the first few measurements that the etch rate was not high as previous calibrations done at R.S.R.E. indicated. A rate of approximately  $0.15\mu\text{m}/\text{min}$  was expected but only  $0.05\mu\text{m}/\text{min}$  was obtained. It was suspected that this might be due to the age of the solutions used and so fresh batches of  $\text{H}_2\text{O}_2$  and ammonium hydroxide solutions were prepared. A sudden and clear increase in the etch rate was seen. Figure 4.5.1 shows the measured etch depth as a function of time. There is a marked change in the slope of the graph after 6 minutes which is the point at which the solution was changed. A rate of  $0.14\mu\text{m}/\text{min}$  was obtained from the new solution: a rate in agreement with previous calibrations. The error bars on the graph are based on repeated Dektak measurements over a small area of the sample and thus indicate the etch depth measurement accuracy. It is therefore extremely important to ensure that the chemicals being used are as fresh as possible so that a consistent etch rate is obtained.

Wet etched waveguides are shown in figure 4.5.2 after removal of the resist. Note the sloping walls of the rib due to undercutting of the resist mask and preferential etching of different crystal planes. This is a typical feature of the wet etching process. The etch profile depends on the alignment of the etch mask with respect to the crystal axes<sup>[17]</sup> and this property has been used by J. J. Isaac<sup>[18]</sup> in identifying the crystal orientation. Wet etching is also known for producing extremely smooth rib walls.

There are disadvantages associated with wet etching. There is a lack of control in determining the profile of etched features since these depend on the orientation of the waveguides with respect to the wafer and it is difficult to control features of size less than  $1\mu\text{m}$  because of resist undercutting. There is also lack of uniformity of etching across large areas because the etch rate is sensitive to the local composition of the solution. This can be alleviated to some extent by agitation of the solution but even so, as was seen when making the etch depth measurements,



The graph shows the results of wet etching sample MA661 in  $\text{H}_2\text{O}_2 : \text{NH}_3 : \text{OH}$  solution. A pronounced increase was seen in the etch rate when a fresh solution of etchant was prepared (after 6 minutes).

**Figure 4.5.1**



SEM photographs showing wet etched rib waveguides. Note the sloping walls due to the poor anisotropy of the wet etching process.

Figure 4.5.2

etch depth rates can vary by up to 10% over large areas. This can be quite significant when etching large ribs. Also, the wet etching process may result in bubble formation on the sample surface and this also contributes to etch nonuniformity.

#### 4.5.2 Reactive Ion Etching of AlGaAs.

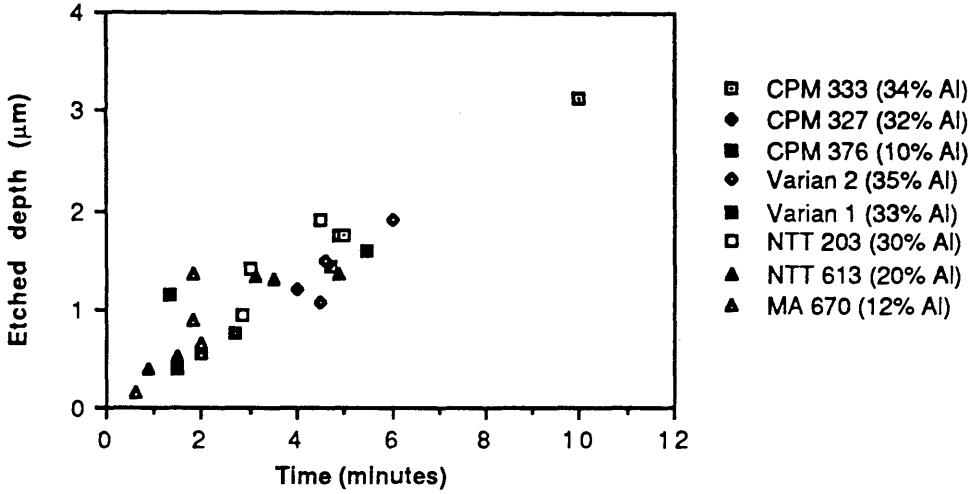
There are many varied dry etching techniques. These range from purely physical processes such as ion beam etching, where the kinetic energy of accelerated ions is used to dislodge particles from the surface, to plasma etching, where chemical reactions transform the constituent atoms on the surface into volatile compounds which are removed in a gaseous form<sup>[19]</sup>. As mentioned above, Reactive Ion Etching is a process which is a combination of the two processes. Here a sample is placed in a chamber which is then evacuated to about 10–50 mtorr. The reactant gases are fed in and are ionised to form a plasma by an r.f. generator. In this project all of the dry etching was done using SiCl<sub>4</sub> as the reactant. The ions are accelerated towards the sample surface by the d.c. self bias present in the "dark" region above the sample which arises because the mass dependant ion distribution produces a potential gradient above the sample. This results in an anisotropic etch which yields good vertically etched rib walls.

The system used in the project was a Plasmatech RIE 80 machine and typical etch rates of around 0.3 μm/min were obtained. Before etching of the actual waveguide samples three calibration runs were always performed to try and establish the etch rate more accurately. These test samples comprised of similar material and were processed identically to the device sample. Usually these were cleaved pieces of a potential device sample on which the lithography was poor and was thus expendable.

Etch depths were measured using a Talystep profile plotter. When a metal mask was employed, its thickness was measured prior to etching. Since the etch rate of the NiCr under these conditions is 80 times slower than the GaAs etch rate, this was subtracted from the subsequent etch depth measurements. When a resist etch mask was used, this was removed before measuring etch depths.

Figure 4.5.3 shows etch depth results for various samples. As can be seen there is a large scatter in the etch rates. There is no correlation with the Al content in the etched layer. Etch rate can depend on an assortment of reasons including the sample preparation in addition to the expected variation due to the plasma and chamber parameters. Calibration runs were thus imperative before etching of the actual sample. Having done this, the required etch depth could

### Results of Reactive Ion Etching



This graph summarises etching results. As can be seen the etch rate varies considerably from run to run over the long term. This means that calibration runs are required before etching the actual devices.

No correlation between etch rate and Al content can be seen from these results.

**Figure 4.5.3**

usually be obtained to within  $0.05\mu\text{m}$ .

Figure 4.5.4 shows some dry etched features. Figures (a) and (b) show sample MA 670 with a photoresist mask. As is apparent, the mask has not been removed at this stage. This sample was etched twice because of a slow initial etch rate and this can be clearly seen by looking at the side walls of the rib. Figure (b) shows the apex of a Y-junction.

#### 4.6 Summary and Conclusions.

This chapter has described the various aspects of the device fabrication process. The three different wafer growth technologies (LPE, MOCVD and MBE) were initially discussed and the merits and disadvantages of each were very briefly considered. MOCVD and MBE both give superior interface quality compared to LPE. The latter is therefore unsuitable for the growth of Multiple Quantum Well structures. Of the former two, MOCVD is the cheaper but it is difficult to eliminate the presence of carbon impurities and it difficult to get an impurity doping density significantly lower than  $10^{14}\text{ cm}^{-3}$ .

The photoluminescence (PL) set-up has been described in detail and it was seen that this is a very useful analytical technique for the assesment of material quality and the determining of Al content in the AlGaAs alloy. The various features of PL spectra have been discussed in considerable detail as they provide an insight into the numerous carrier-carrier interactions which may occur in the material.

Device fabrication procedures have also been decribed. Most of these are well established and routine processes. These generally gave satisfactory results although a thinner than usual photoresist had to be used to achieve well defined Y-junctions.

The processes of dry etching and wet etching were compared and it was confirmed that although the latter gave good smooth ridge walls, the dry etching process was better in terms of etch depth controllability, etch uniformity and verticality of ridge walls and was therefore preferred.

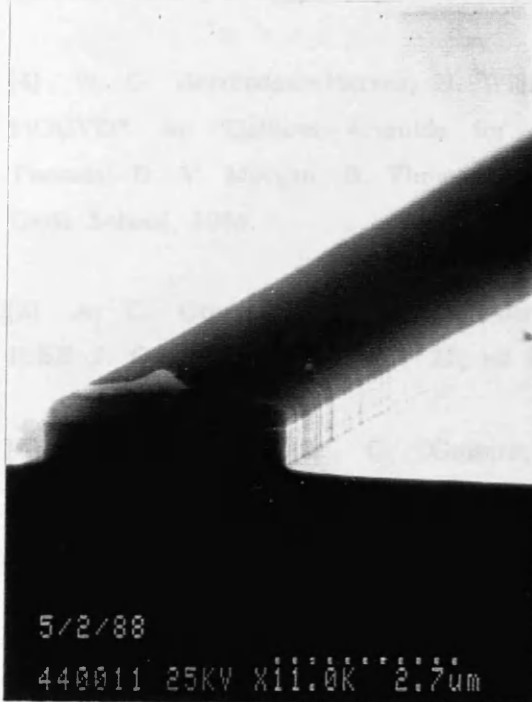
#### 4.7 References to Chapter Four.

- [1] P. A. Houston, "Liquid Phase and Vapour Phase Epitaxy of GaAs and Related Compounds", in "Gallium Arsenide for devices and integrated circuits", Ed. H. Thomas, D. V. Morgan, B. Thomas, J. E. Aubrey, G. B. Morgan, Proc. UWIST

Gene Schott, 1986.

[6] M. J. Falewin, "Micrographically assisted vapour deposition of Si-V heterostructures", *J. Appl. Phys.*, vol. 59, no. 4, pp. 2217-22, 1986.

[7] D. C. Swales, J. May, K. M. Lee, S. S. Khorram, D. Owens, "Excimer photochemical patterning in dry etching of GaAs/GaIn and GaP/GaAs heterostructures", *J. Appl. Phys.*, vol. 61, no. 11, pp. 5972-5974, 1987.



(a)



(b)

SEM photographs showing dry etched waveguides. Figure (a) shows an etched rib with a cleaved end face and (b) shows a Y-junction in detail. The photoresist mask is still present on top of both devices.

Figure 4.5.4

[8] G. B. Sigurdson, "Micrographically assisted vapour deposition of Si-V heterostructures", *J. Appl. Phys.*, vol. 51, no. 4, 1980.

GaAs School, 1986.

[2] M. J. Ludowise, "Metalorganic chemical vapour deposition of III-V semiconductors", J. Appl. Phys., vol 58, no 8, ppR31-55, 1985.

[3] D. C. Bertolet, J. Hsu, K. M. Lau, E. S. Koteles, D. Owens, "Exciton photoluminescence linewidths in very narrow AlGaAs/GaAs and GaAs/InGaAs quantum wells", J. Appl. Phys., vol 64, no 11, pp6562-6564, 1988.

[4] W. G. Herrenden-Harker, H. Williams, "Epitaxial Growth of GaAs:MBE and MOCVD", in "Gallium Arsenide for devices and integrated circuits", Ed. H. Thomas, D. V. Morgan, B. Thomas, J. E. Aubrey, G. B. Morgan, Proc. UWIST GaAs School, 1986.

[5] A. C. Gossard, "Growth of Microstructures by Molecular Beam Epitaxy", IEEE J. Quant. Elec., vol QE-22, no 9, pp1649-1655, 1986.

[6] J. L. Merz, A. C. Gossard, W. Wiegmann, "Alternate-monolayer single-crystal GaAs-AlAs optical waveguides", Appl. Phys. Lett., vol 30, no 12, pp629-631, 1977.

[7] D. J. Ashen, P. J. Dean, D. T. Hurtle, J. B. Mullin, A. M. White, P. D. Greene, "The Incorporation and Characterisation of Acceptors in Epitaxial GaAs", J. Phys. Chem. Solids, vol 36, no 10-B, 1975.

[8] A. Mircea-Roussel, A. Briere, J. Hallais, A. T. Vink, H. Veenuliet, "Photoluminescence investigation of residual shallow acceptors in  $Al_xGa_{1-x}As$  grown by metalorganic vapour phase epitaxy", J. Appl. Phys., vol. 53, no. 6, 4351-4356, 1982.

[9] J. I. Pankove, "Optical Processes in Semiconductors", Prentice-Hall Electrical Engineering Series, 1971.

[10] K. Mohammed, J. L. Merz, D. Kasemset, "Effect of Growth Temperature on the photoluminescence spectra of undoped AlGaAs grown by Metalorganic-chemical vapour deposition", Mat. Lett., vol 2, no 1, pp35-38, 1983.

[11] G. B. Stringfellow, R. Linnebach, "Photoluminescence of shallow acceptors in epitaxial  $Al_xGa_{1-x}As$ ", J. Appl. Phys., vol 51, no 4, 1980.

- [12] R. G. Walker, PhD Thesis, University of Glasgow, 1981.
- [13] E. F. Schubert, E. O. Gobel, Y. Horikoshi, K. Ploog, H. J. Quieser, "Alloy broadening in photoluminescence spectra of  $\text{Al}_x\text{Ga}_{1-x}\text{As}$ ", Phys. Rev. B, vol. 30, no. 2, 813–820, 1984.
- [14] D. A. B. Miller, D. S. Chemla, T. C. Damen, A. C. Gossard, W. Weigmann, T. H. Wood, C. A. Burrus, "Band-edge Electroabsorption in Quantum Well Structures: The Quantum-Confined Stark Effect", Phys. Rev. Lett., vol 53, no 22, pp2173–2176, 1984.
- [15] M. D. A. Macbean, Ph.D. Thesis, University of Glasgow, 1986.
- [16] V. Law, Dept. of Electronic and Electrical Engineering, University of Glasgow, private communication.
- [17] Y. Tarui, Y. Komiya, Y. Harada, "Preferential Etching and Etched Profiles of GaAs", J. Electrochem. Soc : Solid State Science, vol 118, no 1, pp118–122, 1971.
- [18] J. J. Isaac, Ph.D. Thesis, University of Glasgow, 1987.
- [19] S. Somekh, "Introduction to ion and plasma etching", J. Vac. Sci. Technol., vol 13, no 5, pp1003–1007, 1976.

## CHAPTER FIVE

### WAVEGUIDE MEASUREMENTS.

#### 5.1 Introduction.

This chapter describes the experiments performed to characterise the properties of nonlinear waveguide structures. There are three main sections. The first describes the ultrashort pulse laser system employed in the implementation of these investigations. The second describes the measurements of linear properties of waveguides i.e. modal characteristics and propagation losses. Finally, the investigations and results of nonlinear behaviour in the waveguides are reported.

#### 5.2 The Ultra-short pulse laser system.

This section describes the picosecond pulsed laser system which was used in this project. The system comprised of a tunable, mode-locked dye laser synchronously pumped by the frequency-doubled output of a mode-locked Nd:YAG laser. It is important to know the width of the pulses produced by the laser because one needs to calculate the peak optical fields attained. The picosecond pulses produced by a system such as this cannot be observed directly using photodetectors and so have to be measured using an autocorrelation technique. This section therefore also includes a description of the operation of the autocorrelator.

##### 5.2.1 The Pump Laser System.

The pump laser source was a Quantronix 416 system. The laser head consisted of a Krypton flashlamp pumped and water cooled Nd:YAG rod. The laser operated at  $1.06\mu\text{m}$ . The laser was actively modelocked by an intracavity acousto-optic loss modulator. (The principles of modelocking have been presented in a comprehensive article by G. H. C. New<sup>[1]</sup> and will not be reviewed here.) The loss modulation frequency was 76MHz and corresponds to a cavity round trip time of 13ns and a cavity length of 1.95m. Also included within the cavity was an aperture to select single TEM<sub>00</sub> mode operation and a Brewster loss plate which selected vertically polarised modes. (i.e. those which undergo zero reflection losses at each interface of the plate.) Figure 5.2.1 shows a schematic of the Nd:YAG laser.

## Schematic of Nd:YAG Laser

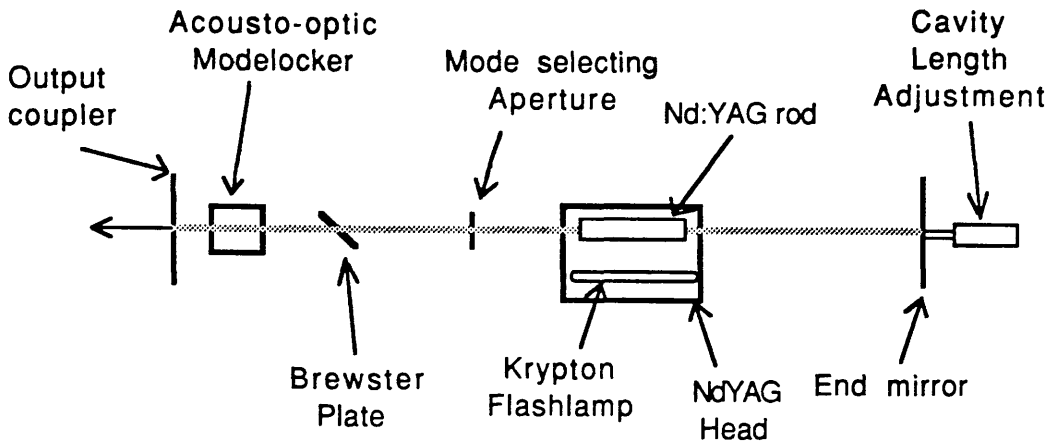


Figure 5.2.1

## Second Harmonic Generation Assembly

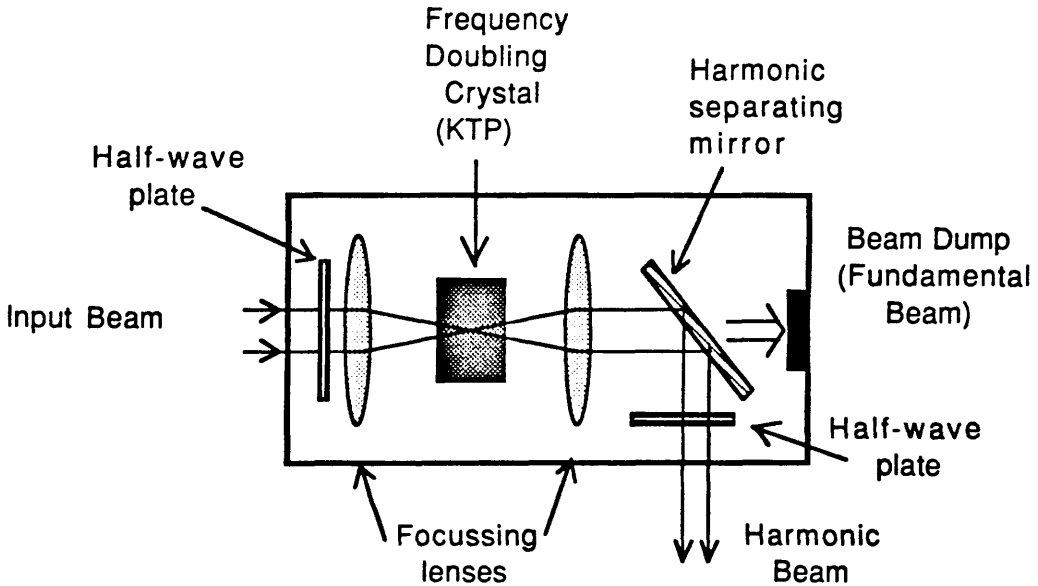


Figure 5.2.2

The modelocked pulses were observed by focussing light from the back mirror of the laser cavity onto an avalanche silicon photodetector and monitoring on a Tektronix 7904 oscilloscope. The response of the photodetector limited the measurable width to about 200ps and therefore pulses shorter than this could not be measured. Manufacturer's specification indicate that the pulse is less than 100ps.

The modelocked Nd:YAG output beam was then frequency doubled by focussing into a second harmonic generating (SHG) crystal. The second harmonic conversion efficiency is proportional to the instantaneous intensity of the fundamental beam<sup>[2]</sup> and therefore is very sensitive to the modelocking condition of the input pulses. For optimum efficiency, narrow pulses with high peak powers and high stability are required. The output beam from the crystal is then collimated by a second lens and is incident on an optically coated beamsplitter which separates the harmonic beam from the fundamental. The SHG assembly is depicted in figure 5.2.2.

Under optimum conditions, a conversion efficiency of 10% can be obtained from the KTP crystal giving 1W of average second harmonic power (at 532nm). An alternative arrangement to the modelocked condition above would be to have the Nd:YAG laser in Q-switched operation. In this case, conversion efficiencies as high as 30-40% can be attained but the beam incident on the crystal has to be unfocussed otherwise the peak electric fields are intense enough to cause permanent damage to the crystal. Although the Nd:YAG laser was not used with a Q-switch in this project, if the laser is sufficiently unstable then it may produce spontaneous Q-switched pulses which in turn damage the frequency doubling crystal. In fact this was a major problem with the frequency doubling system and such spontaneous pulses have damaged the KTP crystal on at least two occasions during the course of this project and each time a long and significant interruption resulted in the course of experimental work. Another potential cause of damage to the crystal is due to the presence of dust on the crystal faces which can cause permanent damage as the Nd:YAG beam burns the dust particles. Extreme care is therefore required in ensuring that the pulses are well modelocked before allowing any light to the KTP crystal and that the crystal is kept clean. It is also imperative that at all times the state of the modelocking was monitored on the fast detector and oscilloscope while the KTP was exposed to the radiation. Figure 5.2.3 shows an extract from the system specifications for the laser modelocked and operating in a single TEM<sub>00</sub> mode.

The frequency doubled light output from the KTP crystal is then used to optically pump the dye laser.

	Fundamental ( $\lambda=1.06\mu\text{m}$ )	Second Harmonic ( $\lambda=532\text{nm}$ )
Average power	10	1
Peak power	1kW	150W
Pulse width	< 100ps	< 70ps

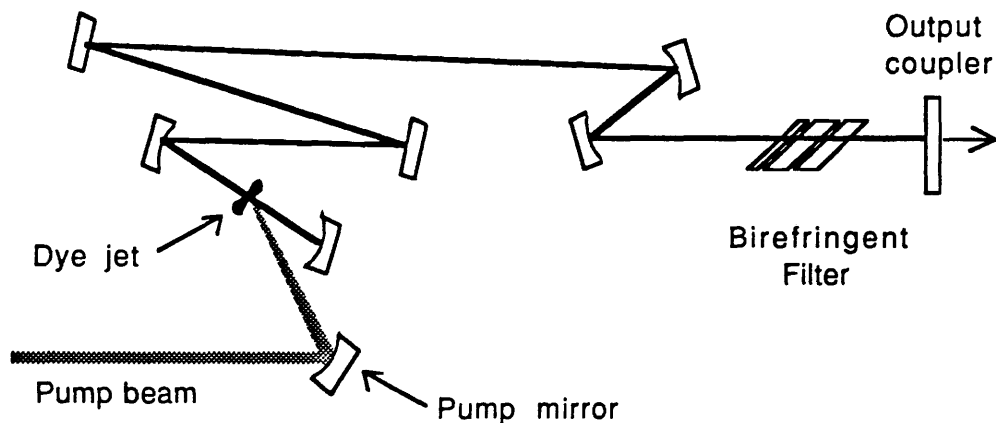
Figure 5.2.3 Extract from Quantronix 416 laser specifications.

### 5.2.2 The dye laser system.

The dye laser used in the system was a Coherent 701 model. The dye is in liquid solution form and is pumped through a nozzle so as to form a thin, flat jet oriented at Brewster's angle with respect to the intracavity beam. The dye consists of complex organic molecules which can be excited into higher vibrational and electronic states. These states are further split into levels associated rotational modes and because of line broadening these are unresolvable and form a continuum. Dyes therefore have a large fluorescence bandwidth which enables lasing operation over a large tuning range. The large bandwidth also means that when modelocked, the laser is capable of producing shorter pulses since the temporal laser output is related to the Fourier transform of the spectral output. In fact the minimum pulse width is limited by the intracavity tuning element which in this system was a birefringent filter. This consists of birefringent plates of crystalline quartz tilted at Brewster angle. Frequency selection occurs because of the plates' birefringence and the consequently varying amounts of retardation for the different wavelengths. Only those TM polarised waves which undergo an integral number of full wave retardations in the plates experience completely lossless transmission and are thus selected. The dye used for this work was Styryl 9 which can lase from 790nm to 900nm. In practise the tuning range also depends on the pump wavelength and the cavity losses particular to the system. In this system the tuning range was from 790nm to 860nm. The output characteristics of the dye laser are examined in more detail in section 5.2.4.

The dye laser resonator is itself a folded cavity consisting of 7 mirrors and is shown schematically in figure 5.2.4. As well as the styryl 9 jet assembly, there is also provision for the use of a second dye jet if a saturable absorber dye (such as IR 140) is needed for further pulse shortening. This facility, however, was not required for the project. The mirrors on either side of each jet assembly are

**Schematic of dye laser optics.**



**The dye laser comprises of 7 mirrors forming a folded resonator. Frequency tuning is done by means of a birefringent filter.**

**Figure 5.2.4**

focussing mirrors and the separation between these is very critical to the alignment. The cavity length of the dye laser has to be equal to that of the pump laser for the shortest pulses. The output coupler is mounted on a translational mount to allow the necessary adjustments to the cavity length. The system can produce average powers of 80–100mW at 830nm (the centre wavelength of the tuning range) when fresh dye is used and when the pump power is above 900mW. In typical operation however, the laser power is normally in the region of 40–80mW.

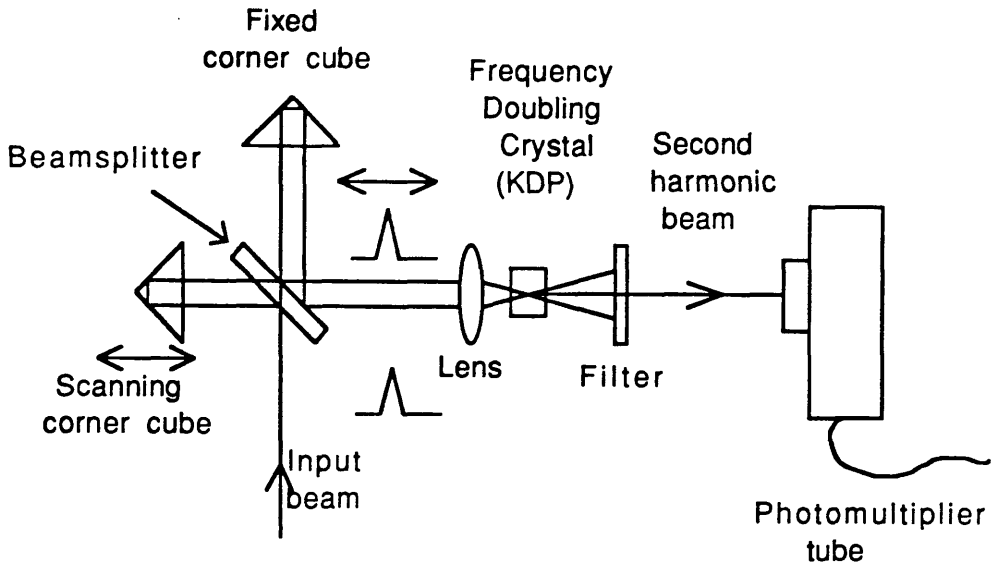
### 5.2.3 The autocorrelator.

An autocorrelator enables assessment of pulse widths by means of a spatial overlap technique. The laser output is split into two beams which are recombined in a nonlinear crystal to produce a second harmonic generated (SHG) signal proportional to the overlap of the two pulses. By varying the relative distance between the two pulses and measuring the variation of the second harmonic signal, one can obtain an indication of the pulse width. An autocorrelator thus effectively performs a time to space mapping and transforms the problem of measuring times of picoseconds into that of measuring submillimetre distances.

The autocorrelator used in this project is shown schematically in figure 5.2.5. It basically consists of a Michelson interferometer where the incident beam is split and recombined using a single beamsplitter. Each of the two paths are approximately equal in length but one of the arms comprises of a retroreflecting corner cube mounted on a vibrator and is continually scanned back and forth driven by a sine waveform. The other reflector is mounted on a translational stage. The two beams are then focussed into the crystal, (potassium dihydrogen phosphate (KDP) in this case), and the SHG signal is detected using a photomultiplier tube (PMT). An optical filter is placed in front of the PMT to prevent any of the fundamental signal reaching the detector. The beams are aligned to give what is described as a *background-free* autocorrelation. In this configuration, a harmonic signal is only generated if the pulses overlap in the crystal. This is achieved by ensuring that the two beams cross within the crystal at a sufficiently large angle so there is little or no SHG contribution from any single beam. The crystal is oriented for phase matching at an angle intermediate to the crossing beams. A net electromagnetic excitation in the phase matched direction therefore only occurs if the pulses from the two beams overlap.

It is important to ensure that the optical path lengths in the two arms of the autocorrelator do not differ too much so that there is a point within the scan range where the pulses overlap completely. The autocorrelation signal detected by

## Schematic of autocorrelator



The laser output is split into two beams which are recombined in a nonlinear crystal to produce a second harmonic signal proportional to the overlap of the two pulses. By varying the relative distance between the two pulses and measuring the varying second harmonic signal, one can obtain an indication of the pulse width.

Figure 5.2.5

the PMT is proportional to the spatial overlap integral of the pulses and reaches a maxima each time the pulses are exactly superimposed during the scan. A series of peaks are therefore seen when observing the real time signal on an oscilloscope. During one cycle of the scan there are two peaks present: one for each direction of the scan. Figure 5.2.6 illustrates autocorrelation traces for various relative positions of the pulses. Case (a) shows the situation where the scan is symmetric about the zero relative delay position. The autocorrelation peaks are equally spaced in this case. When the position of the non-scanning reflector is adjusted the scan becomes asymmetric and the peaks are seen to "pair off" as shown in case (b). Case (c) shows the situation where pulse overlap occurs only at the end of the scan and in this case the two autocorrelated peaks are not resolvable. Case (a) represents the situation which is the simplest to calibrate. The calibration procedure for this case is now considered.

The relative position of the "scanning" beam with respect to the "stationary" beam,  $s$ , is time varying and can be written

$$s = d \sin \omega t .$$

where  $d$  is the scan half-length and  $\omega$  is the angular scanning frequency. (Note that  $s$  represents the relative spatial position of the pulses and not the position of the scanning reflector.) The relative velocity,  $v$ , can thus be expressed

$$v = \omega d \cos \omega t .$$

If the trace is symmetric about the zero delay position (as shown in figure 5.2.6(a)) and the scan distance is several times that of the spatial width of the pulse (noting that 0.3mm is the "length" of a 1 picosecond pulse in free space), then it is accurate to say that the pulses overlap when  $v$  is at a maxima or minima and that the relative speeds of the pulses remains constant at  $v = \omega d$ . Figure 5.2.7 shows an autocorrelation scan. Here  $\Delta t$  represents the full-width at half maximum (FWHM) of the pulse and  $T$  is the period of the scan. The horizontal axis is time and so  $\Delta t$  is actually the duration of the overlap of two identical pulses. Since the relative pulse velocity during the overlap is known it is possible to calculate the spatial extent of the pulse. This is given by

$$v \Delta t = \omega d \Delta t = 2 \pi d \left[ \frac{\Delta t}{T} \right] \quad (5.2.3.1)$$

The scan length can be determined by translating the position of the non-scanning

**Diagrammatic representation of autocorrelation traces with different relative delay between pulses**

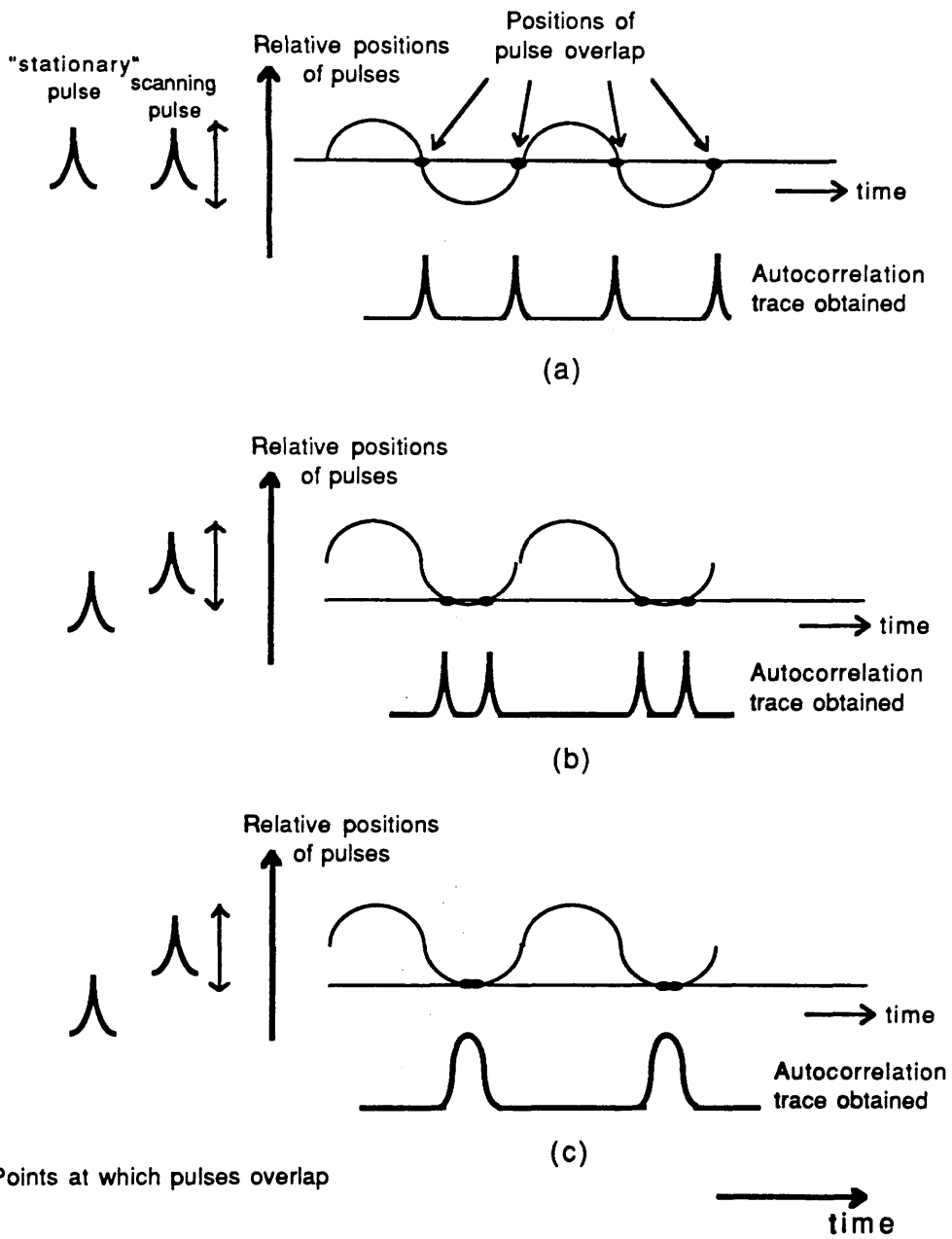


**Figure (a) corresponds to a symmetric scan, (c) is the case where the pulses only overlap at the end of the scan and (b) is an intermediate case.**

**Figure 5.2.6**

**Autocorrelation of well modelocked pulse  
from Styryl 9 dye laser**

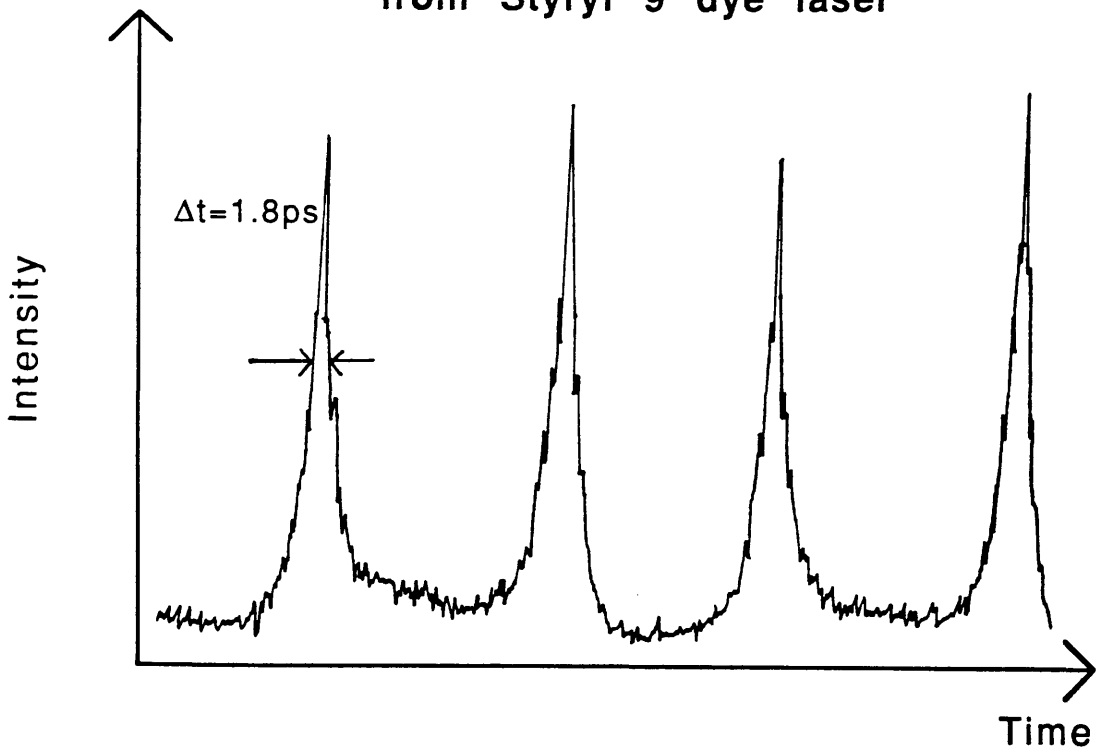


**Figure 5.2.7**

reflector from one extreme of the scan to the other. Both of these positions correspond to opposite extremes of the scan and are both represented by figure 5.2.6(c). The distance moved by the reflector is equal to  $d$ , the scan half-length, because the reflected beam undergoes **two times** the movement of the reflector. The pulse width in seconds can be obtained by dividing  $v\Delta t$  by  $c$ , the speed of light. One does not need to include the refractive index of the crystal when doing this because the measurement of  $d$ , from which the relative pulse width is calculated, is made external to the crystal.

It can be seen that it is therefore only necessary to obtain the ratio  $\Delta t/T$  and the scan distance to calibrate an autocorrelation. Also, if it is assumed that the laser pulses are Gaussian in shape (i.e. represented by a term proportional to  $\exp(-t^2)$ ), then the autocorrelation width should be divided by a factor  $\sqrt{2}$  to give the correct pulse width<sup>[3]</sup>. The FWHM of the laser pulse is thus given by

$$\text{FWHM} = \sqrt{2} \frac{\pi d}{c} \left[ \frac{\Delta t}{T} \right] \quad (5.2.3.2)$$

During the autocorrelator alignment, an initially detected SHG signal could usually be improved immediately by adjustment of the dye laser cavity length. This optimised the pulse shape and hence maximised the signal. Also, when a peak is seen during the alignment, it should be confirmed that the signal is dependant on the light coming from both arms of the autocorrelator by blocking each in turn. If it depends only on the light from the scanning arm then the "peak" is an artifact due to beam misalignment as the reflector is scanned and not a genuine autocorrelated signal. It was found that once the autocorrelated peak was obtained, the optimisation of the modelocking by adjustment of the dye laser cavity length and alignment was a relatively easy procedure. It should however be noted that the autocorrelation does not yield any information about the actual pulse shape. In particular, the shape of the autocorrelation is always symmetric regardless of the shape of the modelocked pulse.

#### 5.2.4 Characterisation of the dye laser.

In this section some observations regarding the output of the dye laser are presented. These give an indication of the behaviour of the laser and help determine the state of modelocking which is all important when doing experiments using short pulses.

The spectral content of the laser was examined by aligning the laser into a Spex monochromator and observing the output directly using an infra-red vidicon

Hamamatsu camera. It was possible to examine the intensity profile along any vertical section of the picture. The real time spectral output of the laser could thus be observed. The monochromator is already calibrated and so by adjusting the grating and observing the resulting movement on the monitor it was possible to calibrate the spectrum. The profile could be directly stored onto computer. This experimental layout is shown in figure 5.2.8.

The spectrum illustrating a well modelocked output is shown in figure 5.2.9. This corresponds to the autocorrelation shown in figure 5.2.7. The FWHM  $\Delta\lambda$  is measured to be  $40\text{\AA}$  (equivalent to  $\Delta\nu$  of  $1.7\times 10^{12}\text{Hz}$ ). The transform limited pulse width is given by<sup>[1]</sup>

$$\Delta t \Delta \nu = 0.44 \quad (5.2.4.1)$$

and indicates a transform limited pulse width of 0.26ps from the above measurement. The actual pulse width from the autocorrelation is measured to be about three times larger at 0.9ps.

It was noticed that the spectrum is characterised by periodic ripples of a separation of about  $4\text{\AA}$  (equivalent to  $1.7\times 10^{11}\text{Hz}$ ). It was suspected that these were due to etaloning effects in the dye jet. The precise dye jet thickness for this system was not given as part of the manufacturer's data but is estimated to be in the region of  $200\mu\text{m}$  from typical values presented in the literature<sup>[4,5]</sup>. From the period of the ripple, which was about  $1.7\times 10^{11}\text{Hz}$ , and assuming a dye refractive index of about 1.5, and also taking into account the tilt at Brewster's angle, the jet thickness is calculated to be  $300\mu\text{m}$  and is in reasonable agreement with the above expectations.

It was stated above that modelocking is particularly sensitive to the cavity length. To illustrate this, figures 5.2.10 show the autocorrelation and the resulting spectrum if the dye laser cavity is slightly detuned. The spectrum has narrowed considerably to about  $5\text{\AA}$  and the pulse width has correspondingly broadened. It was also seen that when poorly modelocked the laser would hop between different longitudinal modes (defined by etaloning effects due to the dye jet) separated by integer multiples of the ripple period. The spectrum corresponding to this situation is shown in figure 5.2.11 where the laser output consists of two distinct lines separated by  $30\text{\AA}$ . The longitudinal mode spacing due to the laser cavity is about  $2\times 10^{-3}\text{\AA}$  and cannot be resolved here.

In summary, these observations indicate that if short pulses are required then it is essential to check the pulse width using the autocorrelator each time the dye laser is adjusted. Once an autocorrelation trace is obtained, it provides a good real time monitor of the modelocking quality and enables quick optimisation of the laser

## Experimental arrangement for observation of dye laser spectrum

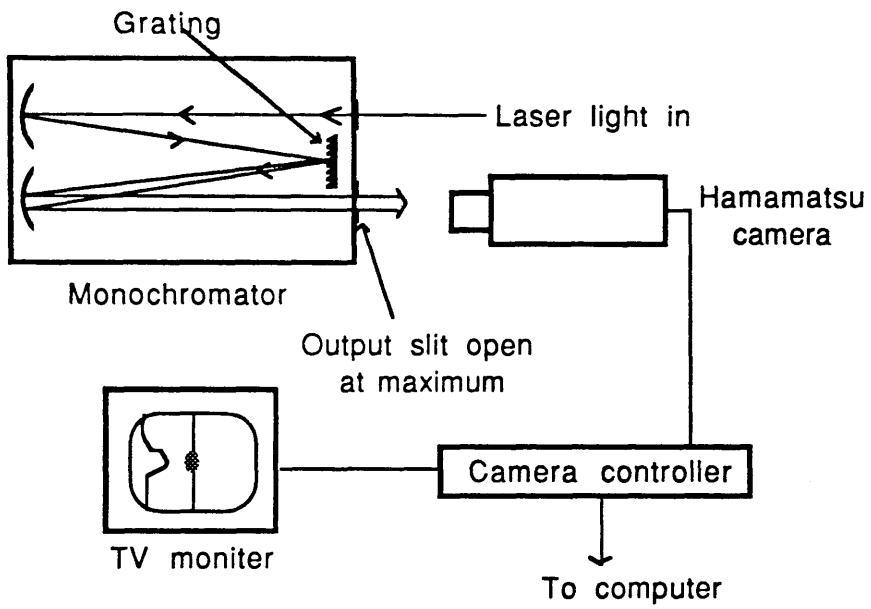


Figure 5.2.8

Spectrum of Dye Laser corresponding to a well modelocked condition.

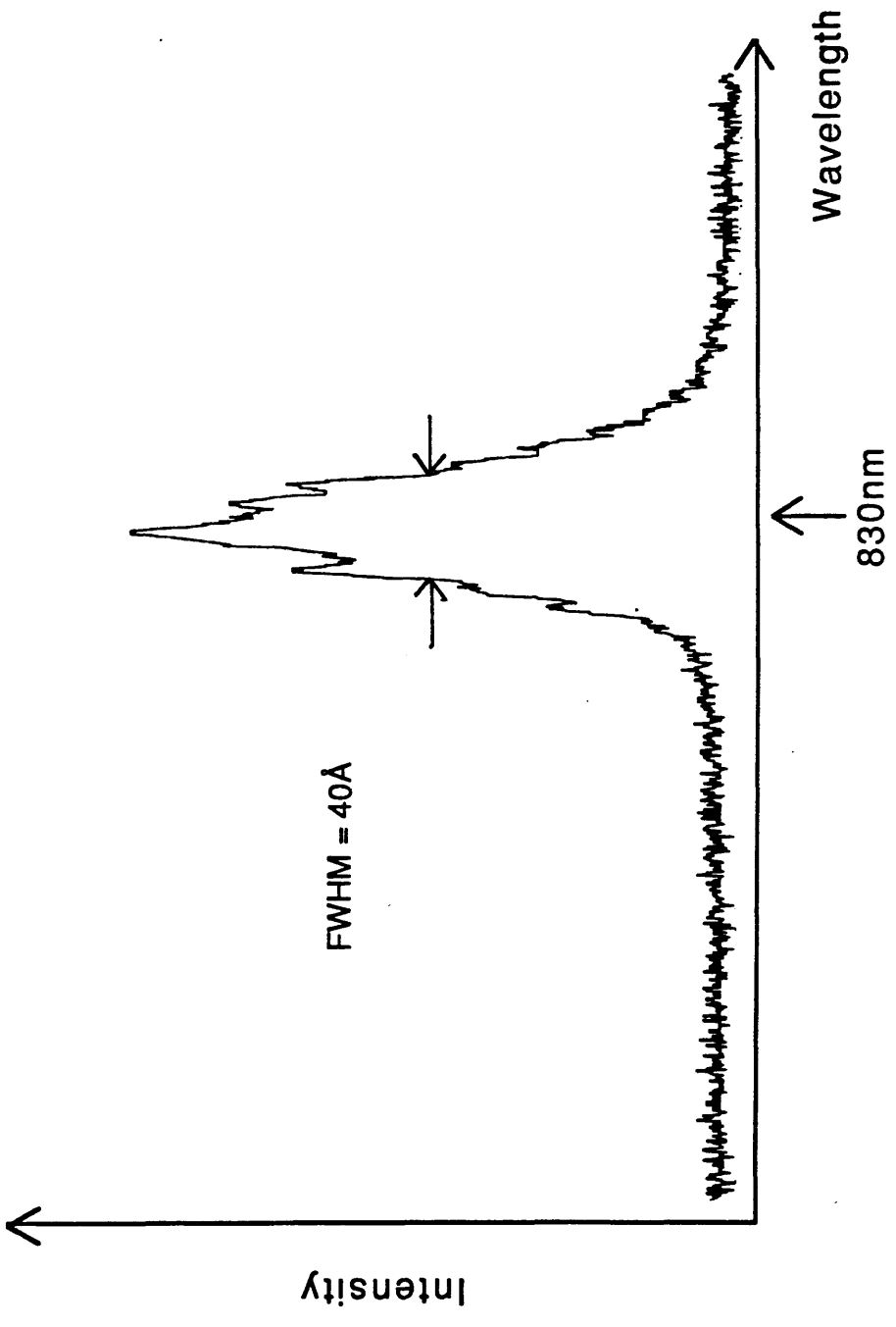
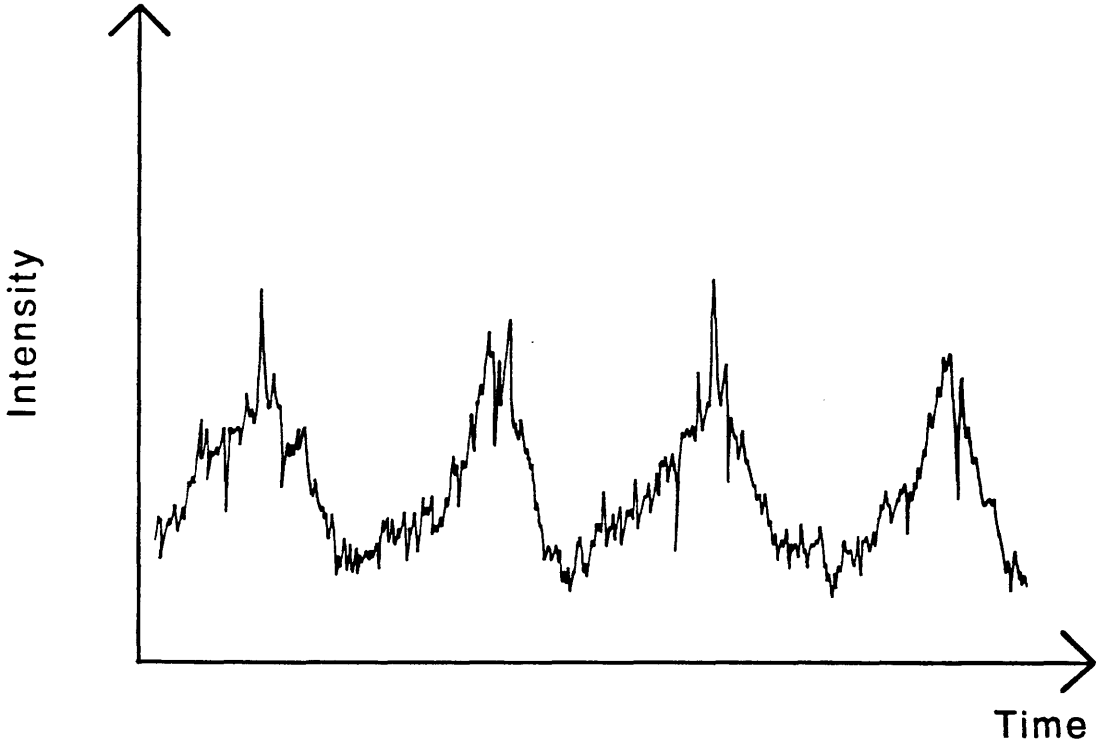


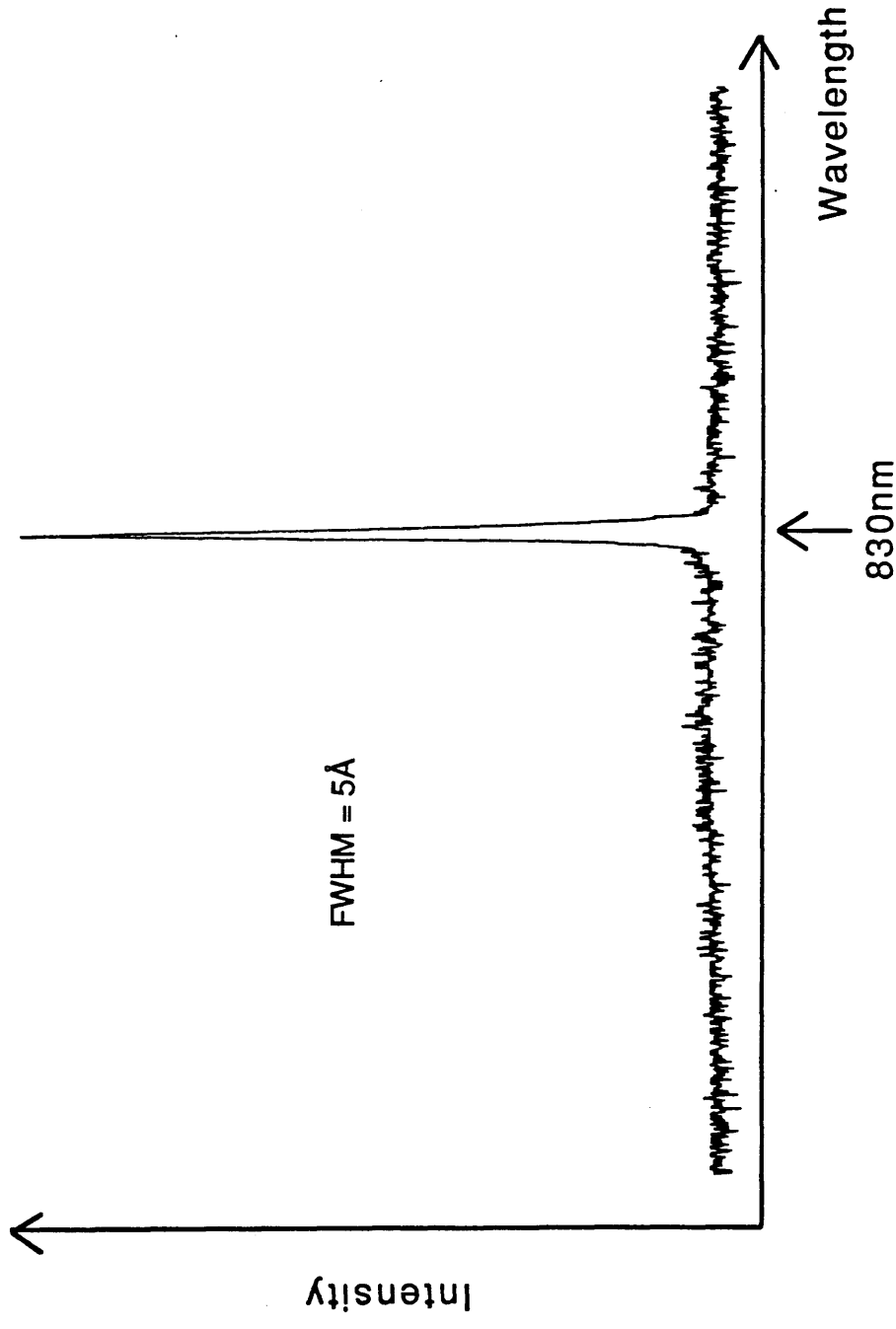
Figure 5.2.9

**Autocorrelation of poorly modelocked pulse**



**Figure 5.2.10(a)**

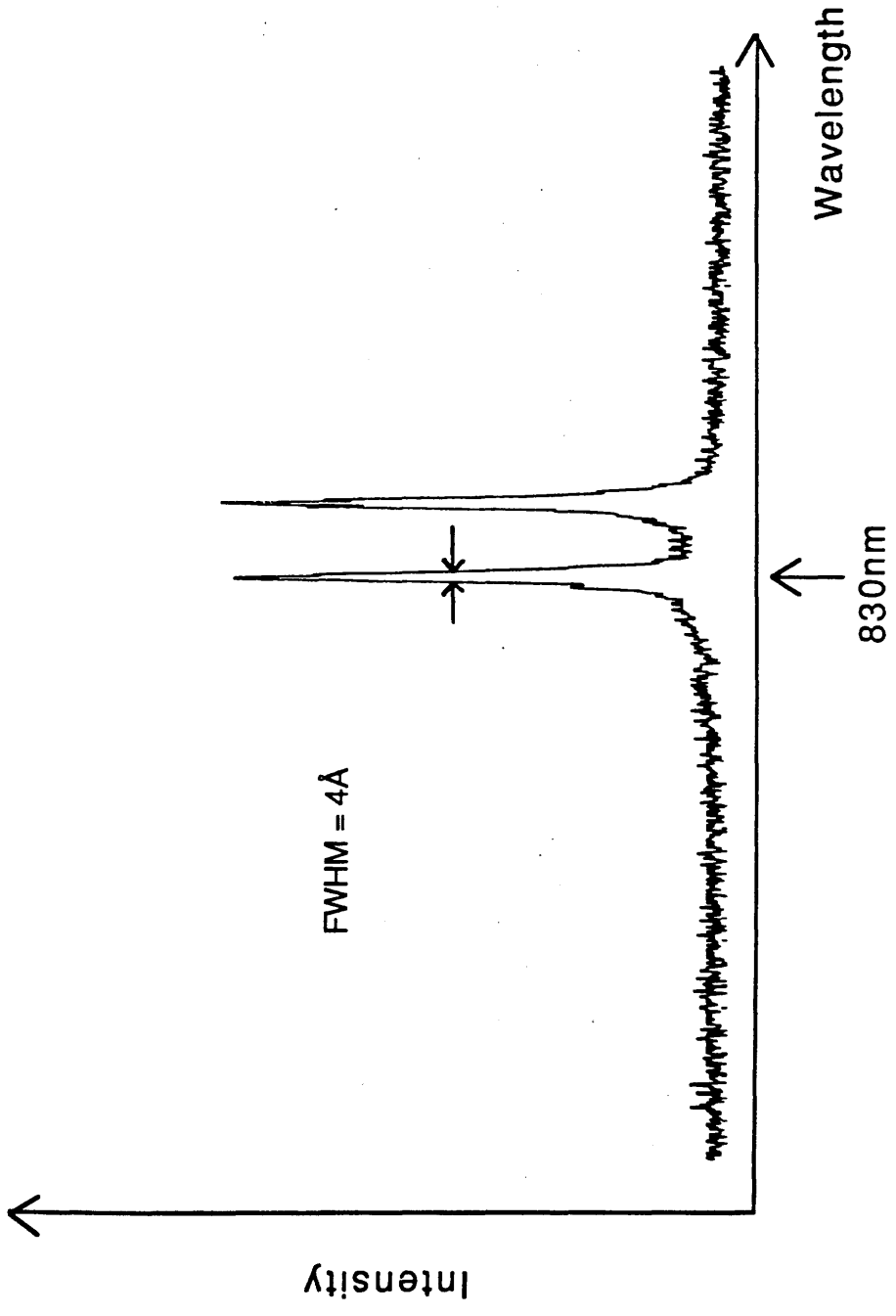
Spectrum of Dye Laser corresponding to a poorly modelocked condition.



The spectrum narrows considerably when the cavity is detuned from its optimum length.

Figure 5.2.10(b)

# Spectrum of Dye Laser showing two longitudinal modes .



When poorly modelocked, the laser is liable to hop between two longitudinal modes as defined by the etaloning action of the dye jet. The peaks are separated by 30Å.

Figure 5.2.11

cavity length and alignment. In fact it was found that the sole monitoring of the output power to optimise the laser does not reliably indicate good pulse quality.

### 5.2.5 Use of mNA for Second Harmonic Generation.

As mentioned in section 5.2.1, there were two occasions when the KTP crystal in the SHG assembly was damaged. On each of these occasions a replacement was ordered and a delay of several months resulted. A cheaper and more easily obtainable alternative to KTP was therefore considered. This was the crystal meta-nitroaniline (mNA) which is a soft yellow crystal and has been used in the past to frequency double the output of pulsed Nd:YAG lasers where conversion efficiencies as high as 65% were obtained<sup>[6]</sup>. Samples of mNA were kindly provided by Mr. G. Simpson and Prof. J. Sherwood of the Department of Chemistry, University of Strathclyde, Glasgow. The feasibility of using mNA as a frequency doubler in the laser system was investigated and test samples were prepared.

There were disadvantages associated with these crystals. The crystal surface is affected by water vapour content in air which tends to turn the crystal surface an opaque cloudy colour. The crystal therefore has to be protected by immersing in a suitable liquid (oil or glycerine)<sup>[7]</sup>. The crystal also has carcinogenic tendencies and therefore precautionary handling measures have to be taken.

The phase-matching properties are of extreme importance. The mNA crystals have natural cleavage planes but these are not perpendicular to any of the phase-matching directions. The crystal orientations for collinear phase matching have been reported by Davydov et al<sup>[7]</sup>. The collinear phase matched directions form a cone with the minimum and maximum apex half-angles of 40° and 50° with respect to the cleavage plane. From this data, to have a perpendicular crystal face to this direction it was necessary to polish the crystal at an angle of about 45° to the cleavage planes. Fine angular adjustments to optimise the phase-matching could be performed with relative ease using the rotational movements allowed on the crystal mount in the SHG assembly.

Polishing was done by Mr. K. Peichowiak, in this department, using an alumina coated abrasive cloth or various grades of silicon carbide powder. Polishing is normally done using a water based mixture of abrasive compounds but, because of mNA's adversity to water, several other solvents were tried including acetone, genklene, toluene and paraffin oil. Acetone and genklene both tended to dissolve the mNA as could be seen since the liquids turned a yellow colour on contact with the crystal. Hence these liquids were not used in the polishing process. On

examination of the polished faces through a microscope abrasive markings could be seen for both the fine grade silicon carbide ( $3\mu\text{m}$  particle size) and the alumina cloth. Also seen were line shaped markings which ran along the direction of the cleavage planes.

It was decided to try to improve the face quality by chemical polishing using the solvent ethyl acetate thinned in toluene: a mixture suggested by Mr. G. Simpson. This was mixed in the ratio 1:10 (v/v) (ethyl acetate : toluene). The crystal face was wiped several times using a cotton bud soaked in this solution. This made the polished face slightly smoother since both the lines and the abrasive markings were no longer seen but there was now a mottled appearance to the surface. The cleaved surface in comparison was much smoother. A polished surface as smooth as that of the cleaved surface could not be obtained at this angle.

The polished sample was inserted in front of the mode-locked Nd:YAG laser. The laser was producing 10W average power and despite using an unfocussed beam the crystal melted almost immediately. The average laser intensity used by Kato<sup>[6]</sup> was approximately  $120\text{kW}/\text{m}^2$ , whereas in this experiment, it was  $26\text{ MW}/\text{m}^2$ : some 200 times larger! It was therefore concluded that because of the high average powers produced by this Nd:YAG laser, and considering the fairly low melting point of the mNA ( $\approx 112^\circ\text{C}$ ), this crystal was not suitable as a frequency doubler for the Nd:YAG laser.

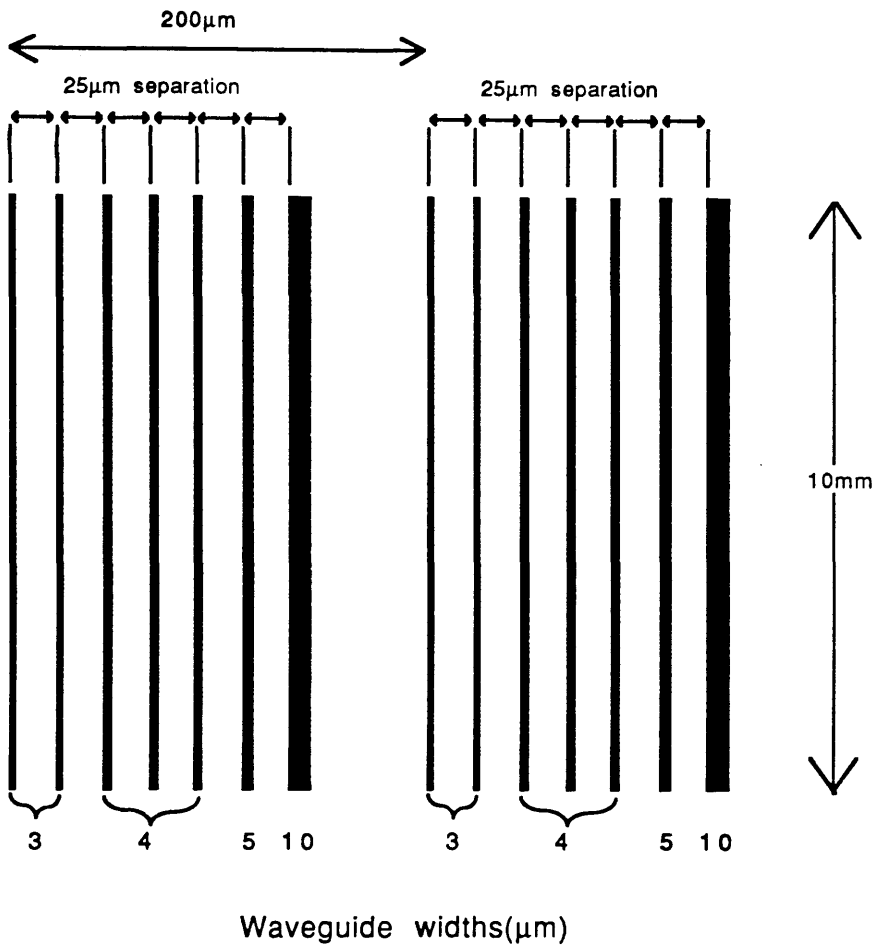
### 5.3 Waveguide Characterisation.

This section describes the testing of the linear properties of single waveguides. This includes a description of the endfire coupling technique, which was used to launch light into the waveguides, and the observations regarding the modal properties of waveguides. Also, the method used to assess the losses in waveguides is described and the results of these measurements are presented. The results described in this chapter all pertain to single waveguides. The photolithographic mask used in the fabrication of these structures is shown in figure 5.3.1 and consists of lines with varying widths to allow characterisation of the waveguide modal properties.

#### **5.3.1 Endfire coupling.**

Endfire coupling is perhaps the easiest method of launching light into a waveguide. Light is launched into the waveguide by focussing onto the input face.

### Schematic of waveguide mask



The mask consists of lines of varying widths to allow characterisation of the waveguide modal properties.

Figure 5.3.1

Other methods like prism coupling and grating coupling<sup>[8]</sup> are more suited for coupling into slab modes. Prism coupling requires that the refractive index of the prism be higher than that of the waveguide material. In particular, it is difficult to obtain prisms with refractive indices higher than that of GaAs. The use of grating couplers to launch light into slab waveguides has been much used<sup>[9]</sup>. Generally both these techniques enable good coupling of an incident beam into slab modes by matching the wave propagation vector of the incident light to that of the slab mode. They do not however offer a similar control over the matching of laterally confined modes. Coupling efficiency is all important when investigating intensity dependant effects in waveguides especially if these effects are small. Endfire coupling provides the most efficient means of coupling into rib waveguide structures.

Any light which is focussed by endfiring onto the waveguide input face will be coupled into the structure's inherent modes (apart from that lost due to Fresnel reflection losses). Generally, these include radiation, substrate and guided modes. The coupling efficiency into a waveguide depends crucially on how well the incident optical field is matched to that of the guided mode<sup>[10]</sup> and is therefore dependent on the overlap between the incident optical field and the particular modal shape. The position, size and shape of the focussed laser beam all significantly affect the coupling efficiency. In endfire coupling, the first two of these parameters can be adjusted quite readily but, unless cylindrical lenses are used, the shape of incident field cannot be changed.

Light was coupled in and out of the waveguide using two similar microscope objectives. A standard endfire rig with a  $\times 40$  microscope lens to focus and position the laser light was used. This lens has a numerical aperture (N.A.) of 0.65. By Abbe's theory of image forming<sup>[11]</sup> the smallest possible focussed spot diameter is related to the N.A. by

$$d = \frac{\lambda}{2 \cdot \text{N.A.}} \quad (5.3.1.1)$$

The effective N.A. of the focussing lens decreases if the lens aperture is not completely filled by the incident beam. If this is not the case then the effective N.A. is reduced by a factor proportional to the ratio of the beam and the lens diameters. The laser beam diameter is nominally 0.5mm (the actual value depending both on laser alignment and wavelength) and the lens diameter is about 5mm. The effective numerical aperture is therefore at least 0.065 and increases if the incident beam is expanded to fill more of the lens. For wavelength of 830nm a spot size of  $6.4 \mu\text{m}$  is calculated. If the lens is completely filled then the

minimum spot size is  $0.64\ \mu\text{m}$ .

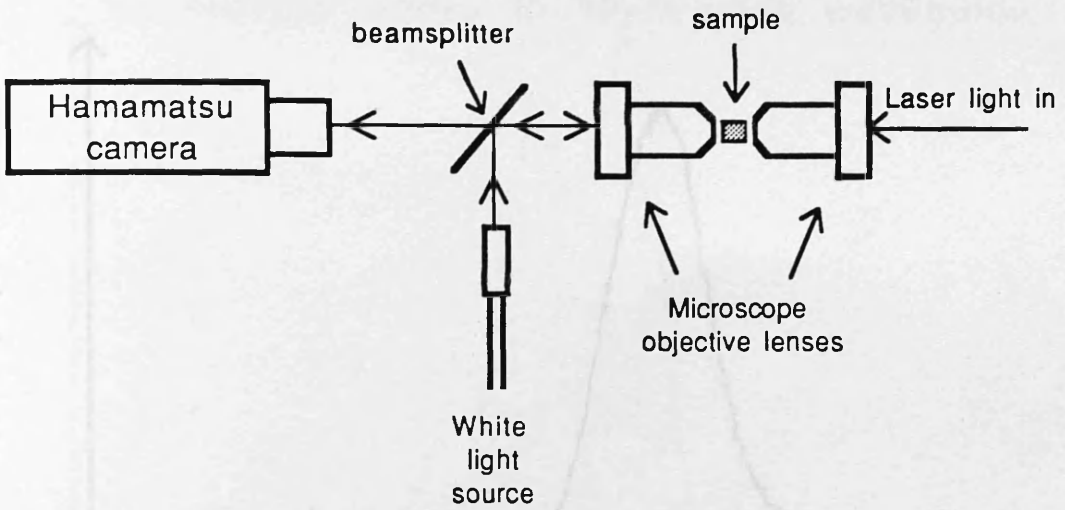
### 5.3.2 Observation of guided modes.

The light produced by the laser was vertically polarised and therefore the waveguide TM modes were excited by endfire coupling. The TE and TM guided modes do not differ significantly if the refractive index difference between guiding and cladding layers is small. The output lens was used to focus the near field pattern (i.e. the field distribution at the output facet) onto a vidicon infra-red Hamamatsu camera. The size of the mode profiles observed on the camera monitor could be calibrated by illuminating and imaging the waveguide output facet with a white light source and beamsplitter arrangement so that the etched rib features could also be seen. Figure 5.3.2 shows this set-up. There is some uncertainty in the rib widths observed because narrowing of the lines from the original widths on the chrome mask may have occurred during the lithographic process. The separation between the rib centres was therefore used for the calibration. Figure 5.3.3 shows such an illuminated rib waveguide. The laser light has to be much attenuated to allow simultaneous observation of the mode and the facet. It was found that because of dispersion in the objective lenses, it was not possible to have both the facet and the output mode in focus at the same time and hence the unclear nature of the rib in the photograph.

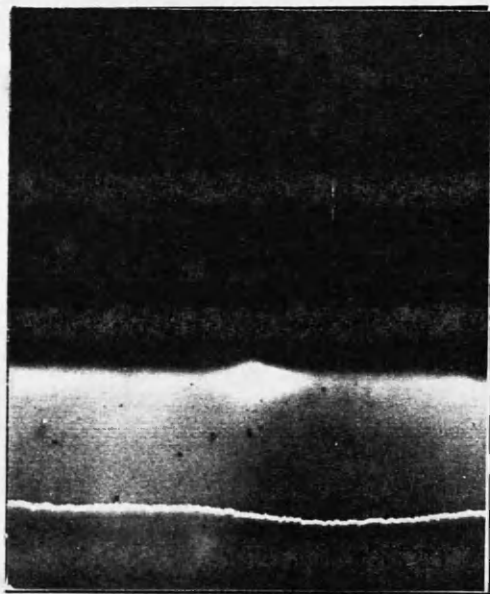
The observed modes in waveguides fabricated in sample Varian 1 are shown to illustrate guiding behaviour. Figure 5.3.4 shows the observed modes in the  $10\ \mu\text{m}$  wide rib structure. Markers indicating the position of the rib are also included. Different modes were excited by adjusting the lateral position of the input coupling lens with respect to the waveguide. Figures (a) and (b) show the first and third modes respectively. Generally speaking, the penetration of the evanescent fields into the cladding regions is larger for higher order modes. This can clearly be seen when comparing (a) and (b). The third order mode is seen to be close to cutoff because the outer intensity peaks are very close to the rib sides. Note the large field present to the left in figure (b). This is because in order to excite this mode the coupling objective was aligned to the position of the left peak. This consequently resulted in significant excitation of radiation modes which account for the field outside the guide. Figure 5.3.4(c) shows multimode guiding in the same waveguide. This is characterised by a presence of more than one peak and nonzero intensity minima.

Figure 5.3.5 shows that the  $5\ \mu\text{m}$  guide supports two TM modes. Again judging by the positions of the intensity maxima in 5.3.5(b), this higher order mode is

**Arrangement for endfire coupling and simultaneous imaging of near field pattern and waveguide facet.**



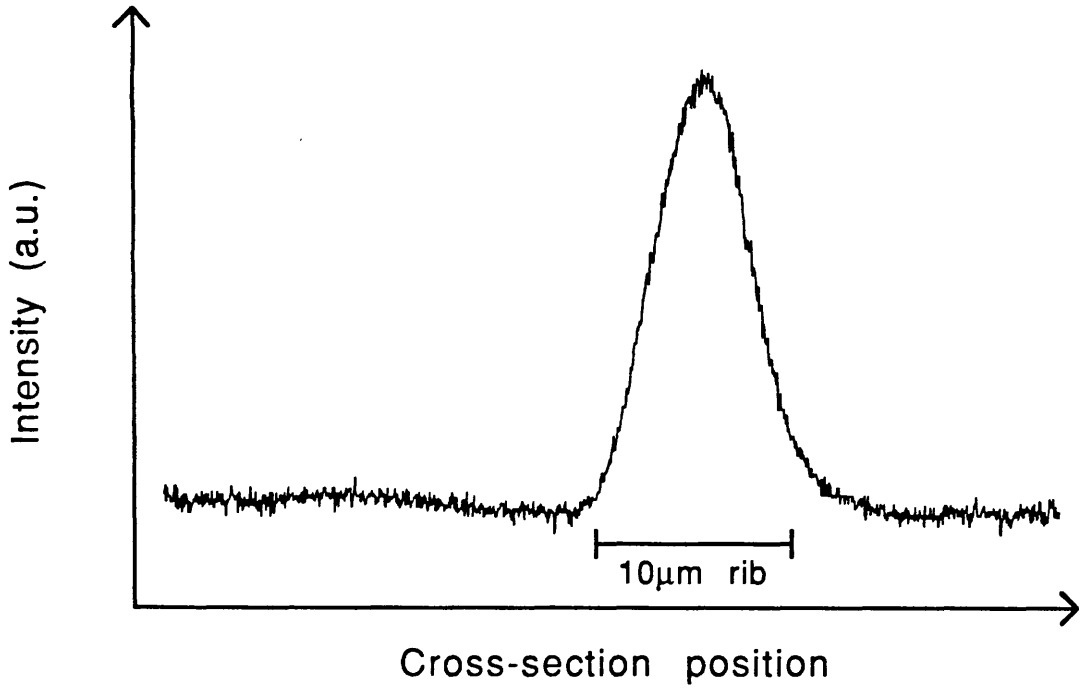
**Figure 5.3.2**



**Photograph showing illuminated end face and a guided mode of a waveguide.**

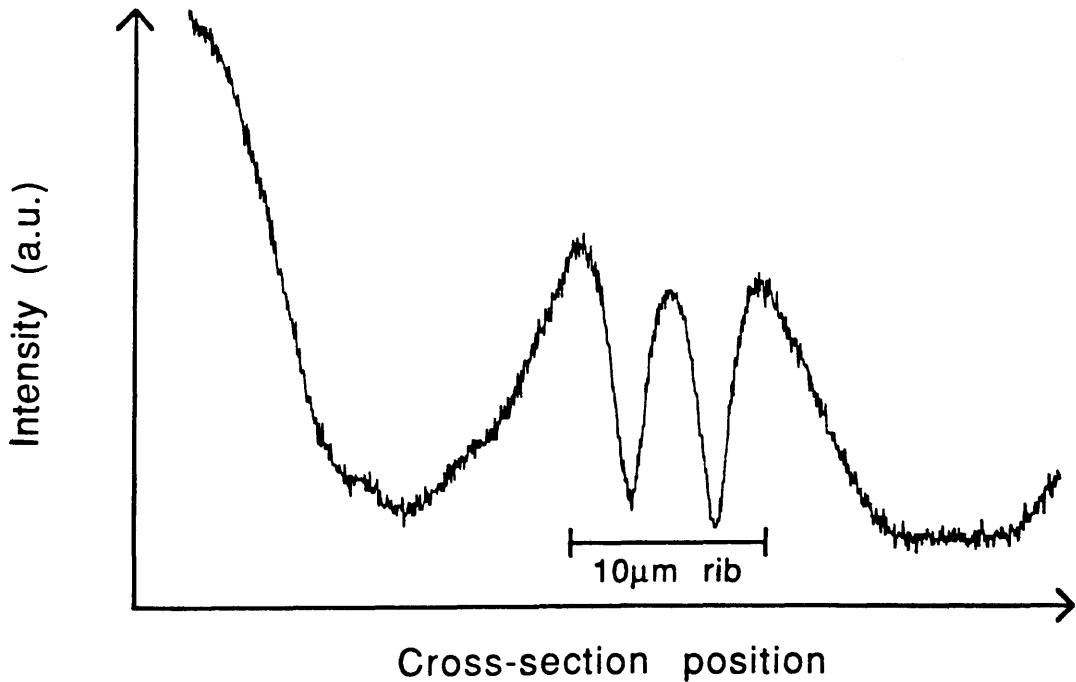
**Figure 5.3.3**

**First order mode in 10 $\mu$ m wide waveguide**



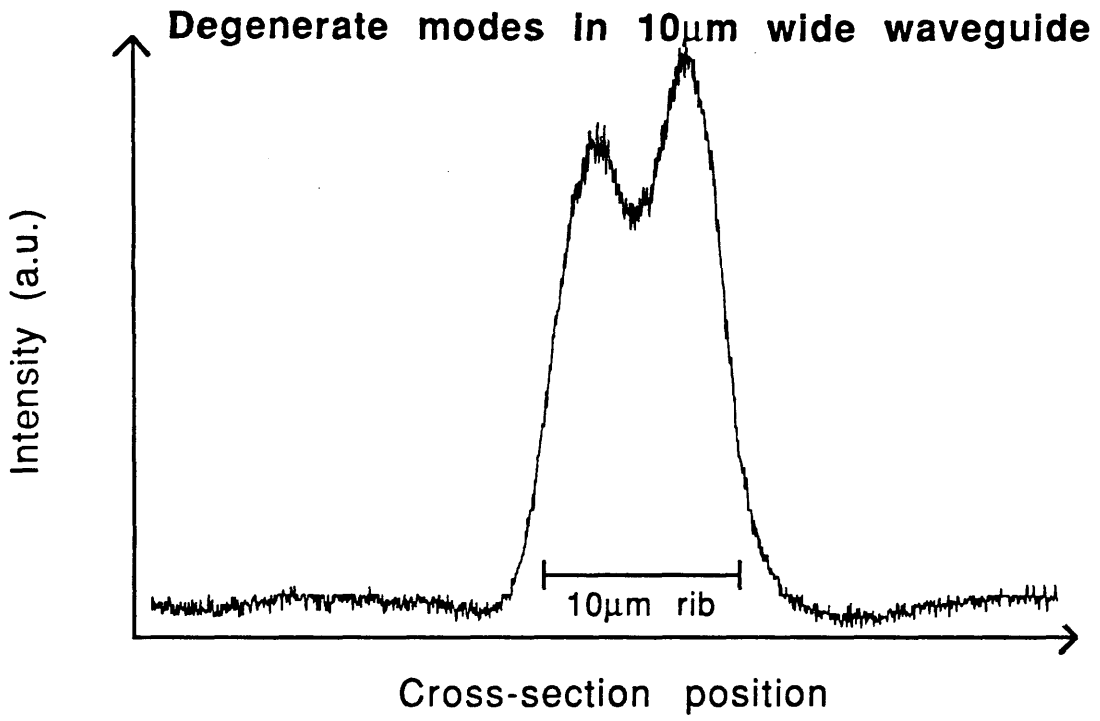
(a)

**Third order mode in 10 $\mu$ m wide waveguide**



(b)

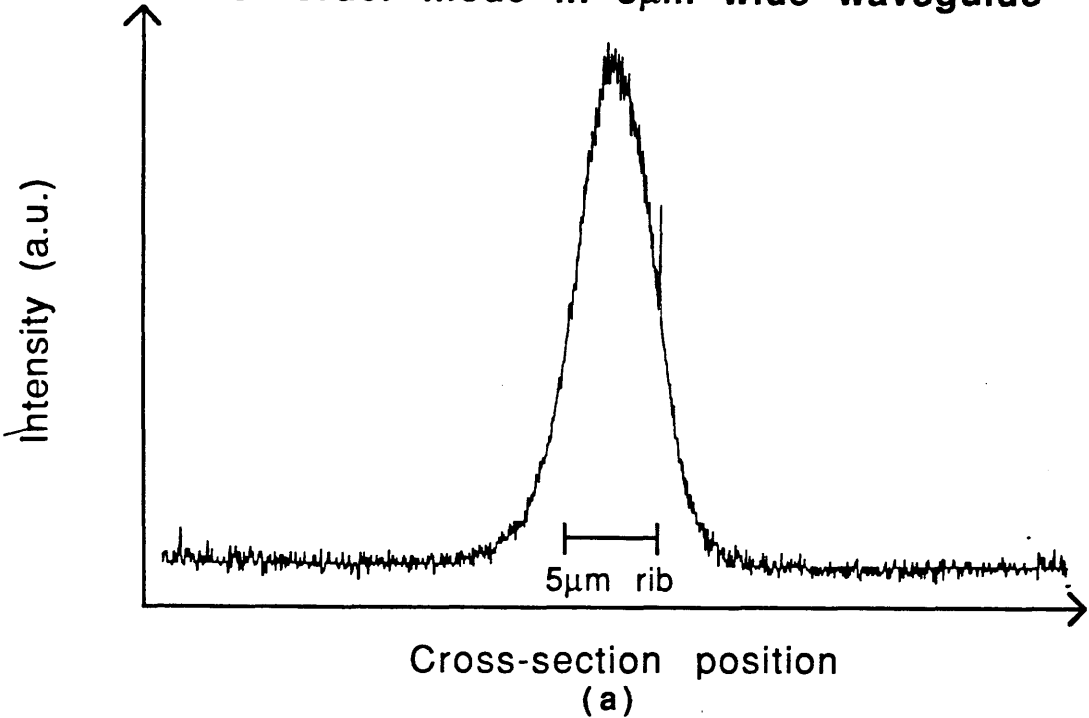
**Figure 5.3.4**



(c)

Figure 5.3.4

First order mode in  $5\mu\text{m}$  wide waveguide



Second order mode in  $5\mu\text{m}$  wide waveguide

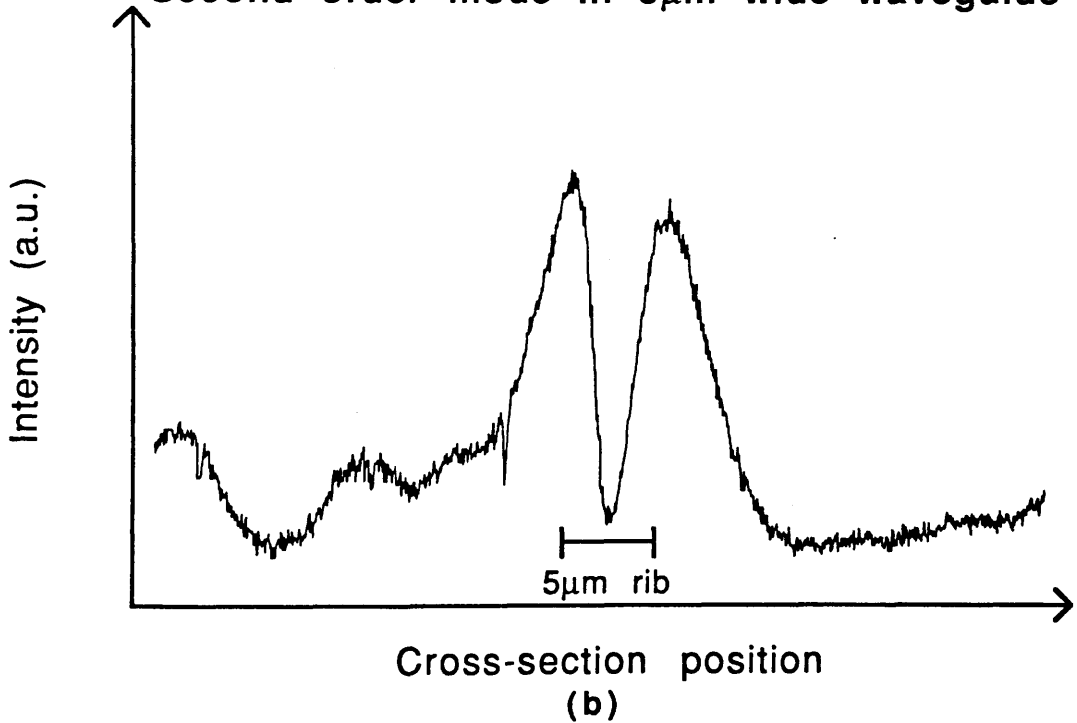


Figure 5.3.5

close to cutoff. Figure 5.3.6 shows the modes in the  $4\mu\text{m}$  and  $3\mu\text{m}$  guides. Both guides are single TM moded.

### 5.3.3 Loss measurements in AlGaAs waveguides.

Evaluation of waveguide propagation loss is necessary and is a very important parameter as far as device performance is concerned. In nonlinear devices this is of additional importance because device operation depends on intensity dependant effects and losses present in waveguides reduce the size of these effects by reducing the effective device length. Consider the total accumulated nonlinear phase change  $\Delta\varphi$  in a waveguide. In a lossless guide this is given by

$$\Delta\varphi = \frac{2\pi n}{\lambda} n_2 I \ell \quad (5.3.3.1)$$

where,  $n$  is the waveguide effective index,  $\lambda$  is the wavelength,  $n_2$  is the nonlinear coefficient,  $I$  is the intensity of the guide light and  $\ell$  is the waveguide length. If waveguide loss is now taken into account, with the intensity  $I$  along the waveguide represented by

$$I = I_0 e^{-\alpha z} \quad (5.3.3.2)$$

where  $z$  is the distance along the waveguide and  $I_0$  is the intensity at  $z=0$ , then the total phase shift is given by

$$\Delta\varphi = \frac{2\pi n}{\lambda} n_2 I_0 \int_0^\ell e^{-\alpha z} dz = \frac{2\pi n}{\lambda} n_2 I_0 \left[ \frac{1-e^{-\alpha\ell}}{\alpha} \right] \quad (5.3.3.3)$$

If  $\alpha\ell$  is large enough ( $>5$ , say) then  $e^{-\alpha\ell} \ll 1$  and the expression becomes

$$\Delta\varphi = \frac{2\pi n}{\lambda} n_2 I_0 \ell_{\text{eff}} \quad (5.3.3.4)$$

where the effective length of interaction  $\ell_{\text{eff}}=1/\alpha$  has been introduced. The presence of loss  $\alpha$  results in a maximum nonlinear effective waveguide length of  $1/\alpha$ .

Propagation loss in a waveguide may be due to two reasons. The first of these is radiation loss. This occurs where power is coupled into radiation modes by waveguide inhomogeneities or by scattering from defects or impurities in the waveguide material or by leaky guiding where optical energy is coupled into

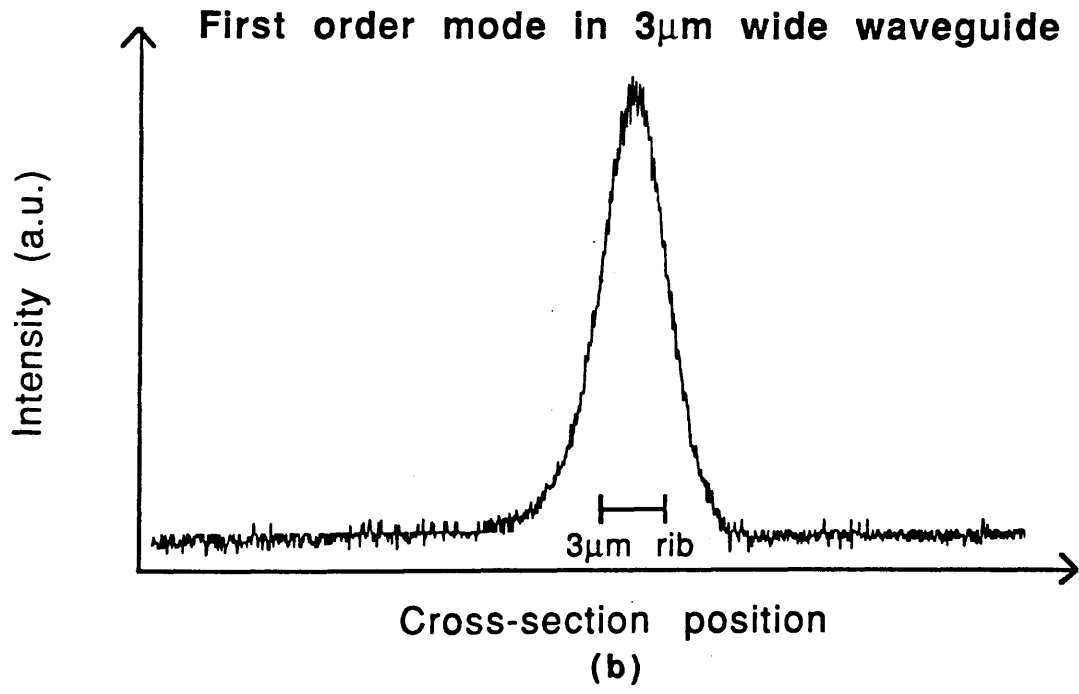
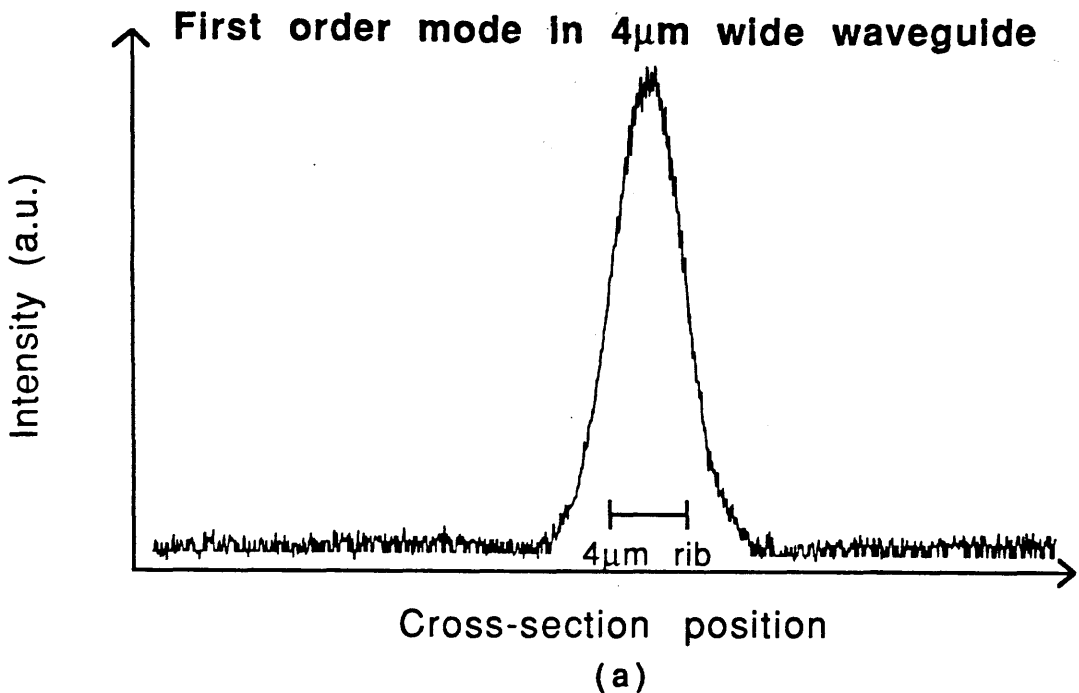


**Figure 5.3.6**

another layer of higher refractive index. The second type of loss occurs where guided energy is absorbed in the material accompanied by the excitation of carriers or impurities into higher energy states. This latter loss usually has a contribution due to free carrier absorption in AlGaAs waveguides but interband absorption is the most significant when operating near the bandgap[12].

One way to determine waveguide loss is by measuring the finesse and visibility of Fabry-Perot fringes arising from multiple reflections in the waveguide cavity[13]. In this case a narrow linewidth laser source is necessary otherwise the fringe visibility is reduced substantially because of the large spectral content of the laser light. The linewidth of the dye laser (when operating in the non-optimally modelocked position) was measured to be 4Å. Li Kam Wa et al[14] have observed that fringe quality using even a 2Å linewidth source (CW Styryl 9 dye laser) gave a deterioration in fringe quality and consequently misrepresented the waveguide losses. The Fabry-Perot method is therefore not suited in this case. Loss was instead measured using a sequential cleaving method. Here transmission is measured as a function of waveguide length and the loss per unit length is thus determined.

Consider the loss mechanisms in endfire coupling. There are reflection losses occurring in both microscope objectives. There are reflection losses at each waveguide facet. There is a coupling loss associated with the modal mismatch between the focussed spot and the waveguide mode. Finally there are propagation losses occurring in the waveguides. The total transmission through the system,  $T$  can therefore be expressed

$$T = \tau^2 t^2 \eta e^{-\alpha l} \quad (5.3.3.5)$$

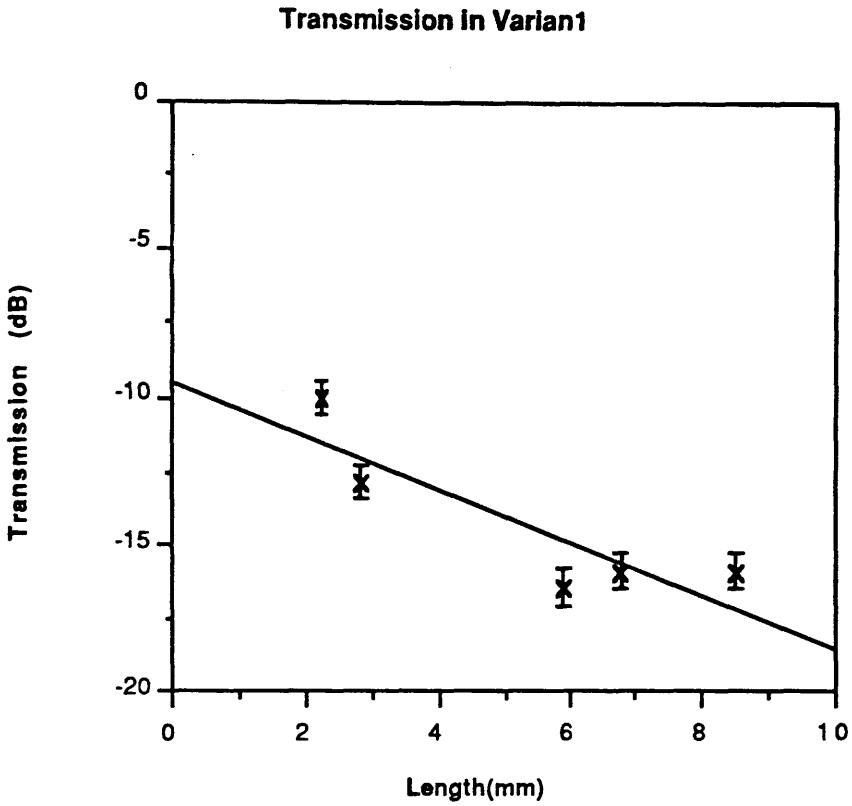
where  $\tau$  is the transmission in each objective,  $t$  is the transmission at each facet,  $\eta$  is the modal coupling efficiency and  $\alpha$  and  $l$  are the waveguide loss and length respectively. The first of these terms,  $\tau^2$ , can be readily determined by direct measurement. The transmission through both objectives was measured as 0.88 which indicates a transmission of  $\sqrt{0.88} = 0.94$  for each objective. The second term can also be determined since the transmission at each of the waveguide/air interfaces is given by  $t = \{4n/(n+1)^2\}$  where  $n$  is the refractive index of the waveguide. For accurate determination of  $t$  the value of  $n$  has to be accurately known. The refractive index is, of course, a function of both the material composition and of the wavelength. Amongst the AlGaAs structures investigated in this project, the refractive index variation is most pronounced in MQW materials where it can vary from 3.5 to 3.6 between photon energies of 1.4eV and 1.5eV where the exciton energy is about 1.45eV[9]. However for the material used in this project, the excitonic contribution to the refractive index does not significantly affect the

reflection coefficient because of the reduced well density. In Chapter Three the refractive index was calculated to vary from 3.441 to 3.425 at energies 3meV to 30meV below the heavy hole exciton energy: a variation of less than 1%. The variation in  $t^2$  (the transmission through both interfaces) is of the order of 0.5% and, as will be seen, this is less than the scatter in the measured data. The wavelength dependent transmission was therefore not taken into account. From equation (5.3.3.5) it can be seen that a logarithmic graph of  $T$  against  $l$  will have a gradient of  $-\alpha$  which is the waveguide propagation loss. The intercept will give an indication of the total endfire coupling losses and from this the modal coupling efficiency,  $\eta$ , can be estimated.

Transmission was measured as a function of waveguide length in sample Varian 1 at a wavelength of 830nm. Guides of different widths were tested but no variation of transmission with width was observed. This is in agreement with the observations of Kapon et al<sup>[15]</sup> who performed measurements on low loss structures. Figure 5.3.7 shows the resulting graph. Experimental error in measurement gave rise to fluctuations of 5% in the transmission. A best straight line fit to these measurements was obtained and this indicates a propagation loss of  $\alpha = 2.1 \text{ cm}^{-1}$  ( $9.0\text{dB cm}^{-1}$ ). The position of the intercept at  $-9.5\text{dB}$  indicates a modal coupling efficiency,  $\eta$ , of 25%. This coupling efficiency will be used in later calculations.

In these waveguides most of the optical field lies within the guiding and cladding layers but some of the optical evanescent field still penetrates into the GaAs layer below the lower cladding. Although only a small fraction of the total field is in the GaAs substrate this can still result in significant losses because of the high absorption which is of the order of  $10^4\text{cm}^{-1}$  in GaAs at this wavelength. Also, the GaAs substrate has a refractive index higher than that of the guiding slab and so there is also coupling of optical energy from the guiding layer into leaky substrate modes. These losses depend on the thickness of the lower cladding layer and calculations indicate<sup>[15]</sup> that there is a loss of  $12\text{dB cm}^{-1}$  for a cladding thickness of  $2\mu\text{m}$ . Most of the measured propagation loss in sample Varian 1 is thus attributed to substrate absorption and leakage. Free carrier absorption also contributes to the total losses but this is only by a small amount of the order of  $0.01\text{cm}^{-1}$ <sup>[16]</sup>.

Some waveguide loss measurements were also performed at RSRE, Malvern. These were done on waveguides fabricated in material MA661 which was obtained prior to MA670 but was grown under identical conditions and to the same specifications as the latter (See appendix III). The guiding and cladding layers consist of 6% Al- and 12% Al-doped AlGaAs respectively. Transmission measurements were carried out at two different wavelengths using a cw Nd:YAG



**Results of sequential cleaving measurements of waveguide loss in Varian1. A propagation loss of 9 dB/cm and a modal coupling efficiency of -9.5dB were measured.**

**Figure 5.3.7**

laser operating at  $1.06\mu\text{m}$  and a diode laser operating at  $862\text{nm}$ . In these measurements a  $\times 20$  objective lens (N.A. of 0.54) was used to endfire couple the light into the waveguide but, unlike before, a  $\times 5$  lens was used prior to the coupling lens to enlarge the beam diameter and to fill the aperture. Spot sizes as small as  $0.98\mu\text{m}$  and  $0.80\mu\text{m}$  were thus attainable for wavelengths of  $1.06\mu\text{m}$  and  $862\text{nm}$  respectively but these do not necessarily correspond to optimum coupling.

Figure 5.3.8 shows the results of these measurements. Propagation losses of  $\alpha = 20\text{cm}^{-1}$  ( $87\text{dB cm}^{-1}$ ) at  $\lambda = 862\text{nm}$  and  $\alpha = 4\text{cm}^{-1}$  ( $17\text{dB cm}^{-1}$ ) at  $\lambda = 1.06\mu\text{m}$  were obtained. The result at  $862\text{nm}$  is at a detuning of  $17\text{meV}$  from the bandgap and the losses here are therefore mainly due to interband absorption. The losses at  $1.06\mu\text{m}$  are mainly attributed to substrate leakage.

It was found in the course of these investigations that the amount of light coupled into the waveguide was very critically dependent on the position of the input coupling lens. Great care was taken to optimise the coupling each time a measurement was taken. It is imperative when making these kind of measurements that the input coupling lens is mounted on good quality translational mounts otherwise it is extremely difficult to achieve optimum input coupling. It was also found that there was initially a large scatter in the transmission measurements due to randomly defective waveguides. These either had lithographic or wafer surface defects or had damaged facets. The damaged guides were identified by examining through an optical microscope and excluded from further measurements. A much reduced scatter in the results was seen after this.

The propagation losses in this material (MA661) at  $1.06\mu\text{m}$  are higher than those of Varian 1 (at  $830\text{nm}$ ). This is due to the geometry of the layers and the resulting degree of penetration of the mode's evanescent field into the substrate. Calculations of the power distribution in a four layer slab (using program FOURLAY as described in Chapter Three) indicate that for Varian 1, a fraction of the total guided energy equal to  $1.5 \times 10^{-9}$  is present in the part of the evanescent field penetrating into the substrate and for MA670 (and MA661) this fraction is calculated to be  $1.5 \times 10^{-6}$ ; some  $10^3$  times larger.

In summary, substrate losses can either be due to absorption or leakage into the substrate. If a substrate absorption of  $10^4\text{cm}^{-1}$  is assumed, the calculated losses due to substrate absorption are still a few orders of magnitude lower than the measured values. The losses in sample Varian 1 and MA661 (at  $1.06\mu\text{m}$ ) are therefore mainly attributed to leakage of energy into the substrate. The losses of MA661 at  $862\text{nm}$  are mainly due to interband absorption.

# Transmission results for sample MA661

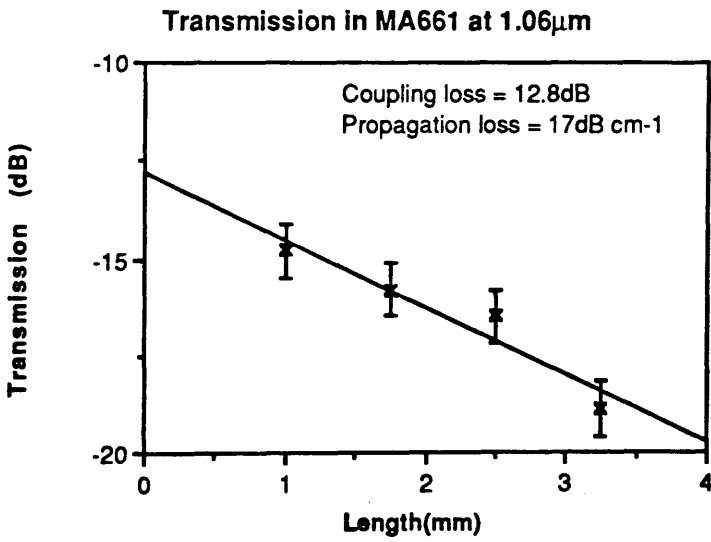
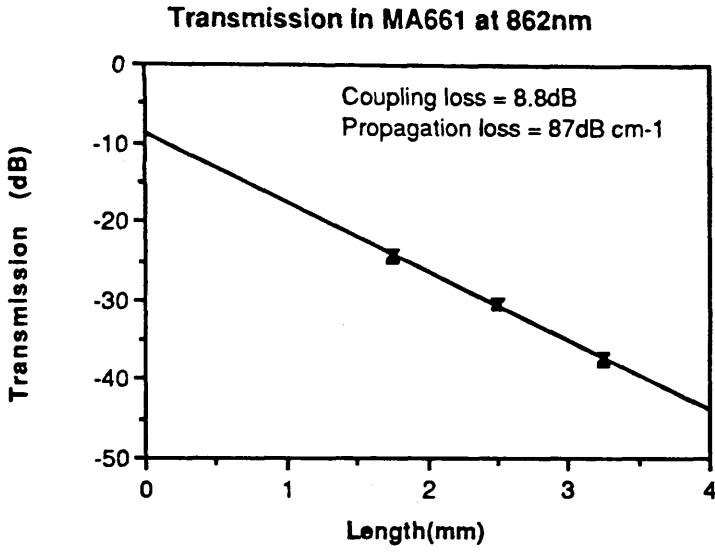


Figure 5.3.8

#### 5.3.4 Loss measurements in MQW waveguides.

Loss measurements in structures MV273 and MV330 were performed using the dye laser. The wavelength was scanned by a motorised driver unit attached to the micrometer control of the birefringent filter. The laser light was endfire coupled into the waveguides. The decoupled light from the guides was focussed onto an iris which was adjusted and positioned to allow through only light transmitted by the waveguide. This helped eliminate the stray light coming from over the top of the sample and the radiation modes transmitted through the cladding from reaching the detector. However, the fact that this nonguided light could never be completely eliminated put a lower limit to the measurable transmission in the waveguide i.e. when the light was tuned sufficiently close to the band-edge the guided light contribution to the total transmitted power was less than the stray, non-guided light contribution. Transmitted power was measured using a silicon detector positioned immediately behind the iris. Lock-in detection was used to improve the signal and the output of the lock-in amplifier was connected to a plotter so that the transmitted power could be plotted directly.

If the output response of the laser is perfectly flat and if the logarithmic output mode of the lock-in amplifier is selected, then the plotted output is directly proportional to the (negative) absorption coefficient. The output response of the laser was checked over the wavelength range of interest (820–850nm) and was found to be flat to  $\pm 0.25\text{dB}$ . This corresponds to an error in the measured loss (for 5mm long waveguides) of  $\pm 0.5\text{dBcm}^{-1}$  or  $\pm 0.12\text{cm}^{-1}$  in the absorption coefficient. This error does not significantly affect the shape of the absorption plot and was smaller than the scatter in the data points used to calibrate the curves. The propagation losses at three selected wavelengths for each plotted curve were measured using sequential cleaving as described in the previous section and these were used to calibrate the curves. The gradient of the best straight line for each set of measurements indicated the propagation loss. A scatter of  $\pm 1\text{dB}$  was seen in the data. The results are shown in figures 5.3.9 and 5.3.10 for MV273 and MV330 respectively for both TE and TM polarised guided light. The dichroism due to the polarisation dependant interaction of electromagnetic fields with the heavy hole excitons is apparent. The heavy hole excitonic contribution to the absorption can clearly be seen in both wafers. The light hole contribution is seen only in MV273. The positions of the exciton peaks agrees well with the photoluminescence results in Chapter Four for these samples.

It is apparent, however, that the excitonic peaks are not as pronounced compared to measurements performed on other MQW structures<sup>[17,18]</sup> with a larger well density. One possible reason for this may be attributable to the

## Absorption In MQW waveguides

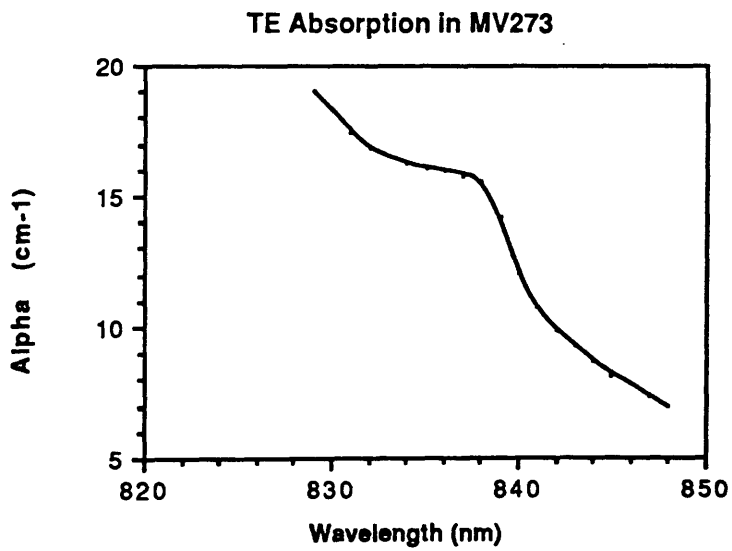
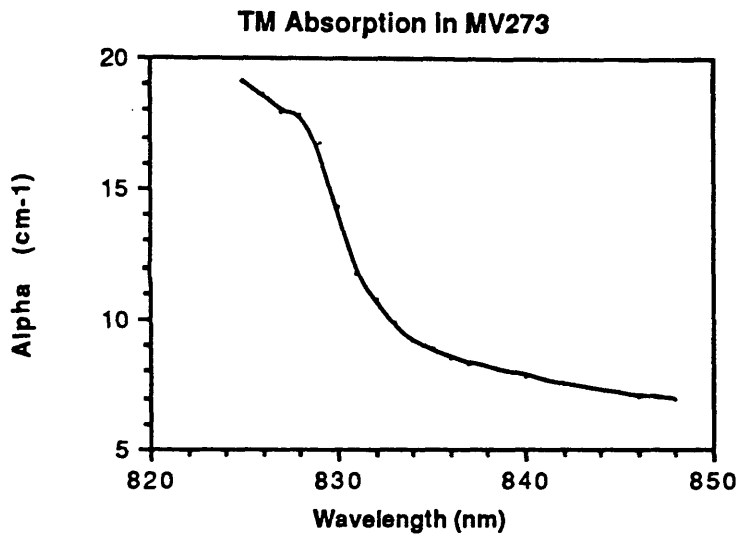


Figure 5.3.9

# Absorption in MQW waveguides

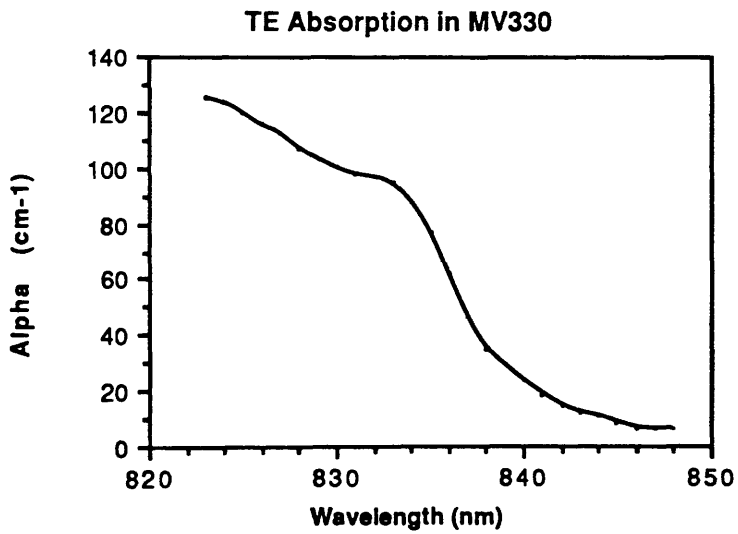
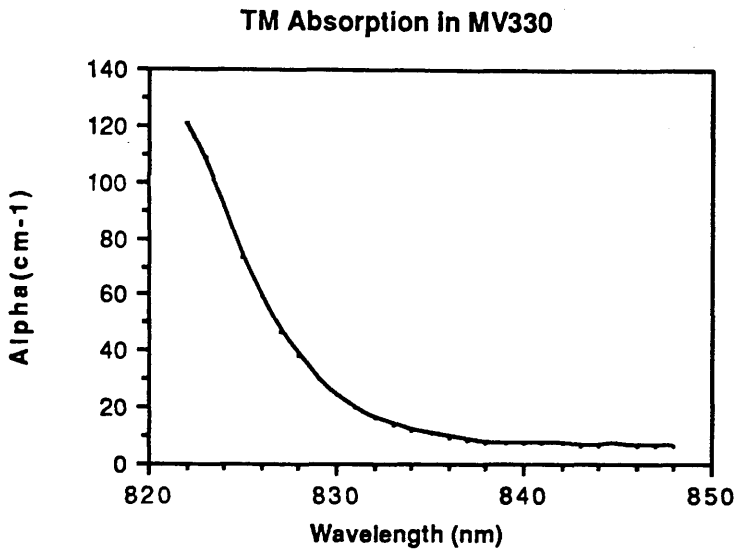


Figure 5.3.10

nonuniform absorption of the mode. This possibility is now discussed.

### 5.3.5 Discussion of loss results in MQW structures.

Any arbitrary intensity distribution in a waveguide structure can be described as a sum of its inherent modes. A finite number of guided modes and an infinite number of radiation modes are associated with all waveguides. For simplicity consider initially a lossless single-mode waveguide in which only the single guiding mode has been launched. The optical field distribution can, in this instance, be represented by a single orthogonal function[8]. If a spatially non-uniform loss is now introduced in the structure (such as that produced by the quantum wells) then the modal intensity distribution will be correspondingly modified. Where originally the field consisted of a single guided mode, there are now also radiation modes present in the waveguide. In other words, absorption in a part of the waveguide can also result in the excitation of additional radiation modes. These unguided radiation modes may still contribute significantly to the optical output of the waveguide and can thus make the measurement of MQW waveguide absorption losses quite difficult. Some authors have overcome this by utilising leaky waveguide[19] structures designed so that unwanted modes are stripped off and do not contribute to the detected output. However, such a waveguide structure is undesirable for nonlinear device applications because large power densities over long waveguide distances are not then attainable. The samples tested here are not leaky structures and are therefore not optimally designed to give accurate MQW absorption results.

Approximate calculations of the expected MQW absorption losses in MV273 and MV330 based on a well "filling factor"[19] are now performed. It is expected that these will overestimate the losses measured in waveguides MV273 and MV330 because the effect of radiation modes contributing to the transmitted intensity is not taken into account. If the net absorption in the guiding layer is assumed to scale linearly with the well density in two MQW systems then the absorption is given by

$$\alpha_1 = \frac{L_{W1}}{L_{B1} + L_{W1}} \times \frac{L_{B2} + L_{W2}}{L_{W2}} \times \alpha_2$$

where  $\alpha_i$  are the MQW absorption coefficients in the MQW system  $i$  and  $L_{B_i}$  and  $L_{W_i}$  are the barrier and well widths in these systems. The results of Whitehead et al[18] are used to estimate the minimum expected absorption in samples MV273

and MV330. Although it is not critically important which of the published results are used to perform these initial estimates of the absorption, the results of these authors were preferred because the measurements were performed on material from the same source (SERC III-V Central Facility, University of Sheffield) as MV273 and MV330. Of course this approximation involves the implicit assumption that the samples MV273 and MV330 are grown to a similar quality as those examined by these authors. Whitehead et al measured an absorption of  $1.7 \times 10^4 \text{ cm}^{-1}$  in a structure comprising of  $60 \text{ \AA}$  wells and  $105 \text{ \AA}$  barriers. In both of samples MV273 and MV330 the well and barrier thicknesses are  $65 \text{ \AA}$  and  $1000 \text{ \AA}$  respectively. Therefore

$$\alpha_{\text{MV273/330}} = \frac{65}{1000 + 65} \times \frac{105 + 60}{60} \times 1.7 \times 10^4 \text{ cm}^{-1}$$

$$\Rightarrow \alpha = 2.8 \times 10^3 \text{ cm}^{-1}$$

To calculate the absorption loss seen by the mode, the fraction of the total guided energy which lies within the MQW layer has to be calculated. Before doing this, one has to remember that the MV273 is a doped p-i-n structure and therefore the doping dependant refractive index has to be accounted for. This is done using the relation given by Garmire<sup>[8]</sup> which expresses the free carrier contribution to the refractive index:

$$\Delta n = \frac{N \lambda^2 e^2}{\epsilon_0 n_s 8 \pi^2 m^* c^2}$$

where  $N$  is the doping density (assumed to be equivalent to the free carrier concentration),  $\lambda$  is the wavelength of light,  $e$  is the electronic charge,  $\epsilon_0$  is the dielectric constant,  $n_s$  is the background refractive index,  $m^*$  is the carrier effective mass and  $c$  is the free space speed of light. Using values for GaAs at  $\lambda = 830 \text{ nm}$  it is found that

$$\Delta n = 9.06 \times 10^{-23} \times \frac{N (\text{cm}^{-3})}{m^*/m_0}$$

In MV273 for a p-doping of  $N = 6 \times 10^{17} \text{ cm}^{-3}$  and using  $m^*/m_0 = 0.34$ , an index change  $\Delta n = 1.60 \times 10^{-4}$  is obtained. For an n-doping of  $N = 2 \times 10^{17} \text{ cm}^{-3}$  and using  $m^*/m_0 = 0.0665$ , an index change  $\Delta n = -2.72 \times 10^{-4}$  is obtained. The

index change in the n-doped layer is larger because of the smaller electron effective mass. Taking these index changes into account, and applying program FOURLAY the energy distributions in the layers in structures MV273 and MV330 were calculated. It was found that there was no significant effect on the power distribution due to the doping variation in MV273 and the percentage of the total power in the MQW slab was 81.2% in both the samples. The results and data used in these calculations are summarised in figure 5.3.11.

Using these results and the estimated absorption in the MQW layer the predicted absorption loss seen by the guided mode at the heavy hole excitonic resonance is expected to be

$$81.2\% \times 2.8 \times 10^3 \text{ cm}^{-1} = 2.27 \times 10^3 \text{ cm}^{-1}.$$

The lack of distinct excitonic features in MV273 and MV330 has been discussed in terms of nonuniform modal absorption and the resulting introduction of radiation modes which mask the excitonic absorption resonances. Of course, this lack of excitonic distinction can also be a result of poor material quality. This possibility is now considered.

Studies performed by H. C. Lee et al<sup>[18]</sup> indicate that, for MOCVD material, high growth temperatures lead to poor excitonic features because of high background carrier concentrations ( $\approx 4 \times 10^{16} \text{ cm}^{-3}$ ). These authors found that the best features were seen with MQW layer growth temperatures of around 650°C where impurity concentrations of around  $6 \times 10^{14} \text{ cm}^{-3}$  were obtained. Polaron measurements performed at Sheffield on the samples MV273 and MV330 indicate that the doping concentrations are around  $10^{16} \text{ cm}^{-3}$  in the MQW layer. Therefore it is possible that an excessive free carrier concentration has contributed to the lack of a distinct excitonic peak in the absorption. The free carrier concentration has been linked by these authors to the linewidth of the room temperature excitonic photoluminescence peak. The linewidth has been seen to increase with higher free carrier concentrations. Lee et al found that, for a sample with background carrier concentrations of  $6 \times 10^{14} \text{ cm}^{-3}$ , a linewidth (FWHM) of 15.4 meV was measured from photoluminescence spectra and distinct excitonic features were obtained in the absorption plots. A concentration of  $\approx 4 \times 10^{16} \text{ cm}^{-3}$  gave a FWHM of 20.8 meV in the photoluminescence spectra and resulted in a poor excitonic feature in the absorption plot. Photoluminescence results of samples MV273 and MV330 indicate considerably large FWHMs of 27.2 meV and 24.0 meV respectively.

These considerations indicate that the primary reason for the poor excitonic features is due to an excessive free carrier concentration in the MQW layers and not the contribution of waveguide radiation modes to the measurements of

**Refractive index data and optical energy distribution in samples MV273 and MV330.**

Sample MV273			Percent power in each layer
n=1	Air		0.000%
n=3.4052	Al <sub>0.3</sub> Ga <sub>0.7</sub> As	( $\rho = 6 \times 10^{17} \text{ cm}^{-3}$ )	9.343%
n=3.441	MQW	undoped	81.236%
n=3.4047	Al <sub>0.3</sub> Ga <sub>0.7</sub> As	( $n = 2 \times 10^{17} \text{ cm}^{-3}$ )	9.421%

Sample MV330			Percent power in each layer
n=1	Air		0.000%
n=3.4050	Al <sub>0.3</sub> Ga <sub>0.7</sub> As	all layers	9.259%
n=3.441	MQW	nominally undoped	81.206%
n=3.4050	Al <sub>0.3</sub> Ga <sub>0.7</sub> As		9.536%

This figure summarises the results of the calculated optical energy distribution in the MQW samples MV273 and MV330. The refractive indices of the MQW layers were first calculated using programs XTON and KRAMERS, and the optical energy distributions were then calculated using program FOURLAY.

**Figure 5.3.11**

transmission. This may be due to poor temperature control during the growth of the MQW layer.

### 5.3.6 Conclusions on loss measurements.

The method for loss measurement and calibration has been described in this section and the results of these measurements have been presented and discussed. In the samples where the laser light was of energy close to that of the band-gap of the guiding layer, the main loss mechanism was due to interband excitation of carriers. In the cases where the photon energy was far beneath the band-gap, the main loss has been attributed to radiation into the substrate as a result of the higher substrate refractive index. Therefore to reduce this loss it is recommended that the guided mode should be optically isolated as much as possible from the substrate (e.g. by increasing the thickness and/or the Al content in the lower cladding). Of course it is not important to do this when one is operating near the band-gap because in this case the interband absorption losses are considerably higher than the radiation loss. In a structure where the nonlinear effect is due to a virtual carrier excitation (e.g. where the Kerr effect or the AC Stark effect provide the optical nonlinearity) then it is worthwhile making this design consideration.

Regardless of whether absorption is significant or not, it is desirable to improve nonlinear device performance by maximising the coupling efficiency of the laser light to the waveguide mode. Coupling losses due to modal mismatch can be reduced by designing a waveguide structure in which the mode is near circular (i.e. by ensuring that the lateral confinement is the same as the vertical confinement). This would ensure an improved overlap between the laser light and the waveguide mode (assuming of course that the laser optical field possesses circular symmetry). Fresnel reflection losses can be reduced by use of an anti-reflectant coating on the waveguide facets. Transmission at an air/GaAs interface is about 68% for normally incident light. If an optical coating is deposited on the GaAs surface, with thickness equal to  $\lambda/n_c^4$ , where  $n_c$  is the refractive index of the coating, then the reflectance is given by

$$R = \left[ \frac{n - n_c^2}{n + n_c^2} \right]^2$$

where  $n$  is the refractive index of the waveguide layer. If magnesium oxide (MgO) (refractive index = 1.7373) is used then a transmittance ( $T = 1 - R$ ) of 91.4% is

obtained. An increase of approximately 30% in the power coupled into the device can thus be achieved.

#### 5.4 Nonlinear Characterisation of Waveguides.

This section describes the experimental work and results regarding measurement of the intensity dependant properties of AlGaAs waveguides. Three main experiments are reported. The first of these is an investigation of self phase modulation with the intention of determining the nonlinear Kerr coefficient,  $n_2$ , of AlGaAs. The second experiment measures the total nonlinear index change using an interferometric technique and this shows the net refractive index change due to the combined electronic and thermal contributions. Thirdly, the measurements of nonlinear absorption are reported. The implications of these results with regard to device design are finally considered.

##### 5.4.1 Self Phase Modulation.

The experiments to characterise the Kerr nonlinear coefficient  $n_2$  in  $\text{Al}_{0.3}\text{Ga}_{0.7}\text{As}$  are described. To date this has not been measured for AlGaAs and only the GaAs value has been reported. This has been measured to be  $4 \times 10^{-18} \text{m}^2/\text{W}$  by J. J. Wynne[20] and  $2 \times 10^{-16} \text{m}^2/\text{W}$  by Chen and Carter. Note that the Kerr  $n_2$  has been measured as positive in both cases and is opposite in sign to the electronic carrier dependant  $n_2$ . An experiment was performed to look at Self Phase Modulation in the AlGaAs samples and to hence determine the nonlinear coefficient.

Self Phase Modulation (SPM) is a nonlinear effect in which the phase relations between different parts of a pulse are modified. Consider a pulse propagating in a nonlinear waveguide where the refractive index can be described by

$$n = n_0 + n_2 I$$

and where all symbols have their usual meaning (see Chapter One). If the pulse intensity is large enough then a refractive index change will be induced. Furthermore, if the effect is fast and has a relaxation time of a few femtoseconds, then the index change will vary with the shape of the pulse. This means that the more intense parts of the pulse experience a higher refractive index. The central portion of the pulse is therefore delayed with respect to the less intense leading

and trailing parts of the pulse and this results in a frequency chirp where the leading part of the pulse is red-shifted and the trailing part is blue-shifted.

SPM is an accumulative effect and over long enough propagation distances the induced chirp may become large enough so that dispersive effects lead to changes in the pulse shape. This is true regardless of whether the group velocity dispersion (i.e.  $\partial v_g / \partial \lambda$ ) is positive or negative. If group velocity dispersion is positive, then the pulse broadens because the red-shifted leading part of the pulse will tend to travel faster than the blue-shifted trailing part. This broadening of the pulse results in a reduction in the pulse peak power and hence further SPM is reduced. If however the group velocity dispersion is negative then the two ends of the pulse move towards each other relatively and thus narrowing the pulse. It is possible that this pulse narrowing due to a combination of dispersion and nonlinear effects is balanced by the broadening caused by dispersion alone and this can result in the formation of optical solitons: light pulses whose envelope shapes either do not change or else change shape periodically as they propagate<sup>[4]</sup>. To see the effect of SPM in the time domain requires the presence of both a large effect and a large group velocity dispersion. It is easier instead to see SPM by direct observation of the frequency broadening of pulses in the spectral domain.

To relate the change in the pulse spectrum to the nonlinear coefficient consider first the delay seen by each part of the pulse. This can be expressed in terms of a phase shift  $\Delta\varphi$  as given in section 5.3.3 by equation (5.3.3.4)

$$\Delta\varphi = \frac{2\pi}{\lambda} n_2 \ell_{\text{eff}} I(t) \quad (5.3.3.4)$$

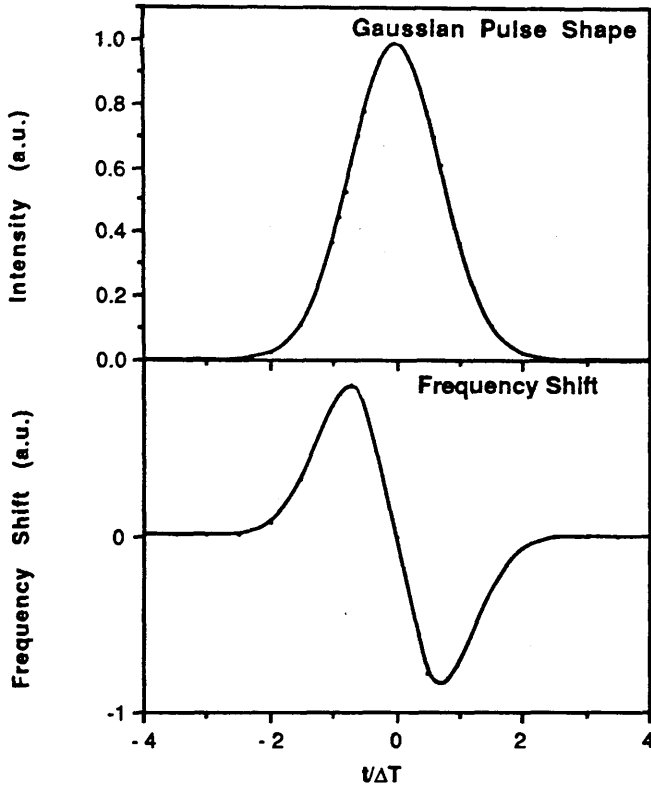
The frequency shift,  $\Delta\omega$ , can then be expressed by differentiating

$$\Delta\omega = - \frac{\partial(\Delta\varphi)}{\partial t} = - \frac{2\pi}{\lambda} n_2 \ell_{\text{eff}} \frac{\partial I(t)}{\partial t} \quad (5.4.1.1)$$

In other words, the frequency shift is proportional to the negative gradient of the pulse intensity envelope. This is illustrated in figure 5.4.1 which shows a Gaussian shaped pulse and the resulting frequency shift. As can be seen there are, in general, two points within each pulse which undergo the same frequency shift. In the frequency domain these will be seen to interfere constructively or destructively depending on their phases and this gives rise to a fringe-like structure in the spectrum of the pulses. Frequency spectra have been calculated by R. H. Stolen et al<sup>[21]</sup> for a Gaussian pulses of varying intensity and these are shown in figure 5.4.2. The spectra are labelled by the maximum phase shift  $\Delta\varphi$  at the peak of the pulse as given by equation (5.3.3.4).

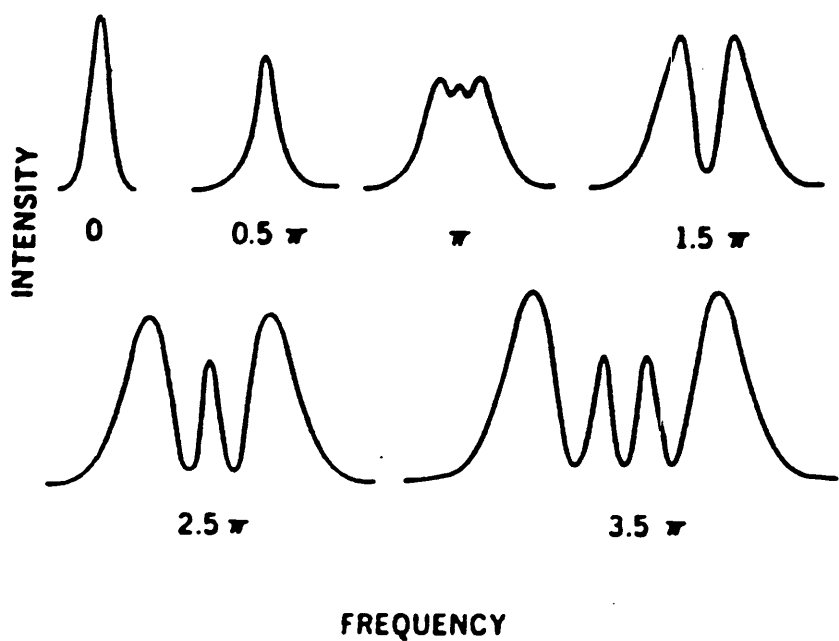
Note that it has been assumed that the nonlinearity causing the spectral

## Gaussian pulse shape and resulting frequency shift due to Self Phase Modulation



When a pulse propagates in a nonlinear medium, the refractive index varies with the pulse envelope and this causes a local frequency shift of the optical field. The above graphs show a Gaussian pulse envelope and the corresponding frequency shift.

Figure 5.4.1



Calculated Spectra illustrating varying amounts of Self-Phase Modulation for a Gaussian pulse. Spectra are labelled by the maximum phase shift at the centre of each pulse. (After R. H. Stolen et al [21].)

**Figure 5.4.2**

broadening has a relaxation time faster than the pulse width. If this was not so, and the effect was slower than the pulse width but still faster than the pulse repetition time, then the frequency shift is seen only on the leading edge of the pulse, i.e. only the redshift is apparent. In the frequency domain this is characterised by an asymmetrically broadened spectrum. If the effect is slower than the pulse repetition time then no broadening will be seen since the index change does not relax between the pulses. It is important to note that, due to these relaxation time considerations, investigation of SPM automatically excludes the slower thermal or carrier population induced refractive index changes from contributing to the observed spectral broadening. Thus only the Kerr-type nonresonant effect contributes to Self Phase Modulation in AlGaAs.

The experimental measurements of SPM were carried out by the author at the Department of Physics, University of St. Andrews. The laser source used in these investigations was a synchronously pumped dye laser pumped by a Krypton ion laser of wavelength 647nm and modelocked at 84MHz. The dye in use was HITCP which enabled lasing from 830nm to 900nm.

The dye laser was used in a cavity dumped mode of operation which results in high energy pulses. When operating in this way, the mirror which normally acts as an output coupler is replaced by one which is near 100% reflecting so that the pulse is totally reflected back into the cavity. This is allowed to happen many times and the pulse undergoes amplification in the dye jet every cavity round trip. The pulse is then released from the cavity by means of an intracavity acoustooptic modulator which deflects the pulse away from the totally reflecting mirror. The output pulse therefore has a much increased energy. The frequency of the modulator could be varied to give different pulse repetition rates and hence different pulse energies. In this mode of operation the average power produced by the laser is considerably lower than that of normal synchronous operation. Also the pulse width is slightly larger but the much larger pulse repetition time still means that there is a large increase in the pulse peak output power. Typically, in non-cavity dumped operation the average power was 20mW, the pulse width was measured to be 3ps and the repetition time was 12ns. These values indicate a peak pulse power of 80 Watts. In cavity dumped operation the average power was 2.7mW, pulse width was 3.9ps, and the pulse repetition rate was 800kHz (repetition time = 1.25ms) and this gives a peak power of 865 Watts: an order of magnitude increase. It should be noted that these measured values refer to the power of the laser beam just before it enters the endfire rig. The actual laser output power was larger than this.

The experimental set-up used in these investigations is similar to that described in section 5.2.4 where the spectral output of the dye laser was

characterised. The only exception is that a CCD linear array detector was used instead of a vidicon camera to observe the spectrum (see figure 5.4.3). Using this, the FWHM of the laser spectrum was measured to be  $5\text{\AA}$  (in the cavity dumped mode of operation). The pulse width (3.9ps) is therefore 3 times larger than the bandwidth limited value. Figure 5.4.4 shows the spectrum obtained for maximum power coupled into a waveguide in sample Varian 2 (an  $\text{Al}_{0.3}\text{Ga}_{0.7}\text{As}$  structure – see Appendix III) and compares this with the spectrum of the laser light. No appreciable change in the shape of the spectrum was seen with the light decoupled from the waveguide. The spectra obtained from the other samples were all similar. Considering the recent reports of  $n_2$  this was a most unexpected result. No SPM was seen and hence a value for  $n_2$  could not be determined. In fact only a maximum possible value of the Kerr  $n_2$  for  $\text{Al}_{0.3}\text{Ga}_{0.7}\text{As}$  could be calculated. As described above, the peak power produced by the laser was 865 Watts. (This was calculated from measurements just before the endfire rig.) Referring to section (5.3.3) the following considerations regarding the coupling losses were made:

- (i) Fresnel reflection losses = 30% (Refractive index= 3.405[22])
- (ii) Modal matching efficiency = 25%
- (iii) Transmission in the input coupling objective = 95%

i.e. the total peak power coupled into the device was therefore

$$P_{in} = 865 \times 0.7 \times 0.25 \times 0.95 = 144 \text{ Watts.}$$

The waveguide modal area has been estimated from observation on the Hamamatsu camera as  $10\mu\text{m}^2$  where the waveguide rib separation was used as a reference. From this a peak intensity of  $1.44 \times 10^{13}$  Watts is obtained. The criterion used for determining the maximum possible  $n_2$  was based on figure 5.4.2 after reference [21]. From this it was determined that the phase shift  $\Delta\varphi$  is less than  $0.5\pi$ . If it was larger then a clear change in shape would be observed. The maximum phase shift is given by equation (5.3.3.4) and using  $\ell_{eff} = 4\text{mm}$  (based on the loss measurement results of section (5.3.3) a maximum possible  $n_2$  of  $3.6 \times 10^{-18}\text{m}^2/\text{W}$  is calculated.

This is lower than any of the recent values cited for GaAs. Gabriel et al[23] have made an estimate of a Kerr  $n_2$  of  $1.2 \times 10^{-17}\text{m}^2/\text{W}$  and Chen and Carter[24] have reported a value of  $2 \times 10^{-16}\text{m}^2/\text{W}$ . The latter authors admit however that there may be a 40% contribution to this number from heating effects[23]. The result reported here agrees most closely with that number originally reported by J. J. Wynne in 1969[20] of  $4 \times 10^{-18}\text{m}^2/\text{W}$ .

## Experimental layout for Observation of Self Phase Modulation

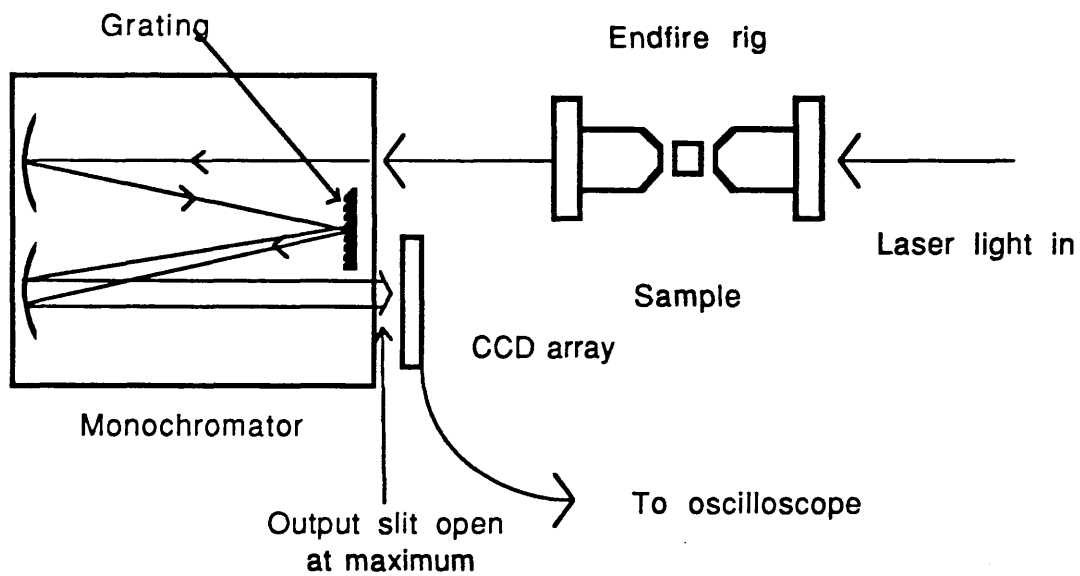
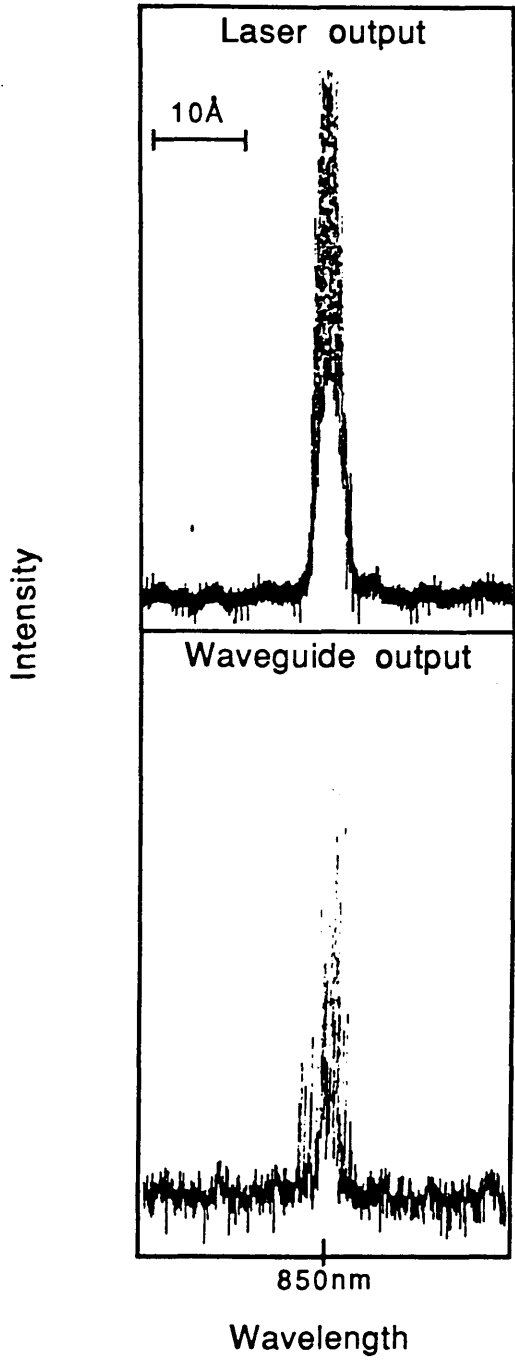


**Figure 5.4.3**

# Comparison of Laser and Device Output Spectra.



No change in width is seen when comparing the spectrum of the device output to the laser output.

Figure 5.4.4

These investigations therefore indicate that the value of  $n_2$  for the Kerr nonlinearity in  $\text{Al}_{0.3}\text{Ga}_{0.7}\text{As}$  is at least an order of magnitude lower than any of the recently published values. It has to be noted that the published values are for GaAs whereas the above sample had a 30% Al content. It is only reasonable to assume that the presence of Al will affect the Kerr coefficient which may account for the discrepancy between the result obtained here and that reported in the recent literature. It must also be noted that the thermal contribution to the nonlinearity has never before been satisfactorily eliminated and it is a possibility that other reported measurements of the "Kerr" nonlinearity may also have contained a thermal contribution to  $n_2$ .

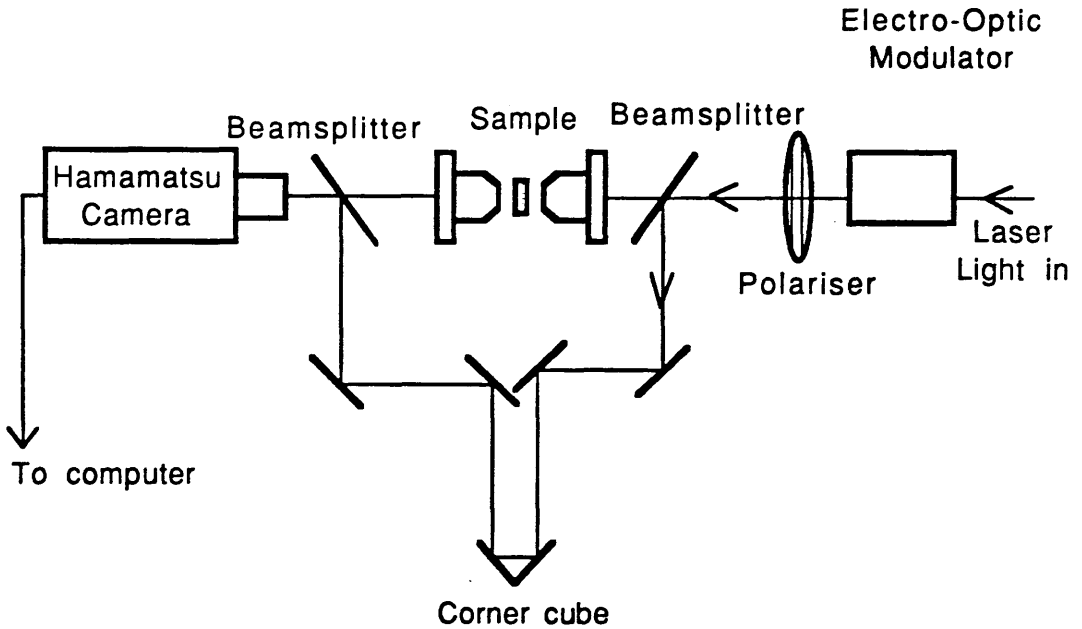
The SPM investigations were carried out under the kind auspices of Prof. Wilson Sibbet at the Dept. of Physics, University of St. Andrews. Much needed experimental assistance with the laser source was provided by the dedicated help of Mr. R. S. Grant and Dr. N. Langford.

#### 5.4.2 Interferometric Measurements of Nonlinear Refractive Index

An interferometric technique was used to measure the intensity dependant refractive index in waveguides. This technique has been demonstrated by Li-Kam-Wa et al<sup>[25]</sup> who measured the nonlinear phase shift in MQW strain induced waveguides in this way. Figure 5.4.5 shows the set-up used in these measurements. Light from the laser is split into two beams. One of these is endfire coupled into the waveguide. The decoupled output beam from the waveguide is then recombined with the other beam to produce interference fringes which are observed on the Hamamatsu vidicon camera. As the optical power is varied, the refractive index in the device changes and this results in a fringe shift. The set-up includes a retro-reflecting corner cube mounted on a translational stage to serve as an optical delay line in the arm external to the device. This is essential to ensure that the optical path lengths in two arms are equal to within the spatial pulse width otherwise interference fringes are not seen. It was found that, because longer pulses are obtained when the dye laser cavity is mismatched, it was easier to obtain fringes with the laser in a poorly modelocked condition. Once these were seen the cavity length and the retro-reflector positions could be alternately adjusted until both the modelocking and the optical delay were optimised.

It was seen that as the retroreflector was scanned and the delay was varied, "ghost" fringes sometimes appeared due to a multiple reflection within one of the arms (e.g. from the beamsplitter). These could be identified by scanning the

**Experimental Arrangement for Nonlinear Fringe shift measurement.**



This figure shows the arrangement of the Interferometer used to make measurements of the nonlinear refractive index. The retroreflecting corner cube is mounted on a translational stage for equalisation of the optical path lengths. This is essential if the beams are to overlap to produce interference fringes.

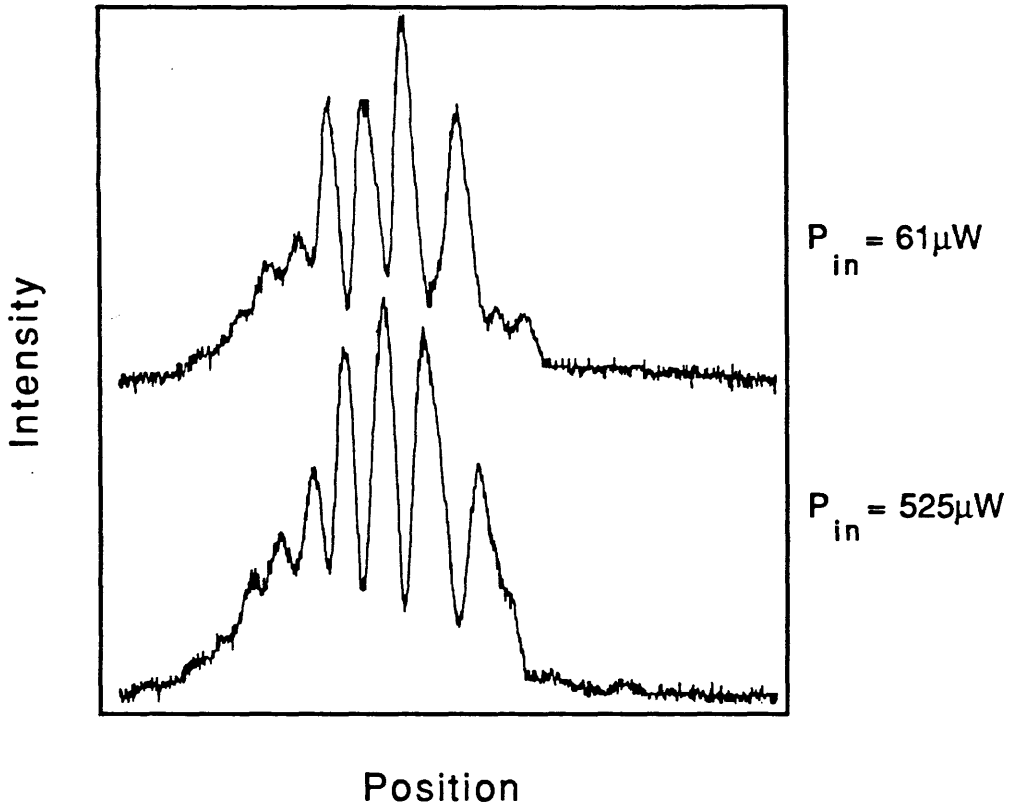
**Figure 5.4.5**

retroreflector further past this position. If these disappeared and fringes with better visibility appeared then the initially observed fringes were due to a multiple reflection. It must be commented that these ghost fringes behaved similarly to the true zero delay fringes in that they shifted by the same amount if the power was varied but the visibility of these was considerably poorer than that of the true fringes. The final adjustment was made to the cavity length to optimise the modelocking by monitoring the pulse width on the autocorrelator. The position of the retro-reflector was critical to submillimetre distances when the laser is well mode-locked and short pulses are obtained.

Having obtained the interference fringes, the amount of power being coupled into the waveguide was varied by using an electro-optic modulator and polariser combination. The modulator was a commercially available mounted lithium niobate crystal which was driven by a high voltage amplifier: both components produced by Electro-Optics Developments. This enabled both d.c. and a.c. control of the polarisation of the light transmitted through the crystal. By using this in conjunction with a polariser placed after the modulator, control of light intensity could be achieved without the need for any physical adjustment of optical components thus eliminating beam misalignment problems.

As the power is varied a shift in the position of the fringes is seen due to the intensity induced change in optical path length in the waveguide. The size of the index change can be calculated from the fringe shift. Fringe stability, however, was a problem with these measurements and generally only an assessment of fringe shifts to an accuracy of about 1/8 of a fringe could be made. Towards the end of the project, an electronic feedback system to improve fringe stability was being designed. This feedback system was based on the use of a split detector comprising of two monolithically integrated photodiodes to detect the fringe movement. The fringes were aligned so that one fringe lay centrally on the two photodetecting surfaces. Any movement of the fringe from this central position resulted in a difference in the signal from the two photodiodes. An error signal derived from this difference was then used to drive a piezo-electric mirror mount and hence correct for any path length changes due to vibration of the optics. A version of this set-up is described in [26]. It was found that when the fringes were sufficiently intense it was possible to translationally move the split detector and observe the fringes following the position of the detector. The actual interference fringes produced by the output of the device were found to be too low in intensity for the electronic signal processing to work. The system is currently being improved but was not available for the measurements carried out in this project. Instead the fringe shifts were measured using the Hamamatsu camera. The results for sample MA670 (an  $\text{Al}_{0.06}\text{Ga}_{0.94}\text{As}$  structure - see Appendix III) are shown in figure

**Nonlinear fringe shift in sample MA 670.**



**A nonlinear fringe shift of  $\lambda/2$  is seen when the optical power coupled into the waveguide is increased from  $61\mu W$  to  $525\mu W$ .**

**Figure 5.4.6**

5.4.6 for a wavelength 846nm (photon energy=1.466eV).

A fringe shift of  $\lambda/2$  was seen when the input power was increased from  $61\mu\text{W}$  to  $525\mu\text{W}$ . (This is the actual power entering the waveguide after having allowed for input coupling losses due to Fresnel reflection and modal mismatch.) From this it is possible to calculate the nonlinear coefficient  $n_2$  using equation (5.3.3.4). However before doing this, the absorption coefficient is required so that the effective length  $\ell_{\text{eff}} (=1/\alpha)$  can be determined. This is estimated using the absorption measurements made at  $\lambda=862\text{nm}$  (1.439eV) and Urbach's rule which can be written for energies below the bandgap ( $\hbar\omega < E_g$ ) as

$$\alpha = A \exp[B(\hbar\omega - E_g)]$$

Here  $E_g$  is the bandgap energy (1.522eV for MA670),  $A$  is the absorption at  $\hbar\omega=E_g$  and  $B$  is the slope of  $\ln(\alpha)$ . Absorption measurements at 862nm (1.439eV) indicate that the absorption coefficient is  $20\text{cm}^{-1}$  (from section 5.3.3). Using the data of Aspnes[22],  $A$  can be determined as  $5 \times 10^3 \text{cm}^{-1}$ .  $B$  is then calculated to be  $66.4\text{eV}^{-1}$ . Having determined these, the value of  $\alpha$  at 846nm is calculated as  $125\text{cm}^{-1}$  and therefore  $\ell_{\text{eff}}$  is  $8 \times 10^{-5}\text{m}$ . Equation (5.3.3.4) is now applied using  $\Delta\varphi=\pi$ , and  $\Delta l = \Delta P/\text{area}$  where  $\Delta P = (525-61)\mu\text{W}$  and  $\text{area} = 10\mu\text{m}^2$ . This yields that the nonlinear coefficient is  $n_2 = 3.2 \times 10^{-11}\text{m}^2/\text{W}$ . The direction of the fringe shift indicates that the effect is a thermal one i.e. increasing the intensity increases the waveguide refractive index and consequently increases the optical path length in the Mach-Zehnder arm with the sample. The direction of the thermal fringe shift was verified by moving one of the mirror mounts gently and relating the direction of the fringe shift with the direction of mirror movement.

The MQW samples (MV273 and MV330) were also tested but the induced index change was smaller and could not be measured using this technique.

### 5.4.3 Nonlinear Absorption in waveguides.

Changes in absorption with intensity are expected to occur when photons of energy close to the bandgap are incident on the sample. These changes can be due to electronic effects where the creation of free carriers by optical excitation results in state-filling and screening effects (see Chapter Two). However, thermal effects also contribute since phonons are created as these photoexcited carriers relax within the conduction band. The crystal is heated up thus causing a thermally induced decrease of the bandgap energy.

The change in absorption was obtained by measuring the nonlinear

transmission in the waveguides. The low intensity transmission is given by  $T_0$  where

$$T_0 = k \exp(-\alpha_0 \ell)$$

where  $k$  is a constant to allow for coupling losses,  $\alpha_0$  is the low intensity absorption and  $\ell$  is the waveguide length. If the intensity of the coupled light is increased then the transmission changes to  $T_1$  where the change is given by

$$\Delta T = T_1 - T_0 = \exp(-(\alpha_0 + \Delta\alpha)l) - \exp(-\alpha_0 l)$$

and the absorption change  $\Delta\alpha$  is given by

$$\Rightarrow \Delta\alpha = -\frac{1}{l} \ln \left[ \frac{\Delta T}{T_0} + 1 \right]$$

Note that it is possible to obtain the absorption change without knowing the actual coupling efficiency of the light into the guide. Only the length  $l$  of the waveguide needs to be known. Figure 5.4.7 shows the experimental arrangement used to make these measurements.

The power entering the device was monitored using a glass beamsplitter to reflect some of the incident light onto a silicon photodetector. This signal was calibrated by using a power meter positioned after the beamsplitter which therefore measured the optical power entering the endfire rig. The device output power was monitored using another silicon photodetector. An iris was used, as before, to help eliminate any contribution to the detected output due to non-guided light. The power coupled into the waveguide was varied using an electro-optic modulator and polariser combination as before.

Nonlinear transmission measurements were thus performed in samples CPM376, MV273 and MV330. In each sample the same result was seen regardless of whether the laser was well mode-locked or poorly mode-locked. The average laser power in both cases remains approximately the same but the pulse width and peak power vary considerably. This invariance of nonlinear transmission with pulse peak power suggests that the effect is not intensity dependant but energy dependant. i.e. it is slower than the pulse repetition time of 13ns and is effectively integrated over many pulses. This is only to be expected for thermal effects since the relaxation time is limited by the slow diffusion of thermal energy away from the waveguide. (The diffusion times associated with both electronic and thermal effects are considered in the next section). Electronic effects due to free carrier excitation will also seem to be energy dependant since the relaxation time of carriers (a few tens of nanoseconds<sup>[27]</sup>) is longer than the pulse repetition time. It is therefore quite

### Experimental Arrangement for Nonlinear Transmission measurement.

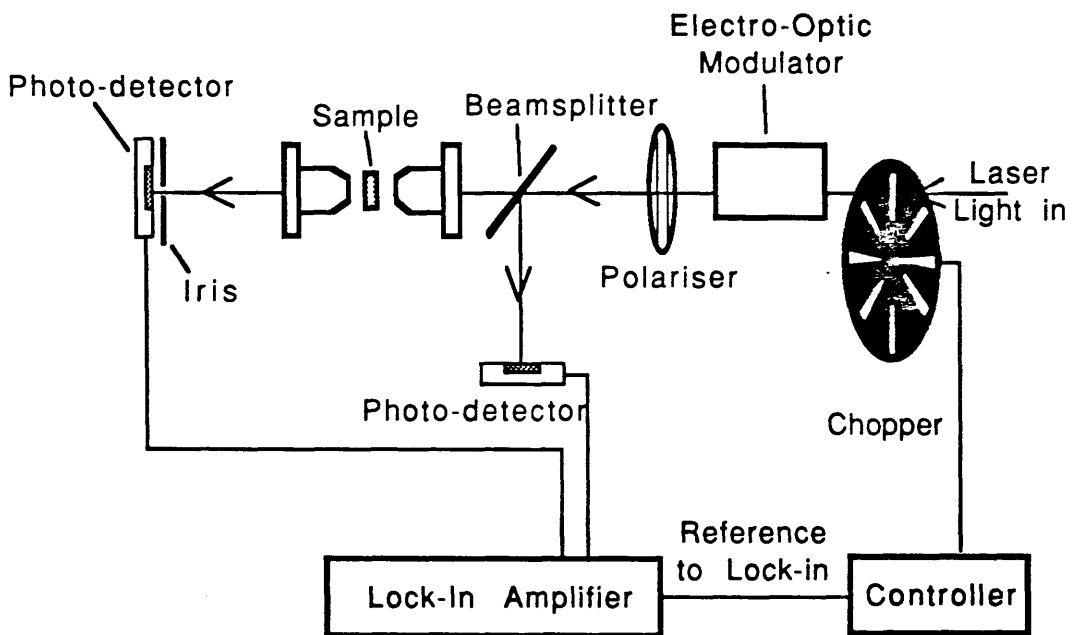


Figure 5.4.7

easily explained why the size of the measured effects is independent of the state of mode-locking under these experimental conditions.

The absorption changes derived from these measurements are shown in figure 5.4.8. The results for sample CPM376 show absorption increasing with intensity. Furthermore, the change in absorption increases as the photon energy approaches the bandgap energy (1.507eV). However it can be seen that the effect is dominantly a thermal one and not an electronic one since the change in the absorption is positive which indicates a red-shift of the bandgap. The limit of the shortest measurable wavelength was determined by the large absorption losses which prevented any characterisation closer to the bandgap.

The results for sample MV273 are more interesting. As the photon energy approaches that of the exciton (at 1.482eV) the change in absorption is positive. Again this is attributed to thermal effects. However, as the laser is tuned past the exciton energy, the absorption change is seen to decrease and finally become negative. This is interpreted as being due to a competing state filling effect which becomes more dominant at the higher photon energies. This behaviour was not observed in MV330 because the higher absorption in this sample meant that the waveguide was too lossy for characterisation past the exciton energy at 1.496eV. Only the redshift resulting from device heating was seen in this sample.

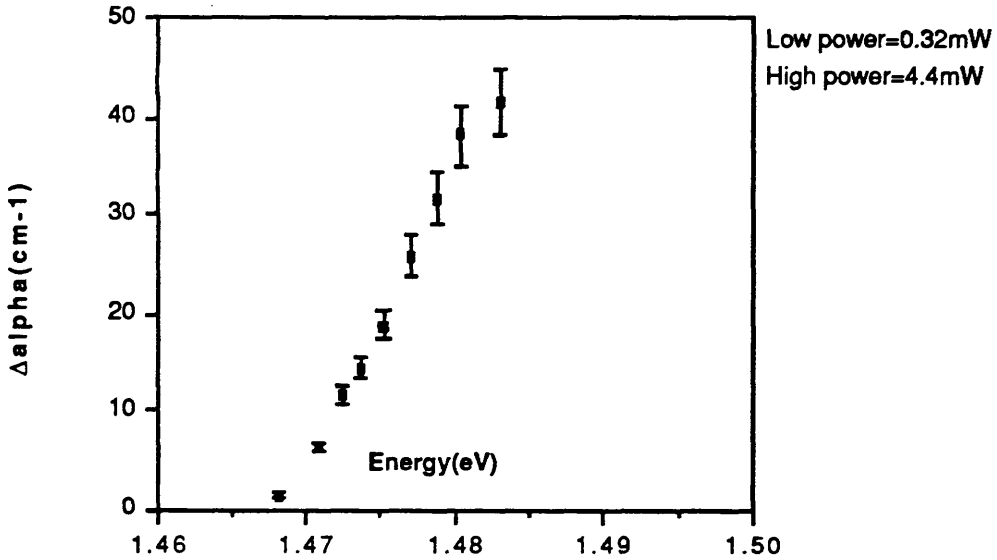
Most of the above measurements indicate a thermal effect but the results from sample MV273 suggest that electronic nonlinear effects are dominant under certain conditions. These conditions have to be carefully considered before undertaking further device design.

#### 5.4.4 Thermal and Carrier Diffusion effects.

The above results illustrate the competition which exists between thermal and electronic effects. There are several factors which determine the dominant effect and one of the most important of these is the relaxation time of the nonlinearity. For electronic nonlinearities, these times will partly depend on the carrier lifetime but will also depend on carrier diffusion effects. For thermal nonlinearities heat dissipation within the waveguide is the important factor. Electronic diffusion effects are considered first.

Effects of carrier diffusion were experimentally investigated by Olsson et al[28] who used a time resolved photoluminescence technique to obtain the temporal and spatial evolution of an initial carrier distribution. These authors have shown that the two-dimensional diffusion equation

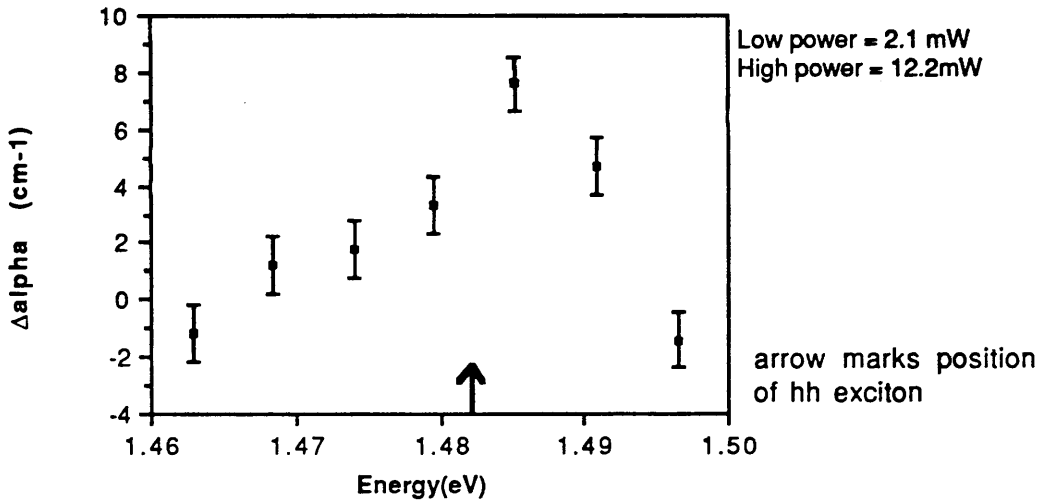
### Nonlinear Absorption in sample CPM376



The change in absorption is positive in this sample indicating a dominant thermal effect. The size of the effect increases as the photon energy approaches that of the bandgap (1.507 eV)

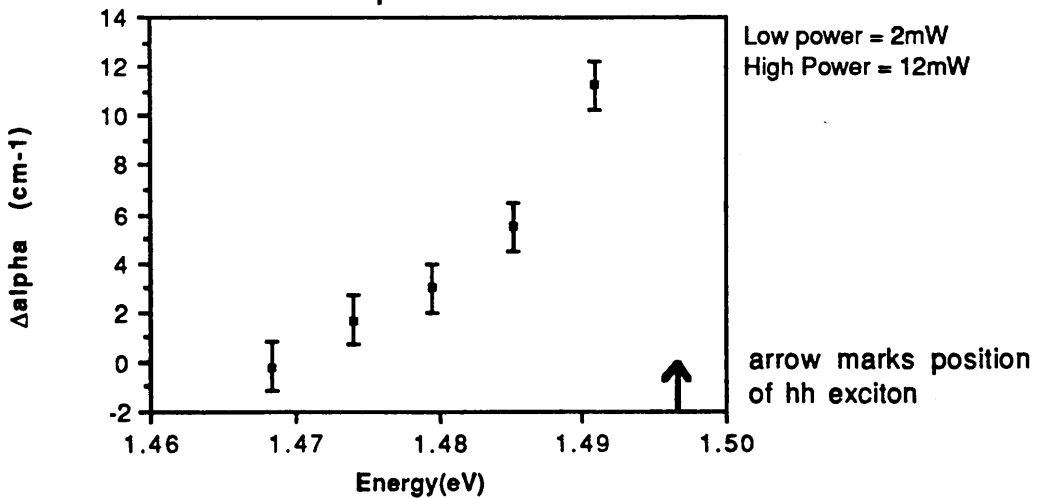
Figure 5.4.8(a)

### Nonlinear Absorption in sample MV273



There is change in the sign of  $\Delta\alpha$  after the photon energy is tuned past the hh excitonic absorption resonance. The measurements were made using TE polarised light

### Nonlinear Absorption in sample MV330



In this sample the  $\Delta\alpha$  remains positive and is increasing up to the hh exciton.

Figure 5.4.8(b)

$$D_c \frac{1}{r} \frac{\partial}{\partial r} \left[ r \frac{\partial N}{\partial r} \right] - \frac{N}{\tau} = \frac{\partial N}{\partial t} \quad (5.4.4.1)$$

where  $r$  is the radial distance,  $N$  is the carrier density,  $D_c$  is the carrier diffusion constant and  $\tau$  is the carrier lifetime, can be solved to give the solution

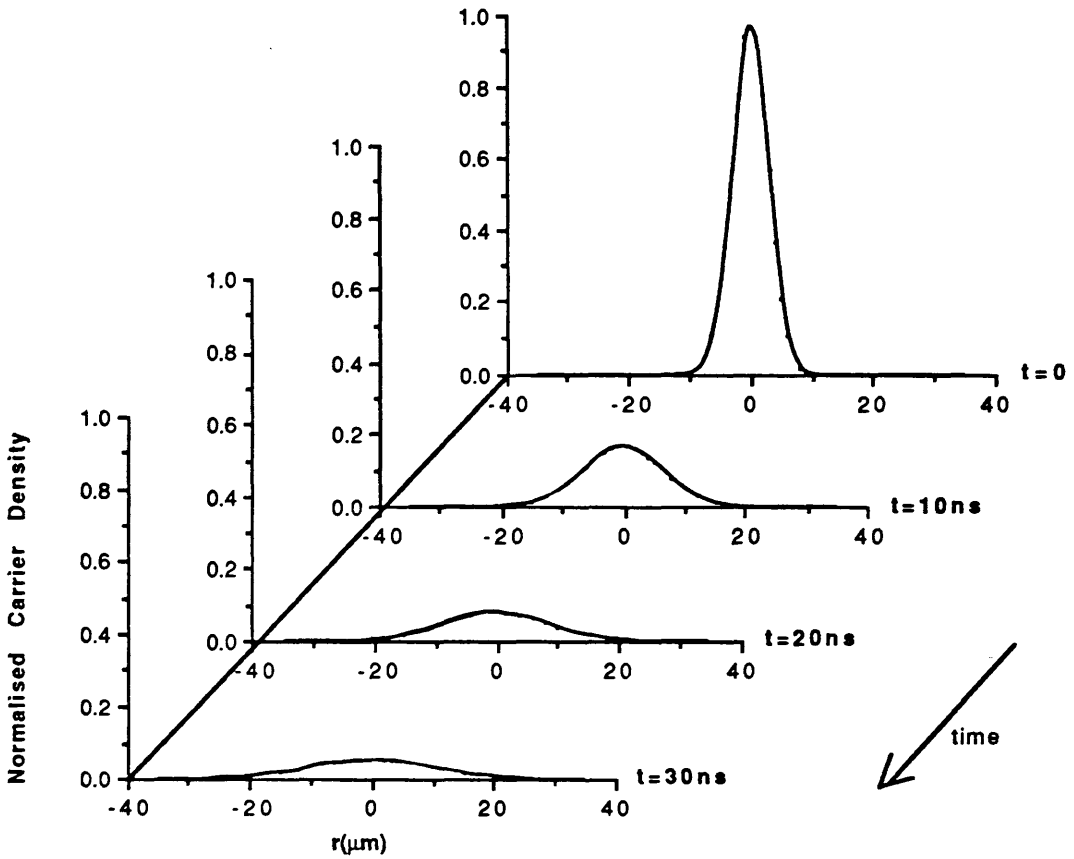
$$N(r, t) = \frac{\sigma_0^2 N_0}{4D_c t + \sigma_0^2} \exp \left[ \frac{-t}{\tau} \right] \exp \left[ \frac{-r^2}{4D_c t + \sigma_0^2} \right]. \quad (5.4.4.2)$$

This solution describes the evolution of an initial Gaussian charge distribution. The equation takes into account the effects of carrier recombination. The results from the work of these authors can be used to obtain an indication of the behaviour of carriers in a waveguide geometry.

The case is considered where a pulse propagates through a waveguide and generates a distribution of photoexcited carriers. Using equation (5.4.4.2) the carrier distribution  $N(r, t)$  can be calculated. It is assumed that the carrier distribution is circular instead of near elliptical (which is the case in the devices fabricated in this project) but this does not invalidate the following discussion. The parameters used in the calculation were  $D_c = 17 \text{ cm}^2 \text{ s}^{-1}$  [28] and  $\tau = 100 \text{ ns}$  [27]. The initial full width at half maximum was set to  $2\sigma_0 = 8 \mu\text{m}$  which is typical of the mode width. Figure 5.4.9 shows the carrier distribution as a function of time. Looking at these graphs, it can be seen that the maximum carrier density decreases to 17% of its initial value after 10ns and to 5% of its value after 30ns. Also, the effects of carrier diffusion can be seen and the FWHM is observed to increase to  $30 \mu\text{m}$  after 30ns.

If the waveguide design is altered to that of a rib geometry so that the optical mode is surrounded on three sides by a semiconductor/air interface then carrier diffusion out of the waveguide is reduced as a result of the enhanced confinement. (Most of the carrier diffusion in a stripe-loaded waveguide will occur in a lateral direction and within the guiding slab because of the potential barrier in the vertical direction between the guiding and the cladding layers. The effect of the rib is to therefore just confine the carriers laterally since vertical confinement was already present in the stripe-loaded structure.) This significantly affects the carrier population decay time. This situation is approximated by setting the diffusion constant  $D$  to zero in equation (5.4.4.2). Figure 5.4.10 shows the results for this situation. Again the parameters  $\tau = 100 \text{ ns}$  and  $2\sigma_0 = 8 \mu\text{m}$  are used. The FWHM of the carrier distribution does not change since there is no diffusion present and the sole mechanism for the population decrease is electron-hole recombination. The carrier population in this case is much longer lived and after 30ns the maximum density has reduced to only 74% compared to 5% when

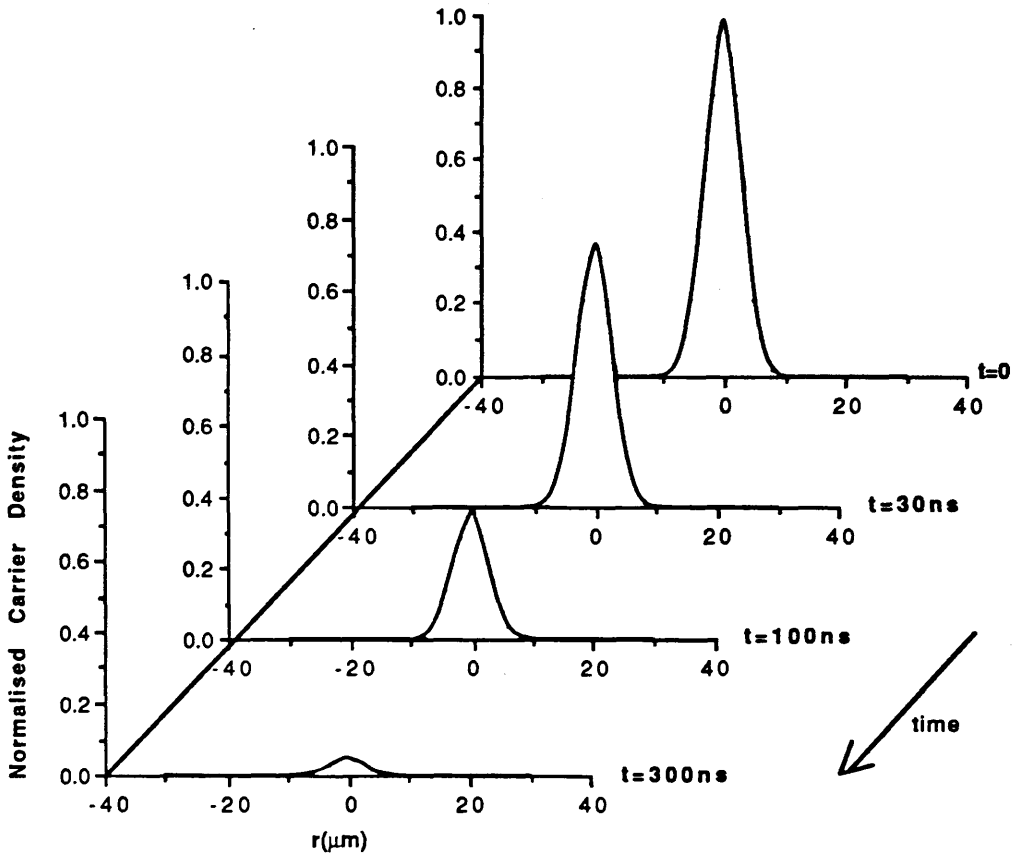
**Time variation of carrier distribution  
including effects of diffusion.**



**These graphs show the time evolution of an initial Gaussian carrier distribution. The carrier density decreases with time due to effects of carrier recombination and carrier diffusion.**

**Figure 5.4.9**

## Time variation of carrier distribution with no diffusion



These graphs show the time evolution of an initial Gaussian carrier distribution with recombination only and no carrier diffusion.

Figure 5.4.10

diffusion is present. It takes 300ns for the 5% value to be reached in this case. Note that surface recombination at the guiding layer/air interface in the latter structure has been neglected.

These considerations make it clear that because of carrier diffusion, the waveguide geometry plays an important part in determining the response time of the nonlinearity. Diffusion effects also contribute to the size of the nonlinearity. The above model represents the carrier diffusion after a single pulse has passed through the waveguide. Clearly if the pulse repetition time is shorter than the carrier decay time then the carrier population decrease will occur much more slowly. The size of the effect will thus depend on the nature of the laser source in use and, for a given average power, will be larger for a cw source than for a pulsed source.

A similar application of the diffusion equation gives the response time of thermal nonlinearities. For the thermal problem equation (5.4.4.1) is rewritten

$$D_{th} \frac{1}{r} \frac{\partial}{\partial r} \left[ r \frac{\partial T}{\partial r} \right] - \frac{\partial T}{\partial t} \quad (5.4.4.3)$$

where  $r$  is the radial distance,  $T$  is the temperature and  $D_{th}$  is the thermal diffusion constant. The solution to this is

$$T(r, t) = \frac{\sigma_0^2 T_0}{4D_{th}t + \sigma_0^2} \exp \left[ \frac{-r^2}{4D_{th}t + \sigma_0^2} \right]. \quad (5.4.4.4)$$

Putting in the value of  $D_{th}=6.77 \times 10^{-6} \text{ m}^2 \text{ s}^{-1}$  for  $\text{Al}_{0.3}\text{Ga}_{0.7}\text{As}$  [29], and using the same value of  $2\sigma_0=8\mu\text{m}$  as above, it can be calculated that it takes over 5 $\mu\text{s}$  for the temperature at the centre of the guide to decay to one tenth of its value. This means that unless the laser pulse repetition time is sufficiently greater, the thermal effect is essentially proportional to the average laser power.

One comment to make is that the diffusion times for both the electronic effects and the thermal effects can be decreased by reducing the dimensions of the waveguide. So if a waveguide of, say, 1 $\mu\text{m}$  radius is used then the temperature at the centre takes only 5ns to reach one tenth of its value. However then the size of the net electronic nonlinearity decreases because of the shorter carrier diffusion times.

In summary, the effects due to carrier diffusion make it important to consider both the waveguide geometry and the nature of the laser source when designing a device. If a large effect is desired then a waveguide geometry which restricts carrier diffusion is preferable but the penalty for this is the slow relaxation time

of the nonlinearity. Since these experiments were performed, further work has been done which confirms this conclusion<sup>[30]</sup>. In these experiments it has been asserted that the observed nonlinear transmission change is much enhanced if carrier confinement is introduced by using a rib waveguide as opposed to a stripe-loaded geometry. The samples used in this latter work had a similar MQW guiding layer to structures MV273 and MV330.

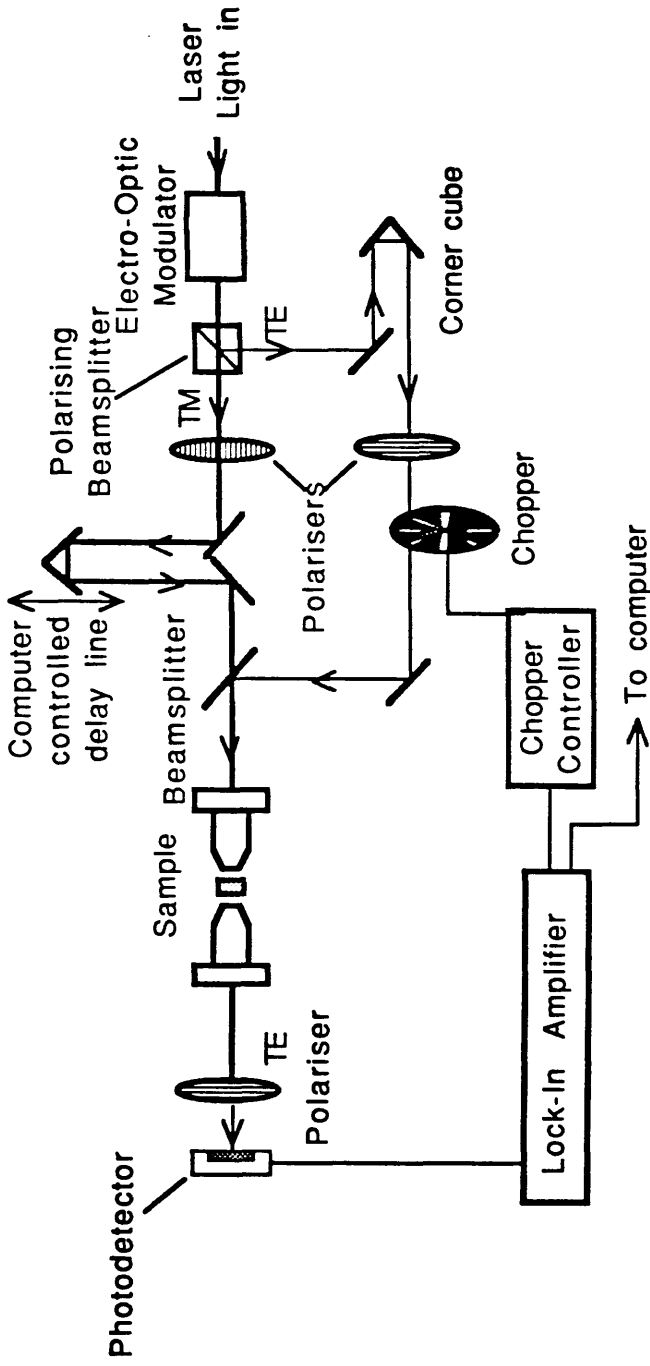
#### 5.4.5 Pump-probe experiments.

A brief mention is now made of the *pump-probe* technique for time resolved nonlinear measurements. The method uses two orthogonally polarised pulsed beams: one is the pump beam which causes the nonlinear effect and the other is the probe which measures this effect. Both these beams are incident on a nonlinear device. A variable delay is introduced in the probe beam by use of a retro-reflecting corner cube mounted on a linear translational stage. Both beams are then coupled into a device. At the device output, the probe is analysed by removing the pump beam with the use of a polariser. By adjusting the relative delay between these sets of pulses, it is therefore possible to characterise the nonlinearity to timescales as short as the pulse width. Figure 5.4.11 shows a pump-probe arrangement for the measurement of nonlinear transmission.

Measurements can be made to within timescales as short as the width of the pulses but not to times greater than the pulse repetition time. This technique has been used successfully to characterise the nonlinear response of Semiconductor-Doped-Glass waveguides<sup>[31]</sup> (see Appendix IV). In this material, the carrier relaxation time is of the order of a few picoseconds because there is a large density of surface states which act as carrier de-excitation sites. The pulse repetition time of the laser used in this project was 13ns, and because the relaxation time of carriers in AlGaAs waveguides is of the order of 10-100ns, it was not possible to time resolve carrier population induced effects in these waveguides. Attempts were made however to observe nonlinear absorption caused by the recently reported a.c. Stark effect in MQW structures<sup>[32]</sup>. The a.c. Stark effect is a resonant nonlinear effect but it does not arise from the creation of free carriers. Instead, it is due to the perturbation of excitonic states by a below-bandgap excitation and is akin to the nonresonant Kerr effect.

Sample MV273 was investigated. Pump-probe experiments were performed using peak pump intensities of about  $10^{11}$  Watts/m<sup>2</sup> coupled into the device with the probe intensity some 150 times smaller. The pulse width was 3ps. The experiments were performed using both possible polarisation configurations of the

## Pump-probe experimental layout.



The schematic shows the experimental layout for a pump-probe experiment. In this configuration, the TM beam serves as the pump and the TE beam is the probe. These can be reciprocated by adjusting the electro-optic modulator bias voltage and rotating the polariser at the output of the device.

Figure 5.4.11

pump and probe i.e. TE pump with TM probe as well as TM pump with TE probe. These measurements were performed for wavelengths ranging from 830nm to 840nm (the heavy-hole exciton is at 837nm in this sample). No change in transmission was seen as the pump-probe delay was varied.

Von Lehmen et al<sup>[32]</sup> have observed the a.c. Stark effect with peak pump intensities of  $10^8$ – $10^{10}$  Watts/m<sup>2</sup>. This is an order of magnitude less than that achieved in the above experiment but even so no fast nonlinear effect was observed here. The conditions for this experiment are however somewhat different from those of Von Lehmen et al because the results of these authors were obtained with both the pump and probe beams incident perpendicularly to the layers. The optical field vectors, therefore, of both beams are parallel to the MQW layers. In the above case however, only one of either the pump or the probe beams is polarised in this direction with the other polarised perpendicularly. The lack of any observed effect may possibly be due to the dichroic nature of the excitonic system with the pump and probe beams effectively interacting with two orthogonal nonlinear systems which are essentially uncoupled. This is certainly true if the dominant contribution to the nonlinearity is from the heavy-hole exciton since this will not directly interact with TM polarised light.

A repetition of the experiment was attempted with the two beams similarly polarised. The probe beam was chopped and lock-in detection was used to decouple this from the pump. This was difficult because separation of the probe from the pump could only be achieved with the probe/pump power ratio less than 1/10. This ratio is insufficient to discriminate between the linear and nonlinear regimes<sup>[31]</sup>.

The a.c. Stark effect certainly requires further investigation especially with regard to the dichroism of MQW structures: a property which is only accessible in waveguides. One possible scheme may be to pump the MQW waveguide with a TM polarised pulse with a much higher intensity than that obtained with the Styryl 9 laser here. Although the TM beam does not directly interact with the heavy-hole exciton, if it is intense enough, it will perturb the finite potential well seen by the electrons and holes within the layers. Therefore an indirect shift of the excitonic energy levels is induced as described by the quantum confined Stark effect<sup>[33]</sup>. One may naively think that the net effect is zero over many optical cycles but this is not so. Regardless of the sign of the field, the net effect is always that of a redshift and so the effect is like that caused by a rectified optical frequency a.c. field. The fields required for the quantum confined Stark shift are not available with the Styryl 9 laser used in the above experiments but may be achievable with higher power laser sources.

#### 5.4.6 Summary of nonlinear measurements.

Three main experiments were performed to observe nonlinear effects in AlGaAs waveguides. The first of these was an attempt to measure the Kerr coefficient of AlGaAs by observing self phase modulation. The results of this indicate that the nonresonant Kerr coefficient is at least an order of magnitude smaller than that reported in the recent literature. The second experiment set out to directly observe the nonlinear index change using an interferometric technique. A measurement of  $n_2$  was obtained but this was mainly due to a thermal index change. Finally, the nonlinear absorption was measured and it was seen from these results that thermal effects were dominant. It was only in one sample (MV273) that these thermal effects were overcome by the negative electronic nonlinearity when the photon energy was close to that of the exciton. It was discussed why electronic effects were weak in these samples and it was concluded after making considerations regarding diffusion effects that this was due to a combination of the nature of the laser source and of the waveguide geometry.

#### 5.5 Conclusions.

The results of the nonlinear investigations indicated that the waveguide geometry and the nature of the laser source all affect the size of the observed nonlinear effect.

Improvements are required before successful nonlinear device operation can be demonstrated. The waveguide geometry can be modified to that of a rib guide where the optical mode is tightly confined within the rib. In this case, the rib would confine carriers thus integrating and therefore increasing the electronic nonlinear contribution. It is also desirable to reduce the competing thermal contribution. One way to do this is to use a pulsed diode laser driven at a sufficiently low repetition rate (as was done by Li-Kam-Wa et al[25]). This will give time for the thermal effects to relax before the next pulse arrives and the thermal contribution is thus not integrated over many pulses. This system however does not provide the tunability and versatility which was considered necessary for the characterisation of different samples. Another alternative is to use a laser in cavity dumped operation with pulse repetition times of the order of a microsecond. Also, because pulse energies are larger, the number of free carriers generated per pulse is larger and this will therefore allow electronic effects to be more dominant. In fact it is using such a cavity dumped laser that the authors Jin et al[34] observed switching in their strip-loaded nonlinear directional couplers.

Unfortunately, access to such a cavity dumped laser was not available until at a very late stage in the project, and because of time limitations, it was not possible to perform extensive characterisation of the above samples using this source.

## 5.6 References to Chapter Five.

- [1] G. H. C. New, "The generation of ultrashort laser pulses", Rep. Prog. Phys., vol 46, pp877–971, 1983.
- [2] A. Yariv, "Optical Electronics", Holt, Rinehart and Winston, 3rd Edition, 1985.
- [3] K. L. Sala, G. A. Kenney–Wallace, G. E. Hall, "CW Autocorrelation Measurements of Picosecond Laser Pulses", IEEE J. Quant. Elec., vol QE–16, no 9, pp990–996, 1980.
- [4] K. Smith, W. Sibbet, J. R. Taylor, "Subpicosecond generation via Hybrid Mode–locking of Styryl 9 in the near infra–red", Opt. Comm., vol49, no 5, 1984.
- [5] N. Langford, K. Smith, W. Sibbet, J. R. Taylor, "The hybrid mode–locking of a cw rhodamine 700 dye laser", Opt. Comm., vol 58, no 1, pp56–58, 1986.
- [6] K. Kato, "High–efficiency high power second–harmonic generation at 5321 Å in Meta–Nitroaniline", IEEE J. Quant. Elec., vol QE–16, no 12, pp1288–1290, 1980.
- [7] B. L. Davydov, L. G. Koreneva, E. A. Lavrovskiy, "An efficient frequency doubler of Neodymium laser radiation employing a molecular crystal of metanitroaniline", Rad. Eng. Elec. Phys., vol 19, pp130–131, 1974.
- [8] T. Tamir (Ed), "Integrated Optics", Topics in Applied Physics, vol 7, Springer–Verlag, 1975.
- [9] G. J. Sonek, J. M. Ballantyne, Y. J. Chen, G. M. Carter, S. W. Brown, E. S. Koteles, J. P. Salerno, "Dielectric properties of GaAs/AlGaAs Multiple Quantum Well Waveguides", IEEE J. Quant. Elec., vol QE–22 no 7, pp1015–1018, 1986.

- [10] M. J. Robertson, S. Ritchie, P. Dayan, "Semiconductor waveguide analysis of coupling between rib waveguides and fibres", SPIE vol 578, Integrated optical circuit engineering II, pp184-191, 1985.
- [11] M. Born, E. Wolf, "Principles of Optics", Pergammon, New York, 1959.
- [12] J. I. Pankove, "Optical Processes in Semiconductors", Prentice-Hall Electrical Engineering Series, 1971.
- [13] R. Regener, W. Sohler, "Loss in low-finesse  $\text{Ti:LiNbO}_3$  optical waveguide resonators", Appl. Phys. B, vol 36, pp143-147, 1985.
- [14] P. Li-Kam-Wa, P. N. Robson, J. P. R. David, G. Hill, P. Mistry, M. A. Pate, J. S. Roberts, "All-Optical Switching Effects in a passive GaAs/GaAlAs Multiple-Quantum-Well Waveguide Resonator", Elec. Lett., vol 22, no 21, 1986.
- [15] E. Kapon, R. Bhat, "Low-loss single-mode GaAs/AlGaAs optical waveguides grown by organometallic vapour phase epitaxy", Appl. Phys. Lett., vol 50, no 23, pp1628-1630, 1987.
- [16] R. G. Hunsperger, "Integrated Optics: Theory and Technology", Springer-Verlag, 1982.
- [17] D. S. Chemla, D. A. B. Miller, P. W. Smith, A. C. Gossard, W. Weigmann, "Room Temperature Excitonic Nonlinear Absorption and Refraction in GaAs/AlGaAs Multiple Quantum Well Structures", IEEE J. Quant. Elec., vol QE-20, no 3, 1984.
- [18] M. Whitehead, G. Parry, J. S. Roberts, P. Mistry, P. Li Kam Wa, J. P. R. David, "Quantum confined Stark shifts in MOVPE-grown GaAs-AlGaAs Multiple Quantum Wells", Elec. Lett., vol 23, no 20, pp1048-1049, 1987.
- [19] J. S. Weiner, D. S. Chemla, D. A. B. Miller, H. A. Haus, A. C. Gossard, W. Weigmann, C. A. Burrus, "Highly Anisotropic optical properties of single quantum well waveguides", Appl. Phys. Lett. vol 47, no 7, 1985.
- [20] J. J. Wynne, "Optical Third-Order Mixing in GaAs, Ge, Si and InAs", Phys. Rev. vol 178, no 3, pp1295-1303, 1969.

- [21] R. H. Stolen, C. Lin, "Self Phase modulation in Silica Fibres", Phys. Rev. A., vol 17, no 4, pp1448-1453, 1978.
- [22] D. E. Aspnes, S. M. Kelso, R. A. Logan, R. Bhat, "Optical properties of  $\text{Al}_x\text{Ga}_{1-x}\text{As}$ ", J. Appl. Phys., vol 60, no 2, pp754-766, 1986.
- [23] M. C. Gabriel, H. A. Haus, E. P. Ippen, "Thermal Index Changes by Optical Absorption in Group III-V Semiconductor Waveguides", J. Lightwave. Tech., vol LT-4, no 10, 1986.
- [24] Y. J. Chen, G. M. Carter, "Measurement of Third Order Nonlinear Susceptibilities by surface plasmons", Appl. Phys. Letts., vol 41, no4, 1982.
- [25] P. Li-Kam-Wa, J. H. Marsh, P. N. Robson, J. S. Roberts, N. J. Mason, "Nonlinear propagation in GaAs/GaAlAs MQW waveguides", SPIE proc., vol 578, pp110-115, 1985.
- [26] D. Cotter, C. N. Ironside, B. J. Ainslie, H. P. Girdlestone, "Picosecond pump-probe interferometric measurement of optical nonlinearity in semiconductor-doped fibres", Opt. Lett., vol 14, no 6, pp317-319, 1989.
- [27] H. Lee, A. Kost, M. Kawase, A. Hariz, P. D. Dapkus, E. M. Garmire, "Nonlinear Absorption Properties of AlGaAs/GaAs Multiple Wells Grown by Metalorganic Chemical Vapour Deposition", IEEE J. Quant. Elec., vol 24, no 8, pp1581-1592, 1988.
- [28] A. Olsson, D. J. Erskine, Z. Y. Xu, A. Schremer, C. L. Tang, "Nonlinear luminescence and time-resolved diffusion profiles of photoexcited carriers in semiconductors", Appl. Phys. Lett., vol 41, no 7, pp659-661, 1982.
- [29] S. Adachi, "GaAs, AlAs and  $\text{Al}_x\text{Ga}_{1-x}\text{As}$ : Material parameters for use in research and device applications", J. Appl. Phys., vol 58, no 3, 1985.
- [30] M. O'Neill, K. Al Hemyara, University of Glasgow, private communication.
- [31] C. N. Ironside, T. J. Cullen, B. S. Bhumbra, J. Bell, W. C. Banyai, N. Finlayson, C. T. Seaton, G. I. Stegeman, "Nonlinear-optical effects in ion-exchanged semiconductor doped glass waveguides.", J. Opt. Soc. Am., vol 5, no 2, pp492-495, 1988.

[32] A. Von Lehmen, D. S. Chemla, J. E. Zucker, J. P. Heritage, "Optical Stark effect on excitons in GaAs quantum wells", *Opt. Lett.*, vol 11, no 10, pp 609-611, 1986.

[33] D. A. B. Miller, D. S. Chemla, T. C. Damen, A. C. Gossard, W. Weigmann, T. H. Wood, C. A. Burrus, "Band-edge Electroabsorption in Quantum Well Structures: The Quantum-Confined Stark Effect", *Phys. Rev. Lett.*, vol 53, no 22, pp2173-2176, 1984.

[34] R. Jin, C. L. Chuang, H. M. Gibbs, S. W. Koch, J. N. Polky, G. A. Pubanz, "Picosecond all-optical switching in single mode GaAs/AlGaAs strip-loaded nonlinear directional couplers", *Appl. Phys. Lett.*, vol 53, no 19, pp1791-1793, 1988.

## CHAPTER SIX

### THE ASYMMETRIC MACH– ZEHNDER INTERFEROMETER.

#### 6.1 Introduction

This chapter describes the design and characterisation of the integrated optical Asymmetric Mach– Zehnder interferometer. This nonlinear switching device comprises of waveguide elements which split up and recombine an optical beam. Switching action results in these devices when the relative phase of the two split beams is altered. When the beams are recombined, and depending on their relative phases, energy is either coupled into the output waveguide or radiated into the surrounding substrate: the situation being akin to that of constructive and destructive interference. Operation of the Asymmetric Mach– Zehnder is discussed in section 6.2 where the response of an ideal, lossless device is calculated using a simple scattering matrix model. The more sophisticated Beam Propagation Method (BPM) is then detailed in section 6.3 which gives a more realistic indication of device behaviour. Section 6.4 describes the fabrication and testing of actual devices and the results are compared with those of the theoretical models. Finally in section 6.5, the investigations into the thermal behaviour of the device are reported.

#### 6.2 The Asymmetric Mach– Zehnder Interferometer: a simple model.

The Asymmetric Mach Zehnder interferometer is particularly suited for performing all– optical logic operations. The device is illustrated in figure 6.2.1. The power from the input waveguide is split into two unequal parts by means of an asymmetric Y– junction. Because of this power imbalance, a nonlinear phase shift occurs between the the two arms of the device and thus a power dependant transmission function is obtained. The switching conditions of the device depend on the size of the nonlinearity and the splitting ratio of the asymmetric Y– junction.

An intensity dependant interferometer can alternatively be implemented by having different path lengths in each of the arms (as proposed by Kawaguchi<sup>[1]</sup>) where the accumulated phase shifts in each of the arms would differ even if the power split symmetrically. However the device is not suited for use with ultrashort pulses because of the difference in path lengths between the two arms, which means that the pulses would fail to overlap at the output Y– junction.

The AMZI is initially modelled using a scattering matrix model. The scattering

# The Asymmetric Mach-Zehnder Interferometer

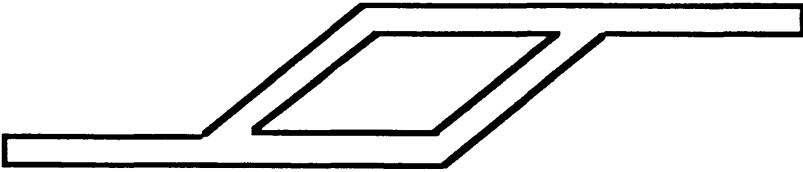


Figure 6.2.1

# Asymmetric Y-junction

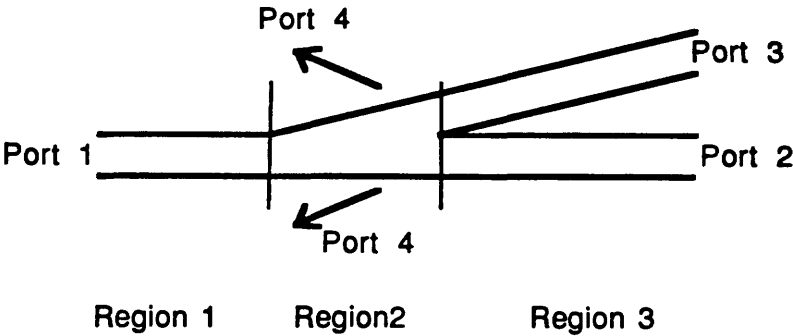


Figure 6.2.2

matrix formalism is now introduced and applied to asymmetric Y-junctions.

### 6.2.1 The Y-junction.

A Y-junction can be considered as consisting of three sections as shown in figure 6.2.2. The first of these is a straight waveguide, the second is a taper region and the third comprises of the two separating branch waveguides.

The Y-junction is a power splitting and recombining device. When a mode is launched into the single waveguide, the modal field undergoes a smooth transition through the taper region and transforms into the respective modes of the two branch waveguides. The device is reciprocal. If the same two modes were propagated back towards the Y-junction with the same relative phase and amplitude, then they would recombine to form the original mode. It is important that the angle of the Y-junction is not too large otherwise large transition losses will occur at each of the two boundaries of the three regions as well as radiation from the taper section. In the derivation of the scattering matrix model it is assumed that the angle is small enough to make these losses negligible. The power splitting ratio between the branch waveguides obviously depends on the geometry of the device: the larger the asymmetry the larger the splitting ratio. This ratio will be calculated in section 6.3 using the Beam Propagation Method.

The characteristics of the Y-junction can be discussed using the following approach where the Y-junction is considered as a four-port device. Three of these ports consist of the three waveguides and the fourth port represents power coupled into radiation modes. The amplitudes of the waves incoming towards the Y-junction can be represented by a matrix with elements  $a_i$  ( $i=1,2,3,4$ ) and those of the outgoing waves by  $b_i$  where each  $i$  denotes a port of the Y-junction as shown in figure 6.2.2. The response of the Y-junction can be described in terms of a scattering matrix  $S$  where

$$\mathbf{b} = \mathbf{S} \mathbf{a}. \quad (6.2.1.1)$$

The scattering matrix can be quite easily derived for an ideal Y-junction by consideration of some of its basic properties. Firstly, the power splitting ratio is defined so that  $b_2 = a_1 \sqrt{1 - \delta}$  and  $b_3 = a_1 \sqrt{\delta}$ . The following relation is therefore obtained:

$$S \begin{bmatrix} 1 \\ 0 \\ 0 \\ 0 \end{bmatrix} = \begin{bmatrix} 0 \\ \sqrt{1-\delta} \\ \sqrt{\delta} \\ 0 \end{bmatrix}$$

From this it can be determined

$$S_{11} = 0$$

$$S_{21} = S_{12} = \pm\sqrt{1-\delta}$$

$$S_{31} = S_{13} = \pm\sqrt{\delta}$$

Secondly, it is assumed that there is no coupling between forward and backward travelling waves, i.e. there are no reflections. This is valid if the angle is small and this leads to

$$S_{22} = S_{33} = 0$$

Finally, the remaining elements are determined by conservation of energy where it is assumed that the total power leaving the Y-junction is equal to that entering it. Therefore

$$S_{14} = S_{41} = S_{44} = 0$$

$$S_{42} = S_{24} = \pm\sqrt{\delta}$$

$$S_{43} = S_{34} = \pm\sqrt{1-\delta}$$

The correct signs for the square root terms are chosen by using the unitary and symmetry properties of the matrix<sup>[2]</sup>. The scattering matrix for the Y-junction can therefore be written as

$$S = \begin{bmatrix} 0 & \sqrt{1-\delta} & \sqrt{\delta} & 0 \\ \sqrt{1-\delta} & 0 & 0 & -\sqrt{\delta} \\ \sqrt{\delta} & 0 & 0 & \sqrt{1-\delta} \\ 0 & -\sqrt{\delta} & \sqrt{1-\delta} & 0 \end{bmatrix} \quad (6.2.1.2)$$

From this scattering matrix an important observation can be made regarding Y-junctions. If a wave is travelling towards the Y-junction through only one of the branches, then a fraction of the power will always be radiated into the substrate. Namely if a signal is incident on port 2, then only a fraction  $(1-\delta)$  of this leaves port 1. Similarly, for a signal entering port 3 only  $\delta$  of this leaves port 1. The

physical explanation for this is that a wave entering the taper region from one of the branch waveguides excites both the fundamental and the 1st antisymmetric mode in the taper. However, as the modes propagate towards the narrower end of the taper, the condition occurs where the width of the tapered section is such that the first order asymmetric mode is below cut-off and is radiated into the substrate (port 4). For the particular case of a symmetrical structure, where  $\delta = (1 - \delta) = 1/2$ , equal energies are imparted to the two modes and therefore a signal entering any single port 2 or 3 undergoes a 3dB attenuation on leaving port 1. For asymmetric structures, a corresponding but unequal energy distribution is obtained between the two modes.

The above scattering matrix can now be used to characterise the response of the AMZI.

### 6.2.2 The Scattering Matrix model.

To apply the scattering matrix, the AMZI is considered as two Y-junctions placed back-to-back as shown in figure 6.2.3. Absorption losses have not been taken into account in this initial analysis and the bending losses in each of the arms are also assumed to be zero. It is therefore possible to obtain the response function of the AMZI by two applications of the scattering matrix.

Initially a wave of unit amplitude is considered incident on port 1. i.e.

$$a_1 = \begin{bmatrix} 1 \\ 0 \\ 0 \\ 0 \end{bmatrix}$$

Application of the scattering matrix yields

$$b_1 = \begin{bmatrix} 0 \\ \sqrt{(1-\delta)} \\ \sqrt{\delta} \\ 0 \end{bmatrix}$$

Before applying the scattering matrix a second time, a relative phase change  $\exp(i\varphi)$  is introduced in one of the arms. Note also that the elements  $b_2$  and  $b_1$  have to be interchanged to maintain the correct definitions of the ports. The scattering matrix is therefore applied to

**The Asymmetric Mach-Zehnder Interferometer  
decomposed into two Y-junctions for  
the Scattering Matrix analysis**

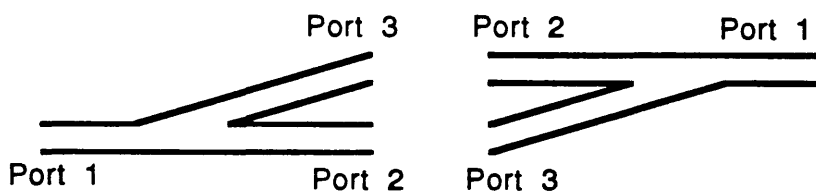


**Figure 6.2.3**

$$\mathbf{a}_2 = \begin{bmatrix} 0 \\ \sqrt{\delta} e^{i\varphi} \\ \sqrt{1-\delta} \\ 0 \end{bmatrix}$$

and this gives

$$\mathbf{S} \mathbf{a}_2 = \mathbf{b}_2 = \begin{bmatrix} \sqrt{(\delta(1-\delta))} (1+e^{i\varphi}) \\ 0 \\ 0 \\ 1 - \delta(1+e^{i\varphi}) \end{bmatrix}$$

The power transmission of the AMZI,  $P_{\text{out}}$ , is the power leaving port 1 and is given by

$$\frac{P_{\text{out}}}{P_{\text{in}}} = 4 \delta(1-\delta) \cos^2 \left[ \frac{\varphi}{2} \right]$$

where  $P_{\text{in}}$  is the input power.

In the AMZI, the phase change is induced by an optical nonlinearity. The differential change in optical path length due to such an effect is

$$\Delta(nl) = \frac{n_2 P_{\text{in}} l (1-2\delta)}{A_{\text{eff}}}$$

where  $n_2$  is the nonlinear coefficient,  $l$  is the length of the interferometer arms and  $A_{\text{eff}}$  is the effective waveguide cross sectional area. The differential phase change between the two arms is given by  $\varphi = (2\pi/\lambda)\Delta(nl)$ . The power output of an ideal, lossless AMZI is thus

$$P_{\text{out}} = 4 P_{\text{in}} \delta(1-\delta) \cos^2 \left[ \frac{\pi n_2 P_{\text{in}} l (1-2\delta)}{A_{\text{eff}} \lambda} \right]$$

This response is plotted in figure 6.2.4 for varying power splitting ratios  $(1-\delta):\delta$  using the values  $n_2 = 10^{-11} \text{ m}^2/\text{W}$ ,  $l = 2\text{mm}$ ,  $\lambda = 830\text{nm}$  and  $A_{\text{eff}} = 10\mu\text{m}^2$ . It can be seen that the output power varies more rapidly for the larger splitting ratios and therefore switching occurs for lower powers. However the largest transmission maxima are obtained for the smaller splitting ratios. The choice of splitting ratio is therefore a compromise between low switching powers or high device transmission.

The scattering matrix model gives a somewhat qualitative indication of the

# Output response of lossless Asymmetric Mach Zehnder Interferometers for various splitting ratios

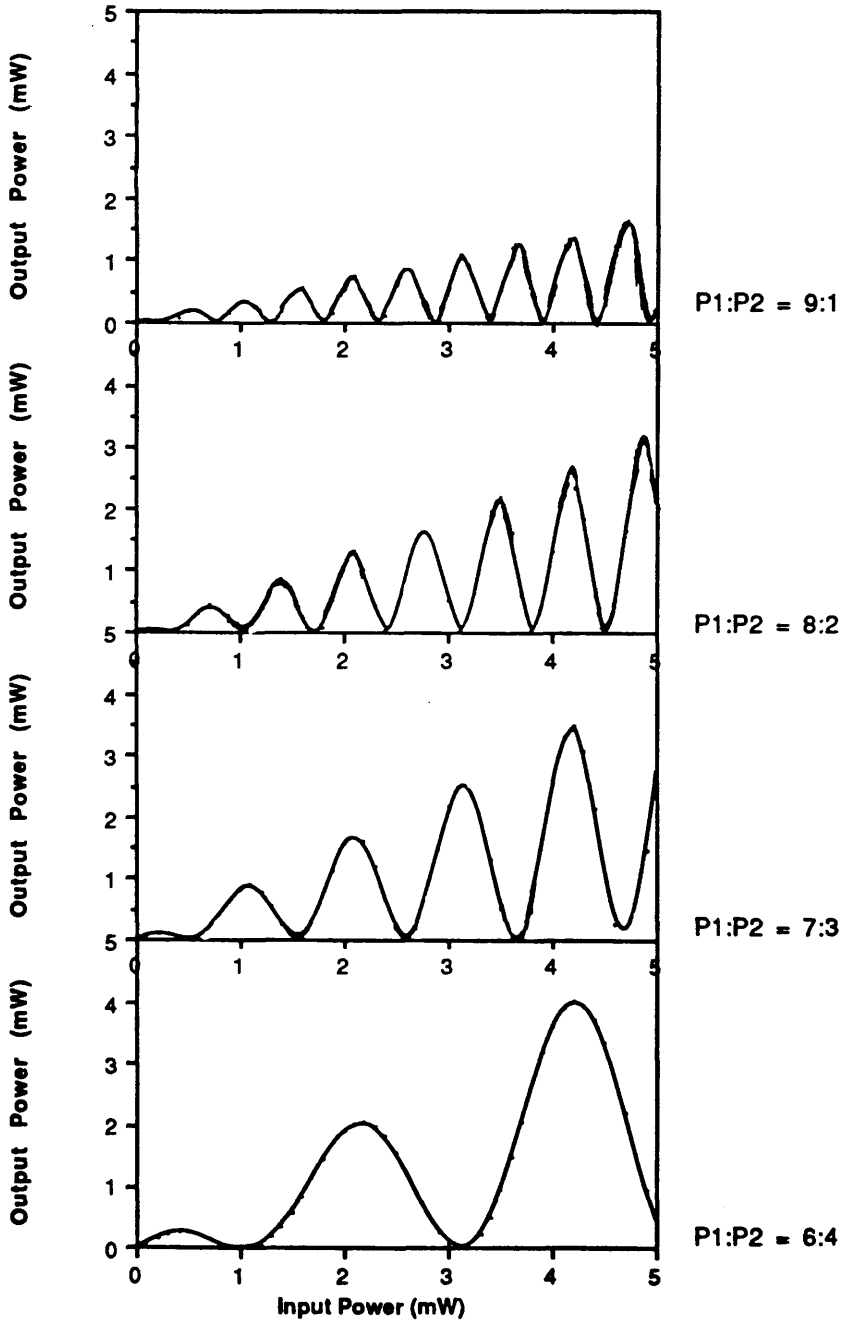


Figure 6.2.4

operating principles of the AMZI but because of the idealisations made about the Y-junctions, it does not give sufficiently good representation of a realistic device. One important property of Y-junctions which has not been included in this scattering matrix approach is the coupling of modes which exists between the two branch waveguides close to the Y-junction. This coupling has to be included for a realistic model. Also, a method for calculating the power splitting ratio of the Y-junction is required. The device behaviour is critically dependent on the splitting ratio as this is an important factor in determining the switching powers.

### 6.3. The BPM model.

Some of the limitations of the scattering matrix model can be rectified by the use of the Beam Propagation Method (BPM). This is a technique which effectively solves the scalar wave equation and calculates the modal field step by step as it propagates along the structure. The detailed mechanics of the BPM have been much documented elsewhere<sup>[3,4]</sup> and its operation will be described here only briefly.

The method is based on a Fourier optics technique. The refractive index variation through a cross section of the device is considered to be a homogeneous index  $n_0$  with a perturbation  $n(x)$  which defines the waveguide. Essentially, the field at a section of the device is Fourier transformed and is then propagated in the spectral domain while assuming that the optical medium is homogeneous with refractive index  $n_0$ . This is then inverse Fourier transformed and the refractive index perturbation,  $n(x)$ , is applied in terms of a phase correction term to the field. In effect, each cross section of the waveguide has been considered as a thin lens.

In the derivation of the phase correction term as used in the program, certain approximations were made<sup>[3]</sup>. It was assumed that the waves are near-paraxial which means that only waves travelling parallel to the waveguide axis have a well approximated phase factor. It was also assumed, for computational convenience, that the refractive index variation in the x direction,  $\text{grad}(n)$ , is small. Because of this, the BPM cannot directly model step index waveguides without a significant increase in the computation time. Also, this version of the BPM only models forward propagating waves and does not calculate any reflected fields. Therefore only structures which are smoothly varying in the direction of propagation, and have no backward travelling fields, can be accurately modelled. For example, the BPM is incapable of modelling grating structures.

Nonlinear effects are implemented in the BPM model by calculating the

intensity induced refractive index change across the waveguide profile at each propagation step. From this, a new refractive index profile for the waveguide is obtained and this is then used to calculate the field distribution for the next propagation step.

The version of the nonlinear BPM program used in this project was developed by Dr T. J. Cullen in this department.

### 6.3.1 Application of the BPM.

The BPM program can, in principle, be used to solve for propagation in a three dimensional structure but this requires a large amount of computation time. A two dimensional version used in conjunction with the effective index method was therefore used.

Because of the reasons described above regarding the derivation of relations used in the BPM, a step index waveguide cannot be used without a significant increase in the computation time. Instead, a " $1/(\cosh)^2$ " index profile was used to define the waveguide as given by

$$n^2(x) = n_c^2 + \frac{2n_c \Delta n}{\cosh^2(2x/h)} \quad (6.3.1.1)$$

Here  $\Delta n$  is the maximum core/cladding index difference,  $n_c$  is the asymptotic cladding index and  $h$  is defined as the guide width. A value for  $h$  has to be found such that this waveguide is equivalent in terms of confinement to a step index waveguide of a given specification. Before doing this, some basic definitions are reviewed.

The confinement parameter, (or normalised thickness),  $V$ , in the waveguide described above is given by [5]

$$V = kh \sqrt{2n_s \Delta n} \quad (6.3.1.2)$$

for  $\Delta n/n_s \ll 1$ , where  $k$  is  $2\pi/\lambda$ . This is related to the cut-off thickness of mode of order  $s$  ( $=0,1..$ ) by

$$V_{\text{cutoff}} = 2s^2 + 1 \quad (6.3.1.3)$$

Note that this is different to the three layer symmetric slab waveguide where the relation between the  $n$ th order mode ( $n=0,1..$ ) cut-off to  $V$  is given by

$$V_{\text{cutoff}} = n\pi \quad (6.3.1.4)$$

However, the definition of  $V$  is the same as (6.3.1.2) in this case.

Using these relations, an equivalent " $1/\cosh^2$ " waveguide was obtained in terms of the  $V$  parameter. This is done by calculating  $V$  in the slab structure and the value of  $V_{\text{cutoff}}$  for the second mode ( $n=1$ ). The margin from cut-off is calculated using

$$\delta V = \frac{V_{\text{cutoff}} - V}{V_{\text{cutoff}}} \quad (6.3.1.5)$$

The values of  $n_s=3.47$  and  $\Delta n=10^{-3}$  are taken as obtained from an application of the effective index method to the typical AlGaAs double heterostructure. The waveguide thickness is  $4\mu\text{m}$  and  $\lambda=827\text{nm}$ . Putting this into (6.3.1.2) gives  $V=2.54$ . The waveguide is single mode and putting  $V_{\text{cutoff}}=\pi$  into (6.3.1.5) gives  $\delta V=0.191$  which represents how close the waveguide is to being double moded. (The waveguide becomes double moded at  $\delta V=0$ .) If now equation (6.3.1.3) is used for the cut-off in the " $1/\cosh^2$ " waveguide, and this is put into (6.3.1.5), then, keeping  $\delta V$  unchanged, an equivalent guide thickness of  $h=3.71\mu\text{m}$  is calculated for this index profile.

The data used in the BPM investigations to define the equivalent single mode waveguides was  $h=3.71\mu\text{m}$ ,  $n_c=3.47$ ,  $\Delta n=10^{-3}$  and  $\lambda=827\text{nm}$ . A propagation step size of  $20\mu\text{m}$  was used throughout. Having done this, the program was used to calculate the field propagation in the device.

The transmission of the device or waveguide is calculated by performing an overlap integral of the input and output field distributions. It is therefore essential that the input field is a true guided mode of the waveguide otherwise unwanted radiation modes will also be propagated. If these were present at the output then the overlap integral would not yield the true modal transmission. Hence the correct input field distribution for the waveguide has to be determined. This is done by initially propagating a "guessed" distribution into a straight section of waveguide and then analysing the waveguide output. More specifically, the output mode spectrum was determined by looking at the field variation in the direction of propagation (i.e. the axial field). This can be understood by considering the following: If there is only a single guided mode present and, assuming no radiation modes, the the axial field varies as  $\cos(\beta z)$  where  $\beta$  is the propagation constant. Then in this case the axial field contains only a single frequency and will be characterised in the frequency domain by a single peak. For a multimode

waveguide, the higher order modes will manifest themselves as distinct peaks in the spatial frequency domain. The positions of these peaks depend on the propagation constants of the respective modes. The higher order guided modes have an effective index lower than that of the fundamental mode. Radiation modes however will form a continuum and the dominant contribution from these will tend to have an effective index higher than that of the fundamental mode. This is because the dominant contribution will be from the rays propagating nearly parallel to the waveguide since the rays which have angles larger than that of the fundamental mode have leaked out. Therefore if a random input field is launched into a multimoded waveguide the spectrum of the waveguide content will consist of a series of peaks all to one side of the peak corresponding to the fundamental mode, and a continuum of radiation modes lying mostly on the other side of this fundamental peak. It is thus possible to assess the modal content of the propagating field distribution.

The results of this axial spectrum analysis can be applied using a filtering technique to obtain a more accurate field profile<sup>[3]</sup> for any of the guided modes. This procedure of propagating a field, analysing the axial spectrum and then filtering to generate a better approximation of the mode profile has to be repeated several times before a sufficiently narrow peak is obtained in the axial spectrum.

BPM results for propagation in a straight waveguide are now shown to illustrate some waveguide properties.

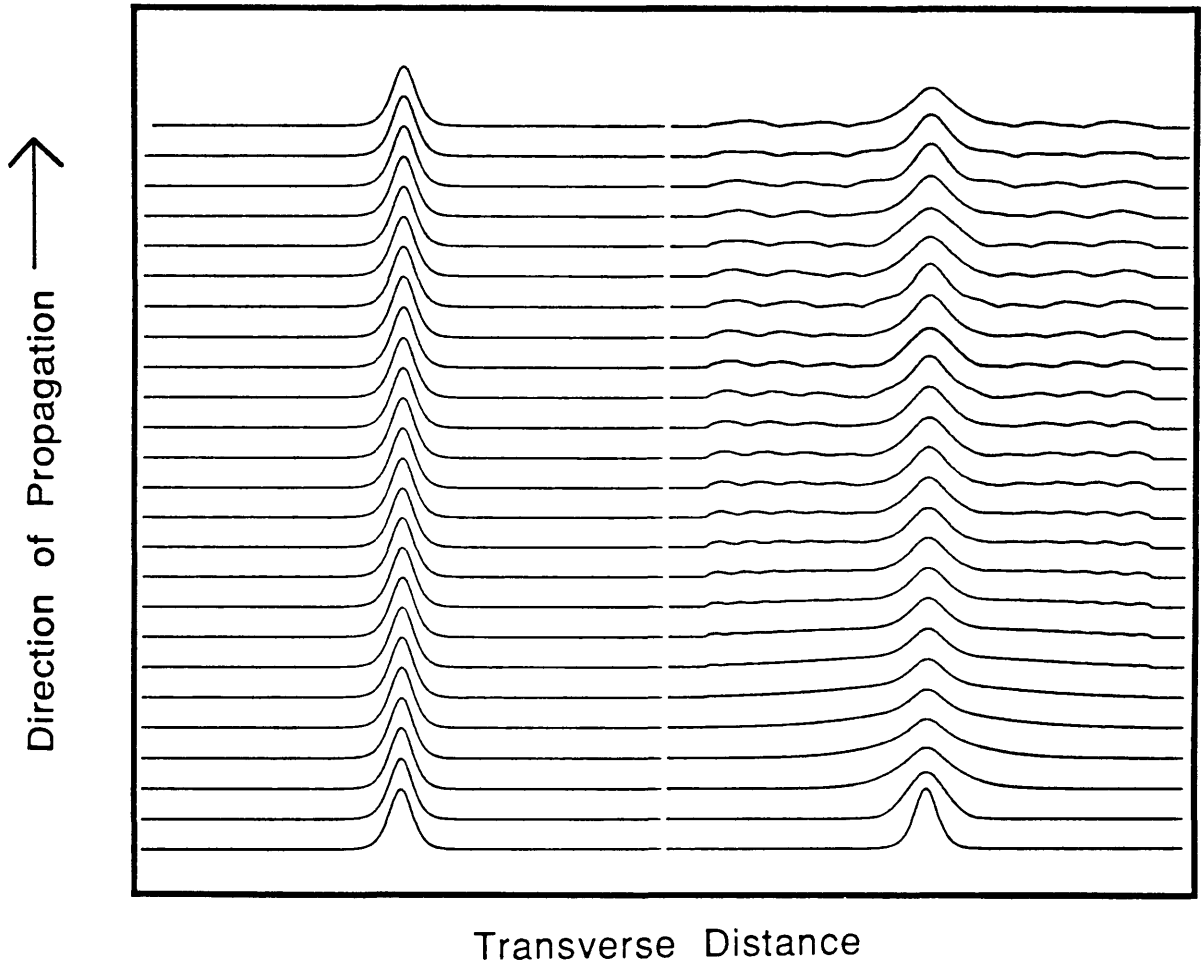
Figure 6.3.1 shows the result of an initial BPM calculation where the input field has a Gaussian profile. The picture on the left shows the refractive index profile across different cross sections of the structure which, in this case, is a straight waveguide. The picture on the right shows the intensity profiles across these same sections. The bottom of each picture is the device input. As can be seen in this figure, the input field is not a pure guided mode of the waveguide. This is apparent from the observed radiation of optical power away from the waveguide.

An interesting and important feature to note is the presence of the "absorber" zones. These have to be introduced because the periodic nature of the Fourier transform means that any field which is radiating out from a side of the window will be seen to re-enter from the opposite side. To prevent this effect from occurring, and hence confusing the results, artificial absorber zones have been included by introducing a complex refractive index at the left and the right hand boundaries of the region. These attenuate any radiation incident on the boundary. The effect of the absorbers is apparent in the right hand picture in figure 6.3.1.

A double moded waveguide is shown in figure 6.3.2. The input field has been laterally offset from the waveguide centre so that both guided modes are excited.

Refractive Index  
Profiles

Intensity  
Profiles

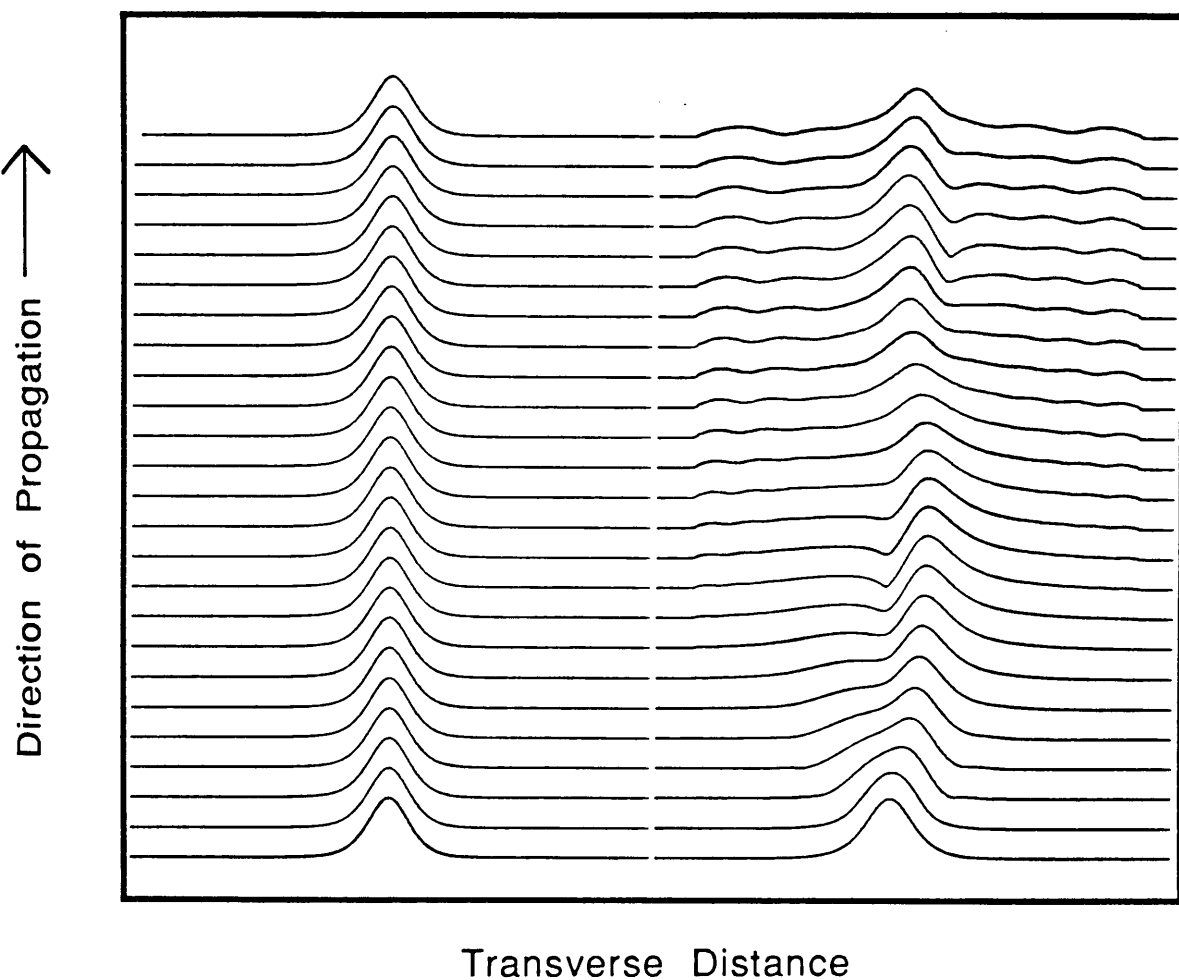


BPM result showing the coupling of a Gaussian profile beam into waveguide. Excitation of the fundamental guiding mode as well as radiation modes results. Note the effect of the absorber zones at the sides of the intensity distributions where there is pronounced attenuation of the field intensity.

Figure 6.3.1

Refractive Index  
Profiles

Intensity  
Profiles



BPM result showing propagation in a dual moded waveguide. The input beam is a Gaussian which has been laterally offset to give a non-zero overlap with the higher order mode.

Figure 6.3.2

The multimoded nature of the waveguide can be seen from the varying position of the intensity maximum as the light propagates along the structure. Again, there is a large presence of radiation due to the modal impurity of the input field.

### 6.3.2 BPM Analysis of the Asymmetric Mach Zehnder Interferometer.

Once a modal field has been obtained for a particular waveguide geometry, one can begin to investigate the properties of the device concerned. Asymmetric Y-junctions are the essential components of the AMZI and hence the properties of these were initially characterised. Junctions with varying angles were examined. The BPM results for angles of  $0.5^\circ$ ,  $0.75^\circ$ ,  $1^\circ$ ,  $1.25^\circ$  and  $1.5^\circ$  are shown in figures 6.3.3.(a), (b), (c), (d) and (e) respectively. The total device length in each of these cases was 2.1mm: the straight waveguide was 0.5mm, the taper region was 1mm and the parallel branch section was 0.6mm. Again, the left hand side pictures show the device refractive index profile and the right hand picture shows the intensity profile.

These results agree with expectations because the power splitting ratio becomes larger for increasing angles. The transmission in each branch was calculated by performing an overlap integral of the input intensity profile with that of the output of the respective branch and these results are shown in figure 6.3.4.

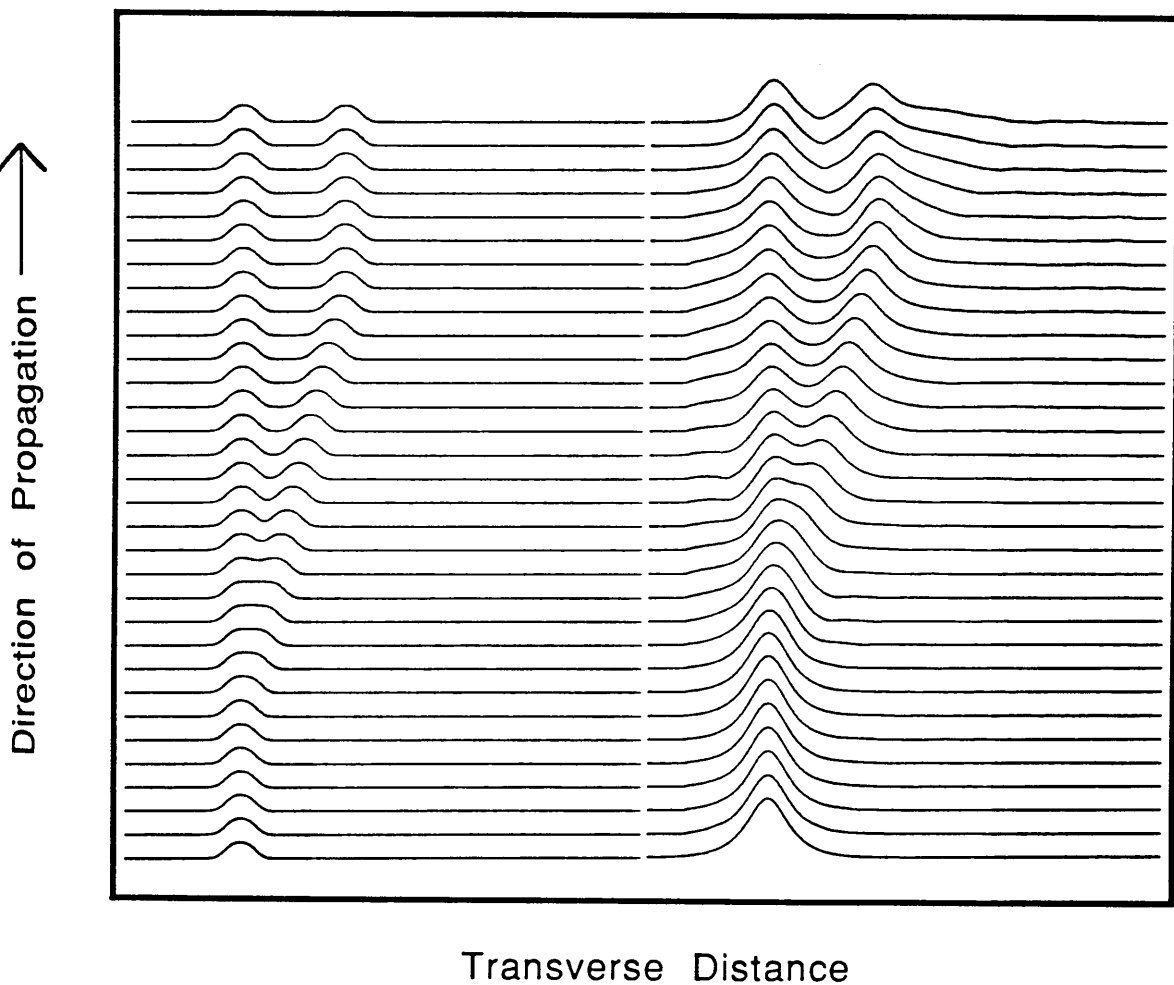
The result for the  $0.5^\circ$  Y-junction indicates almost an equal splitting ratio (0.455/0.431) for the powers transmitted by the straight and the angled branches. In contrast, the result for  $1.5^\circ$  shows that most of the power is transmitted by the straight branch (splitting ratio=0.896:0.016). The splitting ratio varies monotonically between these two angles. These splitting ratios also take into account an additional loss due to the waveguide bend where the angled branch becomes parallel to the straight branch. This is most apparent in the  $1.5^\circ$  angle junction (see figure 6.3.3.(e)) where more than half of the power in the angled branch is radiated into the cladding on the outward side of the branch.

For an efficient device, it has to be ensured that the transmission of the device is not too small. For this reason an excessive splitting ratio is to be avoided. On the other hand, if the splitting ratio is too small, then the device will require larger switching powers. An intermediate angle of  $1^\circ$ , which gives a splitting ratio of 0.774:0.093, was therefore chosen for the following calculations of the linear and nonlinear response of the AMZI.

The BPM results for a  $1^\circ$  AMZI with zero nonlinearity are shown in figure 6.3.5. The total device length here is 4mm. The input and output straight waveguide sections are 1mm long, and the branch section is 2mm long. The guided

Refractive Index  
Profiles

Intensity  
Profiles

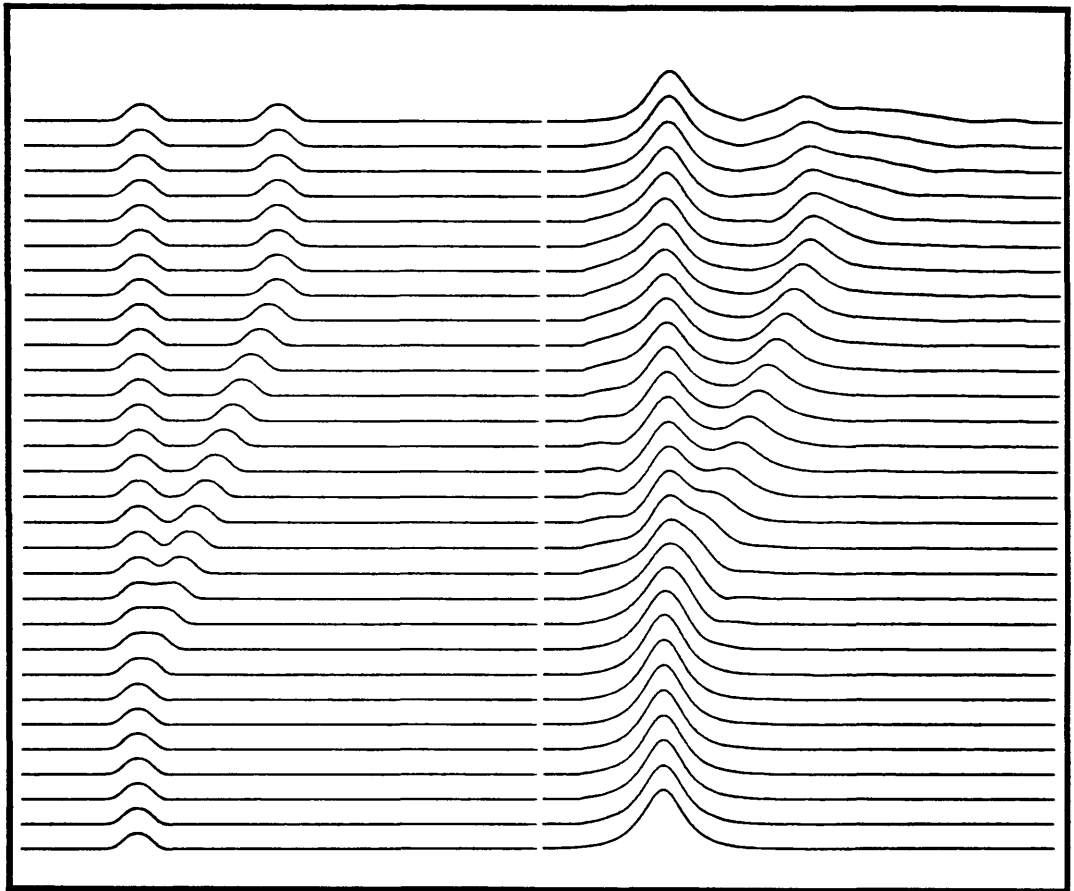


BPM result showing propagation in a 0.5 degree Asymmetric Y-junction. The transmission in the straight and angled branch is 0.455 and 0.431 respectively.

Figure 6.3.3 (a)

Refractive Index  
Profiles

Intensity  
Profiles



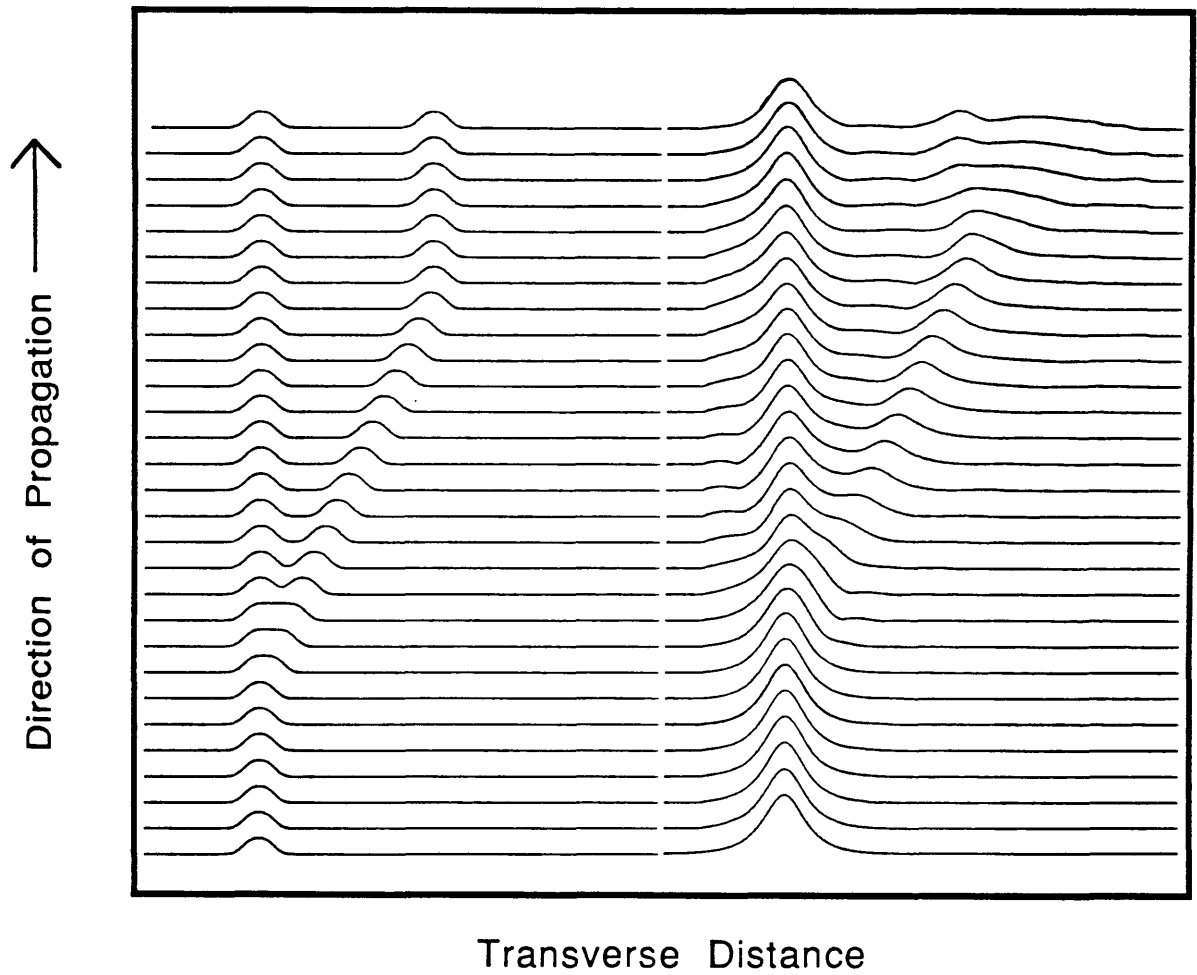
Transverse Distance

BPM result showing propagation in a 0.75 degree Asymmetric Y-junction. The transmission in the straight and angled branch is 0.663 and 0.202 respectively.

Figure 6.3.3 (b)

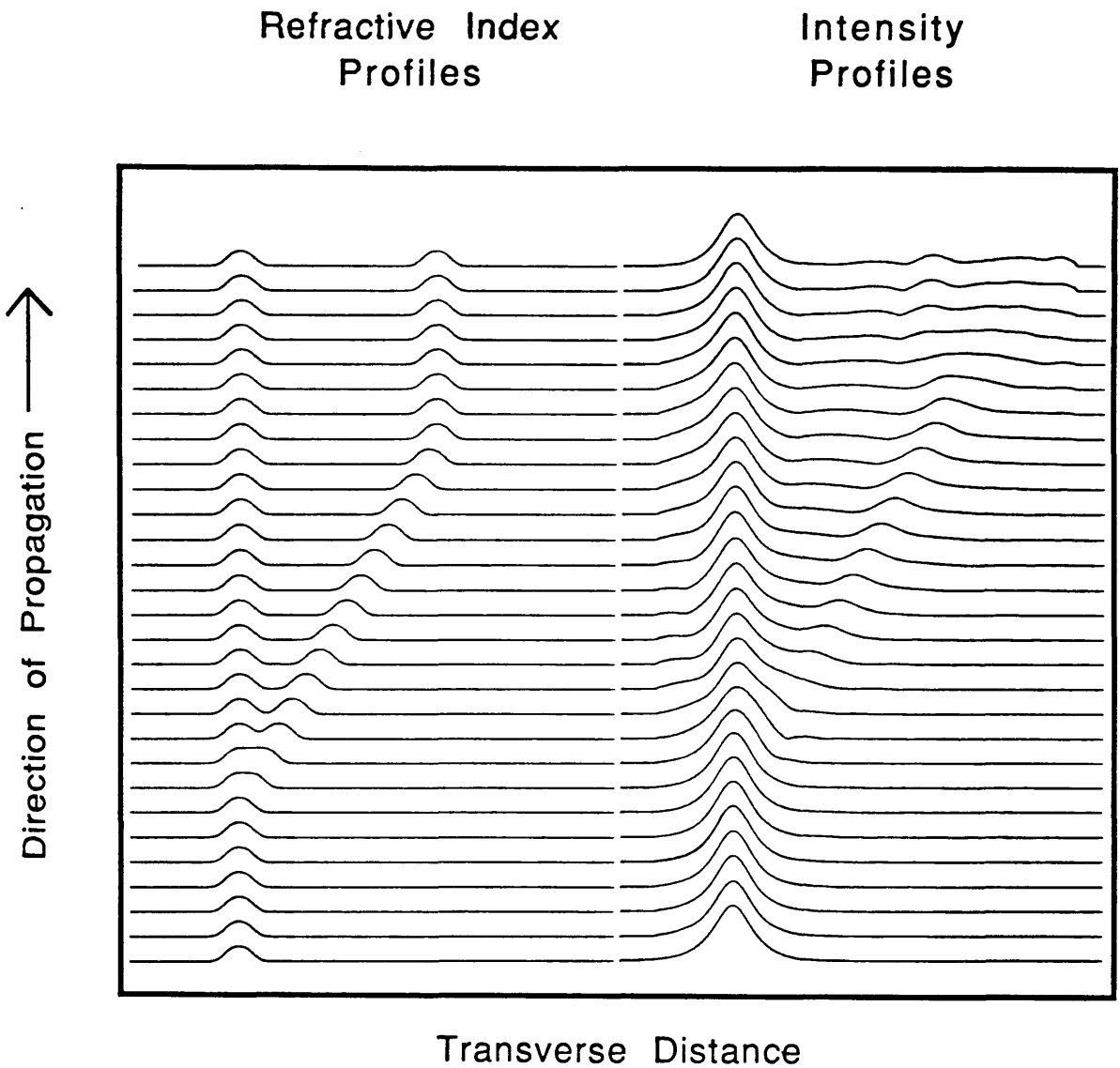
Refractive Index  
Profiles

Intensity  
Profiles



BPM result showing propagation in a 1 degree Asymmetric Y-junction. The transmission in the straight and angled branch is 0.774 and 0.093 respectively.

Figure 6.3.3. (c)

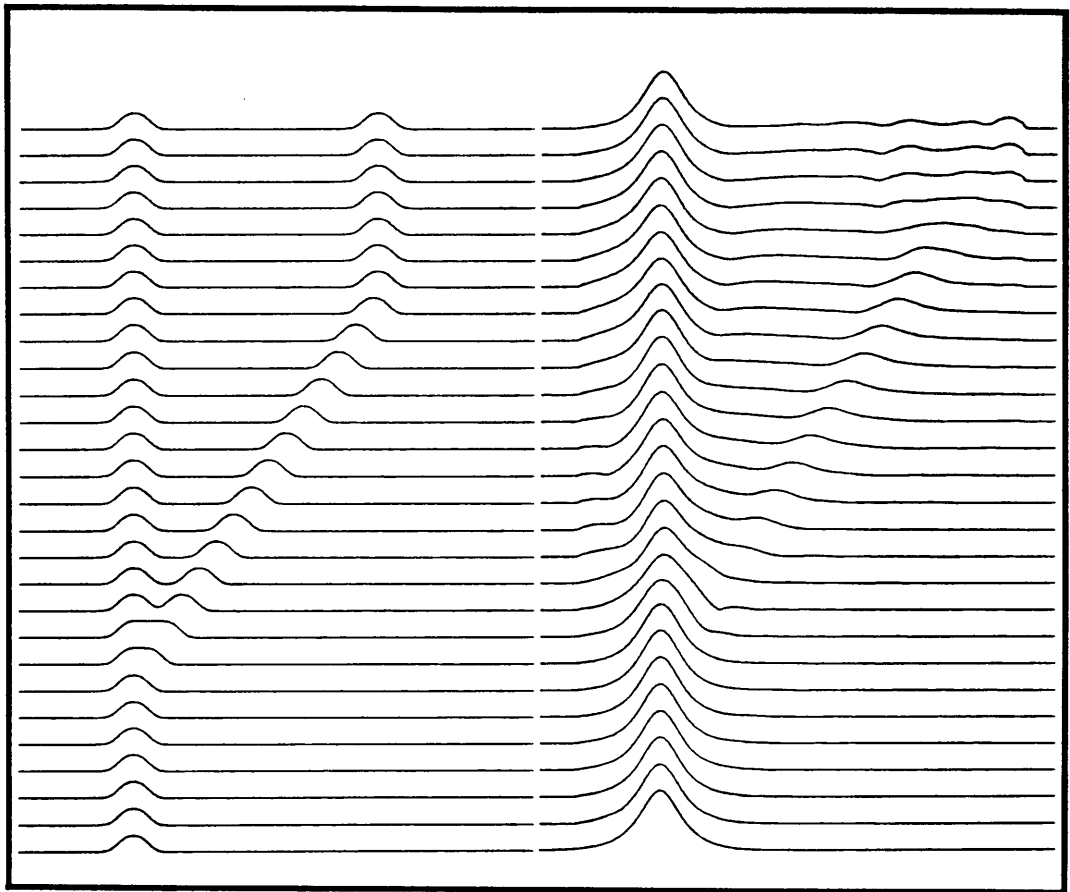


BPM result showing propagation in a 1.25 degree Asymmetric Y-junction. The transmission in the straight and angled branch is 0.864 and 0.035 respectively.

**Figure 6.3.3. (d)**

Refractive Index  
Profiles

Intensity  
Profiles

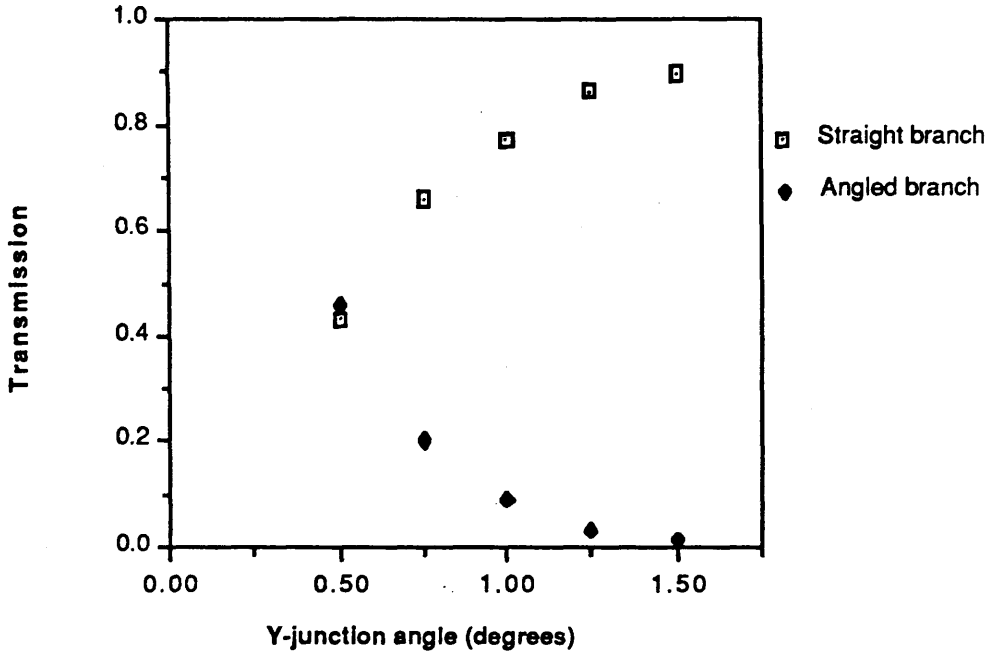


Transverse Distance

BPM result showing propagation in a 1.5 degree Asymmetric Y-junction. The transmission in the straight and angled branch is 0.896 and 0.016 respectively.

Figure 6.3.3. (e)

**BPM results of Power Transmission vs angle  
in Asymmetric Y Branches**

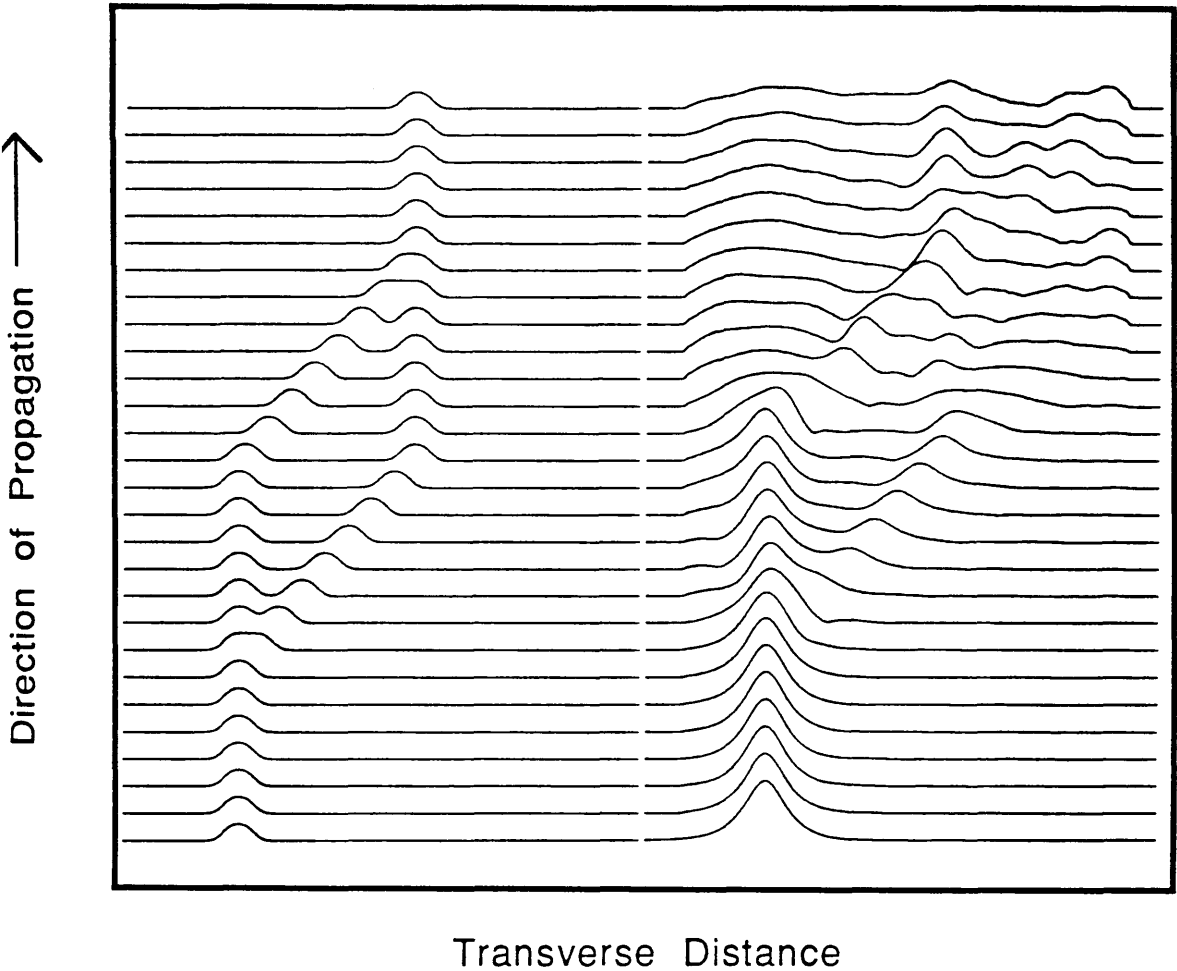


This graph shows the BPM results for propagation in Asymmetric Y-junctions. The transmission of each branch is shown as a function of Y-junction angle.

**Figure 6.3.4**

Refractive Index  
Profiles

Intensity  
Profiles



BPM result for an Asymmetric Mach-Zehnder Interferometer with no absorption loss and no nonlinearity. Note the significant radiation losses at the bends in the device arms. The net device transmission is 0.271.

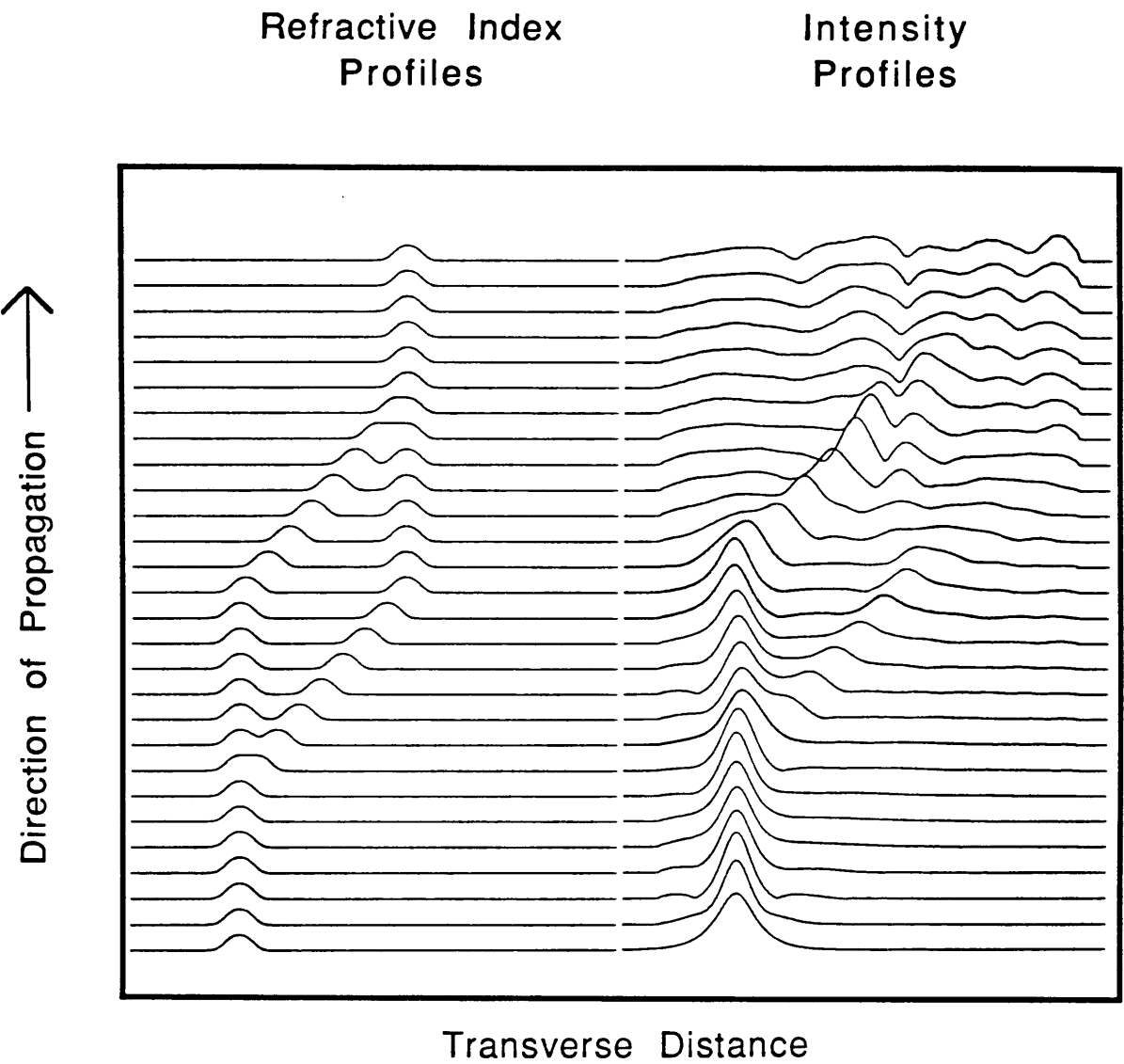
**Figure 6.3.5**

mode in the output waveguide can be seen quite clearly although there is a large presence of radiation from the waveguide bends. The transmission of the device was measured by performing the overlap integral of the output field distribution with the input mode and this was calculated to be 0.271.

The nonlinear response was calculated next. This was done for various intensities. The size of the nonlinearity was set by specifying the maximum nonlinear index change. This could be set to either a positive or a negative value and both of these cases were investigated. Initially, a device with zero absorption was modelled and its transmission was calculated as a function of intensity. Figure 6.3.6 shows the BPM result for a positive nonlinearity corresponding to an intensity of  $750\text{MW/m}^2$  (with  $n_2=10^{-11}\text{ m}^2/\text{W}$ ). This shows the condition where a minimum in the transmission was observed. It has to be commented that the induced index change for this to occur is 0.0075 whereas using the scattering matrix model it is 0.00046. (The latter is obtained using the above splitting ratio of 0.774:0.093, which implies  $\delta=0.107$ , and putting into equation (6.2.1.3) with  $\Delta(nl)=\lambda=830\text{nm}$ .) However the two results can not be compared since the latter assumes that the Y-junction is perfect and all the power is coupled into the AMZI branches. The BPM, on the other hand, indicates that there are radiation losses present in even the first Y-junction and also includes bending losses in the arms of the interferometer. Hence a larger index change is required in the BPM model for switching to occur.

A consequence of this large index change is that the guiding properties of the AMZI are modified significantly. This is apparent in the BPM result for a negative nonlinearity which is shown in figure 6.3.7. For this case it is seen that the confinement of the waveguides is reduced quite severely and there is much radiation loss. Indeed, a transmission minimum such as the one obtained with the positive nonlinearity, is not observed in this case due to the reduced confinement. The graph in figure 6.3.8 shows the transmission of the AMZI as a function of both positive and negative nonlinearity. Note that for the positive nonlinearity, the transmission actually reaches a value higher than its zero intensity value. This is because of the increased confinement which occurs at this large index change. For an increasing positive nonlinearity, the transmission tends to remain constant because self focussing causes the mode to propagate almost entirely into the straight branch which means that there is only one mode incident on the branches of the output Y-junction and hence there is no phase dependant recombination.

The effect of absorption on device response was next introduced. A value of  $\alpha = 10\text{ cm}^{-1}$  was used. The result for a zero nonlinearity is shown in figure 6.3.9. It is not apparent from this figure what the output mode looks like but an overlap integral indicated that the transmission of the device was 0.0033. (A 4mm

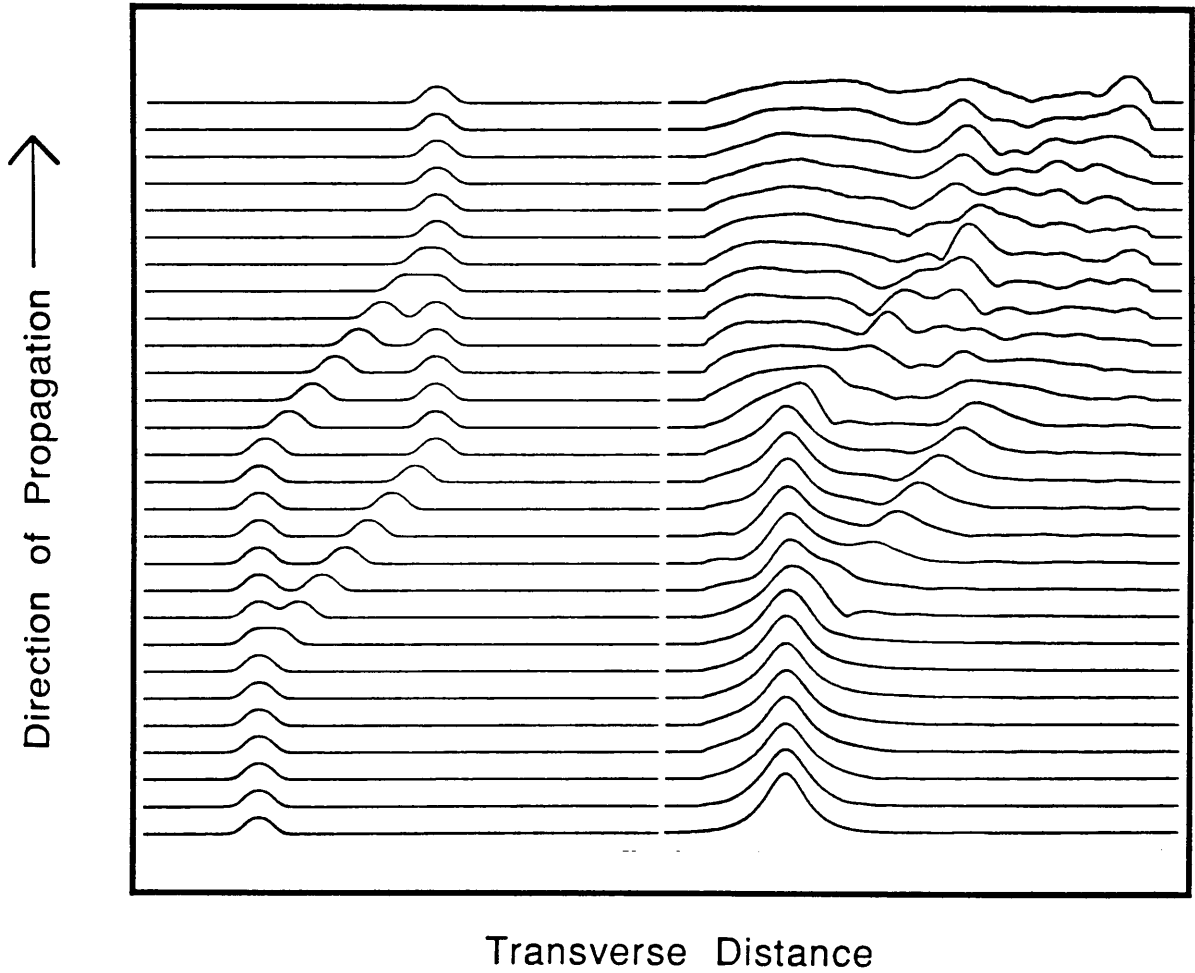


This shows the result when a positive nonlinearity is introduced with  $n_2 = 10^{-11} \text{ m}^2/\text{W}$ , intensity =  $750 \text{ MW}/\text{m}^2$ , absorption = 0.

**Figure 6.3.6**

Refractive Index  
Profiles

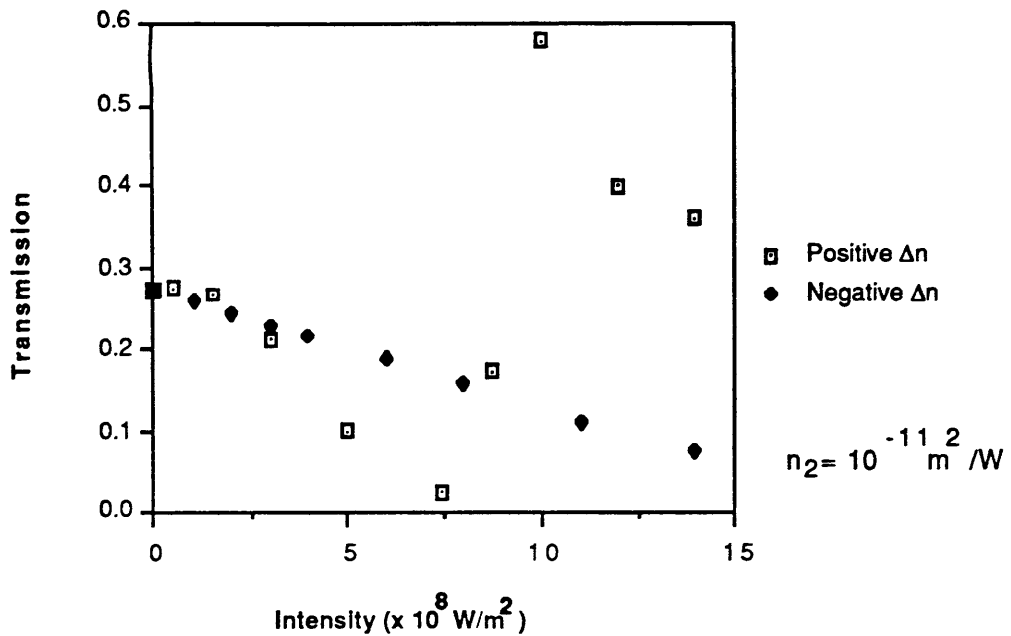
Intensity  
Profiles



This shows the result when a negative nonlinearity is introduced with  $n_2 = -10^{-11} \text{ m}^2/\text{W}$ , intensity=400MW/m<sup>2</sup>, absorption= 0.

Figure 6.3.7

Transmission in a "lossless" NLAMZ  
with 1° branch angle.

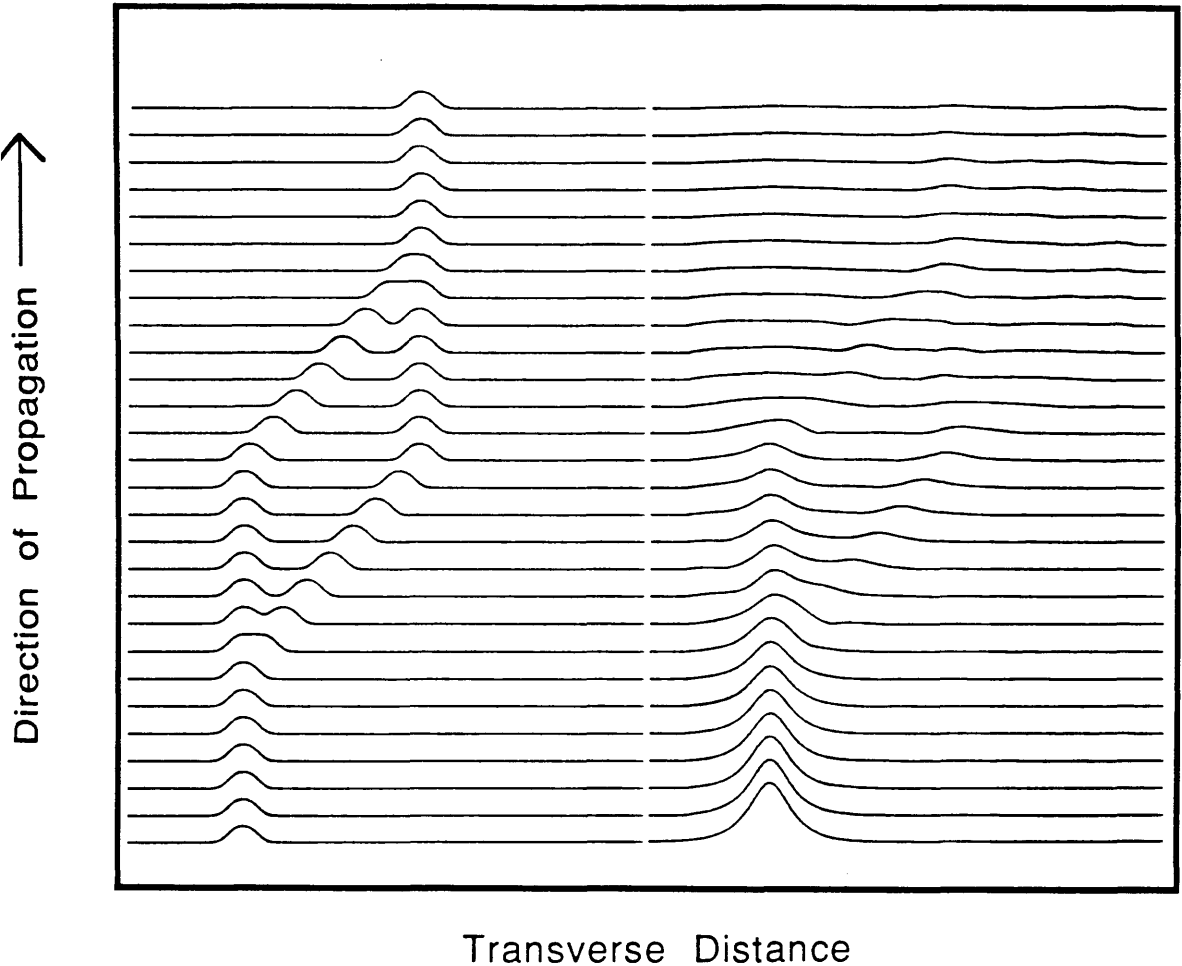


Graph of the predicted switching behaviour of an Asymmetric Mach-Zehnder Interferometer. Both positive and nonlinear index changes have been modelled to show the differences arising from changes in waveguide confinement. No switching behaviour is seen for a negative  $n_2$  because confinement is reduced significantly.

Figure 6.3.8

Refractive Index  
Profiles

Intensity  
Profiles



Transverse Distance

A loss of  $\alpha=10 \text{ cm}^{-1}$  has now been introduced resulting in a device transmission of 0.0033. No nonlinearity has been included in this calculation.

Figure 6.3.9

long waveguide with this absorption would have a transmission of 0.0183.) The nonlinear response of the lossy AMZI was next calculated and is shown in figures 6.3.10(a) and (b). As one would expect, the intensities required to see nonlinear behaviour are considerably higher. Again, for a negative nonlinearity, there are no transmission minima because of the reduction of confinement. For the positive case the transmission is seen to go through two minima.

In summary, two models have been used to calculate the theoretical response of the Asymmetric Mach–Zehnder Interferometer. The first of these was a simple scattering matrix approach which served to illustrate the operating principles of the AMZI but it failed to take into account the presence of radiation losses which occur in real devices. This model also ignored the coupling that exists between the two waveguide branches close to the apex of the junction. These limitations were overcome by use of the BPM model which was then used to predict the AMZI response.

#### **6.4 Experimental Characterisation of the Asymmetric Mach–Zehnder Interferometer.**

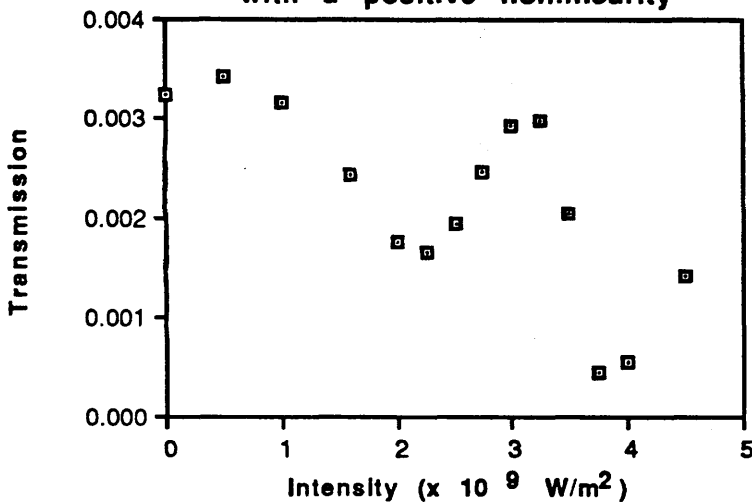
This section describes the experimental work done to characterise the Asymmetric Mach–Zehnder Interferometer. Investigations were carried out to determine the splitting ratios of asymmetric Y–junctions and these results were compared with the theoretical predictions of the BPM. Having done this, the nonlinear response of the AMZI was investigated.

##### **6.4.1 Fabrication details.**

A mask design was produced which included both Y–junctions and AMZIs. Devices with varying Y–junction angles were produced ranging from 1° to 3° in 0.5° increments. A schematic of the mask is shown in figure 6.4.1.

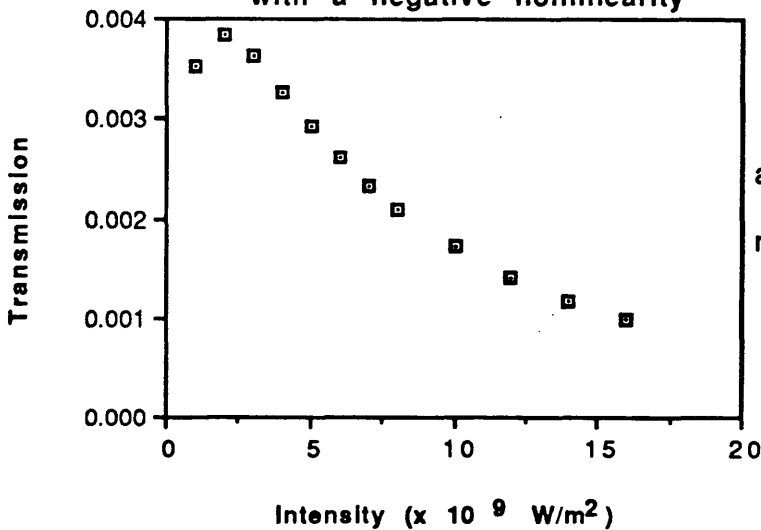
Devices were fabricated in wafers CPM376, MA670 and MV273 (see appendix III for details of wafer structure). Much of the fabrication details have already been described in Chapter Three. It was found, as will be shown in 6.5, that the use of a metal etch mask resulted in the formation of a "blunted" Y–junction. This severely impairs the performance of the device because the mode in the straight waveguide is not coupled efficiently into the branch waveguides and reflection losses occur at the flattened apex. The metallisation process was therefore eliminated by using photoresist as an etch mask. Figure 6.4.2 shows asymmetric Y–junctions patterned in the photoresist and figure 6.4.3 shows a scanning electron

Transmission in lossy 1° AMZI  
with a positive nonlinearity



absorption =  $10 \text{ cm}^{-1}$   
 $n_2 = 10^{-11} \text{ m}^2/\text{W}$

Transmission in 1° lossy AMZI  
with a negative nonlinearity



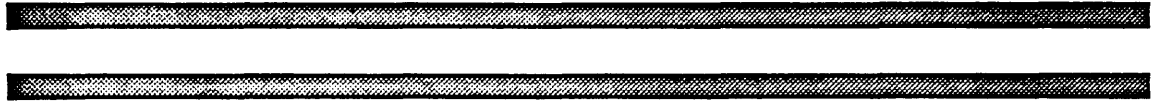
absorption =  $10 \text{ cm}^{-1}$   
 $n_2 = -10^{-11} \text{ m}^2/\text{W}$

The above graphs show the nonlinear transmission in AMZI's when loss ( $= 10 \text{ cm}^{-1}$ ) is introduced. The switching powers required have increased for the positive  $n_2$ .

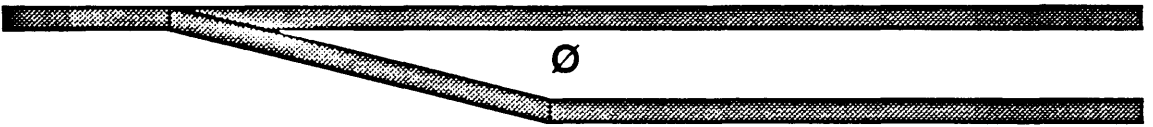
Switching behaviour is still not present for the negative nonlinearity.

Figure 6.3.10

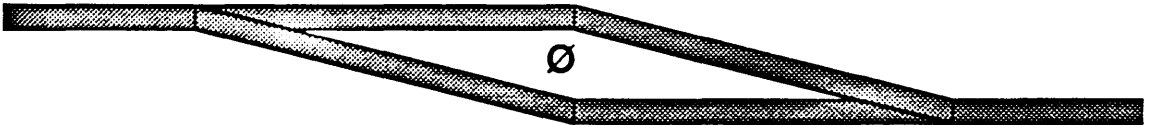
**Main features of mask used to pattern Asymmetric Mach-Zehnders and Y-junctions.**



**Straight waveguides**



**Asymmetric Y-junction**



**Asymmetric Mach-Zehnder Interferometer**

All waveguides  $3\mu\text{m}$  wide.  
 $\emptyset=1, 1.5, 2, 2.5$  and  $3$  degrees

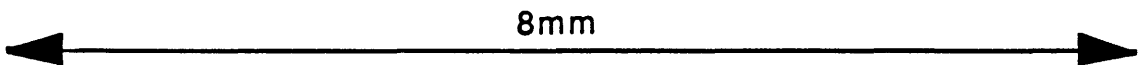
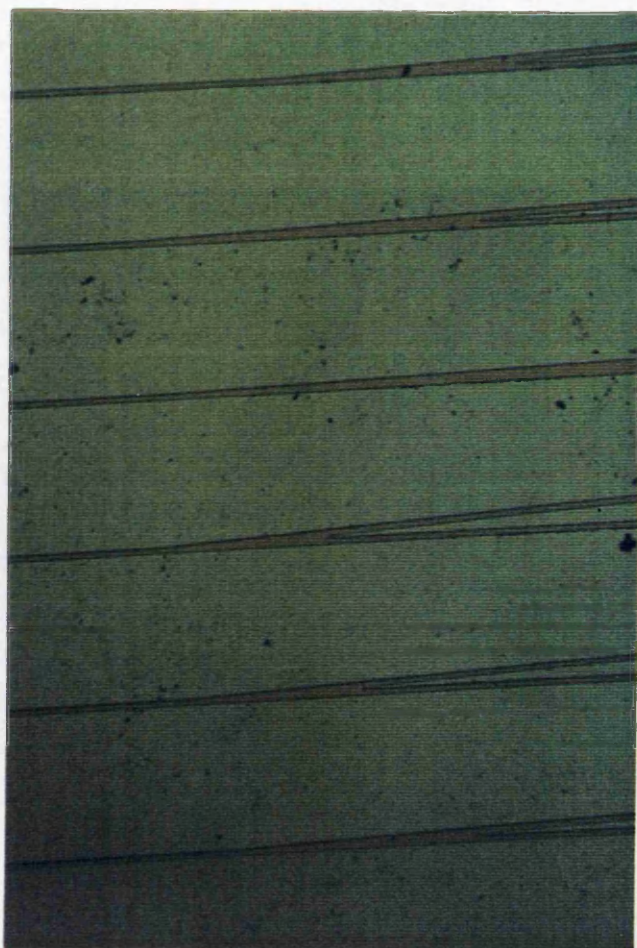


**Figure 6.4.1**



Y-junctions of varying angles (1 to 3 degrees)  
patterned in photoresist.

Figure 6.4.2



micrograph of a  $3^\circ$  asymmetric Y-junction after etching.

#### 6.4.2 Splitting ratio measurements in Asymmetric Y-junctions.

The devices were initially tested by observing the output using the Hamamatsu camera and beam splitter arrangement described in 5.3.2. With this set up, the waveguide end facets as well as the modal field could be imaged on the video monitor. This was important for accurate positioning of the Y-junction with respect to the focussed laser spot at the device input. If the device was not well positioned laterally then it was possible to launch some light into the asymmetric branch of the Y-junction via the slab modes. Alignment was performed by initially coupling light into a straight waveguide. The position for maximum transmission through this waveguide corresponded to optimum positioning of the waveguide with respect to the focussed laser spot. The position of the waveguide rib was then marked on the monitor and the Y-junctions were subsequently positioned by moving the sample laterally and aligning to this mark. This was estimated to give correct lateral positioning to within  $1\mu\text{m}$ . Having aligned the device, the Hamamatsu camera was then used to record the intensity profiles at the outputs of the devices. Figure 6.4.4 shows the output mode profile of the  $1^\circ$  Y-junction as imaged on Hamamatsu camera. In this photograph the mode on the right corresponds to the straight through branch. Profiles were recorded for the Y-junctions of angle  $1^\circ$  and  $1.5^\circ$  and these are shown in figure 6.4.5.(a) and (b) respectively. In these graphs the mode on the left corresponds to the straight through branch. These profiles were obtained from sample MA670 which had been slightly over etched and consequently supported two guided modes. As will be seen below, measurements tend to indicate that the splitting ratio is not significantly altered as long as the power is mainly coupled into the fundamental mode. The higher order mode can be seen in the asymmetric branch of the  $1.5^\circ$  Y-junction. The peaks present immediately to the right of the modes of the straight branch are artifacts of radiation.

These intensity profiles show the form of the output of the asymmetric Y-junctions but do not actually represent the intensity distribution because of the nonlinear response of the vidicon tube in the Hamamatsu camera. The power splitting ratios cannot therefore be determined from these profiles. These were instead measured using a large-area photodetector and an iris arrangement as shown in figure 6.4.6. The Hamamatsu camera was first used to initially align the device and then used to correctly position the iris. The camera was focussed on the plane of the iris as was the output from the endfire rig and, in this manner,

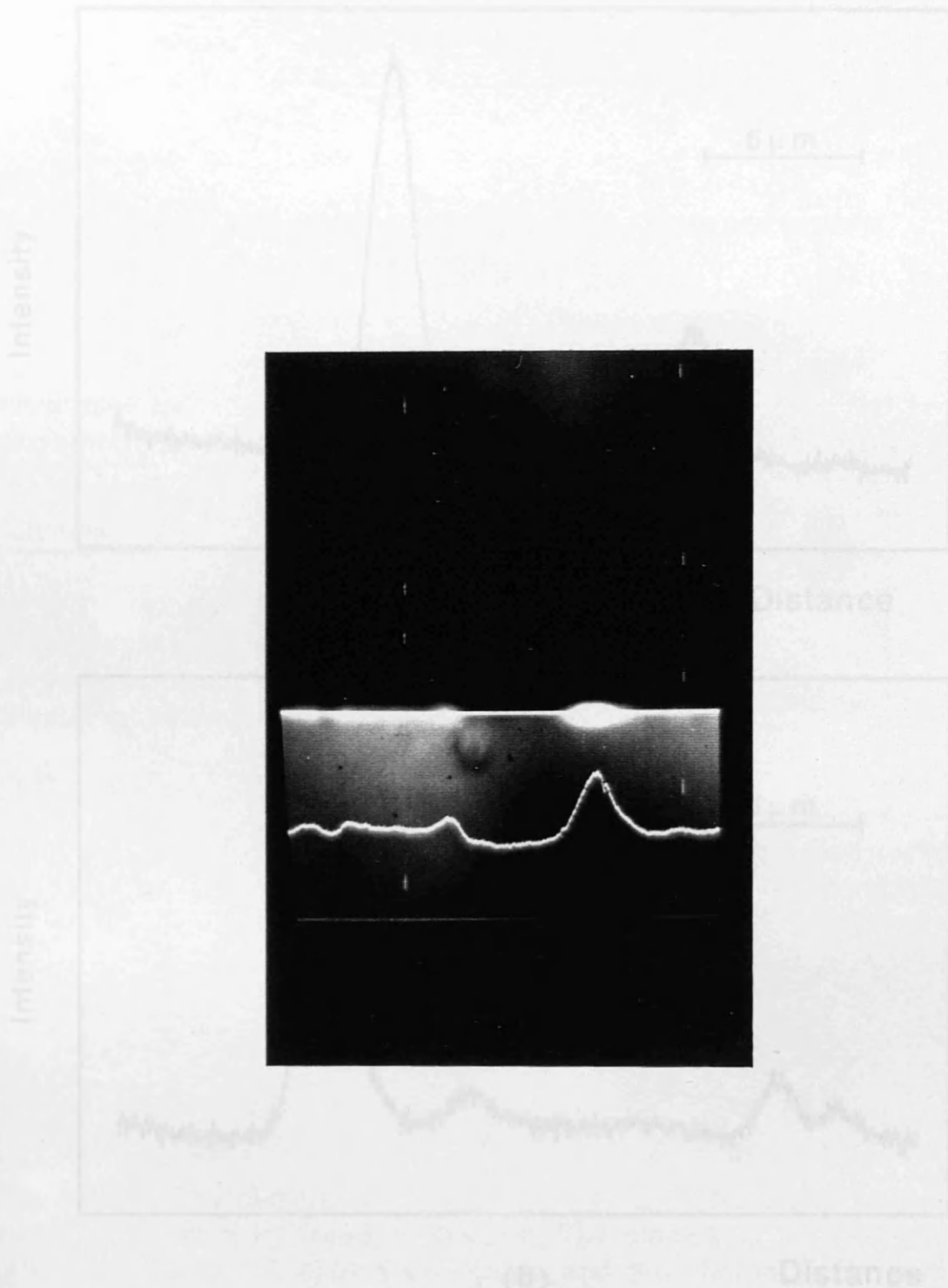
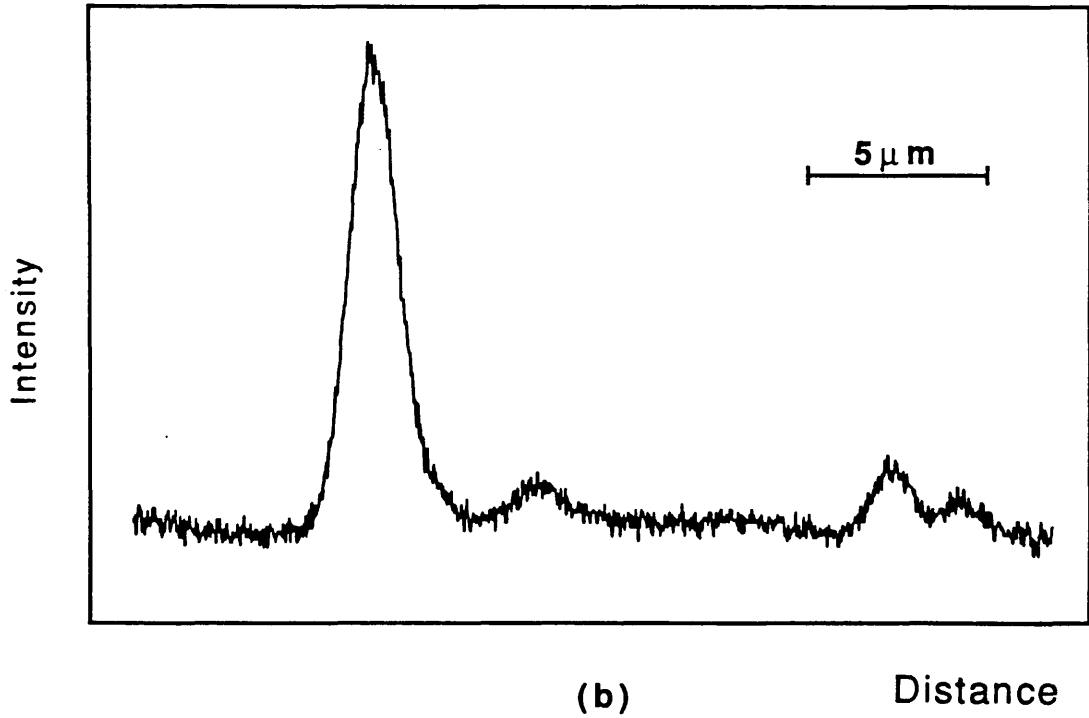
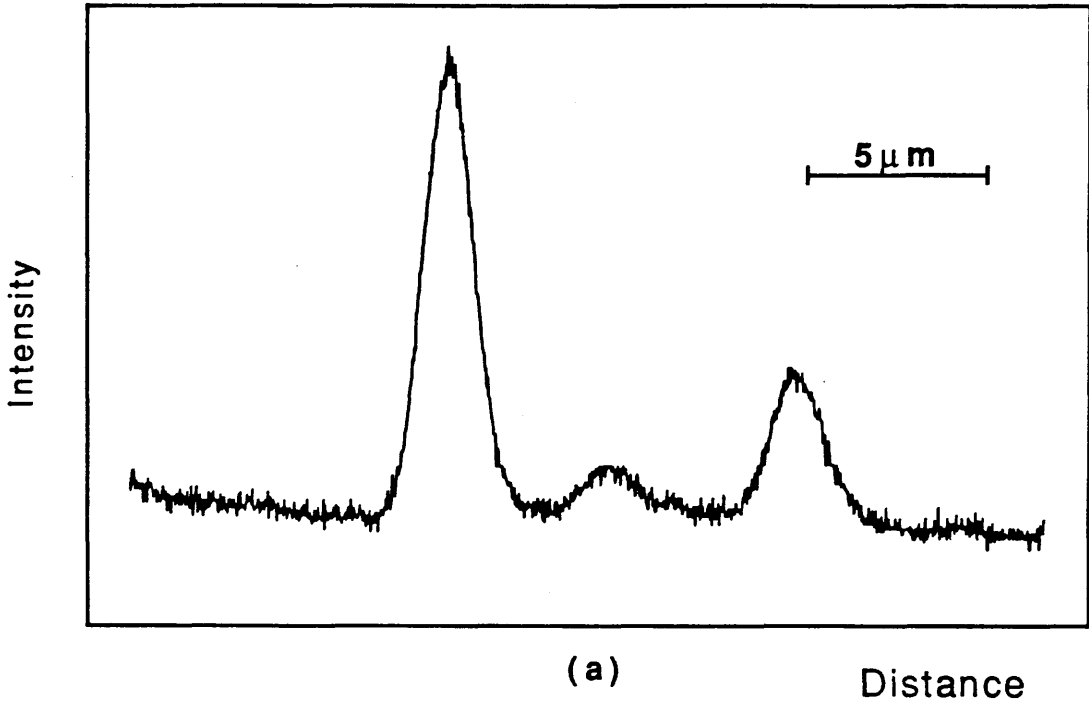


Figure 6.4.4

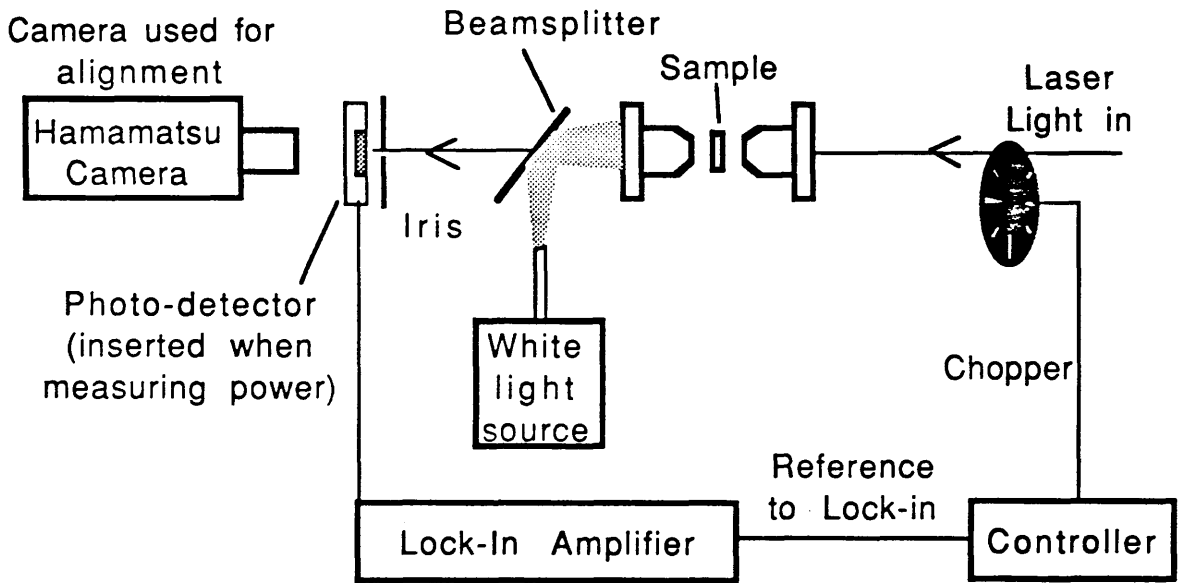
Photograph shows simultaneously imaged waveguide end facet and mode profile of a 1 degree Y-junction. The mode on the right is that of the straight branch and that on the left is of the angled branch.



Mode profiles as obtained from the Hamamatsu camera for (a) 1° , (b) 1.5° asymmetric Y-junctions.

Figure 6.4.5

## Experimental arrangement for measurement of splitting ratios.



The Hamamatsu camera is focussed on the iris. The output of the endfire rig is also focussed on the iris. The camera is initially used to align the iris to the correct waveguide and the photodetector is then positioned immediately behind the iris to make the power measurement.

Figure 6.4.6

both the device output and the iris could be simultaneously imaged on the camera. The iris aperture size and position were then adjusted to allow light through from only one of the branches. The photodetector was positioned immediately behind the iris and the power measurements were made using a lock-in amplifier. For measurement of the power from the other branch the iris and photodetector were realigned using the same procedure. The splitting ratios could thus be determined for each of the Y-junctions.

These measurements were conducted on samples MV273 (MQW), MA670 (6% Al-doped) and CPM376 (5% Al-doped). Sample MA670 had been slightly over etched and supported two guided modes. However there is only a small difference apparent when these results are compared with those of the single moded sample CPM376. The results are summarised below in figure 6.4.7. These are also shown graphically in figure 6.4.8 along with those of the BPM calculations.

ANGLE	SAMPLES		
	MV273	MA670	CPM376
1°	2	3	2.5
1.5°	9.5	8	5

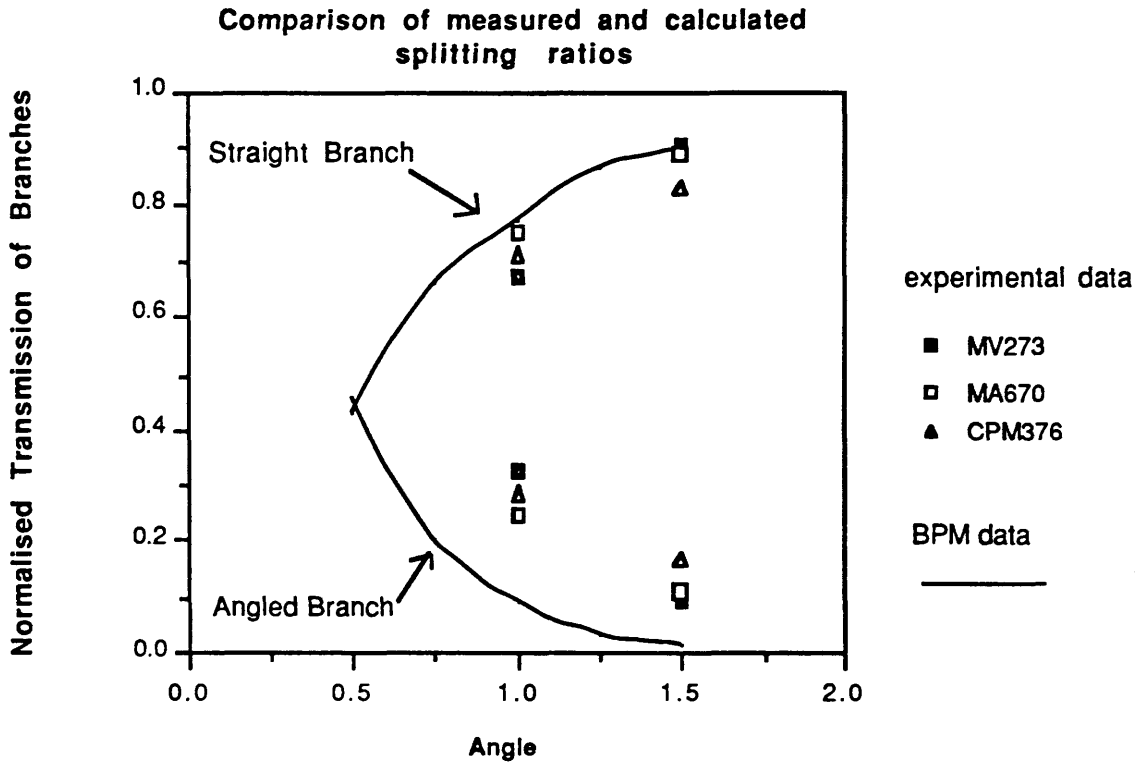
Figure 6.4.7

Summary of splitting ratio results.

The numbers represent the ratio of the power in the straight through branch to that in the asymmetric branch. All measurements were made at  $\lambda = 850\text{nm}$ .

The BPM results agree well with the measured ratios only for the smaller angles. The poor agreement with the larger angle results could possibly be due to a breakdown of the paraxiality approximation used in the BPM model (see section 6.3). This is because, for the larger angled Y-junctions, the deviation from the paraxiality condition leads to an inaccurate phase representation in the model. Alternatively, this discrepancy may be due to fabrication defects.

Although the double mode guiding did not seem to affect the splitting ratio, the presence of higher order modes does however significantly affect the operation of the AMZI. If the waveguides in the AMZI are not single moded then a  $\pi$  phase shift between the two arms will not result in complete radiation of energy into the substrate at the output Y-junction. The switching action of the device in



**Graph showing comparison of theoretical and experimental power splitting results for an Asymmetric Y-junction.**

**Figure 6.4.8**

this case will not be apparent when measuring the device output power.

### 6.4.3. Experimental investigation of the AMZI.

The intensity dependant output of the AMZI was investigated using the iris and photodetector arrangement described above. The power entering the AMZI was monitored by a second photodiode which measured the reflected power from a beamsplitter positioned before the endfire rig. This latter photodiode was calibrated with the power meter reading obtained after the beamsplitter but before the endfire rig. The power was varied using a polariser and electro-optic modulator arrangement as described earlier in section 5.4. The power values which will be quoted here refer to the actual power entering the device after having allowed for coupling losses as discussed in section 5.2

The responses of devices made in CPM376 and MV273 were examined. The CPM376 device was tested at  $\lambda = 850\text{nm}$  which was the shortest wavelength with which a measurable output power was obtained. The power was varied from 0.2mW to 1.3mW. No change in transmission was observed in any of the devices even though nonlinear absorption had previously been seen (section 5.4). Sample MV273 was tested using a fresh dye solution and so higher than normal laser power was available. (The laser was producing 110mW average power at 830nm). A maximum power of 12mW at  $\lambda = 837\text{nm}$ , which corresponds to the energy of the hh-excitonic resonance in this sample, was launched into the device but still no change in transmission was observed in any of the devices.

In order to understand this result, a theoretical estimate of the index change expected from the creation of free carriers is now made for the  $1.5^\circ$  angled device in sample MV273. From above, the power coupled in is 12mW and the splitting ratio is 1:9.5. The absorption coefficient at this wavelength (837nm) has been measured as  $16\text{ cm}^{-1}$  (see 5.3). Assuming that every photon absorbed creates an electron-hole pair it can be calculated that the difference between the number of carriers created in each arm is  $500 \times 10^6$ . This corresponds to an average carrier density difference of  $2.54 \times 10^{16}\text{ cm}^{-3}$  in the volume of the AMZI arm (which has been taken to be the modal area ( $\approx 10\mu\text{m}^2$ ) multiplied by the arm length (=2mm)). The index change per electron-hole pair created has been reported by Manning et al[6] to be  $n_{e-h} = 0.4 \times 10^{-19}\text{ cm}^3$ . Thus a differential change in path length equal to  $2.4\lambda$  is calculated. Note that an average carrier density throughout the length of the arms has been used in this calculation although this is, in fact, clearly not the case. The treatment is valid however since the net change in path length is proportional to the number of carriers interacting with the

propagating mode irrespective of their actual distribution along the waveguides. The calculation indicates that there is sufficient optical power present in the AMZI to produce the phase shifts required for optical switching. To explain why no change in transmission is observed other factors have to be considered.

The nonlinear index change is not uniformly distributed along the length of the waveguide. In fact most of the effect occurs within a distance equal to the effective length  $l_{\text{eff}}=1/\alpha$  of the initial Y-junction. For the case considered above this length is 0.6mm. If the Y-junction angle of  $1.5^\circ$  is considered, this means that over this "active" length, the branching waveguides only separate by  $15\mu\text{m}$  at the most. If the diffusion equation (5.4.4.2) is applied, it is seen that within the pulse repetition time of 13ns, the FWHM of the carrier distribution increases from  $8\mu\text{m}$  to  $20\mu\text{m}$ . This means that because of insufficient waveguide separation the carrier induced index change is spread over both arms of the AMZI. The differential phase change between the two AMZI arms is thus washed out by carrier diffusion. In addition to these carrier effects, thermal diffusion also occurs since there is heating of the device present. For similar reasons, however, a nonlinearity of thermal origin also gives a poor AMZI response as the heat dissipates to the adjacent arm.

The relaxation time of the thermal effect is now considered by application of solution (5.4.4.4) of the thermal diffusion equation

$$T(r, t) = \frac{\sigma_0^2 T_0}{4D_{\text{th}}t + \sigma_0^2} \exp \left[ \frac{-r^2}{4D_{\text{th}}t + \sigma_0^2} \right]. \quad (5.4.4.4)$$

Using the value for  $\text{Al}_{0.3}\text{Ga}_{0.7}\text{As}$ ,  $D_{\text{th}}= 6.77 \times 10^{-6} \text{ m}^2/\text{s}$  obtained from the data given by Adachi[7], and an initial distribution of radius  $\sigma_0=4\mu\text{m}$ , it is calculated that it takes  $5.3\mu\text{s}$  for an initial temperature at the centre of the distribution to decrease by 90%. Aitchison et al[8] have observed an optothermal nonlinearity in AlGaAs waveguides with a recovery time of  $5\mu\text{s}$  which is in good agreement with the above estimate. When the pulse repetition time of the laser (=13ns) is considerably smaller than the heat dissipation time, the waveguide is effectively subjected to continuous heating.

The conclusions of section 5.4 stated that unless a different laser source was used, the electronic nonlinear contribution to these devices is more or less completely subdued by the more dominant heating effects present. Thermal effects are therefore more important in these experiments. A fuller appreciation of thermal effects in the context of their influence on the operation of the AMZI is therefore required. With this aim in mind a new version of the AMZI was designed and

fabricated. This included ohmic heating strips adjacent to the arms of the AMZI making it possible to directly investigate the effects of heating.

## 6.5 The Thermal Asymmetric Mach-Zehnder Interferometer.

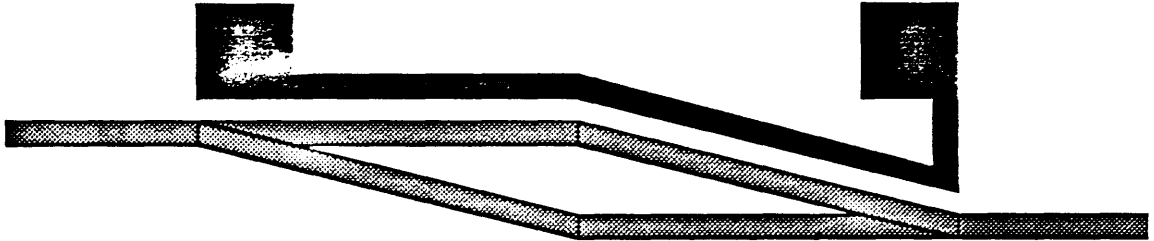
A mask was designed for a new AMZI device in which a thermal refractive index change could be directly induced. This was done by use of "heaters" placed adjacent to the waveguides. These are basically metal strips which are heated by application of a current. Any current flowing through this strip causes ohmic heating which in turn causes a thermal refractive index change in the adjacent waveguide. Using these, an index change could be induced in the waveguides in a repeatable and a controllable manner. The thermal switching characteristics of the AMZI could thus be observed.

### 6.5.1 Fabrication details.

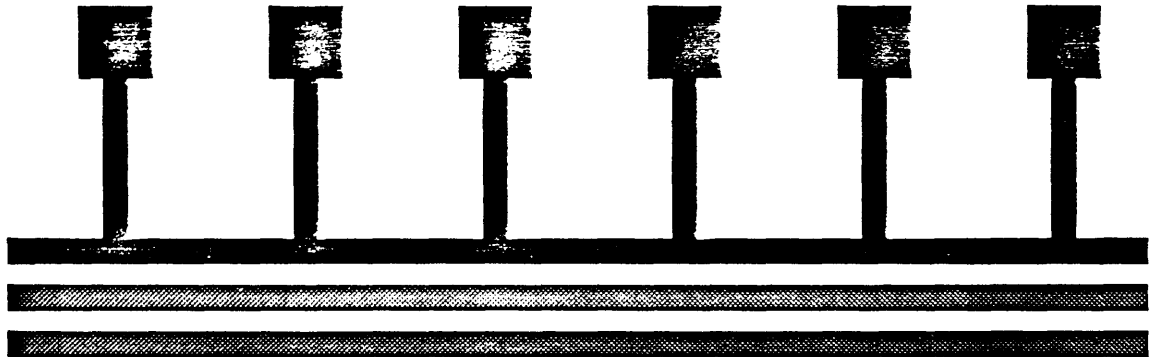
A schematic of the mask is shown in figure 6.5.1. Thermal AMZIs with two angles ( $1^\circ$  and  $1.5^\circ$ ) were produced. The heaters were located alongside one of the interferometer arms. Also included in the mask were asymmetric Y-junctions to provide splitting ratio information for these particular devices. Two pairs of straight waveguides with an adjacent heating element were also incorporated in the mask. In this case the heater strip was connected to six equally spaced pads to which external electrical contacts could be bonded. This arrangement was used so that it was possible to determine the resistance of the heater strip.

Since metal heaters were required on the sample, processing was done using nichrome so that it served as the etch mask to define the waveguides as well as acting as the ohmic heater. However, fabricating Y-junctions with this metal mask results in a blunted feature at the apex of the Y-junction. This results in poor modal transitions in the Y-junctions. The Y-junctions are shown in detail by the two SEM micrographs in figure 6.5.2. The first of these shows a Y-junction apex immediately after metallisation and the second shows an apex after dry etching. (The two pictures actually correspond to different Y-junctions.) The devices were fabricated in sample Varian 1 which is an  $\text{Al}_{0.3}\text{Ga}_{0.7}\text{As}/\text{Al}_{0.33}\text{Ga}_{0.67}\text{As}$  double heterostructure (see Appendix III for details of the structure). The sample was cleaved into two pieces with one containing the AMZI's and the Y-junctions and the other containing the straight waveguide section. Both pieces were mounted using Loctite superglue on separate suitably patterned circuit boards. Electrical contacts

**Main features of mask used to  
investigate thermal effects.**

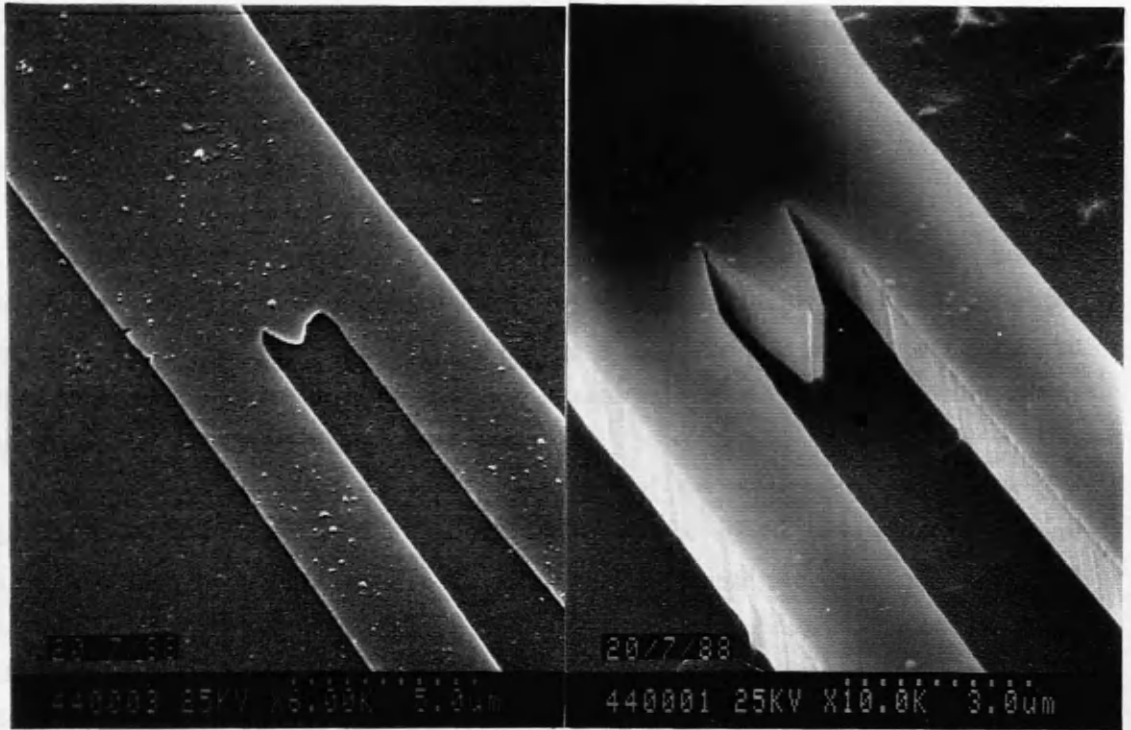


**The Asymmetric Mach-Zehnder with heater  
strip adjacent to one of the arms**



**Two waveguides with one heating strip. A series  
of contacts were included to enable measurement  
of the resistance of the heating strip.**

**Figure 6.5.1**



**SEM photographs of Y-junctions (a) before and (b) after etching showing the "blunted" apex.**

**Figure 6.5.2**

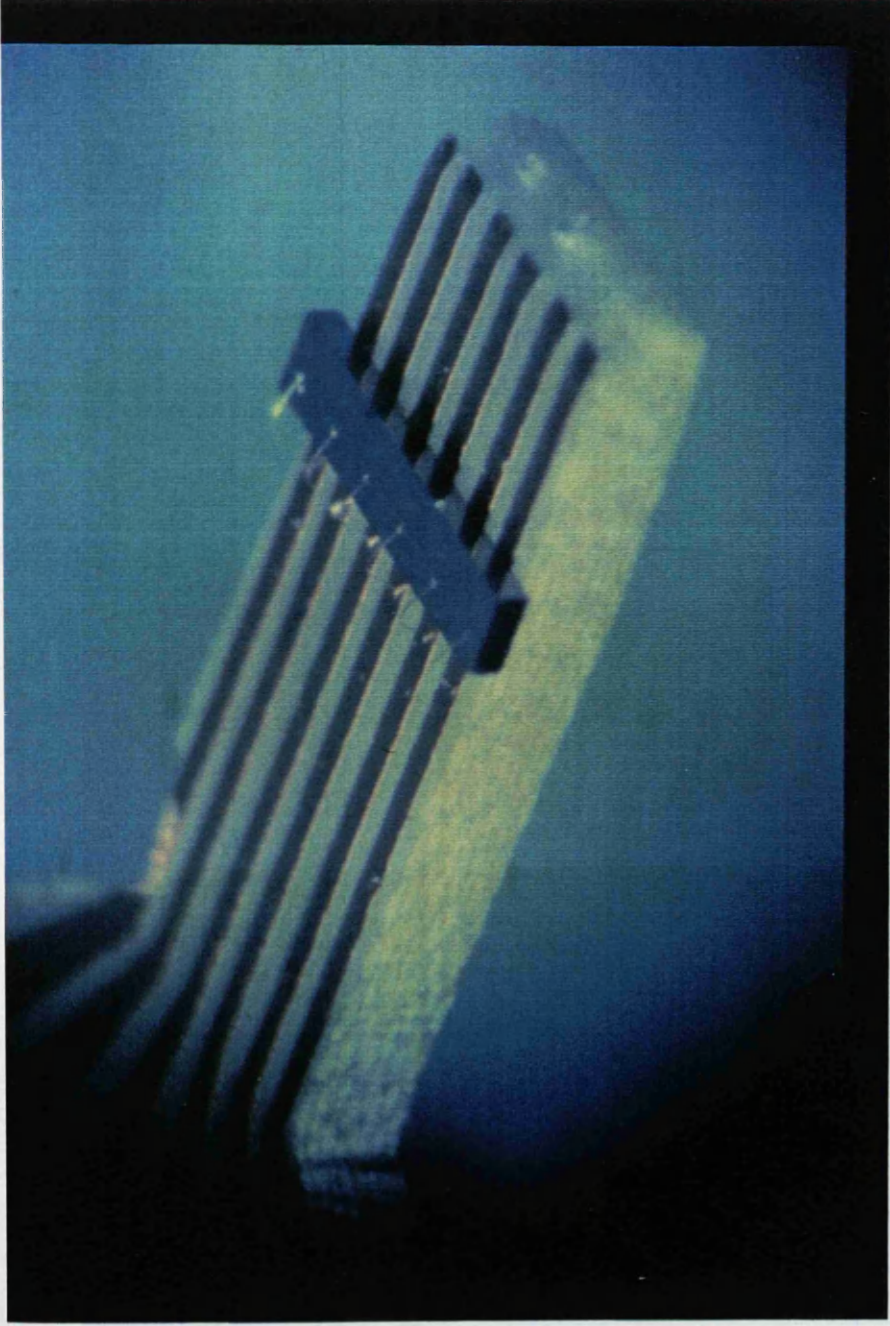
were made using an ultrasonic bonding machine by which aluminium wires could be connected from the nichrome pads on the samples to the copper strips on the circuit boards. Standard multicore copper wires were then soldered onto the circuit board. Figure 6.5.3 shows the straight waveguide section mounted on the circuit board. The six aluminium wires bonded onto the sample can clearly be seen. Figure 6.5.4 shows the thermal AMZI's which have been similarly mounted. There are four devices on the sample and connections to each of the heaters have been made in parallel.

### 6.5.2 Testing of thermal properties in straight waveguides

Initial characterisation of thermal effects was performed in the straight waveguides sample. The thermally induced index change was measured using the external interferometer arrangement of section 5.3.2. The fringe shift was measured as a function of a d.c. heating current. Measuring the index change in this way gives a value of a thermally steady state effect.

The index change was measured for each of the two waveguides beside the heating strip as a function of d.c. current and the results are shown in figure 6.5.5. Any difference in the size of the effect between two adjacent waveguides will depend on the gradient of the temperature distribution. When the index changes were measured no difference was seen between the two waveguides. In both cases a current of 6mA was seen to induce a shift of 50 fringes which corresponds to an index change of  $\Delta n = 6.9 \times 10^{-3}$ . The heater-to-nearest-waveguide separation is  $20\mu\text{m}$  and the next waveguide is a further  $20\mu\text{m}$ . No difference in the index changes was observed between the waveguides separated by  $20\mu\text{m}$ . This result indicates that if steady state heating is present, the waveguide separation in the AMZI arms is insufficient to prevent thermal diffusion from equalising the index changes in two waveguides. Switching therefore cannot be induced in this AMZI by a steady state thermal nonlinearity. However the situation is not the same if a time varying heating current is applied. This was investigated next.

The parameter of initial interest is the relaxation time of the effect. This was determined by using an a.c. heating current to induce the index change which was, again, measured using an external interferometer. This time however a small area photodiode monitored the fringe shift. A triangular waveform was used to drive the heater and the signal power supply was configured with the minima of the waveform at zero so that the applied voltage was always positive. As the signal was applied, a corresponding variation in detected signal was measured as the



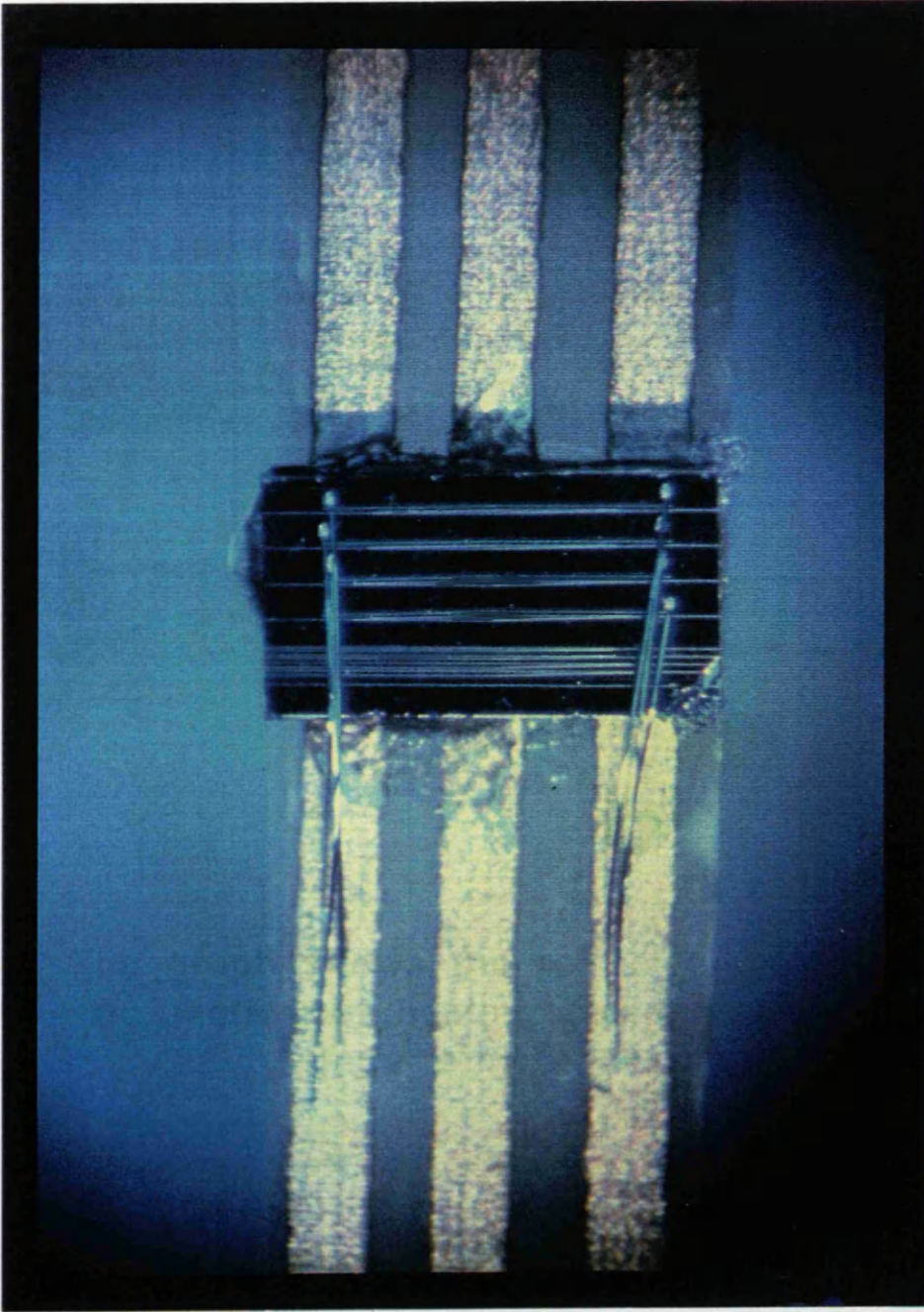
**Straight waveguide with heater mounted on circuit board.**

**Figure 6.5.3**

Asymmetric Bloch-Zehnder device with heater mounted on circuit board.

**Figure 6.5.4**

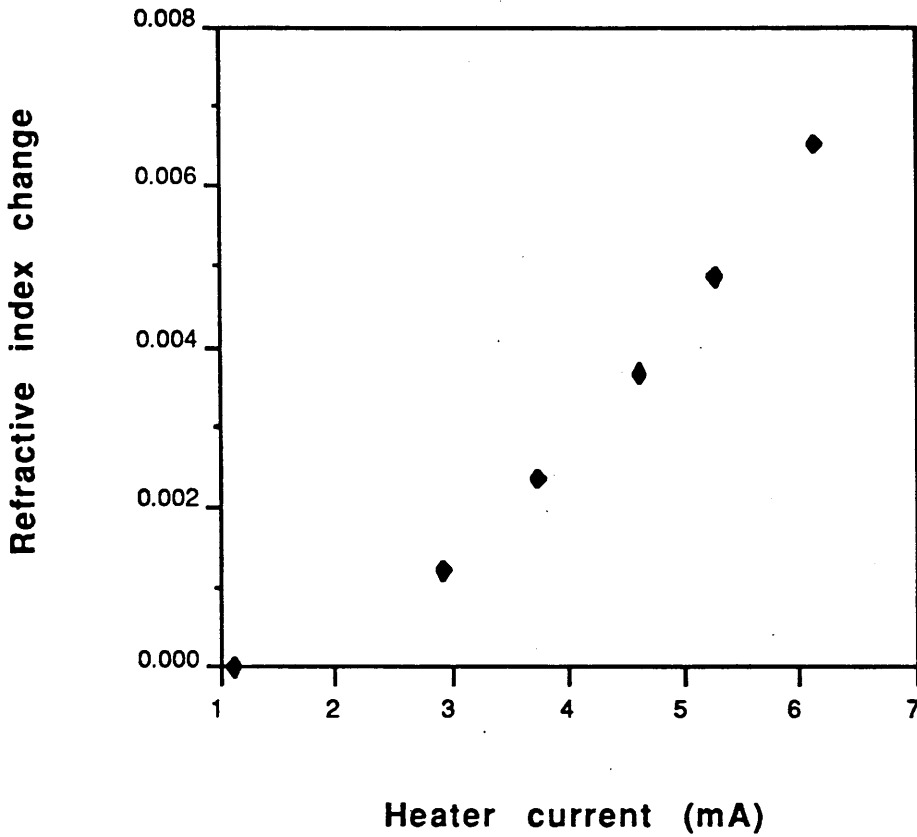
Thermal Refractive Index  
change vs Heater current.



Asymmetric Mach-Zehnder device with heater mounted on circuit board.

Figure 6.5.4

### Thermal Refractive Index change vs Heater current.



The graph shows the refractive index change as a function of heating current as derived from fringe shift measurements.

Figure 6.5.5

fringes moved back and forth over the detector. Figure 6.5.6 shows the heating current and a typical signal from the photodiode as the fringes shift back and forward. One forward and backward shift occurred for each cycle of the supply current. The peak current applied was 4.7mA and this resulted in a shift of about three fringes. (Note that the net fringe shift per unit current with this a.c. configuration has effectively decreased by over an order of magnitude compared with that obtained using the d.c. heating current. By increasing the a.c. frequency and observing when the fringe shift started decreasing, it was possible to determine the time it takes for heat to be dissipated from the vicinity of the waveguide. This is because if the period of the heating current is smaller than the dissipation time, the effects begin to integrate and the magnitude of the variation in refractive index per cycle decreases. This was observed to happen when the frequency reached 12 Hz which corresponds to a heat dissipation time of 83ms as shown in figure 6.5.7.

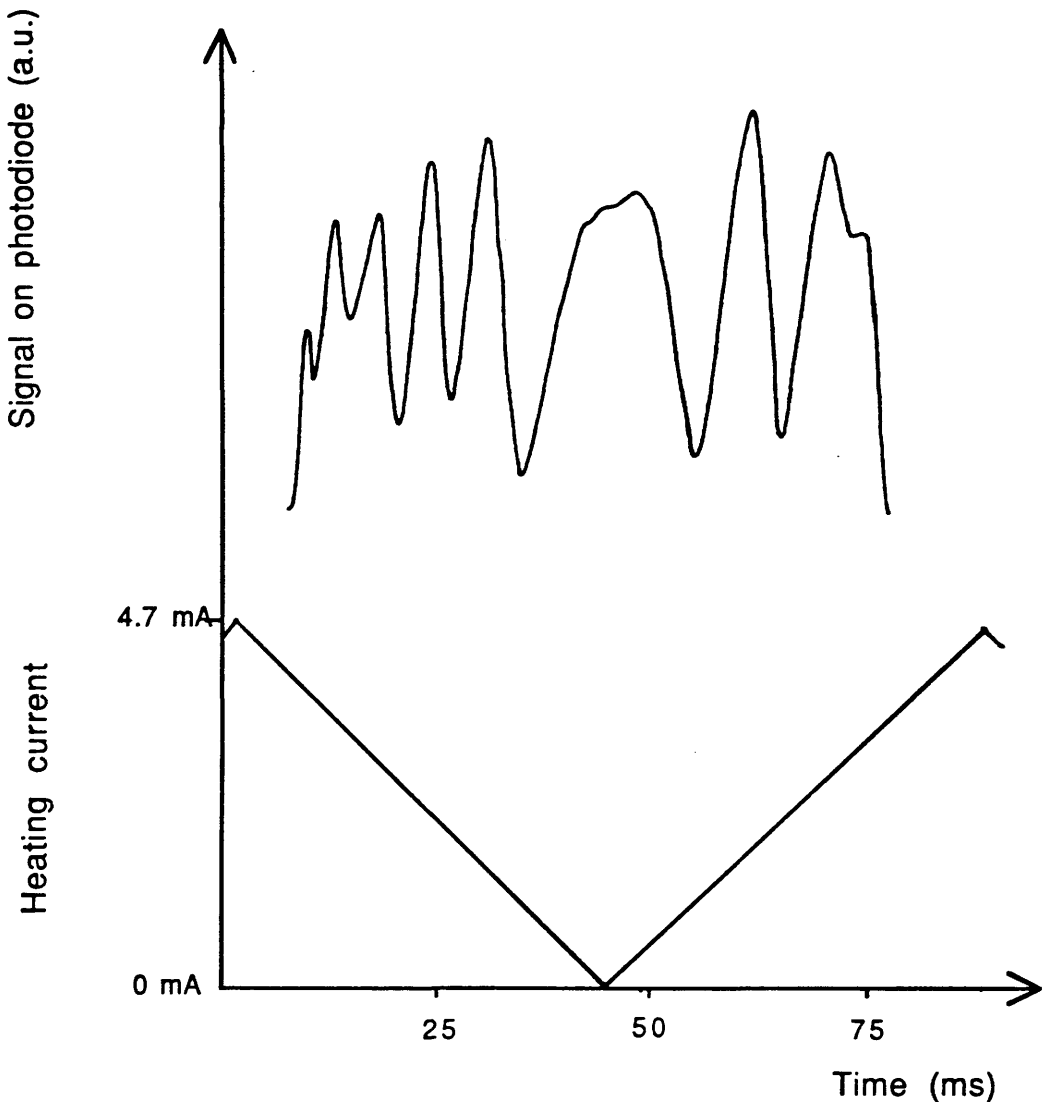
It is important to note the differing conditions between the experiment described here and that performed by Aitchison et al[8]. These authors observed thermal nonlinearities with relaxation times of a few microseconds because they used a pulsed laser with a pulse repetition time considerably larger than the relaxation time of the thermal effect. In the above experiment however the effect is induced by a triangular waveform which has a significant "average value" contribution to the thermal effect. The reason such a waveform was used was because a pulsed heating current with a large mark-to-space ratio could not be readily applied in testing the switching action of the AMZI with the continuous high pulse rate output of the dye laser. Unless the laser beam is pulsed at a similar rate and is in synchronism with the switching current, the switched state of the device output is not observable with current pulses of extreme mark-to-space ratios.

### 6.5.3 Theoretical considerations.

In the above experiment a current of 4.7mA gave rise to a fringe shift of three fringes which is equivalent to a refractive index change of  $\Delta n = 6 \times 10^{-4}$ . To corroborate this observation with the theoretically expected thermal index change it is necessary to first establish the thermal power generated by ohmic heating of the nichrome strips. This requires the resistance to be measured.

Measurements of the resistance were made between the contacts varying in separation from 1000 $\mu\text{m}$  to 5000 $\mu\text{m}$ . Figure 6.5.8 shows these results. A very well defined straight line was obtained indicating a good dimensional and compositional uniformity of the heater. From the slope of the line, the resistance per unit length

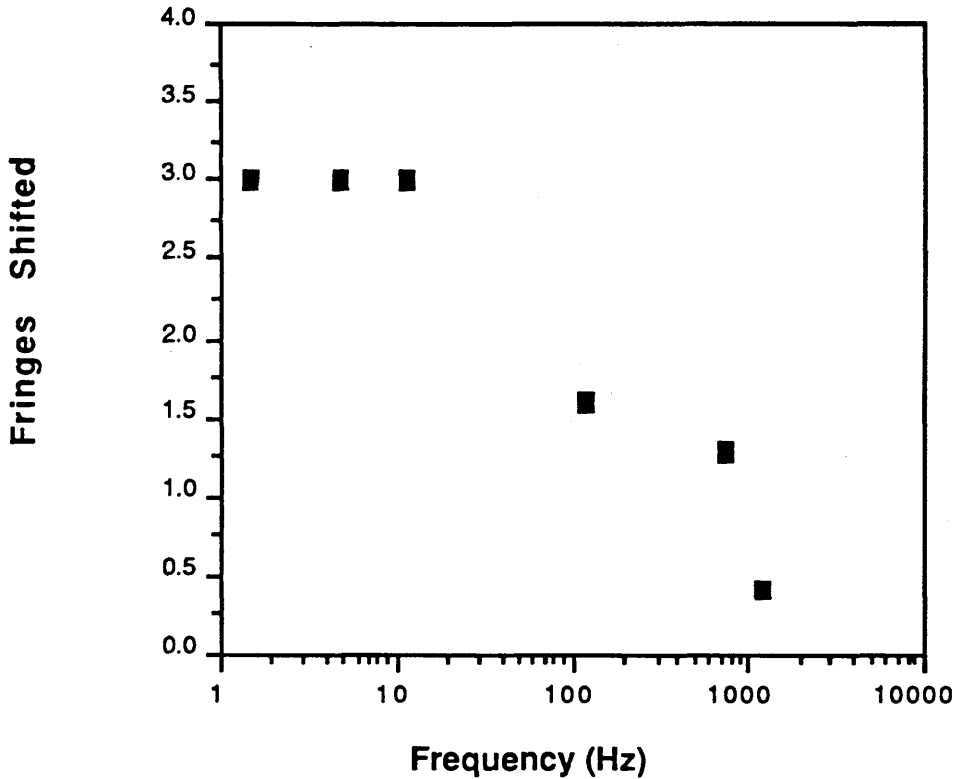
## Photodiode signal and heating current vs time



This graph shows the triangular waveform used to drive the heater (lower trace) and the resulting signal (top trace) from a photodiode onto which interference fringes were incident. The photodiode signal results from the back and forth movement of the fringes as the time varying heating induces a corresponding variation in the refractive index. In the above case the signal frequency is 11.6Hz.

**Figure 6.5.6**

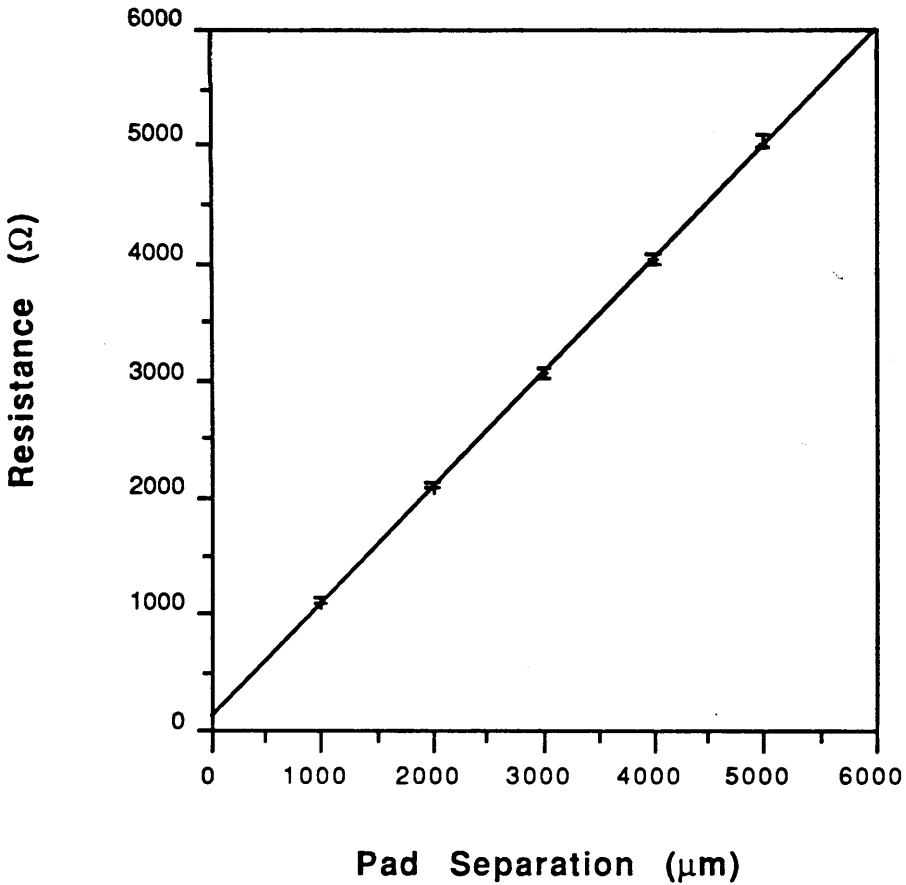
**Maximum fringe shift vs frequency**



The graph shows the maximum thermal fringe shift obtained as a function of frequency. The fringe shift decreases suddenly after a frequency of 12Hz indicating that the heat dissipation time from the vicinity of the waveguide is around 80ms.

**Figure 6.5.7**

### Resistance vs Length of NiCr Pad



The measured resistance of the heating strip as a function of length. The graph indicates that the heater has a resistance of  $981\Omega/\text{mm}$ .

Figure 6.5.8

of the heater strip was found to be  $981\Omega \text{ mm}^{-1}$ . The intercept of the line represents the total resistance of the connections external to the heater strip and these include the length of strip from the pad to the main heater strip, the aluminium bonding wire, the copper strip on the circuit board and the multicore copper wire connected to the power supply. This adds up to a total resistance of  $130\Omega$ . These results can be used to calculate the ohmic heating power of the metal strips.

An estimate is now made of the index change expected from the above conditions. This is done by considering the amount of thermal energy transferred to the material in the vicinity of the waveguide. From a knowledge of some of the thermal parameters of the material, it is possible to estimate the refractive index change induced by the heaters. The current in the above experiment was applied between two contacts connected by a heater length of 4mm. The resistance of the heater is therefore  $3924\Omega$ . The peak current is 4.7mA, and so the peak ohmic power generated is  $(=I^2R)$  87mW. Not all of this energy is dissipated into the sample and some of it is lost to the atmosphere by radiation and convection. It turns out, as will be seen, that the actual amounts lost this way are small. Radiation losses are estimated first.

The amount of energy radiated by the surface of a body depends on the temperature and the surface qualities (e.g. roughness) of the body. The total radiation is given by the Stefan– Boltzmann law [9] which states that

$$E = \epsilon\sigma T^4 \tag{6.5.3.1}$$

where  $E$  is the power radiated per unit surface area ( $\text{W m}^{-2}$ ),  $T$  is the temperature (K),  $\sigma$  is the Stefan– Boltzmann constant with value  $\sigma=5.670 \times 10^{-8} \text{ W m}^{-2} \text{ K}^{-4}$ , and  $\epsilon$  is the emissivity which is a characteristic property of the radiating surface. (For an ideal blackbody  $\epsilon$  is unity). To calculate  $E$  the temperature of the heater is required. However the exact value of this is not known. The case is therefore simplified by considering the upper bound to the temperature of the heater under the measurement conditions so far. From this an upper bound of the power radiated by the heater can be calculated.

The upper bound to the heater temperature can be estimated from the fringe shift measurements of the previous section. The maximum index change was induced with a d.c. current and was about 0.006 (see figure 6.5.5) with a heater current of approximately 6mA. The variation of refractive index with temperature was measured by Aitchison et al[8] to be

$$\frac{\partial n}{\partial T} = 8 \times 10^{-4} \text{ K}^{-1}.$$

This indicates that an increase of about 8 degrees from room temperature is required for a refractive index change of  $6 \times 10^{-3}$ . This corresponds to an absolute heater temperature of about 310K. Using this temperature and an emissivity  $\epsilon = 0.3$ , which is typical of unpolished metals<sup>[9]</sup>, the radiation power density is given by equation 6.5.3.1 to be  $157 \text{ W m}^{-2}$ . The heater area is  $4\text{mm} \times 20\mu\text{m}$  so the total power radiated is therefore  $13\mu\text{W}$ . This is negligible compared to the total power produced by ohmic heating which is at least three orders of magnitude higher. Of course the temperature of the metal may be higher than the 310K used in the calculation since this was derived from the temperature change of the AlGaAs and not the metal directly. However, even if the temperature of the heater was 1000K the radiation power still only constitutes 1% of the total power produced. The amount of energy produced by the heater which is lost by radiation can therefore be neglected.

The calculation of thermal energy loss by convection is not as simple as that for radiation. It has been shown [9] that transport of thermal energy by convection from warm horizontal surfaces is minimal due to restricted flow of convection currents. Convection losses will therefore also be ignored. In summary therefore, it can be concluded that since heat loss by radiation and convection is negligible, virtually all of the thermal power produced by the heater is conducted into the sample.

The expected theoretical index change for non-steady-state heating is now estimated. The energy gained by a given mass,  $m$ , of material is related to its temperature change,  $\Delta T$ , by

$$\Delta E = mc_p \Delta T$$

where  $c_p$  is the specific heat capacity at constant pressure. It follows from this equation that

$$\frac{\Delta E}{\Delta V} = \rho c_p \Delta n \left[ \frac{\partial n}{\partial T} \right]^{-1} \quad (6.5.3.2)$$

where  $\rho$  is the density and  $\Delta V$  is the volume of the region being considered. The values of  $\rho$ ,  $c_p$  and the term in brackets are available from the literature and are summarised below in figure 6.5.9. Here,  $\Delta E$  is the ohmic energy produced in one period of the heating cycle (83ms) and  $\Delta V$  is the volume over which this heat is dissipated. This volume is obtained by application of the solution to the thermal

diffusion equation given earlier in section 5.3.4.

$$T(r, t) = \frac{\sigma_0^2 T_0}{4D_{th}t + \sigma_0^2} \exp \left[ \frac{-r^2}{4D_{th}t + \sigma_0^2} \right]. \quad (6.3.4.4)$$

where the exponential term describes the extent of the temperature distribution. Strictly, the equation is valid only for a cylindrical Gaussian temperature distribution and for radial dissipation. In this non-steady-state case however there is negligible heat exchange occurring between the sample surface and the air above the sample. The situation is therefore approximated by considering the lower "semi infinite" plane of the above analytically obtained distribution.

Applying the diffusion equation and using the value of  $D_{th}$  listed in figure 6.5.9, the 1/e radius of the distribution is found to be 1.50mm. To calculate the effective volume of heating, an effective radius of the Gaussian thermal distribution is calculated. This is defined as the half width of the rectangle which has height equal to the value of the distribution at  $r=0$ , and area equal to the area under the Gaussian. The effective radius,  $r_{eff}$  is related to the 1/e radius,  $r_{1/e}$ , by

$$r_{eff} = \frac{r_{1/e} \sqrt{\pi}}{2}$$

and the effective radius is therefore 1.33mm. The length of the heater section used in this case is 4mm and the half-cylinder of volume heated is therefore  $1.1 \times 10^{-8} \text{m}^3$ . The heating current waveform is triangular with a maximum value of 4.67mA and a period of 83ms in this case. The resistance of the 4mm long heater

PARAMETER	VALUE	REFERENCE
$\rho$	$4.88 \times 10^6 \text{ g m}^{-3}$	[7]
$c_p$	$0.369 \text{ J K}^{-1} \text{ g}^{-1}$	[7]
$\frac{\partial n}{\partial T}$	$8 \times 10^{-4} \text{ K}^{-1}$	[8]
$D_{th}$	$6.77 \times 10^{-6} \text{ m}^2 \text{ s}^{-1}$	[7]

Figure 6.5.9

The parameters used in the calculation of the theoretically expected thermal refractive index change.

pad was  $3924\Omega$  as determined from the measurements reported at the beginning of this section. It can thus be calculated that 2.37mJ of ohmic energy is dissipated into the sample every 83ms. Putting this information into equation 6.5.3.2 along with the data of figure 6.5.9, a refractive index change of  $0.96 \times 10^{-4}$  is expected. The actual index change in this case was  $6 \times 10^{-4}$  which is 6 times larger. This discrepancy is reasonable considering the **approximations made in determining the volume and times of heat dissipation.**

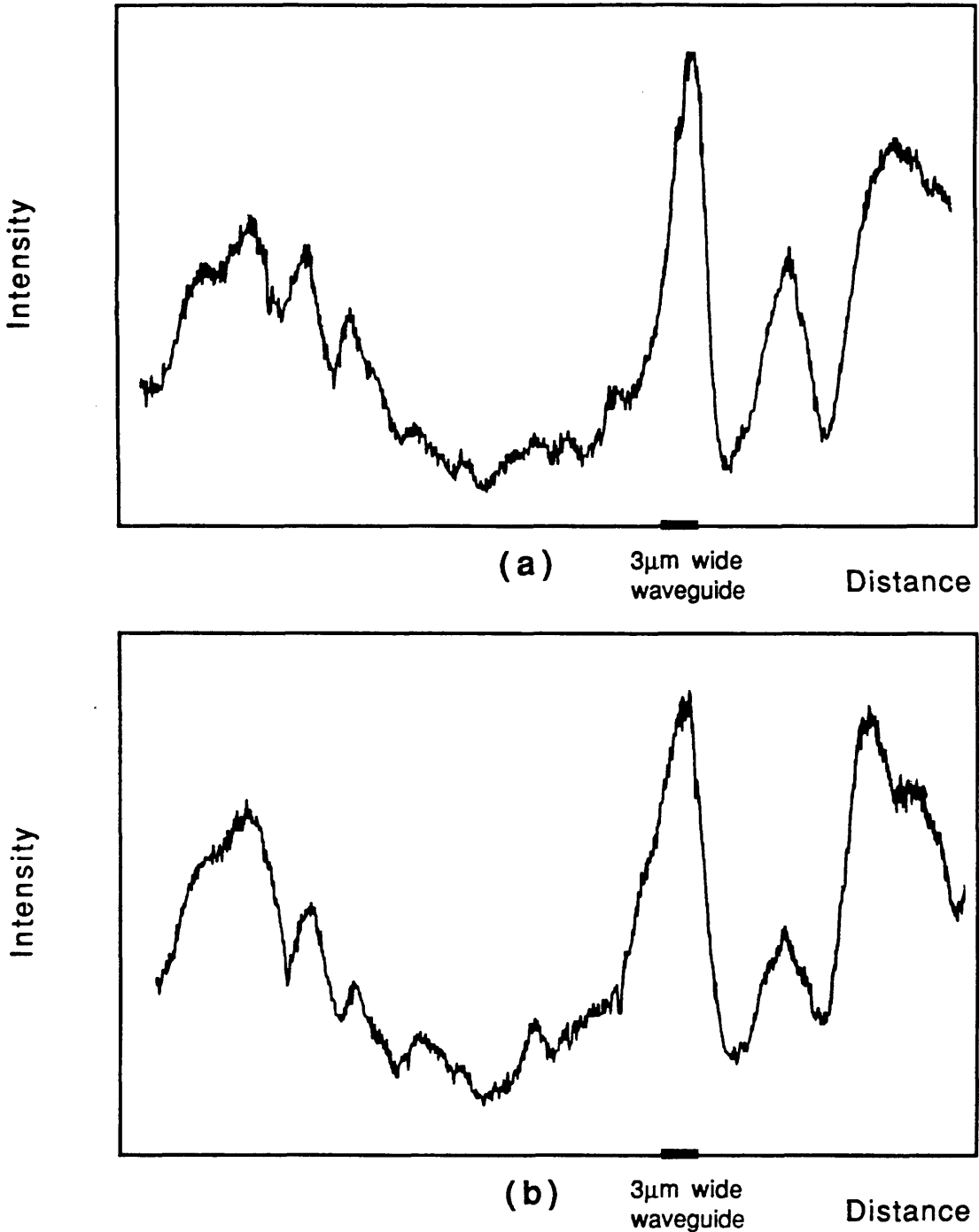
A more detailed study of the thermal characteristics could not be performed because of the restricted time available for the completion of the project and further experimental and theoretical work is necessary especially in terms of characterising the temperature distribution within the sample.

#### 6.5.4 Thermally induced switching in the AMZI.

The device was aligned as described earlier and the modal output was observed on a Hamamatsu camera. The output mode in these thermal AMZI's was not as well defined as that obtained in the all-optical device because of the blunted Y-junctions and this resulted in a significant presence of radiation modes at the output of the device. The  $1.5^\circ$  devices were of poor quality in that a clearly defined output mode was not seen at all. The  $1^\circ$  device had a better defined modal output but even so there was much radiation present in the surrounding slab region.

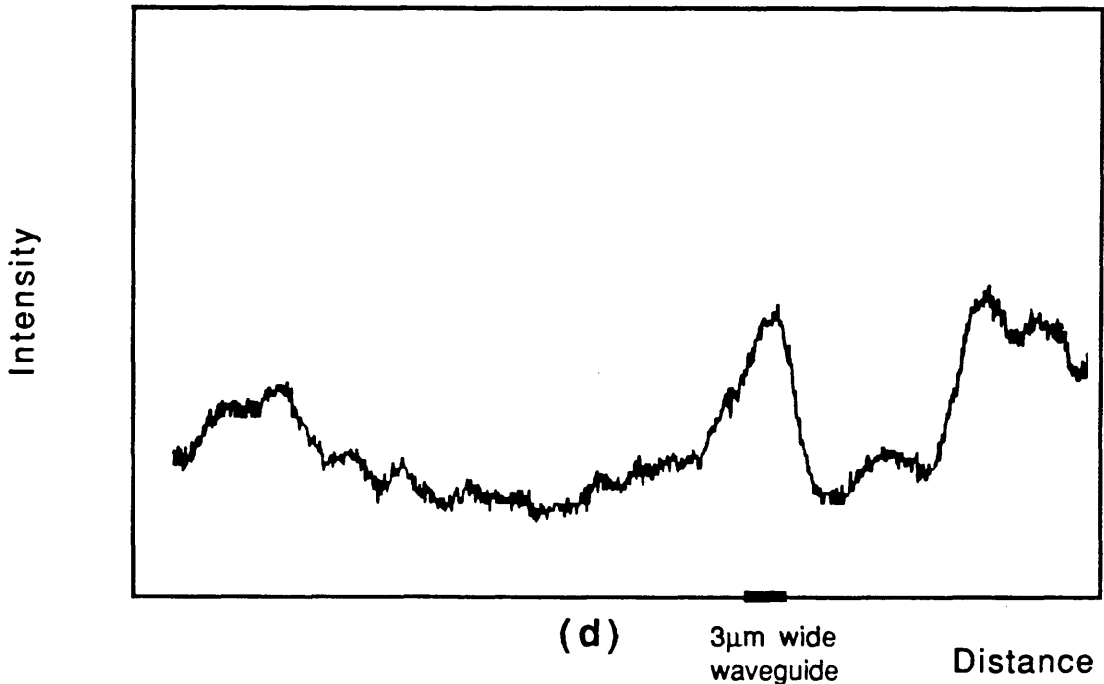
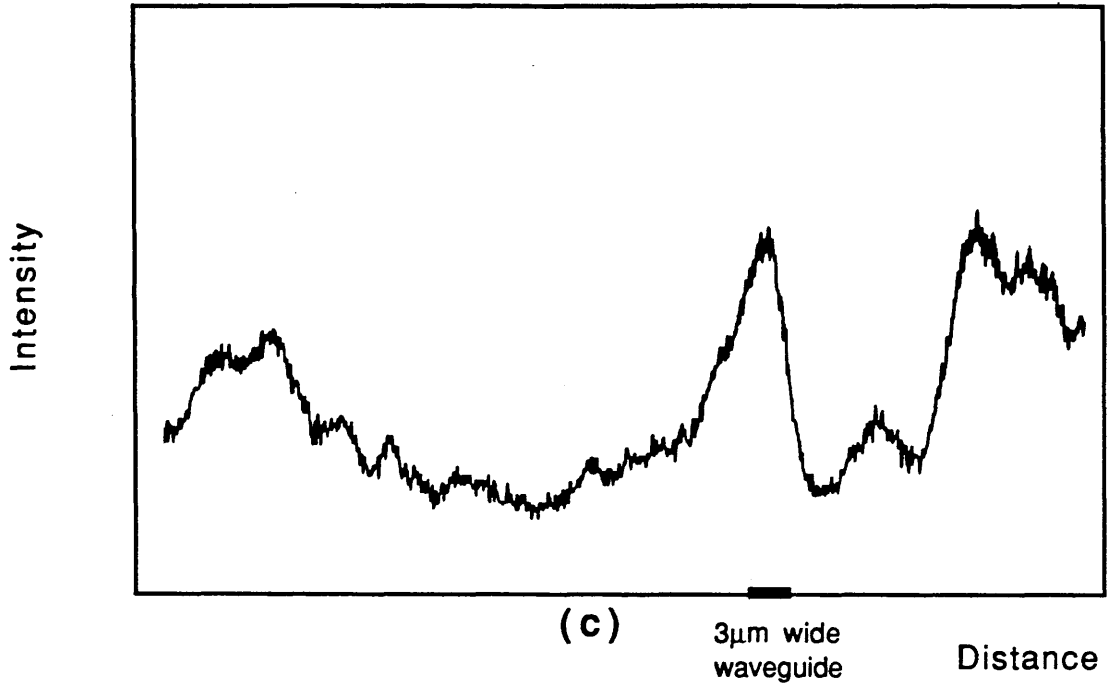
Switching was investigated in the  $1^\circ$  thermal AMZI for different heating currents. The output was observed and recorded before and after switching the supply on.

No immediate change was seen in the output for currents up to 10mA. This is due to the lack of sufficient separation between the arms of the branches and confirms earlier conclusions. The sample eventually heated up resulting in misalignment and a drastic reduction in the input coupling. For a 10mA current, the device became misaligned after 30 seconds. It was only when the current was set to 20mA that modal switching was observed. In this case an immediate and distinct change in the output field was seen when the current was switched on. This is because a larger temperature change is induced in this case and this results in a temperature gradient large enough to give a differential refractive index change between the two AMZI arms. However the sample heated up and became misaligned after 4 seconds. Figures 6.5.10 (a) to (d) show the output mode profiles for a heating current of 20mA at various times after switching on the supply current. Figure (a) shows the output field distribution of the AMZI with no heating



The outputs of the thermal asymmetric Mach-Zehnder device are shown in the above graphs. The poor shape of the output mode profile is indicative of the presence of a large contribution from radiation modes. (a) shows the output with no current and (b) shows the output 1 second after switching on a current of 20mA. The presence of the shoulder-like on the guided mode in (b) indicates that a phase shift has been introduced between the two arms of the device on switching the current.

Figure 6.5.10



The above graphs show the outputs of the thermal asymmetric Mach-Zehnder device. Both graphs are for a heating current of 20mA. (c) shows the output after 2 seconds and (d) shows the output after 4 seconds. The shape of the profile has not changed throughout figures (b), (c) and (d) which suggests that there is no further phase change occurring between the two arms of the device. However the decreasing overall signal indicates that vertical misalignment of the sample is occurring.

Figure 6.5.10

applied. It can be seen that there is much radiation present at either side of the waveguide mode but even so, the modal peak is still very distinct. The reason for the poor modal quality of the device output has already been attributed to the blunted apex of the Y-junction. Figure (b) shows the output 1 second after switching the current on and it can be seen that a shoulder-like feature has appeared at the left side of the main peak which indicates a small change in the relative phases of the two arms. After another second, thermal misalignment starts to become significant and the field intensity across the whole device begins to decrease. The actual shape of the distribution does not change as can be seen in figures (c) and (d) and this suggests that the long term heating introduces vertical misalignment.

Although the change in mode shape in this case was not due to a complete  $\pi$ -phase shift there is nevertheless a distinct switching effect present. This should be more significant for higher heater currents but it was not possible to investigate this because the thermally induced misalignment effects were dominant. When the output of the device was monitored for currents higher than 30mA, immediate misalignment occurred.

One way to overcome this heating induced misalignment in future investigations would be to have a fixed coupling at the device input. This could be done by permanently pigtailed a fibre to the input waveguide for example.

## 6.6 Conclusions.

This chapter has described the investigations carried out to characterise the Asymmetric Mach-Zehnder interferometer. A theoretically predicted response of this device was obtained using the nonlinear BPM program with an effective index approximation to represent the actual waveguide structure. The device was then fabricated and the asymmetric power splitting ratios of the Y-junctions were measured. The nonlinear properties of the device were investigated but no nonlinear response was seen. This was then explained in terms of carrier and thermal diffusion effects which wash out any differential phase shift between the two arms of the device.

The size and relaxation times of thermal refractive index changes were investigated. The time taken for heat to be dissipated from the waveguide has been reported to be of the order of  $5\mu\text{s}$ [8]. It was difficult to verify this without using a pulsed laser with suitable pulse on:off times. The dye laser was not suitable for this because the pulse repetition time (13ns) is considerably smaller than the heat dissipation time of  $5\mu\text{s}$ . The integrating nature of the thermal

nonlinear effect was however verified by measuring the index change as a function of the frequency of the heating current. Under these conditions the relaxation time of the heating effect was measured to be the order of 90ms. On the basis of this, a theoretical index change was estimated and was found to be just over an order of magnitude of the actual measured  $\Delta n$ .

The reason why a pronounced switching action is not seen in the above device is that there is an insufficient differential refractive index change between the two arms of the AMZI. In other words there is an insufficient temperature gradient between the arms of the AMZI. One possible solution to this would be to use a pulsed laser source with a sufficiently long delay between the pulses which would minimise the long term heating effects. There are additional ways of further reducing the problem. One could increase the maximum arm separation by increasing the total length of the AMZI arm section. The waveguide separation is therefore increased at the widest point of the AMZI. However only a fraction of the total arm section experiences this increased separation. Another option would be to incorporate curved waveguides in the branching regions before and after the asymmetric Y-junctions so that the waveguides separate quickly. In this way, for a given device length, a larger fraction of the total arm section sees an increased separation. Efficient heatsinking or thermoelectric cooling of the device would also help as this would mean that higher temperature gradients could be induced by the heater and hence larger differences in the refractive indices between the two arms of the device.

## 6.7 References to Chapter Six.

- [1] H. Kawaguchi, "Proposal for a new all-optical waveguide functional device", *Opt. Lett.*, vol 10, no 8, pp411-413, 1985.
- [2] R. H. Rediker, F. J. Leonberger, "Analysis of Integrated-Optics Near 3dB coupler and Mach Zehnder Interferometric Modulator using a Four-Port Scattering Matrix", *IEEE J. Quant. Elec.*, vol QE-18, no 10, pp1813-1816, 1982.
- [3] T. J. Cullen, Ph.D Thesis, University of Glasgow, 1985.
- [4] P. E. Lagasse, R. Baets, "The Beam Propagation method in Integrated Optics", NATO Advanced Research Workshop on Hybrid formulation of wave propagation and scattering (1983).

- [5] T. Tamir (Ed), "Integrated Optics", Topics in Applied Physics, vol 7, Springer-Verlag, 1975.
- [6] R. J. Manning, D. W. Crust, D. W. Craig, A. Miller, K. Woodbridge, "Transient-grating studies in GaAs/AlGaAs multiple quantum wells", J. Mod. Opt., vol 53, no 3, pp541-551, 1988.
- [7] S. Adachi, "GaAs, AlAs and  $\text{Al}_x\text{Ga}_{1-x}\text{As}$ : Material parameters for use in research and device applications", J. Appl. Phys., vol 58, no 3, 1985.
- [8] J. S. Aitchison, J. D. Valera, A.C. Walker, S. Ritchie, P. M. Rodgers, P. McIlroy, G. I. Stegeman, "Whole-sample and localised induced-absorption optical bistability in GaAlAs waveguides", Appl. Phys. Letts., vol 51, no 8, pp561-563, 1987.
- [9] A. J. Chapman, "Heat Transfer", Collier Macmillan Publishing Co., London, 1984.

## CHAPTER SEVEN

### CONCLUSIONS

#### 7.1 Summary of thesis.

This thesis has reported investigations of nonlinear optical effects in AlGaAs/GaAs waveguides and their application in the implementation of the Asymmetric Mach Zehnder Interferometer: a nonlinear optical logic gate. The various nonlinear optical effects present in AlGaAs/GaAs systems were reviewed and discussed in Chapter Two. Then, in Chapter Three, aspects of the optical properties of waveguides incorporating a multiple quantum well guiding layer were considered and a design procedure for such structures was established. Following this, Chapter Four described the device fabrication and processing steps. Experiments to characterise the linear and nonlinear properties of waveguides were described in Chapter Five where observations of nonlinear effects were reported and discussed. It was also established in this chapter that the optical nonlinearities in these waveguides under these particular excitation conditions were, for the most part, dominated by thermal effects. In Chapter Six, the theoretical and experimental studies of the Asymmetric Mach Zehnder Interferometer (AMZI) were reported. The results of this chapter showed some important limiting factors which affect the operation of the AMZI and means for the reduction of these were then discussed in terms of possible modifications to the device geometry. Also in Chapter Six, thermal effects were investigated and characterised in some detail. A device incorporating heater pads was fabricated and this enabled thermally induced switching to be observed in an AMZI.

#### 7.2 Conclusions and suggestions for future work.

It was the objective of this project to use carrier induced optical nonlinearities arising to fabricate an optical logic gate. Several problems were encountered in the course of this work. The presence of thermal effects made it difficult to observe electronic nonlinearities in the waveguides. Indeed switching action caused by a thermal nonlinearity is undesirable in fast switching devices because of the long relaxation time constants associated with these effects. The thermal nonlinearity has a relaxation time of about  $5\mu\text{s}$  whereas the electronic effect (which is opposite in sign) has a relaxation time of 10–20 ns. In fact, when the waveguide is under pulsed excitation with pulse repetition times of about 10–20ns, the thermal

nonlinearity is integrated over a larger time interval than the electronic effect and is consequently disproportionately larger than the electronic effect.

Another problem which makes it difficult to implement nonlinear switching via an electronic effect was that of carrier interdiffusion. Both the Asymmetric Mach Zehnder Interferometer and the Nonlinear Directional Coupler (which was not investigated in this thesis) depend on an intensity induced differential phase shift between two waveguides in proximity. However, as was discussed in Chapters Five and Six, photoexcited carriers in a stripe-loaded waveguide tend to laterally diffuse out and away from the region of the guided mode and hence reduce any refractive index difference between closely spaced waveguides.

There is, however, a means by which both the problem of the size of the electronic effect and that of carrier interdiffusion may be reduced. The waveguide structure can be modified from a strip-loaded design to that of a rib waveguide by etching completely through the waveguiding layer and thus confining the carriers to within the rib. It was discussed in section 5.4.4 that by preventing the outdiffusion of carriers by this means, the carrier density decay time could be increased from about 10–20ns to about 200–300ns. By increasing the decay time in this way, the net observed electronic effect is increased by over an order of magnitude. This makes it possible for the net electronic effect to be larger than the net thermal effect. It is unlikely that this modification to the waveguide geometry will affect the time constant of the thermal effect since changing the rib height by such a small amount ( $\approx 1\mu\text{m}$ ) does not significantly reduce the downwards heat flow from the rib to the rest of the sample. However, even though several problems are reduced by use of a rib waveguide geometry, this is not an ideal solution for the implementation of a fast switching device because the carrier confinement also decreases the switching speed of the device.

It has been seen that the net thermal effect is larger in magnitude than the electronic effect under the pulsed excitation conditions discussed above, but this may not be a problem in an AMZI since the thermal effect is more widespread in extent and its contribution to the index change in each of the branches is equalised. As long as the *differential* refractive index change between the two arms due to electronic effects is large enough, a non-thermal switching action can still be induced in an AMZI.

It was calculated in section 6.4.3 that there is a sufficiently sized electronic nonlinearity present to induce switching without any need for increasing the effect lifetime. Hence it is not necessary to increase the magnitude of the net electronic effect by etching the rib through the guiding layer. The problem with the AMZI device is therefore that of carrier interdiffusion between the arms of the device. It is therefore suggested that the AMZI is modified in the following manner.

A recess should be etched between the two arms of the device to prevent the carriers diffusing out of any of the arms from entering the adjacent arm. This is shown in figure 7.1. In this way, any electronic nonlinearity is stopped from "spilling over" from one waveguide to another. Also, because the rib has not been completely etched through into the guiding layer, the response speed of the switch is not limited by the presence of the confined carriers within the waveguide. In fact, the device speed is faster than the recombination time of the photoexcited carriers because the carriers diffuse out of the structure in a time shorter than the recombination time.

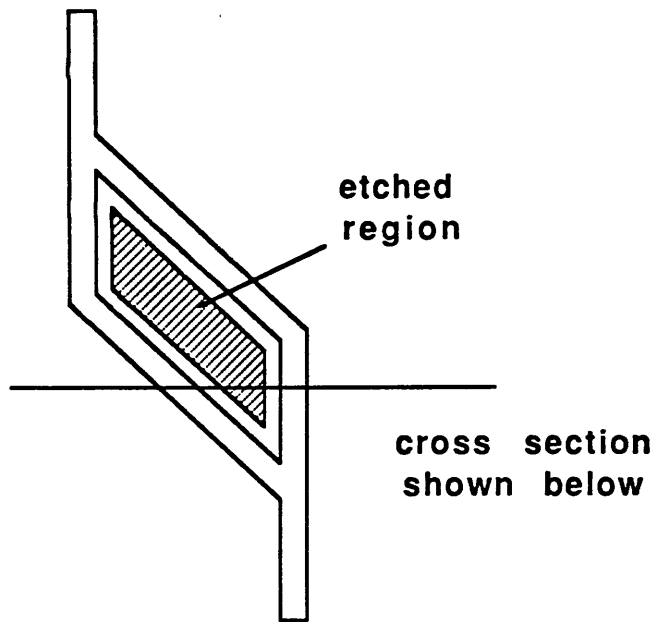
Other additional improvements to the AMZI structure are also recommended:

(i) Curved Y-junction branches should be incorporated so that the arms of the device separate within a shorter distance and thus a shorter device is achieved for a given arm length.

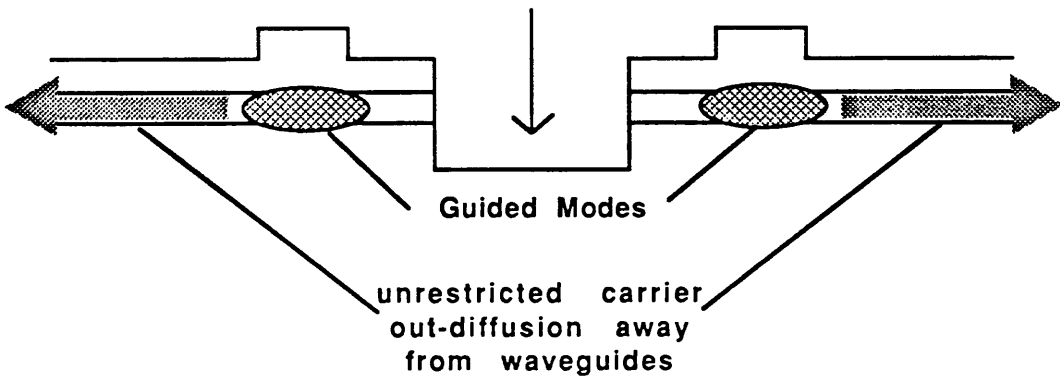
(ii) It was found from the BPM investigations and the experimental observations of Chapter Six that the output waveguide of an AMZI in a switched state may still contain a significant presence of undesirable radiation modes. It is therefore recommended that the output waveguide incorporates a scheme to strip off unwanted radiation modes. This could be implemented by the inclusion of a suitably designed S-bend.

These suggested improvements to the AMZI design should help overcome the problems discovered in the course of this project.

# Improved Asymmetric Mach-Zehnder Interferometer



Etched region restricts carrier interdiffusion between strip-loaded waveguides.



The upper diagram shows the location of an etched region included to prevent carrier interdiffusion between the arms of the device. The lower diagram shows a cross-section of the device.

Figure 7.1

## **APPENDICES**

## APPENDIX I

### DERIVATION OF THE EIGENVALUE EQUATION FOR A SINGLE FINITE WELL WITH CHANGE OF MASS INCLUDED IN BOUNDARY CONDITIONS.

For the structure shown in figure (A.1) there are three regions of interest. The wave functions in these regions can be written

$$\begin{aligned} \text{Region 1:} \quad & \psi_1(x) = Ce^{\alpha x} \\ \text{Region 2:} \quad & \psi_2(x) = A\cos(\beta x) + B\sin(\beta x) \\ \text{Region 3:} \quad & \psi_3(x) = De^{-\alpha x} \end{aligned} \tag{A.1}$$

where

$$\alpha^2 = \frac{2m_b(V-E)}{\hbar^2} \qquad \beta^2 = \frac{2m_w E}{\hbar^2}$$

where  $m$  is the particle mass (subscript denoting whether in barrier or in well),  $V$  is the well depth and  $E$  is the energy eigenvalue with respect to the bottom of the well.

#### Finite Potential Well

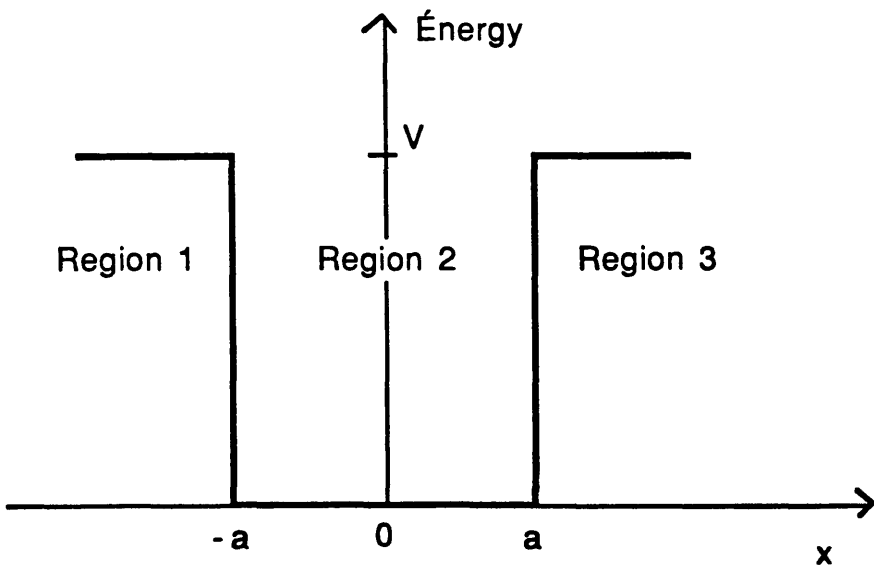


Figure A1.1

The boundary conditions require continuity of  $\psi$  and  $(1/m)(\delta\psi/\delta x)$ . In most textbook derivations the  $1/m$  term is neglected in the boundary conditions because the mass is assumed to remain constant in the well and barrier regions. When applying these boundary conditions to semiconductor structures and when the effective mass approximation is being used the  $1/m$  term has to be included to prevent the conservation of probability from being violated. Applying these boundary conditions to the region interfaces (at  $x = -a$  and  $x = a$ ), equations (A.1) give

at  $x = -a$

$$Ce^{-\alpha a} = A\cos(\beta a) - B\sin(\beta a) \quad (\text{A.2a})$$

$$\frac{\alpha Ce^{-\alpha a}}{m_b} = \frac{\beta A\sin(\beta a) + \beta B\cos(\beta a)}{m_w} \quad (\text{A.2b})$$

at  $x = a$

$$De^{-\alpha a} = A\cos(\beta a) + B\sin(\beta a) \quad (\text{A.2c})$$

$$-\frac{\alpha De^{-\alpha a}}{m_b} = \frac{-\beta A\sin(\beta a) + \beta B\cos(\beta a)}{m_w} \quad (\text{A.2d})$$

Manipulating equations (A.2) gives

$$(C+D)e^{-\alpha a} = 2A\cos(\beta a) \quad (\text{A.3a})$$

$$-(C-D)e^{-\alpha a} = 2B\sin(\beta a) \quad (\text{A.3b})$$

$$\frac{\alpha}{m_b} (C+D)e^{-\alpha a} = \frac{\beta}{m_w} 2A\sin(\beta a) \quad (\text{A.3c})$$

$$\frac{\alpha}{m_b} (C-D)e^{-\alpha a} = \frac{\beta}{m_w} 2B\cos(\beta a) \quad (\text{A.3d})$$

Dividing (A.3c) by (A.3a) and (A.3d) by (A.3b)

$$\frac{\alpha}{m_b} - \frac{\beta}{m_b} \tan(\beta a) = 0 \quad (\text{A.4})$$

$$\frac{\alpha}{m_b} + \frac{\beta}{m_b} \cot(\beta a) = 0$$

where the two equations represent the solutions for the symmetric and antisymmetric wavefunctions respectively.

It is necessary to write equations (A.1) in a more suitable form for solving by numerical means. Multiplying and using the identity " $\cot(x) - \tan(x) = 2\cot(2x)$ " the following equation is obtained:

$$2a\beta - \tan^{-1} \left[ \frac{m_w m_b 2\alpha\beta}{m_b^2 \beta^2 - m_w^2 \alpha^2} \right] - n\pi = 0.$$

which contains the solutions for both the symmetric and antisymmetric wavefunctions. The integer  $n$  labels the different energy levels. The equation can be further simplified by using the identity

$$\tan^{-1} (A) + \tan^{-1} (B) = \tan^{-1} \left[ \frac{A + B}{1 - AB} \right]$$

to give

$$2a\beta - \tan^{-1} \left[ \frac{m_w \alpha}{m_b \beta} \right] - n\pi = 0.$$

This equation is now in the form used to calculate the energy eigenvalues for the finite potential well.

#### References.

(See, for example, A Textbook of Quantum Mechanics, Matthews and Venkatesan, Tata McGraw-Hill Publishing company, New Delhi, 1982.)

## APPENDIX II

### PROGRAM LISTINGS

Program Fourlay3;

```
{**** Calculates effective index for 4 layer slab.      ****}
{**** Uses eigenvalue equation obtained from solving   ****}
{**** boundary conditions for TE and TM modes of       ****}
{**** propagation in the slab.                         ****}
{**** Written by B.S.Bhumbra 16/2/87                   ****}
{**** Routine for power in layer 2 inserted 13/4/89    ****}
```

Const

Error = 1e-7;

Var

```
N1, N2, N3, N4, Eta1, Eta2, Eta3, Eta4,
LambdaInp, Lambda, Kprop, K1, K2, K3, K4, D2Inp, D2,
D3Inp, D3, Neffmin, Neffmid, Neffmax, Fmin, Fmid, Fmax,
A, B, C, D, E, F, Term1, Term2, Term3, Term4,
Sub1, Sub2, Sub3, Frac2, Fracl, Frac3, Frac4,
DlcInp, Dlc, Subst : Real;
Answer : String[2];
LeaveProg, Exit, Foundroot, FirstTime : Boolean;
Mode, Count : Integer;
```

Function FNeff(Neff:Real):Real;

Var

Sub1, Sub2, Sub3, Sub4 : Real;

Begin

```
K1 := Kprop*Sqrt(Neff*Neff-N1*N1);
K2 := Kprop*Sqrt(N2*N2-Neff*Neff);
K3 := Kprop*Sqrt(Neff*Neff-N3*N3);
K4 := Kprop*Sqrt(Neff*Neff-N4*N4);
Sub3 := exp(K3*D3)*(Eta3*K3+Eta4*K4);
Sub4 := exp(-1*K3*D3)*(Eta3*K3-Eta4*K4);
Sub1 := Eta3*K3*(Sub3-Sub4);
Sub2 := Eta2*K2*(Sub3+Sub4);
Sub2 := Sub1/Sub2;
Sub1 := Eta1*K1/(Eta2*K2);
FNeff := K2*D2 - ArcTan(Sub1) -ArcTan(Sub2) -Mode*Pi;
End;
```

Begin (\*\*Main Program\*\*)

ClrScr;

Writeln('Program FOURLAYER - calculates effective index of fourlayer dielectr

Writeln('Can be used for threelayer - recommend use of dummy layer with N3<=N

FirstTime := True;

LeaveProg := False;

Repeat

Writeln;

If FirstTime=False Then ClrScr;

Writeln('Previous data (if any) shown in [ ].');

Writeln('Type only 'Enter' for no change.');

```

Writeln;
Exit := False;
Repeat
  Writeln('Type in N1 N2 N3 N4 ( N1<N2>N3>N4 )');
  If Not(FirstTime) Then Writeln(['',N1:10:6,N2:10:6,N3:10:6,N4:10:6,' ']);
  Readln(N1,N2,N3,N4);
  If ((N1<N2) And (N2>N3)) And (N3>N4) Then Exit := True;
Until Exit;
Writeln('Type in wavelength (nm)');
If Not(FirstTime) Then Writeln(['',LambdaInp:7:0,' ']);
Readln(LambdaInp);
Lambda:=LambdaInp*1e-9;
Writeln('Type in thicknesses D2 D3 in um');
If Not(FirstTime) Then Writeln(['',D2Inp:8:2,D3Inp:8:2,' ']);
Readln(D2Inp,D3Inp);
D2:=D2Inp*1e-6; D3:=D3Inp*1e-6;
Kprop:=2*Pi/Lambda;
Exit := False;
Repeat
  Writeln('What polarisation? (TE/TM)');
  Readln(Answer);
  If ((Answer='TM') or (Answer='tm')) or ((Answer='TE') or (Answer='te'))
Until Exit;
If (Answer='TM') or (Answer='tm') Then
  Begin
    Eta1:=1/(N1*N1); Eta2:=1/(N2*N2); Eta3:=1/(N3*N3); Eta4:=1/(N4*N4);
  End
Else
  Begin
    Eta1:=1; Eta2:=1; Eta3:=1; Eta4:=1;
  End;
Writeln('What Mode? (0,1,2 etc)');
If Not(FirstTime) Then Writeln(['',Mode,'']);
Readln(Mode);
FirstTime := False;
Writeln;Writeln('Calculating');Writeln;
If N1 > N3 Then
  Neffmin := N1 + 1e-10
Else Neffmin := N3 + 1e-10;
Neffmax := N2 - 1e-10;
Exit := False;
Fmax := FNeff(Neffmax);
Fmin := FNeff(Neffmin);
If ((Fmax>0) And (Fmin>0)) Or ((Fmax<0) And (Fmin<0)) Then
  Begin
    Writeln('Mode not propagating. ');
    Exit := True;
  End;
Foundroot := False;
Repeat
  Neffmid := (Neffmax+Neffmin)/2;
  Fmax := FNeff(Neffmax);
  Fmid := FNeff(Neffmid);
  Fmin := FNeff(Neffmin);
  If Fmid > 0 Then Neffmin := Neffmid;
  If Fmid < 0 Then Neffmax := Neffmid;
  If Abs(Neffmax-Neffmin) < Ferror Then
    Begin
      Exit:=True;
      Foundroot := True;
    End;
Until Exit;
If Foundroot Then
  Begin

```

```

Writeln('Effective index      = ',Neffmid:12:7);
Writeln('Effective permittivity = ',Neffmid*Neffmid:12:7);
Writeln('Mode thickness (um)   = ',1e6*(D2 + 1/K1 + 1/K3):12:7);

```

```

(***) Calculate fraction of power in guiding slab (***)

```

```

A:= 1e-16;
B:= A*(Eta3*K3 + Eta4*K4) *exp(K3*D3) / (2*Eta3*K3);
C:= (A - B*exp(-K3*D3)) *exp(-K3*D3);
D:= Eta3*K3*(C-B) / (Eta2*K2);
E:= B+C;
F:= E*cos(K2*D2) - D*sin(K2*D2);
Term1:= F*F/(2*K1);
Sub1:= ( -D*E/K2 + D*D*D2 + E*E*D2 )/2;
Sub2:= (D*D - E*E)/2 * sin(2*K2*D2)/(2*K2);
Sub3:= D*E * cos(2*K2*D2)/(2*K2);
Term2:= (Sub1 - Sub2 + Sub3);
Sub1:= B*B*exp(-2*K3*D3)/(-2*K3);
Sub2:= C*C*exp(2*K3*D3)/(2*K3);
Sub3:= 2*B*C*D3 - ( -B*B + C*C )/(2*K3);
Term3:= ( Sub1 + Sub2 + Sub3);
Term4:= A*A/(2*K4);

```

```

Sub1:= (Term1 + Term2 + Term3 + term4);
Frac1:= 100*Term1/Sub1; Frac2:= 100*Term2/Sub1;
Frac3:= 100*Term3/Sub1; Frac4:= 100*Term4/Sub1;
Writeln('Power distribution in layers:');
Writeln('Layer1 : ',Frac1:6:3,'%');
Writeln('Layer2 : ',Frac2:6:3,'%');
Writeln('Layer3 : ',Frac3:6:3,'%');
Writeln('Layer4 : ',Frac4:6:3,'%');

```

```

Write('Percentage power in substrate(Y/N)? ');
Readln(Answer);

```

```

If Not((Answer='n') or (Answer='N')) Then

```

```

    Begin

```

```

        Writeln('Type in lower cladding thickness in um');

```

```

        Readln(DlcInp);

```

```

        Dlc:=DlcInp*1e-6;

```

```

        Subst:=exp(2*K1*(D2-Dlc))/(2*K1);

```

```

        Writeln('Power in substrate : ',Subst*100,'%');

```

```

        End;

```

```

(***) Fraction calculated (***)

```

```

End;

```

```

Writeln;Writeln('Leave program? (Y/N)');

```

```

Readln(Answer);

```

```

If (Answer='y') or (Answer='Y') Then LeaveProg:=True;

```

```

Until LeaveProg;

```

```

End.

```

Program Kramers;

```
{** Program to calculate change in refractive index **}  
{** from change in absorption using Kramers-Kronig relations **}  
{** Written by B. S. Bhumbra 19/4/88 **}  
{** Absorption generating option inserted 21/10/88**}
```

Const

```
NumOfSteps = 1000;  
MaxData = 50;  
Hbar = 1.0544e-34;  
c = 3e8;  
e = 1.602e-19;  
XgrafWindow = 450;  
YgrafWindow = 100;
```

Type

```
RealDatType = Array[1..MaxData] of Real;  
IntDatType = Array[1..MaxData] of Integer;  
BigArrType = Array[0..NumOfSteps] of Real;  
NameType = String[12];  
AnswerType = String[1];
```

Var

```
EStep, Sub, Sum, Eo, Fraction, EnergyRange,  
ELow, EHigh, AlphaTemp, AlphaMax, AlphaMin,  
YScaling,  
AlphaRange, Emax, Emin, ERange,  
AlMax, FWHM, Ecentre, En, Nu, Tau           : Real;  
XaxisPos, Xpos, Ypos, ArrayPos,  
Xpos1, Ypos1, Xpos2, Ypos2,  
BigCount, CountRange, Count, NumofPts      : Integer;  
Leave, Exit, Quit, Moniter, Ordered         : Boolean;  
EnergyArr, Alpharr                          : RealDatType;  
PosnArr                                      : IntDatType;  
BigEnergyArr, BigAlpharr                   : BigArrType;  
Answer, Select, Lshape                     : AnswerType;
```

```
Function Exist(Filename: NameType) : Boolean;  
{** Returns true if file exists **}
```

Var

```
Fil : File;
```

Begin

```
Assign(Fil, Filename);  
{ $I- }  
Reset(Fil);  
{ $I+ }  
Exist := (IOresult = 0)
```

End;

```
Function Gauss(X,Xo,DX:Real):Real;  
{** Used to calculate Gaussian lineshape **}
```

Var

```
Sub1 : Real;
```

Begin

```
Sub1 := (X-Xo)/DX;  
Gauss := exp(-Sub1*Sub1);
```

End;

```

Function Lorent(X,Xo,DX:Real):Real;
{*** Used to calculate Lorentzian lineshape ***}
Var
  Sub1 : Real;
Begin
  Sub1 := (X-Xo)/DX;
  Lorent := 1/(Sub1*Sub1 + 1);
End;

Procedure Savefile(EDatArr, ADatArr: BigArrType);
{*** Proc to create a file and save data arrays ***}
Var
  FilVar : File of BigArrType;
  Answer : AnswerType;
  Filename : NameType;
  Finished : Boolean;
Begin
  Finished := False;
  Repeat
    Writeln('Type in name of file to be saved');
    Readln(Filename);
    If Exist(Filename) Then
      Begin
        Writeln('Filename exists. Overwrite (Y/N) ');
        Readln(Answer);
        If (Answer='Y') or (Answer='y') Then Finished := True;
      End
    Else If Filename<>' ' Then Finished := True;
  Until Finished;
  Assign(FilVar,Filename);
  Rewrite(FilVar);
  Reset(FilVar);
  Write(FilVar,EDatArr);
  Write(FilVar,ADatArr);
  Close(FilVar);
End; (**File saved**)

Procedure Loadfile(Var EDatArr, ADatArr : BigArrType);
{*** Proc to load data from file and put into data array ***}
Var
  FilVar : File of BigArrType;
  Filename : NameType;
  Answer : AnswerType;
  Finished : Boolean;
Begin
  Finished := False;
  Repeat
    Writeln('Type in name of file to be read');
    Readln(Filename);
    If Exist(Filename) Then
      Begin
        Assign(FilVar,Filename);
        Reset(FilVar);
        Read(FilVar,EDatArr);
        Read(FilVar,ADatArr);
        Close(FilVar);
        Finished := True;
      End
    Else
      Begin
        Writeln('File not found. Try again? (Y/N)');

```

```

    Readln(Answer);
    If (Answer='n')or(Answer='N') Then Finished := True;
    End;
Until Finished;
End; (** File loaded into data array**)

Procedure GoColor;
(*** Procedure to switch to colour moniter ***)
Begin
Mem[0:$410] := ( (Mem[0:$410] And $CF) Or $10 );
End;

Procedure GoMono;
(*** Procedure to switch to monochrome moniter ***)
Begin
Mem[0:$410] := ( Mem[0:$410] Or $30 );
End;

Begin (*** Main program ***)
ClrScr;
Quit := False;
Repeat
    Writeln('Is there a separate colour moniter connected for graphics? (Y/N)')
    Readln(Answer);
    If (Answer='y')or(Answer='Y') Then
        Begin
            Moniter := True;
            Quit := True;
        End;
    If (Answer='n')or(Answer='N') Then
        Begin
            Moniter := False;
            Quit := True;
        End;
Until Quit;
Quit := False;
Repeat

ClrScr;
Writeln('Program Kramers. '); Writeln;
Writeln('Calculates refractive index change at any specified photon energy');
Writeln('by Kramers-Kronig transforming corresponding change in absorption. ');
Writeln('Type number for option');Writeln;Writeln;
Writeln('1. Type in new absorption data');
Writeln('2. Calculate index change');
Writeln('3. Generate absorption line');
Writeln('4. Save data to file');
Writeln('5. Load data from file');
Writeln('6. Draw graph of data');
Writeln('7. Quit program');
Writeln;
Readln(Select);

Case Select of
'1':(*** Collect data ***)
    Begin
        ClrScr;
        Repeat
            Writeln('Type in no. of data points');
            Readln(NumOfPts);

```

```

If NumOfPts > MaxData Then
  Begin
    Writeln('No. of points must not exceed ',MaxData:1);
    Exit := False;
  End
Else
  Exit := True;
If NumofPts=1 Then
  Begin
    Writeln('Program requires more data');
    Exit:= False;
  End;
Until Exit;
Ordered := False;
Repeat
  Writeln('Type in data :photon energy (eV) and absorption (cm-1) in pair
  Writeln('Please ensure data is ordered (ie increasing energy values)');
  Writeln('Energy   Absorption');
  For Count:=1 to NumOfPts Do
    Begin
      Readln( EnergyArr[Count], Alpharr[Count] )
    End;

  (Check if data is ordered)
  Exit := False;
  Count := 2;
  Repeat
    If EnergyArr[Count] > EnergyArr[Count-1] Then
      Begin
        Ordered := True;
        If Count=NumOfPts Then Exit := True;
      End
    Else
      Begin
        Ordered := False;
        Exit := True;
        Writeln;
        Writeln('Data is not ordered correctly');
      End;
    Count := Count+1;
  Until Exit;
Until Ordered;

(** Find positon in big array **)
Writeln('Wait');
Emax := EnergyArr[NumOfPts];
Emin := EnergyArr[1];
ERange := Emax - Emin;
For Count:=1 to NumOfPts Do
  Begin
    PosnArr[Count] := Round( (EnergyArr[Count] - Emin)*NumOfSteps/ERange );
  End;

(** Fill up Big Arrays **)
For Count:= 1 to (NumOfPts-1) Do
  Begin
    CountRange := PosnArr[Count+1] - PosnArr[Count];
    EnergyRange := EnergyArr[Count+1] - EnergyArr[Count];
    AlphaRange := Alpharr[Count+1] - Alpharr[Count];
    BigCount := PosnArr[Count];
    Repeat
      Fraction := (BigCount-PosnArr[Count])/CountRange;
      BigEnergyArr[BigCount] := Fraction*EnergyRange + EnergyArr[Count];
      BigAlpharr[BigCount] := Fraction*AlphaRange + Alpharr[Count];
    Until Fraction = 0;
  End;

```

```

        BigCount := BigCount+1;
    Until BigCount=PosnArr[Count+1]
End;

(*Fill last points in Big Arrays*)
BigEnergyArr[NumOfSteps] := EnergyArr[NumOfPts];
BigAlpharr[NumOfSteps] := Alpharr[NumOfPts];
(** Phew! **)
End;

(** 1st option done **)

'2':(** Do the integration **)
Begin
Repeat
    Writeln;
    Writeln('Type in photon energy at which to calculate index change (eV)')
    Readln(Eo);
    Writeln('Calculating');
    EHigh := BigEnergyArr[NumofSteps];
    ELow := BigEnergyArr[0];
    ERange := EHigh - ELow;
    EStep := ERange/NumofSteps;
    Sum:=0;
    For Count := 0 to NumOfSteps Do
        If Abs(BigEnergyArr[Count]-Eo)>Estep Then
            Begin
                Sub :=(BigEnergyArr[Count]*BigEnergyArr[Count] - Eo*Eo );
                Sum := Sum + EStep*BigAlpharr[Count]/Sub;
            End;
        Sum := Sum*c*hbar*100/(Pi*e);
        Writeln('Calculated change in index for data is ',Sum);
        Writeln('Another energy? (Y/N)');
        Readln(Answer);
        If (Answer='n')or(Answer='N') Then Leave := True
        Else Leave := False;
    Until Leave;
End;

(** 2nd option done **)

'3':(** Generate absorption lineshape **)
Begin
Writeln('Type in peak absorption (cm-1)');
Readln(Almax);
Writeln('Type in FWHM of absorption peak (eV)');
Readln(FWHM);
Writeln('Type in position of peak (eV)');
Readln(Ecentre);
Exit := False;
Repeat
    Writeln('Is lineshape Lorentzian (L) or Gaussian (G) ?');
    Readln(LShape);
    If (LShape='L')Or(LShape='l') Or (LShape='G')Or(LShape='g') Then
        Exit:=True
    Else
        Writeln('Option not recognised. Try again. ');
Until Exit;
If (LShape='L')or(LShape='l') Then
    Begin
        Nu:=FWHM/2;
        ERange := 2*Nu*sqrt(999); (* to get Full Width 1/1000 of max *)
        Emin := Ecentre-ERange/2;
        Emax := Emin + ERange;
    End;

```

```

Estep := Erange/NumofSteps;
Writeln('Calculating Lorentzian lineshape');
  For Count:=0 to NumofSteps Do
    Begin
      En :=Emin+Count*Estep;
      BigEnergyArr[Count] := En;
      BigAlpharr[Count] := Almax*Lorent(En,Ecentre,Nu);
    End;
  End
Else
  Begin
    Tau:=FWHM/(2*Sqrt(ln(2)));
    ERange := 2*Tau*Sqrt(ln(1000));  (* to get Full Width 1/1000 of max *)
    Emin := ECentre-ERange/2;
    Emax := Emin + Erange;
    Estep := Erange/NumofSteps;
    Writeln('Calculating Gaussian lineshape');
    For Count:=1 to NumofSteps Do
      Begin
        En:=Emin+Count*Estep;
        BigEnergyArr[Count] := En;
        BigAlpharr[Count] := Almax*Gauss(En,Ecentre,Tau);
      End;
    End;
  End;
End;

(** 5th option done **)

'4':(** Save arrays to a file **)
  Begin
    Savefile(BigEnergyArr, BigAlpharr);
  End;
(** 4th option done **)

'5':(** Fill arrays from a file **)
  Begin
    Loadfile(BigEnergyArr, BigAlpharr);
  End;
(** 5th option done **)

'6':(** Plot Graph of Data **)
  Begin

    (** Find min and max of data **)
    ELow:=BigEnergyArr[0];
    EHigh :=BigEnergyArr[NumofSteps];
    AlphaMin := BigAlpharr[0];
    AlphaMax := BigAlpharr[0];
    For Count := 1 to NumofSteps Do
      Begin
        AlphaTemp := BigAlpharr[Count];
        If AlphaTemp>AlphaMax Then AlphaMax:=AlphaTemp;
        If AlphaTemp<AlphaMin Then AlphaMin:=AlphaTemp;
      End;

    If Monitor Then GoColor; (**switch to color monitor**)
    HiRes;
    HiRescolor(Black);
    GotoXY(1,9);
    Writeln('Absorption');
    GotoXY(35,17);
    Writeln('Photon Energy');
    Window(10,21,80,25); (** Define text window**)

```

```

GotoXY(1,1);
Writeln('Min energy is ',Elow:10,' eV');
Writeln('Max energy is ',EHigh:10,' eV');
Writeln('Min alpha is ',Alphamin:10,' cm-1');
Write('Max alpha is ',Alphamax:10,' cm-1');

(** Draw border **)
Xpos1 := Round((639-Xgrafwindow)/2);
Ypos1 := Round((149-Ygrafwindow)/2);
Xpos2 := Xpos1+Xgrafwindow;
Ypos2 := Ypos1+Ygrafwindow;
Draw(Xpos1,Ypos1,Xpos1,Ypos2,white);
Draw(Xpos1,Ypos2,Xpos2,Ypos2,white);
Draw(Xpos2,Ypos2,Xpos2,Ypos1,white);
Draw(Xpos1,Ypos1,Xpos2,Ypos1,white);

Yscaling := Ygrafwindow/(Alphamax-Alphamin);

(** Draw X axis if max and min alphas are opposite in sign **)
If (AlphaMax>0) And (AlphaMin<0) Then
  Begin
    XaxisPos := Round(AlphaMax*Yscaling)+ Ypos1;
    Draw(Xpos1,XaxisPos,Xpos2,XaxisPos,white);
  End;

(** Plot Graph **)
For Count := 0 to Xgrafwindow Do
  Begin
    ArrayPos := Round(Count/Xgrafwindow*NumofSteps);
    Ypos := Round((AlphaMax-BigAlpharr[ArrayPos])*Yscaling) + Ypos1;
    Xpos := Xpos1 + count;
    Plot(Xpos,Ypos,White);
  End;
Write(' ':15,'Hit Return');Readln(Answer);
If Monitor Then Gomono; (**switch to mono monitor**)
Textmode;
End;

(** 6th option done **)

'7':(** Quit **)
  Begin
    Quit := true;
  End;
(** 7th option done **)
End;

Until Quit;
End.

```

Program Xton;

```
{***** Program to calculate excitonic energies *****}  
{***** in AlGaAs quantum well systems. *****}  
{***** Program uses finite potential well model *****}  
{***** Program written by B. S. Bhumbra 1/10/87. *****}  
{** Binding energies of lh and hh excitons included **}  
{***** Energy dependant e and lh masses included *****}
```

{\*\*\*\*\* Final Version 23/1/89 \*\*\*\*\*}

Const

```
eV = 1.602193e-19;  
hbar = 1.054925e-34;  
restmass = 9.10956e-31;  
Energys = 1e-5;
```

Type

```
NameType = String[12];
```

Var

```
Xwell, Xbarrier, Wellwidth, Temp, hhmassbarr, hhmasswell,  
lhmasswell, lhmassbarr, emassbarr, emasswell,  
EgBarr, EgWell, Vvband, Vcband, Emin, Emid, Emax,  
Fmin, Fmid, Fmax, Elecenergy, Hholenergy, Lholenergy, Xenergy,  
Wavelength, DelEc, HHBE, LHBE : Real;  
  
Quantum, Ntransition : Integer;  
  
Exit, FoundHhole, FoundLhole, Foundelec, Finish : Boolean;  
  
Answer : String[1];
```

```
Function Einfunc(E,V,mWell,mBarrier,W : Real; n : Integer ):Real;  
{energies(eV's), masses(relative), W(Angstroms)}
```

Var

```
Alpha, Beta, Massratio : Real;
```

Begin

```
W := W*1e-10;  
Massratio := mWell/mBarrier;  
mWell := mWell*restmass;  
mBarrier := mBarrier*restmass;  
E := E*eV; {Change to electron volts }  
V := V*eV;  
Alpha := Sqrt(2*mBarrier/hbar*(V-E)/hbar);  
Beta := Sqrt(2*mWell/hbar*e/hbar);  
Einfunc := W*Beta - 2*ArcTan(Massratio*Alpha/Beta) - n*Pi;  
End;
```

```
Function eEmass(E,V,x : Real ):Real;
```

```
{Returns energy dependant relative electron mass}
```

Var

```
Gamma, mx, Sub1 : Real;
```

Begin

```
Gamma := 4.9e-19; { nonparabolicity from Stevens et al }  
mx := 0.0665 + 0.0835*x; { Zero E mass From Duggan et al }  
Sub1 := (hbar/restmass*hbar/eV)/(2*mx*Gamma);  
eEmass := mx*(1+ (E-V)/Sub1 );
```

End;

```
Function Hholemass(x : Real ):Real;
{Returns relative heavy hole mass at zero energy}
Begin
Hholemass := 0.34 + 0.45*x;      { From Duggan et al }
End;
```

```
Function lhEmass(E,V,x : Real ):Real;
{Returns energy dependant relative light hole mass}
Var
  Gamma, mx, Sub1 : Real;
Begin
Gamma := 7.35e-19;                {nonparabolicity from Stevens et al}
mx := 0.087 + 0.063*x;            {Zero E mass From Adachi}
Sub1 := (hbar/restmass*hbar/eV)/(2*mx*Gamma);
lhEmass := mx*(1+ (E-V)/Sub1 );
End;
```

```
Function Gap(x : Real ):Real;
{Returns Bandgap in eV as function of Al conc.}
{Equation obtained from Aspnes et al.}
Begin
Gap := 1.424 + 1.594*x + x*(1-x)*(0.127 - 1.310*x); { from Aspnes }
End;
```

```
Function EgTemp(T : Real):Real;
{Returns temperature dependant bandgap of GaAs in eV's}
Begin
EgTemp := 1.519 - 5.405e-4*T*T/(204 + T);      { from Kawai }
End;
```

```
Function Exist(Filename: Nametype) : Boolean;
{*** Returns true if file exists ***}
Var
  Fil : File;
Begin
  Assign(Fil, Filename);
  ($I-)
  Reset(Fil);
  ($I+)
  Exist := (IOresult = 0)
End;
```

```
Begin {***** main program*****}
Finish := False;
Repeat
  Repeat
    ClrScr;
    Write('Type in Al concentration in well (%)      ');
    Readln(xWell);
    xWell := xWell*1e-2;
    Write('Type in Al concentration in barrier (%)   ');
    Readln(xBarrier);
    xBarrier := xBarrier*1e-2;
  Until xBarrier>xWell;
```

```

Write('Type in well width (Angstroms)           ');
Readln(Wellwidth);
Write('Type in temperature (K)                 ');
Readln(Temp);
DelEc := 100 - 55*xBarrier;           ( from Batey et al )
Writeln;
Hhmassbarr := Hholemass(xBarrier);
Hhmasswell := Hholemass(xWell);
Egbarr := Gap(xBarrier) + EgTemp(Temp) - 1.424 ;
Egwell := Gap(xWell) + EgTemp(Temp) - 1.424 ;
Vcband := DelEc/100*(Egbarr-Egwell);
Vvband := Egbarr-Egwell-Vcband;
{ Calculate binding energies of excitons (n=1) }
HHBE := 14.47-0.0645*Wellwidth+1.41e-4*Wellwidth*Wellwidth; {from Koteles}
LHBE := 15.74-0.0611*Wellwidth+1.19e-4*Wellwidth*Wellwidth;
{****Print calculated data parameters and set up headings for results****}
Writeln('Well depth in conduction band = ',Vcband:5:3,' eV');
Writeln('Well depth in valence band   = ',Vvband:5:3,' eV');
Writeln('Well bandgap      = ', Egwell:8:4,' eV');
Writeln('Barrier bandgap = ', Egbarr:8:4,' eV');
Writeln('Heavy hole exciton binding energy (n=1) =',HHBE:8:1,' meV');
Writeln('Light hole exciton binding energy (n=1) =',LHBE:8:1,' meV');
Writeln;
Writeln('
           Heavy      Light      Heavy      Light
           Electron  Hole      Hole      Exciton   Exciton
           Energy    Energy   Energy    Transition Transition
           (eV)      (eV)    (eV)      (eV)      (nm)     (eV)      (nm)
Quantum:=0;
Ntransition :=1;
Exit := False;
Repeat
    (***Begin loop for each quantum no.***
    (***Find electron level n ***)
    Emin := Energyres; Emax := Vcband;
    emasswell := eEmass(Emin,0,xWell);
    emassbarr := eEmass(Emin,Vcband,xBarrier);
    Fmin := Einfunc(Emin,Vcband,emasswell,emassbarr,Wellwidth,Quantum);
    emasswell := eEmass(Emax,0,xWell);
    emassbarr := eEmass(Emax,Vcband,xBarrier);
    Fmax := Einfunc(Emax,Vcband,emasswell,emassbarr,Wellwidth,Quantum);
    If ( Fmin<0 ) and ( Fmax<0 ) Then Foundelec := False
    Else
        Begin
            Foundelec := False;
            Repeat
                Emid := (Emin+Emax)/2;
                emasswell := eEmass(Emid,0,xWell);
                emassbarr := eEmass(Emid,Vcband,xBarrier);
                Fmid := Einfunc(Emid,Vcband,emasswell,emassbarr,Wellwidth,Quantum);
                If ( Fmid>0 ) Then Emax := Emid Else Emin := Emid;
                If Abs(Emax-Emin) < Energyres Then Foundelec := True;
            Until Foundelec;
            Elecenergy := Emid;
        End;
    (***Find heavy hole level n ***)
    Emin := Energyres; Emax := Vvband;
    Fmin := Einfunc(Emin,Vvband,Hhmasswell,Hhmassbarr,Wellwidth,Quantum);
    Fmax := Einfunc(Emax,Vvband,Hhmasswell,Hhmassbarr,Wellwidth,Quantum);
    If ( Fmin<0 ) and ( Fmax<0 ) Then FoundHhole := False
    Else
        Begin
            FoundHhole := False;
            Repeat
                Emid := (Emin+Emax)/2;
                Fmid := Einfunc(Emid,Vvband,Hhmasswell,Hhmassbarr,Wellwidth,Quantum);

```

```

        If ( Fmid>0 ) Then Emax := Emid Else Emin := Emid;
        If Abs(Emax-Emin) < Energyres Then FoundHhole := True;
Until FoundHhole;
Hholenergy := Emid;
End;
(**Find light hole level n **)
Emin := Energyres; Emax := Vvband;
lhmasswell := lhEmass(Emin,0,xWell);
lhmassbarr := lhEmass(Emin,Vvband,xBarrier);
Fmin := Einfunc(Emin,Vvband,Lhmasswell,Lhmassbarr,Wellwidth,Quantum);
lhmasswell := lhEmass(Emax,0,xWell);
lhmassbarr := lhEmass(Emax,Vvband,xBarrier);
Fmax := Einfunc(Emax,Vvband,Lhmasswell,Lhmassbarr,Wellwidth,Quantum);
If ( Fmid>0 ) and ( Fmax<0 ) Then FoundLhole := False
Else
Begin
FoundLhole := False;
Repeat
Emid := (Emin+Emax)/2;
lhmasswell := lhEmass(Emid,0,xWell);
lhmassbarr := lhEmass(Emid,Vvband,xBarrier);
Fmid := Einfunc(Emid,Vvband,Lhmasswell,Lhmassbarr,Wellwidth,Quantum);
If ( Fmid>0 ) Then Emax := Emid Else Emin := Emid;
If Abs(Emax-Emin) < Energyres Then FoundLhole := True;
Until FoundLhole;
Lholenergy := Emid;
End;
(**Check for results and print appropriately **)
If Foundelec or FoundHhole or FoundLhole Then
Begin
Write(Ntransition:2);
If Foundelec Then Write(Elecenergy:11:4) Else Write(' -----');
If FoundHhole Then Write(Hholenergy:10:4) Else Write(' -----');
If FoundLhole Then Write(Lholenergy:9:4) Else Write(' -----');
If Foundelec and FoundHhole Then
Begin
Xenergy := Elecenergy + Hholenergy + Egwell - HHBE*1e-3;
Wavelength := 1240.6/Xenergy;
Write(Xenergy:9:4,Wavelength:7:1);
End
Else Write(' ----- ');
If Foundelec and FoundLhole Then
Begin
Xenergy := Elecenergy + Lholenergy + Egwell - LHBE*1e-3;
Wavelength := 1240.6/Xenergy;
Write(Xenergy:9:4,Wavelength:7:1);
End
Else Writeln(' ----- ');
End
Else
Begin
Exit := True;
Writeln;Writeln('No more bound states');
End;
Quantum := Quantum + 1;
Ntransition := Ntransition + 1;
Until Exit;
Writeln; Writeln('Again? (Y/N)');
Readln(Answer);
If (Answer='N') or (Answer='n') Then Finish := True;
Until Finish;
End.

```

### APPENDIX III

### WAFER SPECIFICATIONS

#### MV 273 (MOCVD)

		0.02 $\mu$ m GaAs
$6 \times 10^{17}$ p-type	Upper Cladding	
undoped ( $< 2 \times 10^{17}$ )	Guiding layer	1.0 $\mu$ m Al <sub>0.30</sub> Ga <sub>0.70</sub> As
$1-2 \times 10^{17}$ n-type	Lower cladding	0.75 $\mu$ m MQW (See Note 1)
$10^{17}$ n-type	Buffer layer	1.5 $\mu$ m Al <sub>0.30</sub> Ga <sub>0.70</sub> As
$n^+$	Substrate	0.3 $\mu$ m GaAs
		GaAs

Note 1 : 8 layers 65Å GaAs  
 7 layers 1000Å Al<sub>0.30</sub>Ga<sub>0.70</sub>As

#### MV 330 (MOCVD)

		0.02 $\mu$ m GaAs
$10^{16}$ p-type	Upper Cladding	
	Guiding layer	1.0 $\mu$ m Al <sub>0.30</sub> Ga <sub>0.70</sub> As
$10^{16}$ p-type	Lower cladding	0.75 $\mu$ m MQW (See Note 1)
layers nominally undoped	Buffer layer	1.5 $\mu$ m Al <sub>0.30</sub> Ga <sub>0.70</sub> As
	Substrate	0.3 $\mu$ m GaAs
		GaAs

Note 1 : 8 layers 65Å GaAs  
 7 layers 1000Å Al<sub>0.30</sub>Ga<sub>0.70</sub>As

CPM 333 (MOCVD)

(polaron)		0.01 $\mu\text{m}$	GaAs
$2 \times 10^{17}$ p-type	Upper Cladding	2.10 $\mu\text{m}$	$\text{Al}_{0.34} \text{Ga}_{0.66} \text{As}$
$1.6 \times 10^{17}$ p-type	Guiding layer	1.14 $\mu\text{m}$	$\text{Al}_{0.32} \text{Ga}_{0.68} \text{As}$
$2 \times 10^{17}$ p-type	Lower cladding	2.20 $\mu\text{m}$	$\text{Al}_{0.34} \text{Ga}_{0.66} \text{As}$
	Buffer layer	0.5 $\mu\text{m}$	GaAs
$n^+$	Substrate		GaAs

CPM 376 (MOCVD)

(polaron)		0.02 $\mu\text{m}$	GaAs
	Upper Cladding	1.50 $\mu\text{m}$	$\text{Al}_{0.10} \text{Ga}_{0.90} \text{As}$
$2 \times 10^{15}$ n-type	Guiding layer	0.46 $\mu\text{m}$	$\text{Al}_{0.05} \text{Ga}_{0.95} \text{As}$
$2 \times 10^{15}$ n-type	Lower cladding	1.50 $\mu\text{m}$	$\text{Al}_{0.10} \text{Ga}_{0.90} \text{As}$
	Buffer layer	0.25 $\mu\text{m}$	GaAs
$10^{18}$ n-type	Substrate		GaAs

Varian 1 (MBE)

Upper Cladding
Guiding layer
Lower cladding
Buffer layer
Substrate

0.01 $\mu$ m GaAs

2.10 $\mu$ m Al<sub>0.33</sub>Ga<sub>0.67</sub>As

1.14 $\mu$ m Al<sub>0.30</sub>Ga<sub>0.70</sub>As

2.20 $\mu$ m Al<sub>0.33</sub>Ga<sub>0.67</sub>As

GaAs

GaAs

Varian 2 (MBE)

Upper Cladding
Guiding layer
Lower cladding
Buffer layer
Substrate

0.01 $\mu$ m GaAs

1.70 $\mu$ m Al<sub>0.35</sub>Ga<sub>0.65</sub>As

0.88 $\mu$ m Al<sub>0.30</sub>Ga<sub>0.70</sub>As

1.80 $\mu$ m Al<sub>0.35</sub>Ga<sub>0.65</sub>As

GaAs

GaAs

MA 670 (MOCVD)

Upper Cladding
Guiding layer
Lower cladding
Buffer layer
Substrate

0.02 $\mu$ m GaAs

1.0  $\mu$ m Al<sub>0.12</sub>Ga<sub>0.88</sub>As

0.45 $\mu$ m Al<sub>0.06</sub>Ga<sub>0.94</sub>As

1.5  $\mu$ m Al<sub>0.12</sub>Ga<sub>0.88</sub>As

GaAs

GaAs

## APPENDIX IV

### RELEVANT PUBLICATIONS

(i) C. N. Ironside, T. J. Cullen, B. S. Bhumbra, J. Bell, W. C. Banyai, N. Finlayson, C. T. Seaton, G. I. Stegeman, "Nonlinear Optical Effects in Ion-Exchanged Semiconductor Doped Glass Waveguides.", European Conference on Integrated Optics (ECIO) 1987, Glasgow, Scotland, postdeadline paper.

(ii) M. O'Neill, J. Bell, B. S. Bhumbra, T. J. Cullen, C. N. Ironside, O. Mikami, "The Nonlinear Asymmetric Mach Zehnder Interferometer in GaAs/AlGaAs.", Integrated and Guided Wave Optics (IGWO) conference 1988, Santa Fe, California, U.S.A.

(iii) C. N. Ironside, T. J. Cullen, B. S. Bhumbra, J. Bell, W. C. Banyai, N. Finlayson, C. T. Seaton, G. I. Stegeman, "Nonlinear-optical effects in ion-exchanged semiconductor doped glass waveguides.", J. Opt. Soc. Am. B, vol 5, no 2, pp492-495, 1988.

# Nonlinear Optical Effects in Ion-Exchanged Semiconductor Doped Glass Waveguides

C. N. Ironside, T. J. Cullen, B. S. Bhumbra, J. Bell.  
Department of Electronics and Electrical Engineering,  
University of Glasgow,  
Glasgow G12 8QQ.  
UK

W. C. Banyai, N. Finlayson, C. T. Seaton, G. I. Stegeman.  
Optical Sciences Center,  
University of Arizona,  
Tucson,  
AZ 85721.  
USA

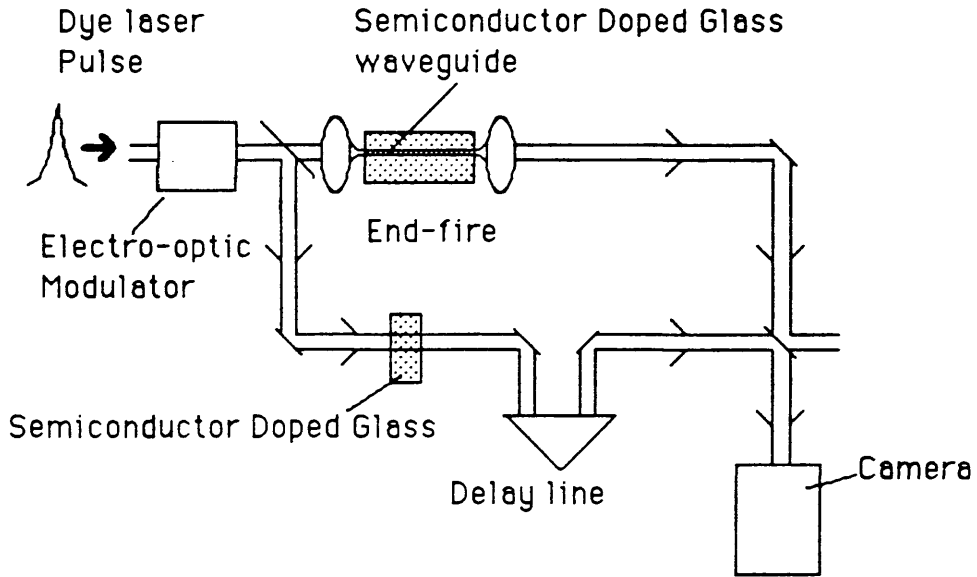
**Abstract:** We have measured for the first time optical nonlinearities in ion exchanged channel waveguide fabricated in semiconductor doped glass. Interferometric and pump-probe experiments, using a picosecond mode-locked dye laser, were used to carry out these measurements in which we were able to distinguish between thermal and electronic contributions to the optical nonlinearities.

## Introduction

Semiconductor-doped glass has been shown to have a relatively large intensity dependent refractive index,  $n_{2,1} = 10^{-14}$  to  $10^{-15}$  m<sup>2</sup>/W and a fast relaxation of around  $10^{-11}$ s. These results have been obtained in bulk glass [1] and in semiconductor-doped glass fibres [2]. In this paper we describe several recent experiments we have performed which show that sodium/potassium ion-exchanged channel waveguides fabricated in semiconductor-doped glass waveguides [3] also exhibit strongly nonlinear optical characteristics. We show that the nonlinearity has both thermal and electronic contributions. For the first time in integrated optical investigations into the semiconductor-doped glasses, we have been able to isolate the electronic from the thermal contribution.

## Experimental

Figure (1)



Figure(1) Experimental arrangement for nonlinear fringe shift in Mach-Zehnder interferometer with a semiconductor-doped glass ion-exchanged waveguide in one arm.

Our experimental arrangement is shown in Fig. 1. A mode-locked, cavity-dumped dye laser with a variable pulse repetition rate is used as the light source. An electro-optic modulator gives control over the intensity of the light without affecting the beam alignment. We employ a Mach-Zehnder interferometer to determine refractive index changes in a single channel waveguide situated in one arm of the interferometer. The optical nonlinearities are resonant with the band-gap and the semiconductor-doped glass was selected to have a band-gap at 590nm convenient for the dye operating wavelengths. The waveguide supports a single mode. A piece of bulk semiconductor doped glass in the reference arm serves to balance the light in the arms thus maximising the fringe visibility. A delay line is used in the reference arm to ensure that the signal and reference pulses overlap. Scanning of the delay line also allows the determination of the sign of the induced refractive index change. The fringe pattern is imaged onto a Hamamatsu vidicon supported by a computer interface from which the fringe data can be acquired.

For pump/probe measurements the apparatus is modified such that a high-intensity pump pulse is coupled into the waveguide together with a low-intensity probe. The interferometer is not used in this case. The probe pulses are polarized orthogonally to the pump pulses in order to prevent saturation of the output detector. High sensitivity is obtained by chopping the probe pulse train to allow for lock-in detection. An on-line

auto-correlator is used in these experiments to monitor the quality of the pulses coming from the dye laser and to detect any pulse distortion arising from nonlinear optical effects in the waveguide.

## Results

Figure (2)

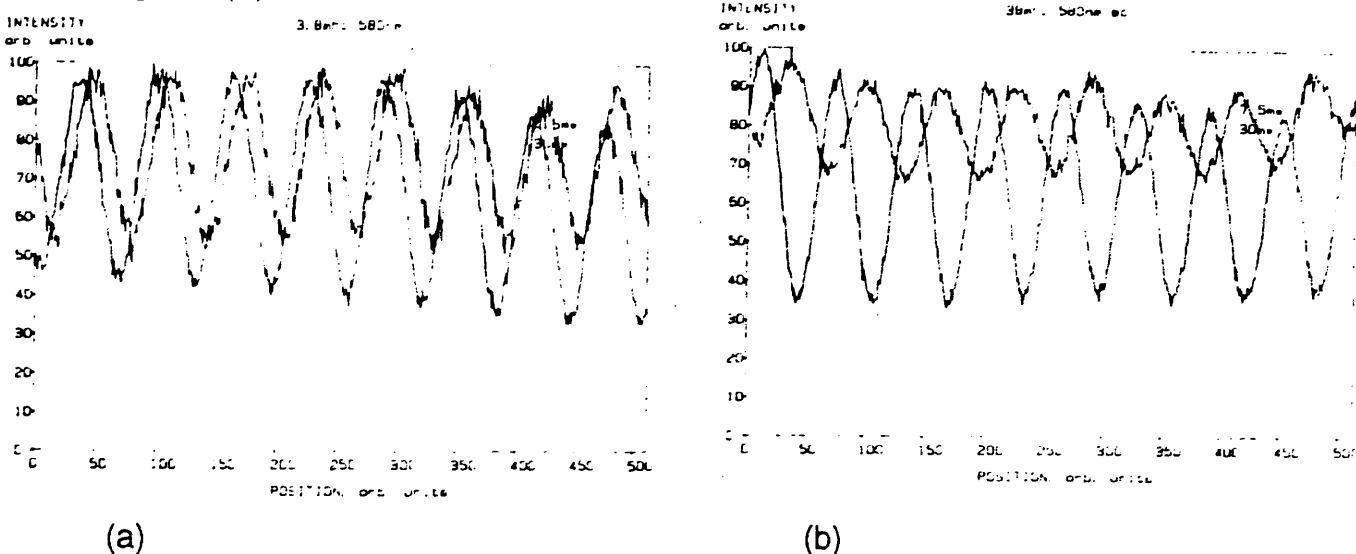
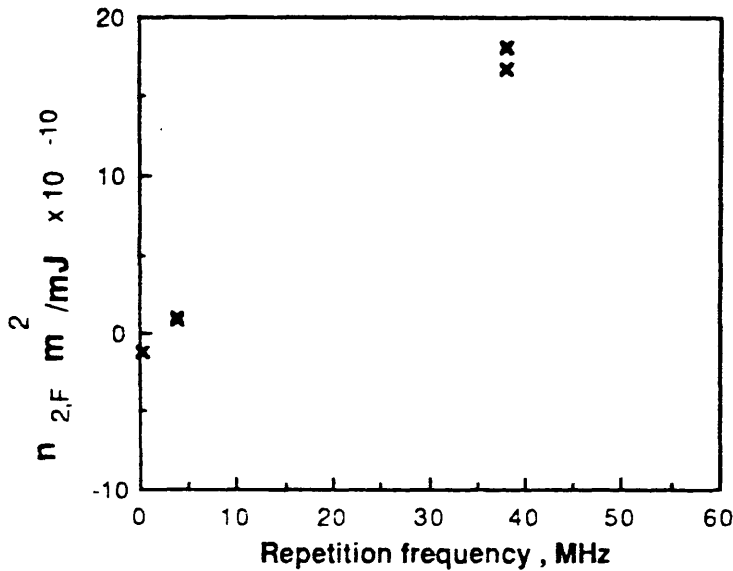


Figure (2). Mach-Zehnder interferometer fringe patterns. One arm of the interferometer includes a single channel waveguide. Laser wavelength 580nm (a) laser repetition rate equals 3.8MHz (b) laser repetition rate equals 38MHz

Typical results of the Mach-Zehnder interferometric experiment are shown in Figs. 2a and 2b. In Fig. 2a the pulse repetition rate is 3.8MHz. Fringe patterns are shown for average incident powers of 7.5 mW and 30 mW. A displacement of the fringes is clearly seen, demonstrating that the refractive index of the waveguide is modified by the light. In Fig. 2b much larger shifts are shown, although the average powers were held constant at the previous values. The laser repetition rate had been increased, however, to 38MHz. A simple interpretation of the differences between Figs. 2a and 2b is available. If we assume that the thermal induced refractive index change is positive and the electronic induced refractive index change is negative (as is well known [1]). At the higher repetition rate the peak intensity of the pulses is smaller than at the lower repetition rate although the average power remains the same. A smaller electronic contribution is therefore obtained, and the thermal contribution dominates. As the repetition rate is lowered the electronic contribution becomes stronger since the pulse intensities increase. At lower rates the thermal contribution will tend to zero and the electronic contribution becomes dominant. The fringe displacements will then be opposite in sign to those previously described. We have observed this behaviour in our

experiments.

Figure(3)



Figure(3) Fluence dependent refractive index,  $n_{2,F}$  plotted against laser repetition rate. At low repetition rates the sign changes.

In Fig. 3 we plot the fluence-dependent refractive index coefficient  $n_{2,F}$  as a function of the laser repetition rate. At low repetition rates the coefficient is negative, being dominated by the electronic contribution. At high repetition rates the coefficient is strongly positive indicating the domination of the thermal contribution.

Figure(4)

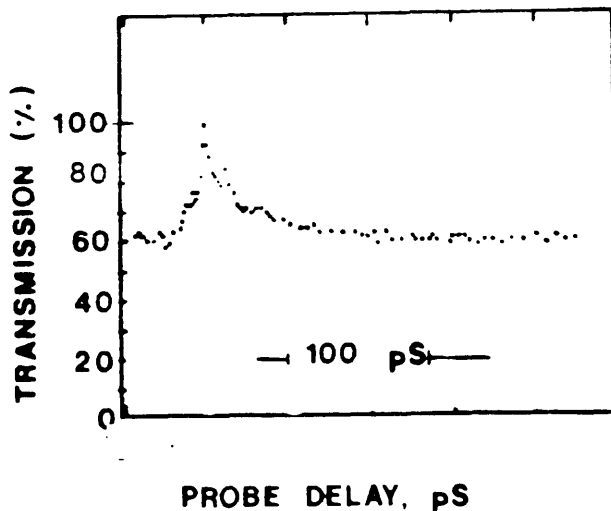


Figure (4) Transmission as a function of probe delay in a single channel waveguide.

Confirmation of strongly nonlinear behaviour in the guides comes from the pump/probe experiment. In Fig. 4 we show the transmission of the waveguide as a function of probe delay. The transmission is seen to peak strongly as the probe pulse travels simultaneously with the pump. This shows that the optical absorption (and therefore the refractive index, through the Kramers-Kronig relations) is power-dependent. The turn-on time is extremely fast as is the initial relaxation time. A longer-lived thermal contribution is observed, in line with measurements made in the bulk glasses [2] and, recently, in fiber waveguides of similar material [3].

### Conclusions

We have reported in this paper the first measurements of nonlinear optical effects in integrated optical channel waveguides in semiconductor-doped glasses. The electronic and thermal contributions to the optical nonlinearity have been clearly distinguished and time-resolved measurements of the power-dependent absorption have been made. The observation of these effects in ion-exchanged channel waveguides indicates that devices utilising the nonlinearities are feasible.

### References

- [1] Roussignol P., Ricard D., Lukasik J. and Flytzanis C. J. Opt. Soc. Am. B **4** 5-12 1987.
- [2] Ainslie B. J., Girdlestone H. P. and Cotter D. , Electron. Lett. **23** 405-406 1987
- [3] Cullen T. J., Ironside C. N., Seaton C. T. and Stegeman G. I. Appl. Phys. Lett. **49** 1403-1405 1986.

# **The Nonlinear Asymmetric Mach Zehnder Interferometer in GaAs/AlGaAs**

**M. O' Neill, J.Bell, B. S. Bhumbra, T. J. Cullen, C. N. Ironside**

**Department of Electronics and Electrical Engineering**

**University of Glasgow**

**Glasgow G12 8QQ**

**U. K.**

**O. Mikami**

**N. T. T., Musashino Electrical Comm. Labs. Tokyo, 180, Japan**

## **Abstract**

We describe the operation of an all-optical switching device based upon an asymmetric Mach-Zehnder Interferometer. Device fabrication techniques in GaAs/AlGaAs materials are summarised. The switching characteristics of the device are analysed using the nonlinear beam-propagation method.

# The Nonlinear Asymmetric Mach Zehnder Interferometer In GaAs/AlGaAs

M. O' Neill, J. Bell, B. S. Bhumbra, T. J. Cullen, C. N. Ironside

Department of Electronics and Electrical Engineering

University of Glasgow

Glasgow G12 8QQ

U. K.

O. Mikami

N. T. T., Musashino Electrical Comm. Labs. Tokyo, 180, Japan

## Abstract

We describe the operation of an all-optical switching device based upon an asymmetric Mach-Zehnder Interferometer. Device fabrication techniques in GaAs/AlGaAs materials are summarised. The switching characteristics of the device are analysed using the nonlinear beam-propagation method.

## Introduction

We report the design and fabrication of a nonlinear optical switch based on the Asymmetric Mach Zehnder Interferometer (AMZI). A schematic diagram of the AMZI is shown in figure 1. The device can be fabricated as single mode waveguides on any material which exhibits an intensity dependent refractive index of the form  $n = n_0 + n_2 I$ , where  $n_0$  is the refractive index at zero intensity,  $I$  is the light intensity, and  $n_2$  is the nonlinear refractive index coefficient. The output power density of an interferometer is dependent on the phase difference between the two beams incident on the output junction. In the nonlinear AMZI this phase difference is intensity dependent since the incident intensity is split unequally between the two arms of the interferometer. The nonlinear switching characteristics of this device are similar to those of the Unequal Arm Interferometer proposed by Kawaguchi.<sup>1</sup>

The ideal optical switch has a large nonlinearity with a picosecond response. The AMZI was designed and fabricated in AlGaAs double heterostructure and multiple quantum well (MQW) materials. At energies far from the bandgap the nonlinearity in GaAlAs is associated with the fast Kerr effect, ( $10^{-13}$ s). However, the magnitude of  $n_2$ , ( $\sim 1 \times 10^{-17} \text{m}^2 \text{W}^{-1}$ ), is too small to be used in a device of reasonable dimensions. At energies close to the bandgap  $n_2$  is resonantly enhanced. However, since it is associated with a band filling process, the nonlinearity is long-lived with a response time, (10ns), determined by the carrier recombination time. In MQW materials the nonlinearity associated with the optical Stark effect<sup>2</sup> may be used to switch the AMZI. In this case, excitation occurs beneath the bandgap resulting in subpicosecond response times with an estimated  $n_2$  of  $2 \times 10^{-15} \text{m}^2 \text{W}^{-1}$ .

## Fabrication

A transverse section of the AlGaAs double heterostructure material used to fabricate the AMZI is illustrated in Fig. 2. In the double heterostructure material  $\text{Al}_{0.06}\text{Ga}_{0.94}\text{As}$  is the waveguiding layer. The MQW material has similar cladding and substrate layers with the guiding layer consisting of 20 10nm thick GaAs/ $\text{Al}_{0.3}\text{Ga}_{0.7}\text{As}$  quantum wells. In each case the thickness of the guiding layer was chosen to support a single TE or TM slab mode only. Stripe loaded single mode waveguides were designed using the effective index method<sup>3</sup>. Firstly, ribs were defined in photoresist on the semiconductor material. Reactive ion etching in  $\text{SiCl}_4$  was then used to etch the surrounding cladding layer, to an accuracy of 0.05 $\mu\text{m}$ , so that the slab no longer supported a guided mode. Light was then confined in channel guides beneath the ribs.

## Device design

For nonlinear switching to occur in an AMZI the optically induced refractive index changes in the arms must produce a phase difference of  $\Delta\phi = \phi_1 - \phi_2 = \pi$  between the two beams at the output junction, where  $\phi_i$ , the nonlinear phase shift accumulated over the length  $l$  of arm  $i$ , is given by

$$\phi_i = \Delta k_i l = \frac{2\pi n_2 P_i l}{\lambda} \quad (1)$$

$\lambda$  is the wavelength of light in the device and  $P_i$  the power density in arm  $i$  at the output junction. As a first approximation, absorption and bending losses along the arms of the Mach Zehnder are ignored. Then at the first junction to the device the fraction of light split in each arm may be defined as  $P_1 = FP_{in}$  and  $P_2 = GP_{in}$ , where  $P_{in}$  is the input power density. Therefore the phase difference induced along the total length of the Mach-Zehnder is given by

$$\Delta\phi = \frac{2\pi n_2 P_{in} l}{\lambda} (F-G) \quad (2)$$

Taking the asymmetry of the device into account, the fields recombine at the output junction of the Mach Zehnder to give an intensity dependent power density of

$$P_{out} = 4P_{in} FG \cos^2 \left[ \frac{\pi n_2 P_{in} l (F-G)}{\lambda} \right] \quad (3)$$

The beam propagation method<sup>4</sup> was used to calculate the splitting ratios as a function of the branch angle of the Mach Zehnder. These calculations take into account the coupling effects between the arms which occur at short distances from the apex; hence the oscillations at small angles. Measurements of splitting ratios were obtained by end-fire coupling low intensity light at a wavelength of 850nm into the input waveguide of an asymmetric Y junction and measuring the normalised power out of each of the branching waveguides. These results are shown in figure 3 and, considering fabrication errors, reasonable agreement is obtained between experimental and theoretical results. The source of these fabrication errors is under further consideration.

A nonlinear beam propagation method<sup>5</sup> was used to calculate the nonlinear switching

characteristics of the AMZI. This method takes bending and linear absorption losses into account but ignores the nonlinear transmission changes ( $\Delta T$ ) and saturation effects which occur along the arms of the device. These effects become more important near the bandgap (when  $\Delta T > \Delta n = n_2 P$ ) and lead to smaller modulation depths at the output of the interferometer. Although the beam propagation method becomes less reliable as  $\Delta n$  increases it corrects for the changes in beam confinement which occur because of  $\Delta n$ . Thus beam focussing and defocussing is predicted if for a large negative  $\Delta n$  and multimode guiding for a large  $\Delta n > 0$ . Figure 4 shows the output power density in the first order mode of a AlGaAs AMZI with a branch angle of 1 degree as a function of  $dn$  where  $dn = n_2 P_{in}$ . The absorption coefficient ( $\alpha$ ) is taken as  $1 \text{ mm}^{-1}$  and  $l = 2 \text{ mm}$ . Because of absorption losses the maximum  $P_{out}$  predicted by (3) is not reached for small values of  $dn$ . Indeed, a  $\cos^2$  variation of  $P_{out}/P_{in}$  is not found since  $\Delta n$  does not remain constant along the device. Multimode waveguiding may explain the smaller modulation depth which is observed when  $\Delta n$  changes by  $2\pi$ .

### Conclusions

The nonlinear beam propagation method predicts that the output of an AMZI will switch by 4.5dB for  $dn = 0.011$ . Such nonlinearities should easily be achieved in AlGaAs/GaAs materials. Improved modulation depths may be obtained by reducing absorption losses and maximising the product FG. Since the switching characteristics are critically dependent on  $\alpha$  an experimental study of the variation of  $n_2$  with  $\alpha$  is being carried out. These results and the experimental measurements of nonlinear switching in AlGaAs/GaAs AMZIs will be presented at IGWO '88.

### References

- 1 H. Kawaguchi, Optics Letters **10** 411 (1985).
- 2 A. Von Lehmen, J. E. Zucker, J. P. Heritage, D.S. Chemla, IQEC/CLEO (1986)
- 3 T. Tamir, Topics in Applied Physics, Vol 17, Springer Verlag (1979)
- 4 K. Ogusu, Opt. Comm. **53** 169 (1985).
- 5 L. Thylen, E.M. Wright, G.I. Stegeman, C.T. Seaton and J.V. Maloney. Opt. Letts. **11** 739 (1986).

Figure1 The Mach Zehnder Interferometer with branch angle  $c$ . The input power density  $P_{in}$  is split as shown.

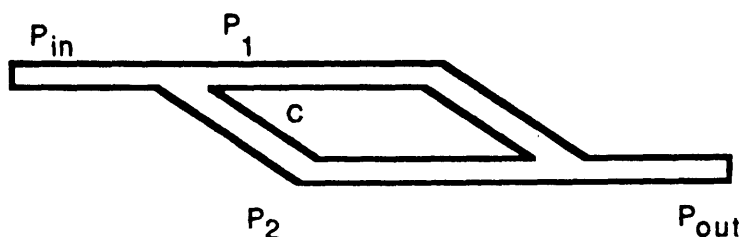


Figure 2 Transverse section of AlGaAs double heterostructure material

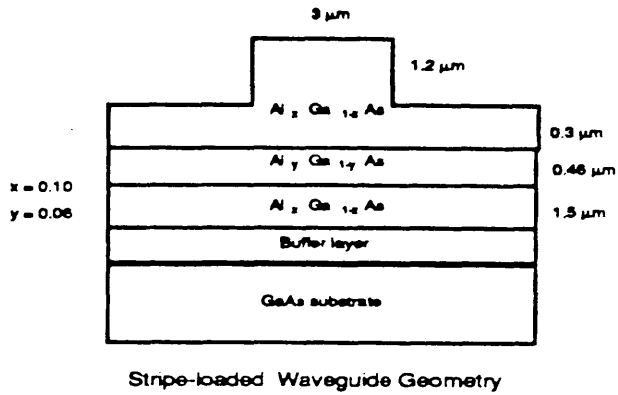


Figure 3 Variation of splitting ratios, F and G, with  $c$ , the angle of the Mach Zehnder

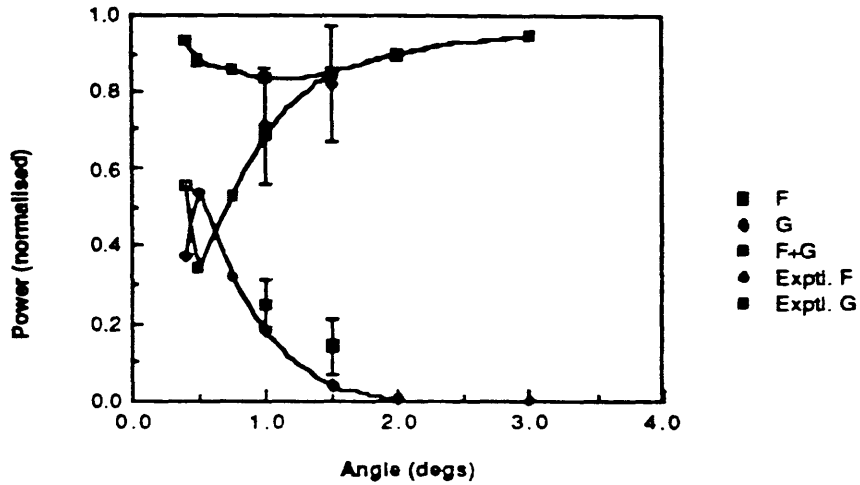


Figure 4 A nonlinear beam propagation method calculation showing the variation of the normalised output power density from an AMZI with  $dn (= n_2 P_{in})$ .

